Transverse Target-Spin Asymmetry Associated with Deeply Virtual Compton Scattering on the Proton and A Resulting Model-Dependent Constraint on the Total Angular Momentum of Quarks in the Nucleon

D I S S E R T A T I O N

zur Erlangung des Doktorgrades
des Fachbereichs Physik
der Universität Hamburg

vorgelegt von

Zhenyu Ye
aus HUNAN, China

Hamburg
2006

Gutachter der Dissertation:	Dr. M. Diehl Prof. Dr. R.-D. Heuer
Gutachter der Disputation:	Prof. Dr. R.-D. Heuer Dr. H. Jung
Datum der Disputation:	19 December, 2006
Vorsitzender des Prüfungsausschusses:	Dr. H. D. Rüter
Vorsitzender des Promotionsausschusses:	Prof. Dr. G. Huber
Leiter des Department Physik:	Prof. Dr. R. Klanner
Dekan der Fakultät für Mathematik, Informatik und Naturwissenschaften:	Prof. Dr. A. Frühwald

Abstract

In this thesis we report on the first results on the transverse target-spin asymmetry associated with deeply virtual Compton scattering on the proton. It is shown that this asymmetry can provide one of the rare possibilities to access the Generalized Parton Distribution (GPD) E of the nucleon, and thus, through models for E, also to the total angular momentum of u and d quarks in the nucleon. The measurement was performed using the 27.6 GeV positron beam of the HERA storage ring and the transversely polarized hydrogen target of the HERMES experiment at DESY. The two leading azimuthal amplitudes of the asymmetry are extracted from the HERMES 2002-2004 data, corresponding to an integrated luminosity of 65.3 pb^{-1}. By comparing the results obtained at HERMES and theoretical predictions based on a phenomenological model of GPDs, we obtain a model-dependent constraint on the total angular momentum of quarks in the nucleon.

Kurzfassung

In dieser Arbeit werden erste Ergebnisse zur transversalen Target-Spin-Asymmetrie in tief virtueller Compton-Streuung am Proton vorgestellt. Es wird gezeigt, dass diese Asymmetrie eine der seltenen Möglichkeiten darstellt, auf die Verallgemeinerte Partonverteilungsfunktion E des Nukleons zuzugreifen, und damit – über Modelle für diese Funktion – auch auf den Gesamtdrehimpuls der Quarks im Nukleon. Die Messung wurde am Positronenstrahl des HERA Speicherrings bei einer Energie von 27.6 GeV unter Verwendung des transversal polarisierten HERMES-Gastargets am DESY durchgeführt.Die beiden führenden Asymmetrieamplituden wurden aus den HERMES-Daten der Jahre 2002-2004 extrahiert, welche einer integrierten Luminosität von 65.3 pb^{-1} entsprechen. Durch Vergleich der bei HERMES erhaltenen Ergebnisse mit einem phänomenologischen GPD-Modell wurde eine modellabhängige Einschränkung für den Gesamtdrehimpuls der u- und d-Quarks im Nukleon erhalten.

Contents

Contents **i**

1 Introduction **1**

2 Generalized Parton Distributions **5**

2.1 Definitions 5
2.2 Interpretations 7
2.3 Properties 8
2.3.1 Symmetry Properties 8
2.3.2 The Forward Limit 9
2.3.3 Link with Nucleon Form Factors 9
2.3.4 Polynomiality 10
2.4 Total Angular Momentum of Partons in the Nucleon 11
2.5 GPD Models Based on Dynamics 11
2.5.1 GPDs from the MIT Bag Model 12
2.5.2 GPDs from the Constituent Quark Model 12
2.5.3 GPDs from the Chiral Quark-Soliton Model 13
2.5.4 GPDs from Lattice QCD 14
2.6 Transition GPDs 15

3 Deeply Virtual Compton Scattering **17**

3.1 Kinematics 18
3.2 Amplitudes at Leading Order 19
3.3 Experimental Observables 22
3.3.1 Azimuthal Asymmetries 22
3.3.2 Cross Sections 28

4 The HERMES Experiment **31**

4.1 The Polarized $e^{\pm}$ Beam at HERA 32
4.2 The Polarized Hydrogen/Deuterium Target of HERMES 34
4.3 The HERMES Forward Spectrometer 37

4.3.1 The Spectrometer Magnet 38
4.3.2 The Tracking Chambers 38
4.3.3 Particle Identification Detectors 40
4.3.4 The Luminosity Monitor 44
4.3.5 The Trigger System 45
4.4 Data Acquisition and Processing 45

5 Data Analysis **48**
5.1 Data Quality 48
5.2 Event Selection 49
5.2.1 Cuts Related to the Scattered Positron 50
5.2.2 Cuts Related to the Photon 51
5.2.3 Beam Polarization Balancing 53
5.3 Monte Carlo Simulation 54
5.3.1 Generating MC Events 54
5.3.2 Comparison between MC and Experimental Data 56
5.4 Detector Resolutions 62
5.5 Methods to Extract Azimuthal Asymmetries 64
5.5.1 The Method of Least Squares 66
5.5.2 The Method of Maximum Likelihood 67
5.5.3 Performance of the Two Methods 69
5.5.4 Sensitivity to the Fit Function and Cross Check 75
5.6 Corrections for Detector Responses 78
5.6.1 Influence of the Transverse Target Magnet 78
5.6.2 Misalignment of the Spectrometer and Beam 80
5.6.3 Miscalibration of the Calorimeter 83
5.6.4 Detection Efficiency 85
5.6.5 Smearing and Acceptance Effects 88
5.7 Correction for Background Contributions 91
5.7.1 Background Contributions 94
5.7.2 Asymmetry of the Semi-inclusive Background 95

6 Results and Discussion **101**
6.1 Transverse Target-Spin Asymmetry Amplitudes 101
6.1.1 Statistical Uncertainties 101
6.1.2 Systematic Uncertainties 101
6.1.3 Summary 104
6.2 Constraint on the Total Angular Momentum of Quarks in the Nucleon . 107
6.2.1 A Parameterization of GPDs 107
6.2.2 Constraining J_u vs J_d 110
6.2.3 Summary and Discussion 116

7 Summary and Outlook **118**

A Conventions **121**
A.1 Light-Cone Coordinates 121
A.2 Dirac Matrices 122

B VGG Code **123**
B.1 Description of the Code 123
B.1.1 Inputs 124
B.1.2 Outputs 125
B.2 TTSA Calculation 126

List of Tables **127**

List of Figures **128**

Bibliography **136**

Acknowledgements **146**

Chapter 1

Introduction

People started long ago to think about questions related to fundamental understanding of the universe, those like what stuff is composed of and what the structure of material objects is. As early as 400 B.C., some Chinese philosophers proposed the idea that matter is composed of five basic elements, i.e., gold, wood, water, fire, and earth, which are generated from "*Yin*" and "*Yang*" by their interactions. At about the same time, Greek philosophers proposed the idea that the elements of matter include wind, water, fire, and earth, which are built up by indivisible building blocks known as "*atomos*".

Our knowledge has continuously improved since then. We know that material objects are made from atoms. The latter are composed of a dense, massive atomic nucleus of positive electric charge, surrounded by a much larger electron cloud of negative electric charge. The interaction between the nucleus and electrons is the electromagnetic force, which can be described by the theory of Quantum ElectroDynamics (QED). We also know that nuclei are made of positively charged protons and neutrally charged neutrons, which are collectively called "nucleons". The latter, which are about 1,800 times more massive than electrons, are bound together in nuclei by the strong force.

Is this the end of the story? Are the nucleons "fundamental" particles? Do we have a theory that is able to describe the strong force?

The answer to the first two questions is no, and the answer to the last question is probably yes. The first indication that the nucleons are not point-like came from Stern's experiments in the 1940's [Est37]. The magnitude of the magnetic moment of the proton was found to be much larger than expected if the nucleon was a point-like object. In the 1960's the dependence of the nucleon form factors, F_1 and F_2, on the squared momentum transfer to the nucleon was measured by Hofstadter *et al.* [Hof61] in elastic electron scattering off the nucleon, $e + N \rightarrow e' + N'$. These form factors characterize charge and magnetic moment distributions in the nucleon. The measurements revealed deviations from those of a point-like object and demonstrated for the first time that the nucleon has a spatial extension of about 10^{-15} m.

After electron beams of higher energies had become available at SLAC, the internal structure of the nucleon was studied in inclusive Deep-Inelastic electron Scattering (DIS), $e + N \rightarrow e' + X'$, in which only the scattered electron e' was detected [Blo69]. An unexpected weak dependence of the DIS cross sections on the photon virtuality Q^2 was observed in these early measurements [Bre69]. Structure functions encoding information about the internal structure of the nucleon are extracted from the measured cross sections. It was discovered that these structure functions have a scaling behavior, namely, they depend only on a single variable x_B, the Bjorken scaling variable, rather than on the two (x_B and Q^2) allowed by kinematics [Bjo69]. These observations were inconsistent with the general belief at that time that the nucleon had a diffuse internal structure, and suggested the existence of point-like constituents in the nucleon.

The constituent structure of the nucleon was confirmed by extensive measurements of the structure functions in the following years. The point-like constituents in the nucleon, which were called "partons" by Feynman [Fey72], were found to be fermions of spin 1/2 [Cal69] and were identified with quarks. The latter were proposed somewhat earlier by Gell-Mann [Gel64] and Zweig [Zwe64] to understand the properties of the many discovered hadronic resonances. Quarks had been thought as only a mathematical tool due to lack of direct observations in experiment.

It was very important for the acceptance of the quark-parton model that the model was identified to conform to Quantum ChromoDynamics (QCD), the theory of the strong force describing the interactions of "colored" quarks via the exchange of "colored" gluons. The predictive power of QCD rests on the regularization of divergent quantum corrections and on the renormalization procedure which introduces a scale-dependent running coupling constant [Buc06]. The vacuum is understood as a polarized medium of virtual particles and is paramagnetic in QCD so that the effective coupling constant decreases with increasing energy. This asymptotic freedom property of QCD [Gro73, Pol73] provides an explanation of the scaling behavior of the structure functions: at large Q^2 where the effective strong coupling constant is small, the incoming lepton scatters almost incoherently on partons in the nucleon. Hence the structure functions can be given in terms of Parton Distribution Functions (PDFs), $q(x, \mu^2)$ for quarks and $g(x, \mu^2)$ for gluons, which characterize momentum distributions of partons in the nucleon. The PDFs depend logarithmically on the factorization scale μ^2 which represents the physical scale at which the partons are resolved. The factorization scale μ^2 is usually chosen to be Q^2 in DIS. The PDFs also depend on x, the longitudinal momentum fraction carried by the struck parton, which coincides with x_B in inclusive DIS.

Today our knowledge has matured into the Standard Model with a precise and comprehensive description of the constituents of matter and their interactions. The Standard Model is based on quantum field theory, incorporating relativity and quantum mechanics. According to the Standard Model, the fundamental constituents of ordinary matter are quarks and leptons, interacting via electromagnetic, weak, and strong forces. (The gravitational force is ignored.) The electromagnetic force is mediated by the exchange of photons. The weak force is mediated by the exchange of W and Z bosons. The strong force is mediated by the exchange of gluons. The electromagnetic and weak forces can be unified above the “unification energy” $\sim 10^2$ GeV. Furthermore, the coupling constants of the strong force and the unified electroweak force unify at a scale $\sim 10^{14}$ GeV .

In principle, almost all physics quantities can be calculated from first principles within the framework of the Standard Model. In practice, theoretical predictions are made perturbatively. Extensive tests have been performed of the electroweak theory in regions where perturbative theory is applicable: at LEP at CERN and SLC at SLAC in e^+e^- collisions, and at Tevatron at Fermilab in $p\bar{p}$ collisions. Similarly, tests of QCD have been performed at LEP, Tevatron, and at HERA at DESY in ep collisions. The Standard Model has become the most predictive and best tested scientific framework yet developed [Lyk06]. QED has been called as "the jewel of physics" for its extremely accurate predictions of quantities like the anomalous magnetic moment of the electron.

On the other hand, no efficient analytical tool based on first principles has been developed so far in the non-perturbative regime. This is a problem only at asymptotically high energy for the electroweak force, as in QED, the vacuum is regarded dielectric and the effective coupling constant becomes weaker at larger distances. Such a problem is irrelevant at the energy scales currently reachable in experiments. It is, however, a quite different situation in the strong force sector, where the effective coupling constant is larger at lower energies. The nucleon form factors and PDFs are examples of non-perturbative quantities which are not yet derivable from first principles. Present knowledge on them has to rely on measurements. The situation may change in the near future with the development of Lattice QCD. Measurements on the nucleon structure, and their comparisons to Lattice QCD calculations, will serve as an essential tool for understanding and testing QCD in the non-pertubative regime.

A fundamental property of elementary particles is spin which determines their symmetry behavior under space-time transformations. Through exploring the spin degrees of freedom, precise and sometimes unique information can be obtained on the fundamental interactions and on the nucleon structure. The spin structure of the nucleon can be studied in DIS with polarized lepton beams scattering off polarized targets, and in polarized pp collisions (see, e.g., Ref. [Lea01]). Polarized structure functions (g_1 and g_2) can be extracted from the measured double-spin asymmetries in cross sections. The polarized structure functions can be expressed in terms of helicity-dependent PDFs, $\Delta q(x, \mu^2)$ for quarks and $\Delta g(x, \mu^2)$ for gluons, which describe helicity distributions of partons in the nucleon.

The first results in polarized DIS were obtained at large x_B ($x_B > 0.1$) in experiments E80 [Alg76, Alg78] and E130 [Bau80, Bau83] at SLAC. They confirmed the naive quark-parton model prediction that the double-spin asymmetries on the proton would be large and positive. The EMC experiment [Ash88, Ash89] at CERN was performed with muon beams of high energy which made it possible to measure at small x_B down to $x_B \sim 10^{-4}$. The results turned out to be very surprising and suggested that the spin of the quarks contributes only a small part to the spin of the nucleon, contrary to the expectation of the naive quark-parton model. This is the so-called "spin crisis" [Lea88].

The helicity of the nucleon can be written as the sum of the helicities and angular momenta of quarks and gluons in the nucleon

$$s^z = \frac{1}{2} = \frac{1}{2}\Delta\Sigma(\mu^2) + \Delta G(\mu^2) + L_q^z(\mu^2) + L_g^z(\mu^2), \tag{1.1}$$

where $\Delta\Sigma = \sum \Delta q$ ($q = u,\ d,\ \cdots$) is the fraction of the nucleon helicity carried by quarks and antiquarks, ΔG the contribution from gluon helicities to the nucleon spin, and L_q^z (L_g^z) the contribution from orbital angular momentum of quarks and antiquarks (gluons). In the naive quark-parton model, all the nucleon spin is carried by quark spin. Possible solutions beyond the naive quark-parton model to the "spin crisis" include non-vanishing gluon spin and/or non-vanishing orbital angular momenta of partons.

Generalized Parton Distributions (GPDs) [Mul94, Ji97a, Ji97b, Rad97] are universal, non-perturbative quantities involved in the description of hard exclusive processes. GPDs contain a wealth of information about the quark and gluon structure of the nucleon; they are generalized in the sense that they embody nucleon form factors and ordinary PDFs as limiting cases. Great interest arose in GPDs after it was realized that the total angular momentum carried by quarks, $J_q = \frac{1}{2}\Delta q + L_q^z$, and by gluons, $J_g = \Delta G + L_g^z$, in the nucleon may be accessed through GPDs [Ji97a]. GPDs also encode three-dimensional distributions of partons in the nucleon [Bur00, Bur03a].

Hard exclusive electroproduction of a real photon off the nucleon is also known as Deeply Virtual Compton Scattering (DVCS). Among the presently accessible processes in experiment, it is the theoretically cleanest one to access GPDs. Studies on DVCS have been performed via measurements of absolute cross sections or azimuthal asymmetries in cross sections. The Transverse Target-Spin Asymmetry (TTSA) associated with DVCS on the proton is measurable using an unpolarized lepton beam and a transversely polarized hydrogen target. It has been found [Ell05] and will be shown in this thesis that this asymmetry can provide a rare possibility to access the GPD E of the nucleon, and thus through models for E, also to the total angular momentum of quarks in the nucleon.

In this thesis we will report on the first results on the TTSA associated with DVCS, obtained at the HERMES experiment at DESY. By comparing the HERMES results and theoretical predictions based on a GPD model, we obtain a model-dependent constraint on the total angular momentum of quarks in the nucleon. The thesis is organized as follows: In chapter 2 a brief introduction to GPDs is given; In chapter 3 the DVCS process and the TTSA are described; In chapter 4 a description of the HERMES experimental setup relevant to the present analysis is presented; In chapter 5 the data analysis to extract the TTSA associated with DVCS is described; In chapter 6 the results on the TTSA are presented, together with the derived model-dependent constraint on the total angular momentum of quarks in the nucleon; Summary and outlook are given in chapter 7.

Chapter 2

Generalized Parton Distributions

In this chapter we will discuss the theory of Generalized Parton Distributions (GPDs). Recent reviews on GPDs can be found in Refs. [Ji98a, Rad01, Goe01, Die03, Bel05]. Definitions of GPDs are given in section 2.1 according to the conventions given in App. A. Their interpretations are discussed in section 2.2. Properties of GPDs deduced from general symmetry considerations and relations of GPDs to ordinary Parton Distribution Functions (PDFs) and nucleon Form Factors (FFs) are described in section 2.3. The connection between GPDs and the total angular momentum of partons in the nucleon is described in section 2.4. Knowledge obtained from dynamical models of GPDs is briefly reviewed in section 2.5. A brief introduction to the so-called transition GPDs is given in section 2.6.

2.1 Definitions

GPDs can be defined through non-forward matrix elements of bilocal operators constructed by quark and gluon fields. At leading twist[1] (twist-two) level, there are four quark helicity-conserving GPDs. They can be defined, according to Ref. [Ji97a], as[2]

$$\begin{aligned} F^q &= \int dz^- e^{ix\bar{P}^+z^-} \langle p'|\bar{\psi}_q(-z/2)\gamma^+\psi_q(z/2)|p\rangle\Big|_{z^+=\vec{z}_T=0} \\ &= \frac{1}{\bar{P}^+}\bar{u}(p')\left[H^q(x,\xi,t,\mu^2)\gamma^+ + E^q(x,\xi,t,\mu^2)\frac{i\sigma^{+\alpha}\Delta_\alpha}{2m_N}\right]u(p), \end{aligned} \tag{2.1}$$

[1]The "twist" of an operator is defined as the dimension minus the spin of the operator. The twist of a GPD is given by the twist of the operator defining the GPD.

[2]The gauge link between the two fields at positions $-z/2$ and $z/2$ has been omitted.

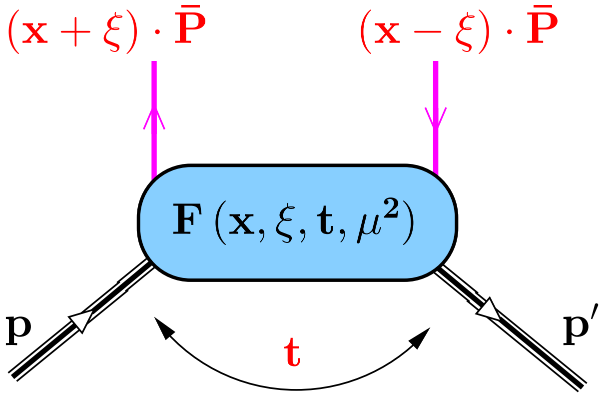

Figure 2.1: Diagram illustrating the definition of the generalized parton distributions.

$$
\begin{aligned}
\widetilde{F}^q &= \int dz^- e^{ix\bar{P}^+z^-} \langle p'|\bar{\psi}_q(-z/2)\gamma^+\gamma_5\psi_q(z/2)|p\rangle\Big|_{z^+=\vec{z}_T=0} \\
&= \frac{1}{\bar{P}^+}\bar{u}(p')\left[\widetilde{H}^q(x,\xi,t,\mu^2)\gamma^+\gamma_5 + \widetilde{E}^q(x,\xi,t,\mu^2)\frac{\gamma_5\Delta^+}{2m_N}\right]u(p),
\end{aligned}
\tag{2.2}
$$

where $x \pm \xi$ (see Fig. 2.1) are the longitudinal momentum fractions carried by the involved quarks, $\bar{P} = (p+p')/2$ the average of the initial (p) and final (p') nucleon four-momenta, ψ_q the quark field of flavor q, u the nucleon spinor, $\Delta = p' - p$ the four-momentum transfer between the initial and final nucleons, $t = \Delta^2$ the Mandelstam invariant, μ^2 the factorization scale, and m_N the nucleon mass. Here and below we have used $\hbar = c = 1$.

The right-hand side in the first line of Eqs. (2.1) and (2.2) can be interpreted as Fourier integrals along the light-cone distance z^- of matrix elements of bilocal quark field operators, sandwiched between the initial and final nucleons. These Fourier integrals are parameterized by the four functions shown in the second line, namely, at the nucleon side, a vector transition parameterized by the function H^q, a tensor transition by E^q, an axial-vector transition by $\widetilde{H}^q$, and a pseudoscalar transition by $\widetilde{E}^q$. The GPDs H^q and $\widetilde{H}^q$ conserve the nucleon helicity, while E^q and $\widetilde{E}^q$ do not. The GPDs H^q and E^q ($\widetilde{H}^q$ and $\widetilde{E}^q$) are also called "unpolarized" ("polarized") due to the corresponding vector (axial-vector) quark field operator.

The four quark helicity-flip GPDs can be defined as [Die01],

$$
\begin{aligned}
F_T^{q,\perp} &= \int dz^- e^{ixP^+z^-} \langle p'|\bar{\psi}_q(-z/2) i\sigma^{+\perp}\psi_q(z/2)|p\rangle\Big|_{z^+=\vec{z}_T=0} \\
&= \frac{1}{P^+}\bar{u}(p')\Big[H_T^q(x,\xi,t,\mu^2) i\sigma^{+\perp} + \widetilde{H}_T^q(x,\xi,t,\mu^2)\frac{P^+\Delta^\perp - \Delta^+P^\perp}{m_N^2} \\
&\quad + E_T^q(x,\xi,t,\mu^2)\frac{\gamma^+\Delta^\perp - \Delta^+\gamma^\perp}{2m_N} + \widetilde{E}_T^q(x,\xi,t,\mu^2)\frac{\gamma^+P^\perp - P^+\gamma^\perp}{m_N}\Big] u(p),
\end{aligned}
\tag{2.3}
$$

where $\perp = 1, 2$ is a transverse index.

Similar definitions can be written for the gluon GPDs. For example, the two "unpolarized" gluon helicity-conserving GPDs, H^g and E^g, can be defined as (according to the convention in Ref. [Die03])

$$
\begin{aligned}
F^g &= \frac{1}{P^+}\int dz^- e^{ixP^+z^-} \langle p'|G^{+\mu}(-z/2) G_\mu{}^+(z/2)|p\rangle\Big|_{z^+=\vec{z}_T=0} \\
&= \frac{1}{2P^+}\bar{u}(p')\left[H^g(x,\xi,t,\mu^2)\gamma^+ + E^g(x,\xi,t,\mu^2)\frac{i\sigma^{+\alpha}\Delta_\alpha}{2m_N}\right] u(p),
\end{aligned}
\tag{2.4}
$$

where $G^{\mu\nu}$ denotes the gluon field strength.

2.2 Interpretations

GPDs can be regarded as parton-nucleon scattering amplitudes. For example, in the region $x > \xi$ ($x < -\xi$) referred to below as the DGLAP[3] region, F^q can be interpreted as the amplitude for taking a quark (antiquark) of longitudinal momentum fraction $x+\xi$ out of the nucleon, changing the fraction to $x-\xi$, and inserting the parton back to form a recoiled nucleon. In the region $-\xi < x < \xi$ referred to below as the ERBL[4] region, F^q is the amplitude for taking out a quark-antiquark pair with four-momentum $-\Delta$.

A probability density interpretation for GPDs holds at $\xi = 0$, with the light-cone gauge $A^+ = 0$ in the infinite-momentum frame, where the initial and final nucleons are moving quickly along the positive z-direction. It has been shown [Bur00] that, in impact parameter space within the infinite-momentum frame,

$$
h^i\left(x, \vec{b}_\perp, \mu^2\right) = \int \frac{d^2\vec{\Delta}_\perp}{(2\pi)^2} e^{i\vec{b}_\perp\cdot\vec{\Delta}_\perp} H^i\left(x, \xi = 0, -\vec{\Delta}_\perp^2, \mu^2\right) \tag{2.5}
$$

[3]The name follows that of the DGLAP evolution equations [Gri72, Lip75, Alt77, Dok77], which govern the dependence of GPDs on the factorization scale μ^2 in this region.

[4]The name follows that of the ERBL evolution equations [Lep79, Efr80], which govern the dependence of GPDs on the factorization scale μ^2 in this region.

has the probabilistic interpretation to find a parton species i with momentum fraction x and relative distance $\vec{b}_\perp$ from the center of momentum of the nucleon. Integrating $h^i(x, \vec{b}_\perp, \mu^2)$ over $\vec{b}_\perp$ recovers the ordinary PDF $q(x, \mu^2)$ or $g(x, \mu^2)$.

The nucleon helicity-flip GPD E^i has a density interpretation at $\xi = 0$ [Bur03a], similar to the case of the GPD H^i discussed above. In impact parameter space one obtains the density

$$h^i\left(x, \vec{b}_\perp, \mu^2\right) - \frac{1}{2m_N}\frac{\partial}{\partial b_y} e^i\left(x, \vec{b}_\perp, \mu^2\right) \tag{2.6}$$

of unpolarized partons in a nucleon polarized along the positive x-direction, where

$$e^i\left(x, \vec{b}_\perp, \mu^2\right) = \int \frac{d^2\vec{\Delta}_\perp}{(2\pi)^2} e^{i\vec{b}_\perp\cdot\vec{\Delta}_\perp} E^i\left(x, \xi = 0, -\vec{\Delta}_\perp^2, \mu^2\right). \tag{2.7}$$

The impact parameter distribution of partons in a transversely polarized nucleon is thus shifted in the direction perpendicular to the polarization.

2.3 Properties

2.3.1 Symmetry Properties

In the following $A_{Hh,H'h'}$ is used to label the amplitude of the parton-nucleon scattering process (see Fig. 2.1)

$$N(H) + l(h) \to N'(H') + l'(h'), \tag{2.8}$$

where H, H' are the helicities of the initial N and final nucleon N', h and h' those of the partons l and l', respectively. Parity invariance relates the helicity-dependent amplitudes pairwise, namely,

$$A_{Hh,H'h'} = A_{-H-h,-H'-h'}. \tag{2.9}$$

By counting the number of GPDs parameterizing the corresponding helicity-dependent amplitudes of parton-nucleon scattering, one finds the number of GPDs in Eqs. (2.1), (2.2) and (2.3).

Similarly time reversal invariance imposes the constraint on the helicity-dependent amplitudes

$$A_{Hh,H'h'} = A_{H'h',Hh}. \tag{2.10}$$

Thus one has [Bel05]

$$F(x, \xi, t, \mu^2) = F(x, -\xi, t, \mu^2) \tag{2.11}$$

for $F = H$, $\widetilde{H}$, E, $\widetilde{E}$, H_T, $\widetilde{H}_T$, E_T, and

$$\widetilde{E}_T(x, \xi, t, \mu^2) = -\widetilde{E}_T(x, -\xi, t, \mu^2). \tag{2.12}$$

Finally taking the complex conjugate of the defining matrix elements gives [Bel05]

$$\left[F(x,-\xi,t,\mu^2)\right]^* = F(x,\xi,t,\mu^2). \tag{2.13}$$

for $F = H$, $\widetilde{H}$, E, $\widetilde{E}$, H_T, $\widetilde{H}_T$, E_T, and

$$\left[\widetilde{E}_T(x,-\xi,t,\mu^2)\right]^* = -\widetilde{E}_T(x,\xi,t,\mu^2) \tag{2.14}$$

The relations (2.11-2.14) imply that the GPDs are real-valued functions.

2.3.2 The Forward Limit

In the forward limit $\Delta = 0$, the GPDs H and $\widetilde{H}$ for quarks and gluons, and H_T for quarks reduce to the ordinary PDFs. In the quark sector one has

$$H^q(x,\xi=0,t=0,\mu^2) = \begin{cases} q(x,\mu^2) & \text{for } x>0, \\ -\bar{q}(-x,\mu^2) & \text{for } x<0, \end{cases} \tag{2.15}$$

$$\widetilde{H}^q(x,\xi=0,t=0,\mu^2) = \begin{cases} \Delta q(x,\mu^2) & \text{for } x>0, \\ \Delta\bar{q}(-x,\mu^2) & \text{for } x<0, \end{cases} \tag{2.16}$$

$$H_T^q(x,\xi=0,t=0,\mu^2) = \begin{cases} \delta q(x,\mu^2) & \text{for } x>0, \\ \delta\bar{q}(-x,\mu^2) & \text{for } x<0, \end{cases} \tag{2.17}$$

where $q(x)$, $\Delta q(x)$, and $\delta q(x)$ are the unpolarized quark distribution functions, polarized quark distribution functions, and transversity distributions, respectively. Similar expressions hold for the gluon GPDs H^g and $\widetilde{H}^g$. There is no correspondent for the other GPDs, as their Dirac structure vanishes in the forward limit where $\Delta \to 0$.

2.3.3 Link with Nucleon Form Factors

Integrating over x the matrix elements defining GPDs gives matrix elements of local quark-antiquark or gluon operators [Ji97a]. Therefore the Mellin x-moments of GPDs are related to form factors of local currents. The first x-moments of GPDs are related to the nucleon FFs,

$$\int_{-1}^{1} dx\, H^q(x,\xi,t,\mu^2) = F_1^q(t), \quad \int_{-1}^{1} dx\, E^q(x,\xi,t,\mu^2) = F_2^q(t), \tag{2.18}$$

$$\int_{-1}^{1} dx\, \widetilde{H}^q(x,\xi,t,\mu^2) = G_A^q(t), \quad \int_{-1}^{1} dx\, \widetilde{E}^q(x,\xi,t,\mu^2) = G_P^q(t), \tag{2.19}$$

$$\int_{-1}^{1} dx\, H_T^q(x,\xi,t,\mu^2) = G_T^q(t), \tag{2.20}$$

where the Dirac F_1, Pauli F_2, axial G_A, pseudoscalar G_P, and tensor G_T FFs are defined for each quark flavor separately. The conventional proton and neutron FFs are given in terms of quark ones

$$F^p_{1,2} = e_u F^u_{1,2} + e_d F^d_{1,2}, \quad F^n_{1,2} = e_d F^u_{1,2} + e_u F^d_{1,2}, \tag{2.21}$$

where e_q ($q = u,\ d$) is the quark charge of flavor q in unit of the positron charge. Note that in the above equation the contribution to the nucleon FFs from the strange quarks is neglected. Analogous decompositions can be written down for the other nucleon FFs. The normalization of the nucleon FFs at $t = 0$ is given in Tab. 2.1.

	$F_1(0)$	$F_2(0)$	$G_A(0)$	$G_P(0)$	$G_T(0)$
proton	1	$\kappa^p = 1.793$	$g^p_A = 1.267$	$4g^p_A m^2_p/m^2_\pi$	unknown
neutron	0	$\kappa^n = -1.913$	$g^n_A = -1.267$	$4g^n_A m^2_n/m^2_\pi$	unknown

Table 2.1: Normalization of nucleon form factors, with κ being the anomalous magnetic moment of the nucleon, g_A the nucleon axial charge, and $m_{p,n}$ (m_π) the nucleon (pion) mass.

.

2.3.4 Polynomiality

A non-trivial property of the Mellin x-moments of the quark helicity-conserving GPDs is their polynomiality in ξ following from Lorentz invariance [Ji97a]:

$$\int_{-1}^{1} dx\, x^n H^q(x,\xi,t,\mu^2) = h^q_{0,n}(t,\mu^2) + \cdots + h^q_{n+1,n}(t,\mu^2)\xi^{n+1}, \tag{2.22}$$

$$\int_{-1}^{1} dx\, x^n E^q(x,\xi,t,\mu^2) = e^q_{0,n}(t,\mu^2) + \cdots + e^q_{n+1,n}(t,\mu^2)\xi^{n+1}, \tag{2.23}$$

$$\int_{-1}^{1} dx\, x^n \widetilde{H}^q(x,\xi,t,\mu^2) = \tilde{h}^q_{0,n}(t,\mu^2) + \cdots + \tilde{h}^q_{n,n}(t,\mu^2)\xi^{n}, \tag{2.24}$$

$$\int_{-1}^{1} dx\, x^n \widetilde{E}^q(x,\xi,t,\mu^2) = \tilde{e}^q_{0,n}(t,\mu^2) + \cdots + \tilde{e}^q_{n,n}(t,\mu^2)\xi^{n}. \tag{2.25}$$

Time reversal invariance implies that only even powers of ξ are contained in the right-hand side of the above equations. This provides that the highest power of ξ for the GPDs H and E is $n+1$ for odd n and n for even n, and the highest power of ξ for the GPDs $\widetilde{H}$ and $\widetilde{E}$ is $n-1$ for odd n and n for even n. Furthermore due to the fact that the nucleon has spin 1/2, the coefficients of the highest power of ξ for odd n are related to each other [Ji97a]:

$$h^q_{n+1,n}(t,\mu^2) = -e^q_{n+1,n}(t,\mu^2) = \int_{-1}^{1} dz\, z^n\, D^q(z,t,\mu^2). \tag{2.26}$$

Here $D^q(z,t,\mu^2)$ is the so-called D-term [Pol99] which complements the parametrization of GPDs in terms of double distributions [Rad99, Mus00] (see section 6.2.1).

2.4 Total Angular Momentum of Partons in the Nucleon

A gauge-invariant decomposition of the nucleon spin into quark spin $\Delta\Sigma$, quark orbital angular momentum L^q, and gluon total angular momentum J^g has been presented in Ref. [Ji97a]:

$$\frac{1}{2} = J^q(\mu^2) + J^g(\mu^2) = \frac{1}{2}\Delta\Sigma(\mu^2) + L^q_z(\mu^2) + J^g(\mu^2). \tag{2.27}$$

Here the quark total angular momentum $J^q(\mu^2)$ allows a gauge-invariant decomposition into spin $\Delta\Sigma(\mu^2)$ and orbital $L^q_z(\mu^2)$ contributions, contrary to the gluon case.

Recent data on polarized deep-inelastic scattering (see, e.g., Ref. [Air06b]) confirms the EMC results [Ash88, Ash89] which demonstrated that quark spin only contributes a very small amount to the nucleon spin, i.e., $\Delta\Sigma(Q^2 = 5\text{GeV}^2) = 0.330 \pm 0.039$ in the $\overline{MS}$ scheme [Air06b]. Such an observation is inconsistent with the result $\Delta\Sigma^{QM} = 1$ anticipated by the naive quark-parton model, and is also far away from calculations based on relativistic quark models [Jaf90, Suz98] suggesting $\Delta\Sigma \simeq 2/3$. Significant contributions from quark orbital angular momentum and/or from gluon angular momentum are a possible solution to the problem.

Presently, the only known way to access the orbital angular momentum of quarks in the nucleon is provided by GPDs. The total angular momentum of quarks, J^q, has been connected to the second x-moment of the GPDs H^q and E^q [Ji97a]:

$$J^q(\mu^2) = \frac{1}{2}\lim_{t\to 0}\int_{-1}^{1} dx\, x\, \left[H^q(x,\xi,t,\mu^2) + E^q(x,\xi,t,\mu^2)\right]. \tag{2.28}$$

A similar expression holds for gluons.

2.5 GPD Models Based on Dynamics

The lack of knowledge regarding GPDs may be increased by non-perturbative model calculations. Studies on nucleon GPDs have been performed in the framework of the MIT bag model, the constituent quark model, the chiral quark-soliton model, and Lattice QCD. The main features and the results from these approaches are summarized below.

2.5.1 GPDs from the MIT Bag Model

In the MIT bag model [Cho74], the hadron is taken to be a finite region of space (bag) containing quark fields. A minimum number of quarks, which are only weakly coupled to one another, is confined within the bag by a constant and universal energy per unit volume. The quark wave functions in such a sphere of fixed radius can thus be obtained by solving the field equations satisfying the boundary conditions imposed by energy-momentum conservation. From calculations using this model it is found that, at the assumed very low scale $\mathcal{O}(0.2)$ GeV^2 associated with the model, the ξ-dependence of the quark helicity-conserving GPDs [Ji97c] and the one of the helicity-flip GPD H_T^q [Sco05b] is quite weak, while the t-dependence roughly follows that of the nucleon FFs. As the calculation disregarded antiquark degrees of freedom, the observed vanishing contribution in the ERBL region $-\xi < x < \xi$ is not fully reliable, which is crucial for calculations of cross sections. The weak ξ-dependence of the GPDs is also suspected to become stronger with a more transparent prescription for restoring momentum conservation. Possible improvements towards full modeling of GPDs were discussed in Ref. [Sco05b], including accounting for the role of antiquarks, using a better prescription for restoring momentum conservation, etc.

2.5.2 GPDs from the Constituent Quark Model

In the constituent quark model hadrons are simple bound states of a few massive quark constituents. Confinement is implemented by an *ad hoc* potential. The connection between GPDs and constituent quark model wave functions was first studied in Ref. [Sco03] where a non-relativistic, point-like constituent quark model was used to calculate the GPD H^q. At the low scale $\mu^2 = 0.34$ GeV^2 associated with the model, the ξ-dependence of the valence quark GPD H was found to be weak, and the t-dependence was strong, in comparison with the one predicted in the MIT bag model [Ji97c]. The GPD E was not studied due to the non-relativistic condition. Neither was the ERBL region explored as the simple constituent quark model only effectively simulates the valence quarks.

There are two main directions in the developments of the constituent quark model approach. One direction is to consider the constituent quarks as complex systems so that the sea quark contribution can be evaluated and the resulting GPDs are valid also in the ERBL region. A stronger ξ-dependence of the quark GPDs H and $\widetilde{H}$ in the ERBL region than the one in the DGLAP region $|x| > \xi$ was found in Ref. [Sco04, Sco05a]. The other direction makes use of light-front dynamics, which allows the estimation of relativistic effects in a covariant framework. In this framework, all the eight twist-two quark GPDs may be evaluated by assuming that at the low scale valence quarks can be interpreted as the constituent quarks. This assumption is based on the idea that there exists a scale μ^2 where the short range (perturbative) part of the interaction is negligible and, thereafter, the gluons and sea quarks are suppressed, while the long

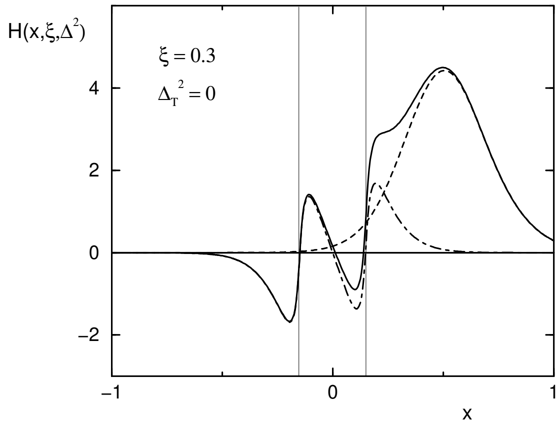

Figure 2.2: Figure taken from Ref. [Pet98]: the flavor-singlet GPD $H^{u+d}(x, \xi, \Delta_T^2)$ for $\Delta_T^2 = 0$ ($\Delta_T^2 \equiv -\Delta^2 - \xi^2 m_N^2$) and $\xi = 0.15$ (the ξ in the figure as defined in Ref. [Pet98] is two times of the ξ used here). *Dashed line*: contribution from the discrete level. *Dashed-dotted line*: contribution from the Dirac continuum. *Solid line*: the total distribution (sum of the dashed and dashed-dotted curves). The vertical lines mark the crossover points $x = \pm\xi$.

range (confining) part of the interaction produces a proton composed mainly by (three) valence quarks [Par76]. The studies in Refs. [Bof03, Bof04, Pas05] observed a weak ξ-dependence and strong t-dependence of the valence quark GPDs at low scales, similar to the one observed in the MIT bag model [Ji97c, Sco05b].

2.5.3 GPDs from the Chiral Quark-Soliton Model

According to the chiral quark-soliton model [Dia88], the nucleon can be viewed as N_c "valence" quarks bound in a self-consistent pion field whose energy coincides with the aggregate energy of the Dirac sea of quarks. At the limit of large N_c, the nucleon is heavy and can be regarded as a "soliton" of the pion field. The GPDs derived according to such a picture were explicitly proved to satisfy general requirements, such as their connections to PDFs and nucleon FFs [Pet98, Pen00], and the polynomiality property [Sch02, Sch03]. Calculations were firstly performed for flavor combinations leading in N_c of the four quark helicity-conserving GPDs at a low scale $\mu^2 = 0.36$ GeV^2 [Pet98, Pen00, Goe01]. The authors of Refs. [Pet98, Pen00] found that the contribution from the Dirac sea of quarks to the flavor-singlet GPD H^{u+d} and to the flavor non-singlet GPD $\widetilde{H}^{u-d}$ exhibited fast crossovers approximately at the points $x = \pm\xi$ (see Fig. 2.2).

Further investigations in Ref. [Pen00, Goe01] lead towards some interesting observations of the behavior of the GPDs. It was found that the chiral quark-soliton model did not support a factorized t-dependence for the quark flavor-singlet GPD H^{u-d} [Goe01],

$$H(x, \xi, t) = H(x, \xi) \cdot F_1(t), \tag{2.29}$$

or for the quark flavor non-singlet GPD $\widetilde{H}^{u-d}$ [Pen00],

$$\widetilde{H}(x, \xi, t) = \widetilde{H}(x, \xi) \cdot G_A(t). \tag{2.30}$$

However, a Regge-theory inspired ansatz, i.e.,

$$\begin{aligned} H^q(x, \xi = 0, t) &= \frac{1}{x^{\alpha' t}}\, q(x), \\ \widetilde{H}^q(x, \xi = 0, t) &= \frac{1}{x^{\alpha' t}}\, \Delta q(x), \end{aligned} \tag{2.31}$$

where α' can be interpreted as the slope of a Regge trajectory, described qualitatively their results.

The nucleon helicity-flip GPD E was studied in Ref. [Goe01]. The authors found that the forward limit of the quark flavor non-singlet GPD $E^{u-d}(x, \xi = 0, t = 0) = e^u(x) - e^d(x)$ consisted of a valence contribution whose shape is well described by $u_{val}(x) + d_{val}(x)$, and a sea part peaked around $x = 0$ (see Fig. 2.3). The study in [Pen00] showed that the flavor non-singlet GPD $\widetilde{E}^{u-d}$ is dominated in a large range of t and ξ by the pion pole contribution

$$\lim_{t \to m_\pi^2} \widetilde{E}_\pi(x, \xi, t) = -\frac{4 g_A m_N^2}{|\xi|\,(t - m_\pi^2)} \theta(|x| < \xi) \Phi_\pi(x/\xi), \tag{2.32}$$

where $\Phi_\pi(z) = 3(1 - z^2)/4$ is the asymptotic pion distribution amplitude. By taking the numerical results in [Pet98], the first few coefficients in the Gegenbauer expansion for the D-term [Pol99] were obtained and quoted in Ref. [Kiv01]. These numerical results were found to be compatible with the ones calculated using explicit model expressions [Sch02].

In section 6.2 a parameterization of GPDs proposed in Ref. [Goe01] is described, which is based on the above chiral quark-soliton model results. This parameterization is used to obtain a constraint on the total angular momentum of quarks in the nucleon.

2.5.4 GPDs from Lattice QCD

Lattice QCD is a computational approach to investigate the strong interaction between quarks and gluons. In this framework, quarks are placed at the interstices of a lattice and interact with each other via the exchange of gluons along the links between the quarks. On the lattice, one cannot calculate the GPDs directly but rather their Mellin

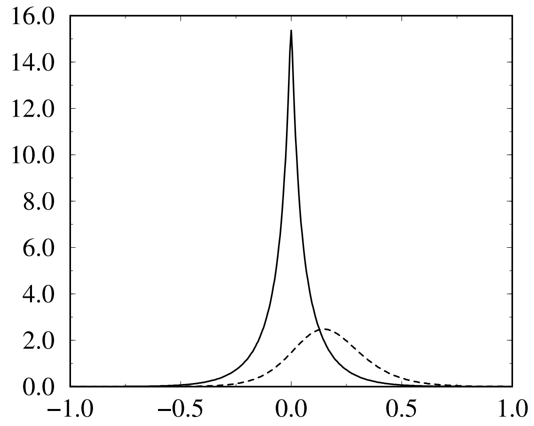

Figure 2.3: Figure taken from Ref. [Goe01]: The GPD $E^{u-d}(x, \xi = 0, t = 0) = e^u(x) - e^d(x)$ as a function of x. Dashed curve: contribution from valence level. Solid curve: contribution of the Dirac continuum.

x-moments. Results from Lattice QCD were recently reported on the orbital angular momentum of quarks in the nucleon [Hag03, Goc04], the transverse structure of the nucleon [Neg04, Goc05a], and the quark helicity-flip GPDs [Goc05b]. The time-consuming calculation for disconnected diagrams was however not included in these studies. An unquenched Lattice QCD calculation gave $2J_{u+d} \sim 0.675 \pm 0.007$ with vanishing quark orbital angular momentum $L_{u+d} \sim 0$ at $m_\pi^2 \sim 900$ MeV^2 [Hag03], compatible with a quenched calculation result $J_u = 0.37 \pm 0.06$, $J_d = -0.04 \pm 0.04$, which was extrapolated linearly in m_π^2 to the physical pion mass [Goc05a]. In Refs. [Neg04, Goc05a] it was found that the lowest three x-moments of the quark helicity-conserving GPDs follow a form-factor-like dipole shape in t. It was also found that the t-dependence of these moments gets flatter when the order of the moments in x increases. Such an observation disfavors the factorized t-dependence of GPDs, as does the chiral quark-soliton model. As more weights are received by the x-moments from the large x region when the order of the moments in x increases, the flatter t-dependence of the higher order x-moments implies that the transverse size of the nucleon decreases when $x \to 1$. Such a behavior is expected in Ref. [Bur03a].

2.6 Transition GPDs

So far the discussion was focused on GPDs which describe an elastic transition, say from a proton to a proton. The definition of these GPDs in section 2.1 can be extended to the case where the final target nucleon is another baryon, e.g. $p \to n$ or $p \to \Delta$, and even to continuum states like $p \to n\pi^+$. The extension is straightforward, e.g.

$$\begin{aligned} & \int dz^- e^{ix\bar{P}^+ z^-} \langle n(p')|\bar{\psi}_d(-z/2)\gamma^+\psi_u(z/2)|p(p)\rangle\Big|_{z^+=\vec{z}_T=0} \\ = & \frac{1}{\bar{P}^+}\bar{u}(p')\left[H^{du}_{p\to n}(x,\xi,t,\mu^2)\gamma^+ + E^{du}_{p\to n}(x,\xi,t,\mu^2)\frac{i\sigma^{+\alpha}\Delta_\alpha}{2m_N}\right]u(p), \end{aligned} \tag{2.33}$$

where the newly introduced transition GPDs, $H^{du}_{p\to n}$ and $E^{du}_{p\to n}$, are related to the usual ones by [Man99]

$$\begin{aligned} H^{du}_{p\to n} &= H^u_p - H^d_p, \\ E^{du}_{p\to n} &= E^u_p - E^d_p \end{aligned} \tag{2.34}$$

with the same arguments x, ξ, t, and μ^2.

A recent discussion on the nucleon-to-Δ transition GPDs has been given in Ref. [Gui03]. In the limit of a large number of colours, three $N - \Delta$ transition GPDs are non-zero and are related to the usual GPDs by [Gui03]

$$\begin{aligned} H_M &= \frac{2}{\sqrt{3}}\left(E^u_p - E^d_p\right), \\ C_1 &= \sqrt{3}\left(\widetilde{H}^u_p - \widetilde{H}^d_p\right), \\ C_2 &= \frac{\sqrt{3}}{4}\left(\widetilde{E}^u_p - \widetilde{E}^d_p\right). \end{aligned} \tag{2.35}$$

Models for these transition GPDs are important to describe the background contribution in all those experiments [Gui03], for which a full decomposition of various nucleon resonances is required.

Chapter 3

Deeply Virtual Compton Scattering

In Deeply Virtual Compton Scattering (DVCS), a virtual photon (emitted by an incoming lepton) is absorbed and a real photon is produced by the nucleon, with the recoiling nucleon being in its ground state[1], i.e., $\gamma^*(q)N(P) \to \gamma(q')N(P')$. It has been proved [Ji98c, Rad98, Col99] that, in the general Bjorken limit, namely, at large Q^2 and fixed x_B and $-t$ (these kinematic variables will be explained in section 3.1), the leading twist[2] (twist-two) amplitude of DVCS can be factorized into a partonic scattering amplitude calculable in perturbative theory, and a non-perturbative part parameterized in terms of GPDs defined in section 2.1

$$\mathcal{A}(\xi, t, Q^2) = \sum_{q=u,d,\ldots} \int_{-1}^{1} dx\, F_q(x, \xi, t, Q^2) \cdot \sigma_{\gamma^* q \to \gamma q}(x, \xi, t, Q^2) + \cdots\,, \tag{3.1}$$

where $\xi \simeq x_B/(2 - x_B)$ in the general Bjorken limit, F_q refers to the GPD of the quark species q and the ellipsis denotes power-suppressed contributions. The diagram for the leading order contribution to DVCS is shown in Fig. 3.1.

In the Bethe-Heithler (BH) process, a virtual photon is absorbed by the nucleon and a real photon is emitted by the incoming or scattered lepton (see Fig. 3.1). The BH process interferes with the DVCS process as they have the same final state. The amplitude of the BH process can be explicitly calculated in Quantum ElectroDynamics (QED) in terms of nucleon form factors (FFs), whose values at low $-t$ have been precisely measured in elastic electron-nucleon scattering. It has been shown that the BH-DVCS interference can be studied through azimuthal asymmetries with respect to beam spin, beam charge, and target spin [Bel02]. Given the known BH amplitude, both the magnitude and the phase of the DVCS amplitude can be extracted from such a measurement, while, by

[1]In this chapter we only deal with elastic processes where the recoiling nucleon is in the ground state. A discussion on associated processes where the recoiling nucleon is not in the ground state will be given in section 5.2.

[2]Kinematic definition of twist is adopted here, i.e., terms suppressed by powers of $1/Q$ are of higher twists.

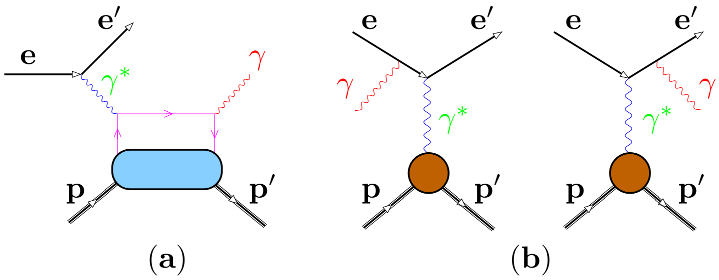

Figure 3.1: (a) Diagram for deeply virtual Compton scattering, the blob connecting the incoming and outgoing nucleons as described by GPDs; (b) diagram for the Bethe-Heithler process, the blob connecting the incoming and outgoing nucleons as described by nucleon FFs.

measurements of the DVCS cross section, only the magnitude of the DVCS amplitude is accessible.

In this chapter we will discuss the theory of DVCS. The kinematic variables are described in section 3.1. Results for the BH and DVCS amplitudes to leading order accuracy in perturbative theory are presented in section 3.2. A brief review on observables associated with DVCS and experimental results is given in section 3.3.

3.1 Kinematics

For eletroproduction of a real photon off the nucleon

$$l(k) + N(P) \longrightarrow l(k') + N(P') + \gamma(q'), \tag{3.2}$$

kinematic variables are given by the four-momenta of the initial (final) electron and nucleon, k and P (k' and P'), respectively. The photon virtuality Q^2 and the Bjorken variable x_B are defined as

$$Q^2 \equiv -q^2 = -(k-k')^2, \tag{3.3}$$

$$x_B \equiv \frac{Q^2}{2Pq}, \tag{3.4}$$

where q denotes the four-momentum of the virtual photon. In the laboratory frame where the target is at rest (see Fig. 3.2), they can be calculated as

$$Q^2 \overset{\text{lab.}}{=} 4EE_e \sin^2\left(\frac{\theta_e}{2}\right), \tag{3.5}$$

$$x_B \overset{\text{lab.}}{=} \frac{Q^2}{2m_N\nu}, \tag{3.6}$$

where E (E_e) is the energy of the incoming (scattered) lepton, θ_e (ϕ_e) the lepton scattering polar (azimuthal) angle, m_N the nucleon mass, and $\nu = E - E_e$ the energy of the virtual photon. The variable

$$y \equiv \frac{Pq}{Pk} \stackrel{\text{lab.}}{=} \frac{\nu}{E} \tag{3.7}$$

represents the fraction of the beam energy carried by the virtual photon. The invariant mass of the system of virtual photon and nucleon is given by

$$W^2 \equiv (p+q)^2 \stackrel{\text{lab.}}{=} m_N^2 + 2m_N\nu - Q^2. \tag{3.8}$$

The invariant momentum transfer from initial to final nucleon, defined as

$$t \equiv (P - P')^2, \tag{3.9}$$

can be calculated either using the photon energy E_γ

$$t \stackrel{\text{lab.}}{=} -Q^2 - 2E_\gamma \left(\nu - \sqrt{\nu^2 + Q^2}\cos\theta_{\gamma^*\gamma}\right), \tag{3.10}$$

or without using the photon energy E_γ by assuming that the recoiling proton is in the ground state,

$$t_c \stackrel{\text{lab.}}{=} \frac{-Q^2 - 2\nu\left(\nu - \sqrt{\nu^2 + Q^2}\cos\theta_{\gamma^*\gamma}\right)}{1 + \frac{1}{m_N}\left(\nu - \sqrt{\nu^2 + Q^2}\cos\theta_{\gamma^*\gamma}\right)}. \tag{3.11}$$

Here $\theta_{\gamma^*\gamma}$ is the angle between the virtual photon and the real photon:

$$\theta_{\gamma^*\gamma} \equiv \arccos\frac{\vec{q}\cdot\vec{q'}}{|\vec{q}|\left|\vec{q'}\right|}. \tag{3.12}$$

3.2 Amplitudes at Leading Order

Higher order corrections in the QCD coupling constant α_S and $1/Q$ power-suppressed corrections have been studied to understand better the theory background and experimental data on DVCS. Hard scattering amplitudes of the partonic subprocesses have been fully calculated to next-to-leading order (NLO) in α_S [Ji98b, Man98, Bel00b]. Partial results at next-to-next-to-leading order (NNLO) also exist [Mul06]. The evolution kernels for GPDs have been evaluated to NLO [Bel00a]. Power-suppressed corrections to DVCS have been calculated to LO [Bel00c] and NLO [Kiv03]. Moderate effects from higher order and power-suppressed corrections are found in these studies. Results presented below are limited to LO in perturbative theory at twist-three level.

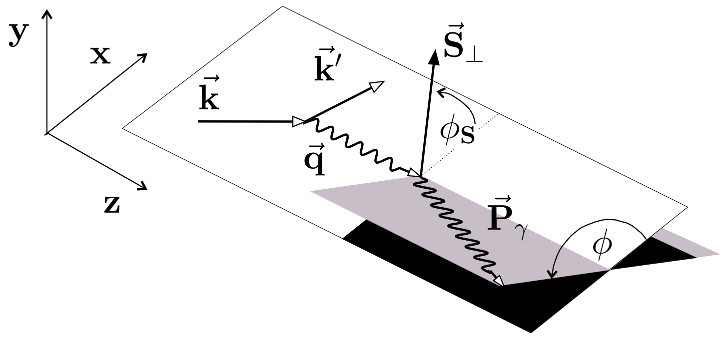

Figure 3.2: Kinematics of real photon production in the target rest frame. The z-direction is chosen along the three-momentum of the virtual photon.

The five-fold cross section for the process (3.2) can be written as [Bel02]

$$\frac{d\sigma}{d\phi d\phi_S dQ^2 dx_B dt} = \frac{\alpha_{em}^3 x_B y}{16\pi^2 Q^2 \sqrt{1 + 4x_B^2 m_N^2/Q^2}} \cdot \left|\frac{\mathcal{T}}{e^3}\right|^2, \tag{3.13}$$

where α_{em} denotes the fine-structure constant, e the electron charge magnitude. The amplitude $\mathcal{T}$ is the coherent sum of the DVCS amplitude $\mathcal{T}_{DVCS}$ and the BH amplitude $\mathcal{T}_{BH}$:

$$|\mathcal{T}|^2 = |\mathcal{T}_{BH}|^2 + |\mathcal{T}_{DVCS}|^2 + \underbrace{\mathcal{T}_{BH}\mathcal{T}_{DVCS}^* + \mathcal{T}_{BH}^*\mathcal{T}_{DVCS}}_{\mathcal{I}}. \tag{3.14}$$

The azimuthal angles ϕ and ϕ_S are defined in the target rest frame, as shown in Fig 3.2, where ϕ denotes the azimuthal angle between the lepton scattering plane and the photon production plane,

$$\phi = \frac{\vec{q} \times \vec{k} \cdot \vec{P}_\gamma}{\left|\vec{q} \times \vec{k} \cdot \vec{P}_\gamma\right|} \cdot \arccos\left(\frac{\vec{q} \times \vec{k} \cdot \vec{q} \times \vec{P}_\gamma}{\left|\vec{q} \times \vec{k}\right| \left|\vec{q} \times \vec{P}_\gamma\right|}\right), \tag{3.15}$$

and ϕ_S denotes the azimuthal angle between the lepton scattering plane and the polarization direction of the transversely polarized target $\vec{S}_\perp$,

$$\phi_S = \frac{\vec{q} \times \vec{k} \cdot \vec{S}_\perp}{\left|\vec{q} \times \vec{k} \cdot \vec{S}_\perp\right|} \cdot \arccos\left(\frac{\vec{q} \times \vec{k} \cdot \vec{q} \times \vec{S}_\perp}{\left|\vec{q} \times \vec{k}\right| \left|\vec{q} \times \vec{S}_\perp\right|}\right). \tag{3.16}$$

The squared magnitude of the BH amplitude $|\mathcal{T}_{BH}|^2$, the one of the DVCS amplitude

$|\mathcal{T}_{DVCS}|^2$, and the interference term $\mathcal{I}$ read [Bel02]

$$|\mathcal{T}_{BH}|^2 = \frac{e^6}{x_B^2 y^2 (1+4x_B^2 M^2/Q^2)\,\mathcal{P}_1(\phi)\mathcal{P}_2(\phi) t} \times \left\{ c_0^{BH} + \sum_{n=1}^{2} c_n^{BH} \cos(n\phi) + s_1^{BH} \sin(\phi) \right\}, \tag{3.17}$$

$$|\mathcal{T}_{DVCS}|^2 = \frac{e^6}{y^2/Q^2} \times \left\{ c_0^{DVCS} + \sum_{n=1}^{2} \left[c_n^{DVCS} \cos(n\phi) + s_n^{DVCS} \sin(n\phi) \right] \right\}, \tag{3.18}$$

$$\mathcal{I} = \frac{\pm e^6}{x_B y^3 \mathcal{P}_1(\phi)\mathcal{P}_2(\phi) t} \times \left\{ c_0^{I} + \sum_{n=1}^{3} \left[c_n^{I} \cos(n\phi) + s_n^{I} \sin(n\phi) \right] \right\}, \tag{3.19}$$

where the + (−) sign in the interference term stands for the negatively (positively) charged lepton beam, $\mathcal{P}_1(\phi)$ and $\mathcal{P}_2(\phi)$ are the lepton propagators:

$$Q^2\mathcal{P}_1(\phi) \equiv (k-q')^2, \tag{3.20}$$

$$Q^2\mathcal{P}_2(\phi) \equiv (k-q+q')^2. \tag{3.21}$$

The Fourier coefficients c_n can be decomposed into an unpolarized part $c_n^{U,U}$, a target-transversely-polarized part $c_n^{U,T}$, and two doubly-polarized parts $c_n^{L,L}$ and $c_n^{L,T}$,

$$c_n = c_n^{U,U} + \Lambda_T \cdot c_n^{U,T} + \lambda \cdot \Lambda_L \cdot c_n^{L,L} + \lambda \cdot \Lambda_T \cdot c_n^{L,T}, \tag{3.22}$$

where λ denotes the beam longitudinal polarization, Λ_L (Λ_T) the target longitudinal (transverse) polarization. On the other hand, the Fourier coefficients s_n is non-vanishing when either the beam or the target is polarized:

$$s_n = \lambda \cdot s_n^{L,U} + \Lambda_L \cdot s_n^{U,L} + \Lambda_T \cdot s_n^{U,T} + \lambda \cdot \Lambda_T \cdot s_n^{L,T}. \tag{3.23}$$

The Fourier coefficients c_n and s_n for the squared DVCS amplitude (interference term) are bilinear (linear) in the Compton form factors (CFFs), which are convolutions of GPDs with hard-scattering kernels:

$$\left\{ \begin{array}{c} \mathcal{H} \\ \mathcal{E} \end{array} \right\} (\xi, t, \mu^2) = \int_{-1}^{1} C^{(-)}(x,\xi) \left\{ \begin{array}{c} H \\ E \end{array} \right\} (x, \xi, t, \mu^2), \tag{3.24}$$

$$\left\{ \begin{array}{c} \widetilde{\mathcal{H}} \\ \widetilde{\mathcal{E}} \end{array} \right\} (\xi, t, \mu^2) = \int_{-1}^{1} C^{(+)}(x,\xi) \left\{ \begin{array}{c} \widetilde{H} \\ \widetilde{E} \end{array} \right\} (x, \xi, t, \mu^2). \tag{3.25}$$

On the right-hand side of the above equations there is a summation over the quark species involved,

$$C^{(\pm)}F = \sum_{q=u,d,s} C^{(\pm)} e_q^2 F_q, \tag{3.26}$$

with $C^{(\pm)}$ having the perturbative expansion

$$C^{(\pm)}(x,\xi) = \frac{1}{x-\xi-i0} \pm \frac{1}{x+\xi-i0} + \mathcal{O}(\alpha_S), \tag{3.27}$$

where e_q denotes the charge of the quark species q. The CFF $\mathcal{F}$ contain both a real part $\Re\mathcal{F}$ and an imaginary part $\Im\mathcal{F}$

$$\mathcal{F} = \Re\mathcal{F} + i\Im\mathcal{F}, \tag{3.28}$$

which are given to LO in α_S by

$$\begin{aligned} \Re\mathcal{F} &= \mathcal{P}\int_{-1}^{1} dx \left(\frac{F}{x-\xi} \pm \frac{F}{x+\xi}\right), & (3.29)\\ \Im\mathcal{F} &= F(x,\xi) \pm F(x,-\xi). & (3.30) \end{aligned}$$

Here $\mathcal{P}$ denotes Cauchy's principle value.

3.3 Experimental Observables

The ratio of the squared DVCS to BH amplitude, $\mathcal{T}_{DVCS}^2/\mathcal{T}_{BH}^2$, behaves approximately according to $-(1-y)t/(yQ)^2$ [Bel02]. At HERMES kinematics, the cross section of the BH process dominates that of DVCS [Kor02]. Cross section differences with respect to beam spin, beam charge, and target spin can serve as a natural tool to study the BH-DVCS interference[3]. The latter was accessed at HERMES by measuring asymmetries of cross sections with systematic uncertainties under well control. On the other hand, at the kinematics of the HERA collider experiments H1 and ZEUS, the magnitude of the DVCS cross section is of the same order as that of the BH process. The DVCS cross section was measured by subtracting the BH background. In the following these observables, their relations to GPDs, and experimental results are described.

3.3.1 Azimuthal Asymmetries

As in the kinematic region of the HERMES experiment the DVCS cross section is typically much smaller than the BH cross section, the contribution of DVCS to the total

[3]Recently, results on cross section differences with respect to beam helicity were reported in Ref. [Cam06].

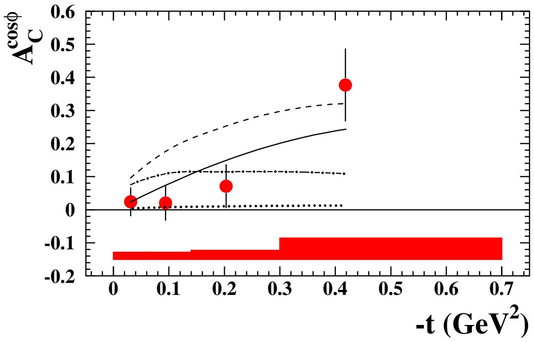

Figure 3.3: Beam-charge asymmetry A_C on the proton measured at HERMES [Air06a]. The $A_C^{\cos\phi}$ amplitude as a function of $-t$, after background correction. The error bars (band) represent(s) the statistical (systematic) uncertainties. The calculations based on GPD models [Van99, Goe01] use either a factorized t-dependence with (dashed-dotted) or without (dotted) the D-term contribution, or a Regge inspired t-dependence with (dashed) or without (solid) the D-term contribution.

cross section is neglected in the following. Since $\xi \simeq x_B/(2-x_B)$ is small in a wide range of experimentally relevant kinematics, terms with pre-factor ξ or x_B can also be neglected, except for the GPD $\widetilde{E}$ because the pion pole contribution to $\widetilde{E}$ scales like ξ^{-1}.

Beam-Charge Asymmetry

The Beam-Charge Asymmetry (BCA), measurable using unpolarized electron/positron beam and an unpolarized target, is defined as

$$A_C(\phi) \equiv \frac{d\sigma(e^+,\phi) - d\sigma(e^-,\phi)}{d\sigma(e^+,\phi) + d\sigma(e^-,\phi)}, \tag{3.31}$$

where the $+$ $(-)$ sign stands for the positively (negatively) charged lepton beam. It is approximately given by a $\cos\phi$ dependence, whose amplitude is proportional to the real part of the CFF $\mathcal{H}$

$$A_C(\phi) \approx A_C^{\cos\phi} \cdot \cos\phi \propto F_1 \cdot \Re\mathcal{H} \cdot \cos\phi, \tag{3.32}$$

where F_1 is the Pauli form factor of the nucleon. Results on the BCA have been reported by the HERMES experiment [Air06a] (see Fig. 3.3). Also shown in Fig. 3.3 are LO calculations based on GPD models in Ref. [Goe01]. It can be seen that these initial data can already be used to distinguish among theoretical models for GPDs.

Beam-Spin Asymmetry

The Beam-Spin Asymmetry (BSA), measurable using a longitudinally polarized (L) lepton beam and an unpolarized (U) target, is defined as

$$A_{LU}(\phi) \equiv \frac{d\sigma(\overrightarrow{e},\phi) - d\sigma(\overleftarrow{e},\phi)}{d\sigma(\overrightarrow{e},\phi) + d\sigma(\overleftarrow{e},\phi)}, \tag{3.33}$$

where $\rightarrow$ ($\leftarrow$) stands for the positive (negative) beam helicity. It is approximately given by a $\sin(\phi)$ dependence, whose amplitude is proportional to the imaginary part of the CFF $\mathcal{H}$

$$A_{LU}(\phi) \approx A_{LU}^{\sin\phi} \cdot \sin\phi \propto F_1 \cdot \Im\mathcal{H} \cdot \sin\phi, \tag{3.34}$$

The BSAs measured at HERMES [Air01] and CLAS [Ste01] are shown in Fig. 3.4. The $A_{LU}^{\sin\phi}$ amplitude measured at HERMES is -0.23 ± 0.04 (stat) $\pm$ 0.03 (syst) at the average kinematics $\langle x_B \rangle = 0.11$, $\langle -t \rangle = 0.27$ GeV^2, $\langle Q^2 \rangle = 2.6$ GeV^2. The $A_{LU}^{\sin\phi}$ amplitude measured at CLAS is -0.202 ± 0.028 (stat) $\pm$ 0.013 (syst) at the average kinematics $\langle x_B \rangle = 0.19$, $\langle -t \rangle = 0.19$ GeV^2, $\langle Q^2 \rangle = 1.25$ GeV^2. Note that the difference in the sign of the extracted $A_{LU}^{\sin\phi}$ amplitudes at HERMES and CLAS is due to the different charge of the lepton beams used. Also shown in Fig. 3.4 are LO model calculations [Kiv01, Goe01].

Longitudinal Target-Spin Asymmetry

The Longitudinal Target-Spin Asymmetry (LTSA), measurable using an unpolarized (U) lepton beam and a longitudinally polarized (L) target, is defined as

$$A_{UL}(\phi) \equiv \frac{d\sigma(\overset{\Rightarrow}{N},\phi) - d\sigma(\overset{\Leftarrow}{N},\phi)}{d\sigma(\overset{\Rightarrow}{N},\phi) + d\sigma(\overset{\Leftarrow}{N},\phi)}, \tag{3.35}$$

where the $\Rightarrow$ ($\Leftarrow$) stands for the target polarization being antiparallel (parallel) to the three-momentum of the virtual photon. It is approximately given by a $\sin(\phi)$ modulation

$$A_{UL}(\phi) \approx A_{UL}^{\sin\phi} \cdot \sin\phi \propto F_1 \cdot \Im\widetilde{\mathcal{H}} \cdot \sin\phi. \tag{3.36}$$

Results on the LTSA measured on the proton and deuteron have been reported by HERMES [Kop05] (see Fig. 3.5). While the $\sin 2\phi$ dependence is theoretically expected to be kinematically suppressed with respect to the $\sin\phi$ dependence (see Fig. 3.5), a sizable $\sin 2\phi$ dependence is observed in the experiment. This observation may suggest that the contributions to twist-three GPDs from quark-gluon correlations, which are not included in the calculation shown in Fig. 3.5, are significant. Note that a measurement of the LTSA with 5.7 GeV electrons and a polarized NH_3 target was recently reported by the CLAS collaboration [Che06].

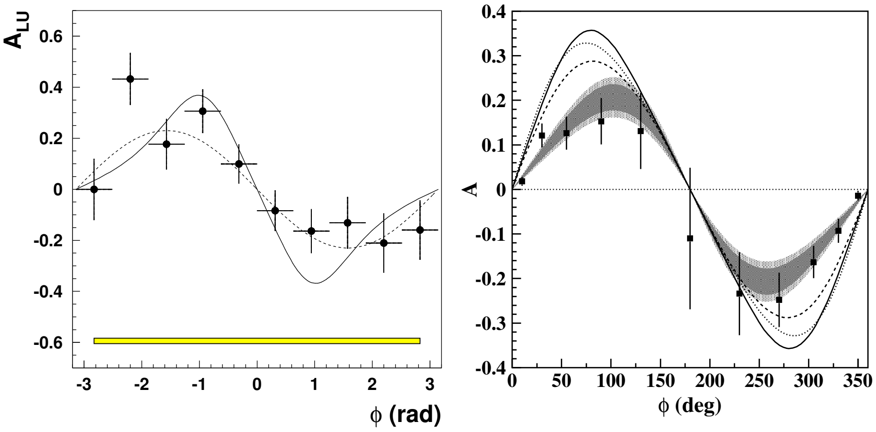

Figure 3.4: Beam-spin asymmetry A_{LU} on the proton measured at HERMES (left panel) [Air01] and CLAS (right panel) [Ste01]. Left: the dashed curve represents a $\sin\phi$ dependence with an amplitude of 0.23, while the solid curve represents the result of a model calculation at twist-three level from Ref. [Kiv01]. The error band below shows the systematic uncertainty. Right: the shaded regions represent the experimental results, while the curves represent model calculations from Refs. [Van99, Goe01]. The dashed (dotted) curve is a calculation with ξ-independent (ξ-dependent) GPDs at leading-twist. The solid curve includes twist-three effects.

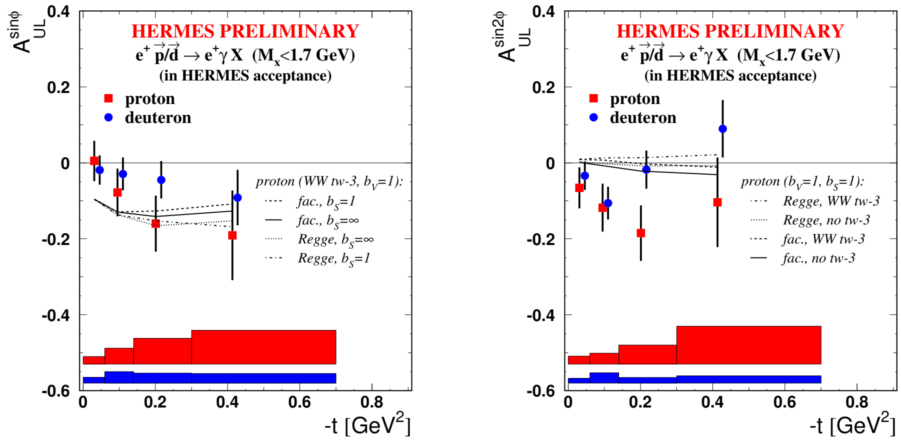

Figure 3.5: Longitudinal target-spin asymmetry A_{UL} on the proton and deuteron measured at HERMES [Kop05]. The $A_{UL}^{\sin\phi}$ amplitude is shown as a function of $-t$, after background correction. Error bars and bands represent the statistical and systematic uncertainties, respectively. The curves shown are calculations based on GPD models [Goe01] for the proton, using either a factorized or a Regge inspired t-dependence with or without twist-three effects in the Wandzura-Wilczek (WW) approximation [Goe01].

Transverse Target-Spin Asymmetry

The theoretical formulae used below refer to the target being transversely polarized with respect to the virtual photon direction, while in the experiment the target polarization is transverse with respect to the incident lepton direction. At HERMES kinematics, these two directions are approximately parallel and the small longitudinal component ($< 10\%$) of the target polarization along the virtual photon direction is neglected in this study. Thus the reasonable approximation

$$d\sigma = d\sigma_{unp} + \Lambda_T \cdot d\sigma_{TP} \tag{3.37}$$

may be used, where $d\sigma_{unp}$ ($d\sigma_{TP}$) denotes the unpolarized (transverse) component of the cross section, and Λ_T the transverse polarization value of the target. The transverse component of the BH-DVCS interference term can be approximated as:

$$\mathcal{I}_{TP} \propto \Im\widehat{M}_N \cdot \sin(\phi - \phi_S)\cos\phi + \Im\widehat{M}_S \cdot \cos(\phi - \phi_S)\sin\phi, \tag{3.38}$$

where $\widehat{M}_N$ and $\widehat{M}_S$ are certain linear combinations of the CFFs $\mathcal{H}$, $\mathcal{E}$, $\widetilde{\mathcal{H}}$ and $\widetilde{\mathcal{E}}$. The full expressions for $\widehat{M}_N$ and $\widehat{M}_S$ can be found in Eq. (71) in Ref. [Bel02] or in Eq. (60) in Ref. [Die05b], and can be approximated as:

$$\begin{aligned} \widehat{M}_N &\simeq -\frac{t}{4M^2} \cdot \left(F_2\mathcal{H} - F_1\mathcal{E}\right), \\ \widehat{M}_S &\simeq -\frac{t}{4M^2} \cdot \left(F_2\widetilde{\mathcal{H}} - F_1\xi\widetilde{\mathcal{E}}\right), \end{aligned} \tag{3.39}$$

where F_2 is the Dirac form factor of the nucleon.

In order to constrain the GPDs involved in Eq. (3.39), the transverse polarization component of the interference term, $\mathcal{I}_{TP}$, has to be singled out. This can be accomplished by forming the transverse (T) target-spin asymmetry with unpolarized (U) beam:

$$A_{UT}(\phi, \phi_S) \equiv \frac{d\sigma(\phi, \phi_S) - d\sigma(\phi, \phi_S + \pi)}{d\sigma(\phi, \phi_S) + d\sigma(\phi, \phi_S + \pi)}. \tag{3.40}$$

It is approximately given by a $\sin(\phi - \phi_S)\cos\phi$ dependence plus a $\cos(\phi - \phi_S)\sin\phi$ dependence, whose amplitudes are given by

$$A_{UT}^{\sin(\phi-\phi_S)\cos\phi} \propto -\frac{t}{4m_N^2} \cdot \left(F_2 \cdot \Im\mathcal{H} - F_1 \cdot \Im\mathcal{E}\right), \tag{3.41}$$

$$A_{UT}^{\cos(\phi-\phi_S)\sin\phi} \propto -\frac{t}{4m_N^2} \cdot \left(F_2 \cdot \Im\widetilde{\mathcal{H}} - F_1 \cdot \Im\widetilde{\mathcal{E}}\right). \tag{3.42}$$

At present, there exists a code [Van03] designed to calculate observables in the exclusive reaction $ep \to ep\gamma$. It is based on the GPD model proposed in Ref. [Goe01], in which the total quark angular momentum in the nucleon, J_u and J_d, enters as free parameters for the GPD E. It has been used to evaluate the TTSA arising from the BH-DVCS interference [Ell05] (see App. B). The projections for $A_{UT}^{\sin(\phi-\phi_S)\cos\phi}$ and $A_{UT}^{\cos(\phi-\phi_S)\sin\phi}$ are calculated for different values of J_u. Since the contributions of u-quark and d-quark are proportional to the corresponding squared charge, the d-quark contribution is suppressed and hence in the calculations a fixed value is used for J_d. The latter was chosen to be $J_d = 0$, inspired by the results of recent lattice calculations (see e.g. Ref. [Goc04]). Using both Regge and factorized ansätze, the asymmetries are calculated for the four possible cases setting the profile parameters b_{val} and b_{sea} to either one or infinity. Comparing all sets of projections to each other, the amplitudes of the TTSA appear to be sensitive only to the change in b_{sea} from one to infinity. The corresponding differences are small and can be seen by comparing Figs. 3.7 and 3.8, where the amplitudes are shown in dependence on Q^2, x_B and $-t$ together with the projected statistical errors for 8 million DIS events. In order to study the contributions of the GPDs H, $\widetilde{H}$ and $\widetilde{E}$ alone, calculations are done for $E = 0$ as well.

As expected from Eqs. (3.41) and (3.42), variations in the parameter settings for the GPD E become manifest in $A_{UT}^{\sin(\phi-\phi_S)\cos\phi}$ while $A_{UT}^{\cos(\phi-\phi_S)\sin\phi}$ shows only minor changes. The latter are apparent only in the kinematic regime of large x_B or correspondingly large Q^2 since the contribution of the GPDs E_q to $A_{UT}^{\cos(\phi-\phi_S)\sin\phi}$ is suppressed by x_B and thus has been neglected in Eq. (3.42). Further discussions on theoretical predictions of the TTSA amplitudes will be given in section 6.2.

Double-spin asymmetries

Double-spin asymmetries can be measured with a longitudinally (L) polarized lepton beam and a longitudinally (L) or transversely (T) polarized target. They can be defined as

$$\begin{aligned}
A_{LL}(\phi) &\equiv \frac{d\sigma(\overrightarrow{e},\overset{\Rightarrow}{N},\phi) - d\sigma(\overleftarrow{e},\overset{\Rightarrow}{N},\phi) - d\sigma(\overrightarrow{e},\overset{\Leftarrow}{N},\phi) + d\sigma(\overleftarrow{e},\overset{\Leftarrow}{N},\phi)}{d\sigma(\overrightarrow{e},\overset{\Rightarrow}{N},\phi) + d\sigma(\overleftarrow{e},\overset{\Rightarrow}{N},\phi) + d\sigma(\overrightarrow{e},\overset{\Leftarrow}{N},\phi) + d\sigma(\overleftarrow{e},\overset{\Leftarrow}{N},\phi)}, \qquad (3.43)\\
A_{LT}(\phi,\phi_S) &\equiv \frac{d\sigma(\overrightarrow{e},\phi,\phi_S) - d\sigma(\overrightarrow{e},\phi,\phi_S+\pi) - d\sigma(\overleftarrow{e},\phi,\phi_S) + d\sigma(\overleftarrow{e},\phi,\phi_S+\pi)}{d\sigma(\overrightarrow{e},\phi,\phi_S) + d\sigma(\overrightarrow{e},\phi,\phi_S+\pi) + d\sigma(\overleftarrow{e},\phi,\phi_S) + d\sigma(\overleftarrow{e},\phi,\phi_S+\pi)}.
\end{aligned}$$

Unlike the single-spin asymmetries which vanish in the BH process alone, the double-spin asymmetries receive contributions from pure BH cross sections. Moreover, the azimuthal dependence of the double-spin asymmetries are cosine-like, while the one of the single-spin asymmetries are sine-like. Until now, no measurement of double-spin asymmetries has been performed.

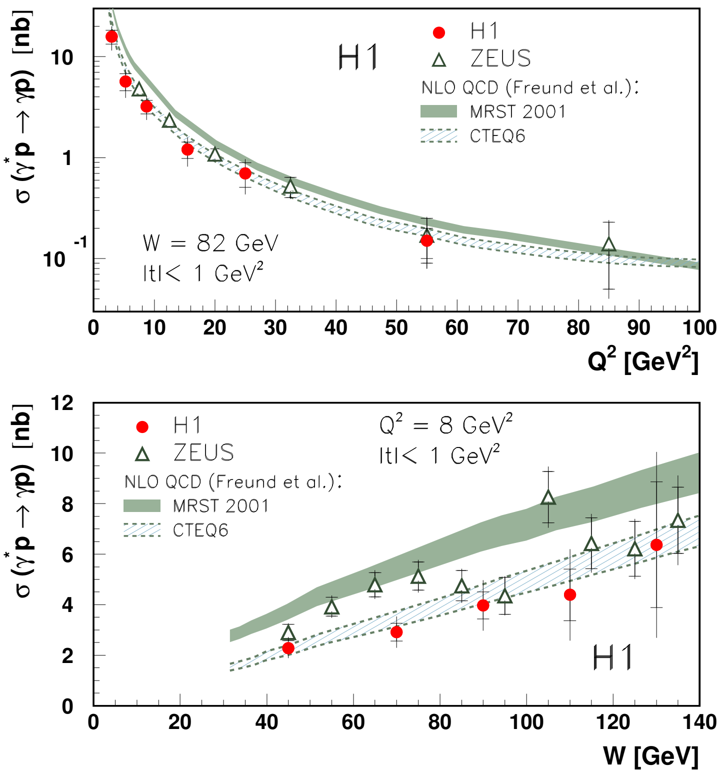

Figure 3.6: DVCS cross section measured at H1 and ZEUS [Akt05, Che03]. Also shown are NLO QCD calculations (bands) using a parameterization of the GPDs proposed in Ref. [Fre03].

3.3.2 Cross Sections

Results on the DVCS cross sections have been reported by the H1 experiment [Adl01, Akt05] and the ZEUS experiment [Che03] (see Fig. 3.6). The cross section has been measured in the kinematic region $30 < W < 140$ GeV, $2 < Q^2 < 80$ GeV^2, and $-t < 1$ GeV^2 as a function of Q^2 and as a function of W, and differentially in t. NLO QCD calculations give a good description of the normalization as well as of the Q^2-dependence and W-dependence using a parameterization of the GPDs proposed in Ref. [Fre03]. The calculations rely on ordinary PDFs in the DGLAP region and generate the skewness dynamically. The GPDs in the ERBL region are taken to be arbitrary analytical functions ensuring a smooth continuation to the DGLAP region.

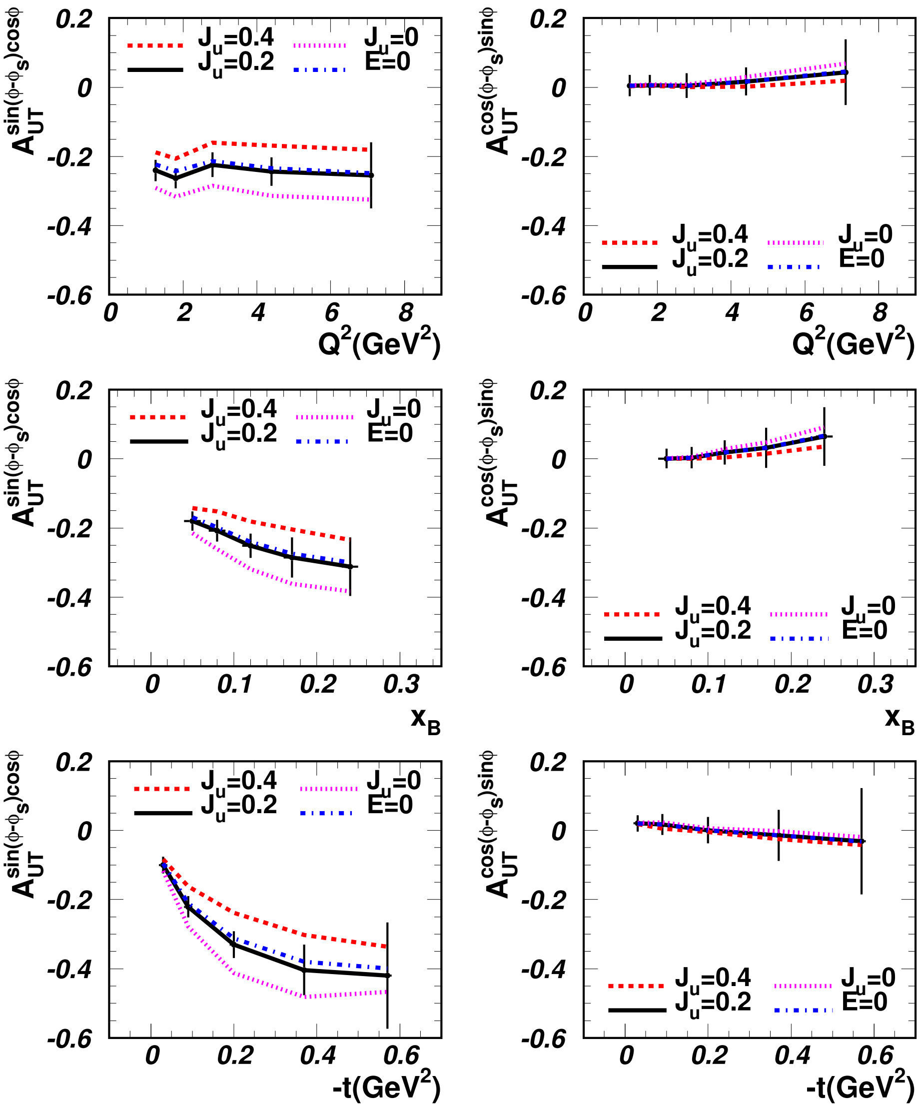

Figure 3.7: Theoretical predictions on the TTSA amplitudes $A_{UT}^{\sin(\phi-\phi_S)\cos\phi}$ and $A_{UT}^{\cos(\phi-\phi_S)\sin\phi}$ in the Regge ansatz for $b_{val} = 1$, $b_{sea} = \infty$, $J_u^{VGG} = 0.4\ (0.2, 0)$, $J_d^{VGG} = 0$. $E = 0$ denotes zero effective contribution from the quark GPDs E_q. The D-term is modeled according to the chiral quark-soliton model result [Goe01]. The predictions are made at the values of the kinematic variables given in Tab. B.1. See App. B for further details.

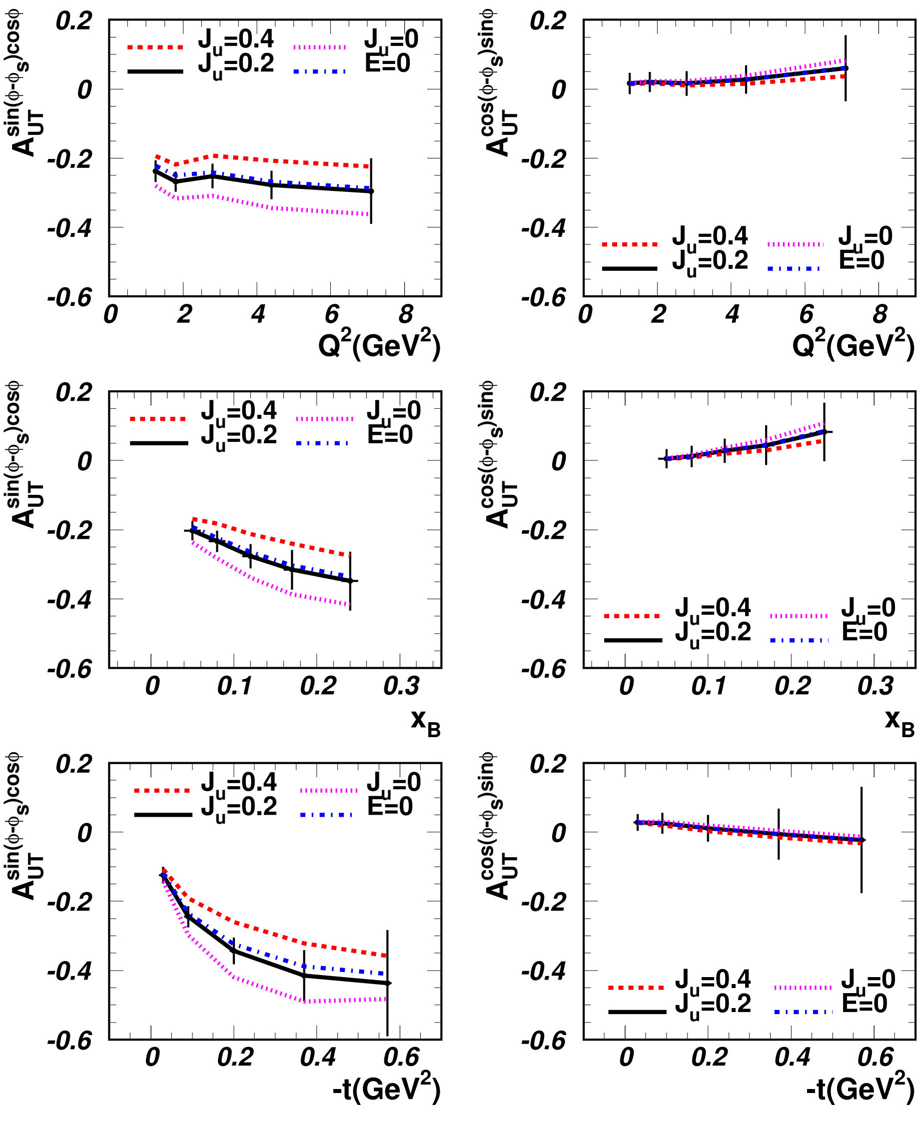

Figure 3.8: Same as Fig. 3.7 but for $b_{val} = 1$, $b_{sea} = 1$.

Chapter 4

The HERMES Experiment

The HERMES (**HER**A **ME**asurement of **S**pin) experiment is located in the east section of the HERA storage ring complex[1] at DESY (see Fig. 4.1). It is a fixed target experiment initially designed to study the spin structure of the nucleon through polarized deep-inelastic scattering (DIS). Longitudinally polarized positrons or electrons scatter on a polarized gas target internal to the HERA e-storage ring. Scattered leptons and produced particles in DIS are detected by a forward spectrometer with large momentum and solid angle acceptance [Ack98].

HERMES used longitudinally polarized atomic hydrogen, deuterium and helium-3 targets in the years 1995-2000. Precision measurements of the spin dependent structure function g_1 of proton, deuteron, and neutron [Air06b], as well as the first measurement of the tensor structure function b_1 of the deuteron [Air05b] have been obtained during this period. Note however that only information of scattered leptons is used in these inclusive DIS studies. With the virtue of the large acceptance of the forward spectrometer combined with hadron identification and the purity of the targets, HERMES is also able to provide precise data on semi-inclusive DIS processes in which hadrons are detected in coincidence with the scattered lepton. HERMES has recently reported results on the quark helicity densities $\Delta q(x)$ in the nucleon for up, down, and strange quarks from semi-inclusive DIS [Air05a].

After the high luminosity upgrade of HERA in the years 2000-2001, HERMES has taken data with a transversely polarized atomic hydrogen target in the years 2002-2005. The first measurement of the transverse target-spin asymmetry associated with DVCS has been performed. As described in section 3.3.1, such a measurement may provide an access to the GPD E and hence to the quark total angular momentum in the nucleon. Single-spin asymmetries for electroproduction of charged pions in semi-inclusive DIS have also been measured for the first time [Air05d]. Such an asymmetry may arise due to non-vanishing quark transversity distributions $\delta q(x)$ in conjunction with the Collins

[1] HERA is an ep collider but HERMES only uses the positron/electron beam.

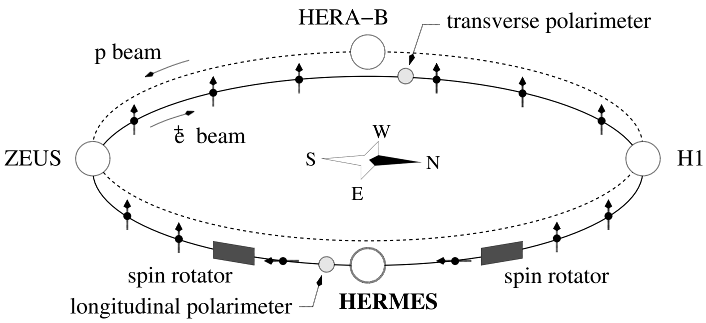

Figure 4.1: Schematic diagram of the HERA storage ring layout as of the year 2000, with the location of the four experiments. Also shown are the locations of the spin rotators and the two polarimeters.

fragmentation function, or due to a correlation between the transverse polarization of the nucleon and the intrinsic transverse momentum of quarks, represented by the Sivers distribution function.

Not only studying the spin structure of the nucleon using polarized targets, has HERMES also taken data with unpolarized hydrogen, deuterium, helium-3, helium-4, nitrogen, neon, krypton, and xeon targets over short periods of time in order to study other important properties, e.g., the flavor asymmetry of the sea in the nucleon [Ack98a], hadronization in nuclei [Air03, Air06c], as well as quasi-real photoproduction of exotic baryons [Air04, Air05c].

In this chapter, we will describe the HERMES experimental setup. The polarized $e^{\pm}$ beam at HERA is described in section 4.1. The polarized hydrogen target of HERMES is described in section 4.2. The forward spectrometer of HERMES is described in section 4.3. Data acquisition and processing are described in section 4.4.

4.1 The Polarized $e^{\pm}$ Beam at HERA

The HERA storage ring can be filled with either positrons or electrons that are accelerated to energies of 27.6 GeV. As most of the physics processes studied at HERMES are identical for positrons and electrons, the term “positron” will be used for both in the following unless otherwise stated. The current of the positron beam is typically about 40 mA at injection and decreases exponentially with a lifetime in the order of 8 hours:

$$I(t) = I_0 \cdot \exp(-t/\tau), \qquad \tau \sim 8 \text{ hours.} \tag{4.1}$$

The beam is dumped and the ring refilled when the beam current decreases to about 10 mA, typically 8-12 hours after the injection. Up to 220 bunches of positrons can be injected into the storage ring. They are separated by a time interval of 96 ns. The design parameters for the beam size at the H1 and ZEUS interaction points, after the HERA high luminosity upgrade, are $\sigma_x = 112$ μm, $\sigma_y = 30$ μm, and $\sigma_z = 10.3$ mm [Hof00].

The emission of synchrotron radiation from charged particles involves a small asymmetry in spin-flip amplitudes which enhances the population of the spin state antiparallel to the direction of the magnetic bending field [Sok64]. Due to this effect, positron beams in high energy storage rings can become transversely self-polarized. Based on the fact that the magnetic moment (spin) of charged particles precesses in a magnetic field, the transverse polarization of the beam can be rotated into the longitudinal direction. Such a rotation is performed by a spin rotator consisting of interleaved horizontal and vertical bending magnets [Buo86]. A pair of spin rotators is installed up- and downstream the HERMES experiment [2]. The upstream spin rotator rotates the direction of the beam polarization into the beam direction, while the downstream one rotates the direction of the beam polarization back into the vertical direction.

With the first pair of spin rotators at HERA, longitudinal positron polarization was achieved for the first time in a high energy storage ring in 1994 [Bar95]. Since then, the polarization direction has been reversed typically every few months by moving the magnets of the spin rotators. Longitudinal polarization was routinely obtained in the range 40%-65% in the years 1995-2000. Due to the high luminosity upgrade of HERA in the years 2000-2001, longitudinal polarization of the beam was very low in the year 2002 but went back to between 20% and 55% in the years 2003-2005.

The polarization of the positron beam is continuously monitored by two polarimeters, which operate on the principle of the spin dependence in Compton scattering of circularly polarized photons on positrons. The longitudinal polarimeter is located between the spin rotators close to the HERMES experiment. It measures the asymmetry in energy of the back-scattered photons between two helicity states of a laser beam [Bec02]. A measurement of the longitudinal beam polarization to an absolute statistical uncertainty of 0.01 can be performed in one minute. The fractional systematic uncertainty is 1.6%. The transverse polarimeter is located in the HERA west section. It measures the up-down spatial asymmetry of the back-scattered photons with respect to the orbital plane of the positrons for the two helicity states of a laser beam [Bar93]. Its fractional systematic uncertainty has been improved to 3.4% [Bec02]. For most of the time the two polarimeters have provided consistent measurements of the positron beam polarization (see Fig. 4.2).

[2] During the high luminosity upgrade of HERA in the years 2000-2001, two additional sets of spin rotators were installed for the H1 and ZEUS experiments.

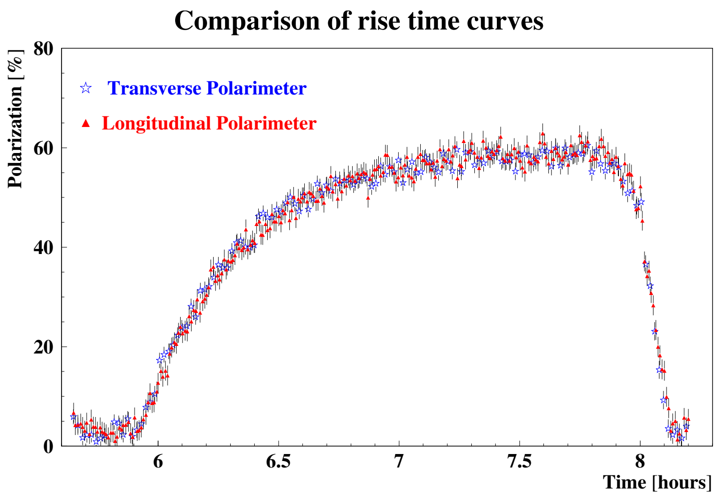

Figure 4.2: Beam polarization values measured by the transverse and longitudinal polarimeters. It is difficult to distinguish between the results of the two polarimeters as they overlap on each other. Such a fact proves the good performance of the polarization measurements.

4.2 The Polarized Hydrogen/Deuterium Target of HERMES

A polarized hydrogen/deuterium gas target [Air05e] is used in the HERMES experiment. It has high polarization, almost no dilution for hydrogen/deuterium atoms, and the capability to reverse the polarization direction in milliseconds. It mainly consists of an atomic beam source (ABS) [Nas03], a target gas analyzer (TGA) [Bau03b], a Breit-Rabi polarimeter (BRP) [Bau02], and a storage cell [Bau03a]. A schematic view of the whole target setup is given in Fig. 4.3.

The ABS is used to generate nuclear-polarized beams of hydrogen or deuterium atoms. Hydrogen (deuterium) molecules are dissociated via electron impact provided by a radio frequency (microwave) dissociator. The dissociated atoms expand through a nozzle which is cooled down to 100 K by helium. An atomic beam of high intensity is formed after a skimmer and a collimator. The atomic beam is polarized by a set of sextupole magnets, which focuses (deflects) atoms with positive (negative) electron spin, and by high frequency transition (HFT) units, which exchange populations of certain hyperfine states of hydrogen/deuterium atoms. The HERMES ABS can provide a nuclear polarized beam of hydrogen (deuterium) atoms with an intensity of approximately $6.5 \times 10^{16} s^{-1}$ ($5.7 \times 10^{16} s^{-1}$). Nuclear polarization values of 0.97 (0.92) at a degree of dissociation of 0.92 (0.95) for the hydrogen (deuterium) target have been reached.

A necessary requirement for the HERMES experiment is a sufficiently large luminos-

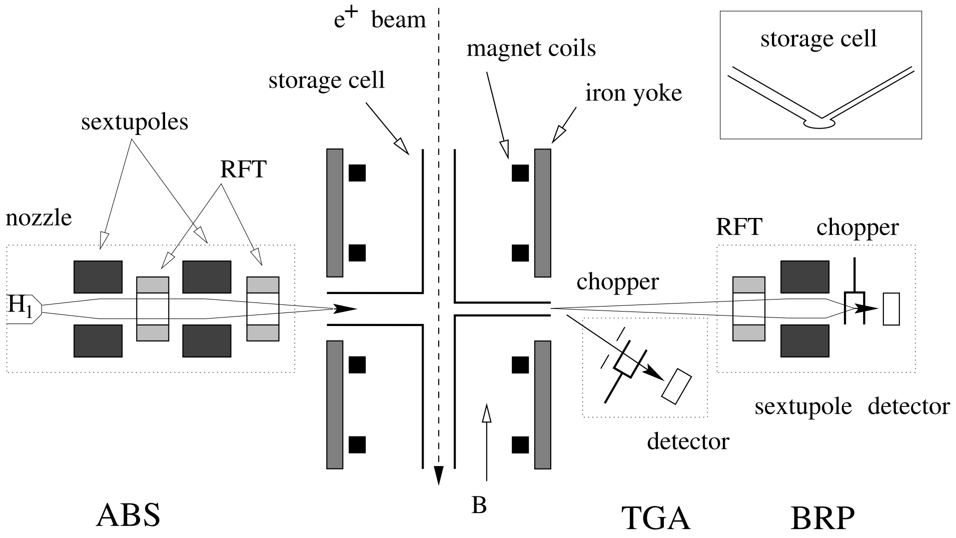

Figure 4.3: Schematic view of the HERMES longitudinally polarized target. From left to right: Atomic Beam Source (ABS), target chamber with cell and magnet, and diagnostic system composed by Target Gas Analyzer (TGA) and Breit-Rabi Polarimeter (BRP).

ity which is proportional to the areal density of the target. The densities achieved with gas jet targets are however not enough. A storage cell, i.e., an open-ended tube made of 75 μm thin, ultra-pure aluminum sheets, has been used to increase the target areal density by two orders of magnitude: atoms injected from the center of the cell by the ABS collide with the cell surface hundreds of times before they flow out of the cell (see Fig. 4.3). The cell used in the years 2002-2005 is 40 cm long and has an elliptical cross section of 21×8.9 mm^2. The profile of the target density from Monte Carlo calculations is shown in Fig. 4.4. As the cell acts also as a part of the positron beam pipe, a smooth transition between it and the rest of the circular beam pipe has been carefully designed to suppress beam wake fields which may heat the target cell as well as enlarge the beam emittance.

The target cell is placed inside a vacuum chamber which is evacuated by two turbo-molecular pumps with a combined pumping speed of 4400 l$\cdot$s^{-1}. The chamber pressure is typically in the 10^{-7} mbar range as the target gas escapes through the pumping holes along the ends of the target cell. A 0.3 mm thick, stainless steel exit window on the downstream end of the target chamber allows the scattered positrons and produced particles to leave the target chamber and be detected by the HERMES spectrometer. A magnet surrounding the storage cell provides a holding field, which defines the polarization direction and prevents spin depolarization processes. For longitudinal running in the years 1995-2000, a longitudinal target magnet field (up to 350 mT) has been generated by a superconducting magnet. The target was modified after 2000 to become

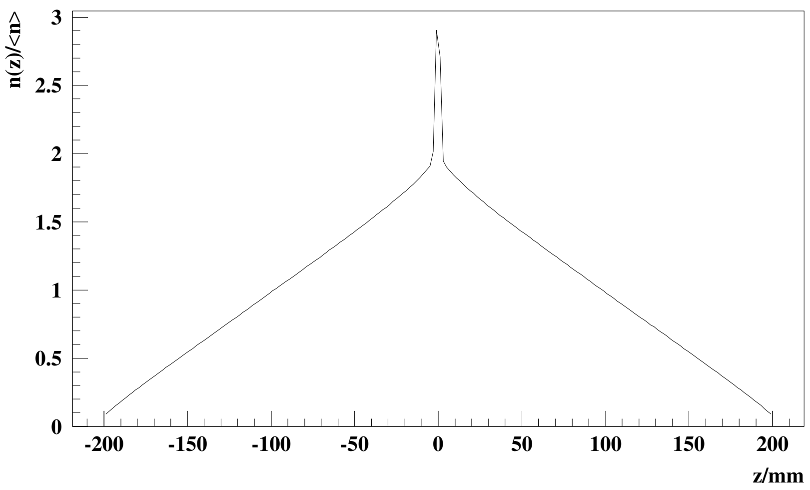

Figure 4.4: The profile of the target density from Monte Carlo.

a transversely polarized target. A dipole magnet was built operating at a field value of $B = 297$ mT in the axis. In these data taking periods, the polarization direction of the target was flipped every 90 s.

A sample of target gas is analyzed by the TGA and BRP. The TGA measures the atomic and molecular relative contents of the gas sample. The BRP is instrumented with sextupole magnets and HFT units. It measures the polarization of the hydrogen/deuterium atoms. The effective polarization of the target is obtained from the above measurements, taking into account recombination of atoms in the target cell and the possibility of finite polarization of molecules as well as sampling corrections. The polarization of the longitudinally polarized hydrogen (deuterium) target has been measured to be $\pm0.851\pm0.031$ ($+0.851\pm0.029$ and -0.840 ± 0.026) in the year 1997 (2000). The polarization of the transversely polarized hydrogen target has been measured to be $\pm0.783\pm0.041$ ($\pm0.796\pm0.033$) in the year 2002 (2003). Due to a few changes in the running conditions, the HERMES target group released several values for the transverse target polarization in the year 2004, each of which corresponds to one certain period of time. The average value of the target polarization weighted by the luminosity for the combined data of the years 2002-2004 is calculated to be [Els05]

$$\langle P_T \rangle = \pm 0.754 \pm 0.050. \tag{4.2}$$

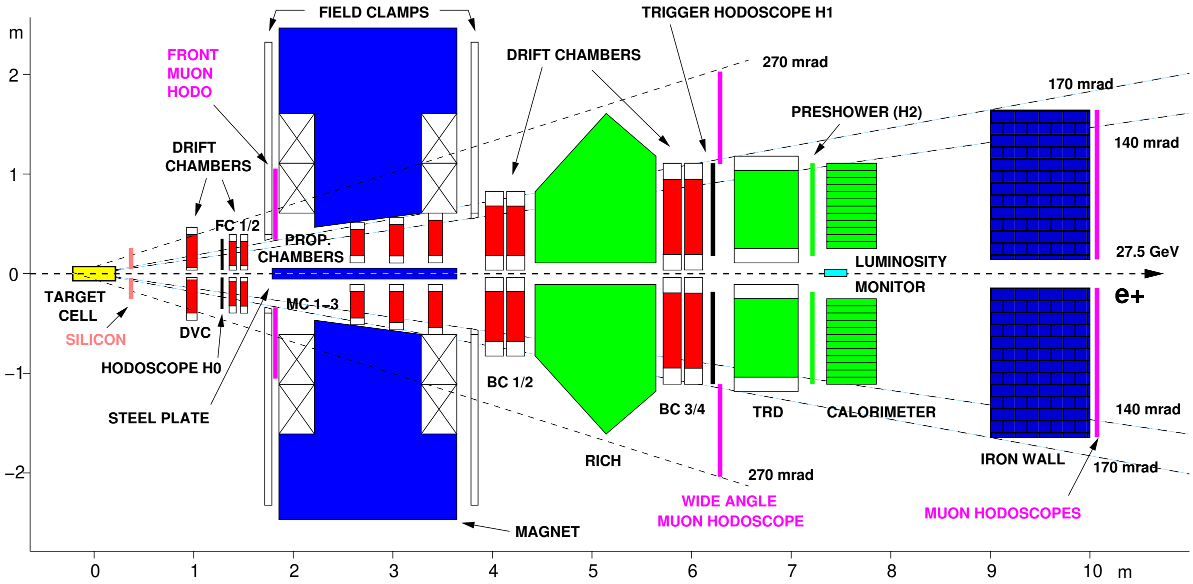

Figure 4.5: Side view of HERMES spectrometer configuration in the years 2001-2005.

4.3 The HERMES Forward Spectrometer

The HERMES spectrometer is a forward-angle instrument of conventional design. A full description has been given in Ref. [Ack98]. The spectrometer consists of two identical halves above and below the positron beam. Scattered positrons and produced particles are detected and identified within an angular acceptance ±170 mrad horizontally and ±(40-140) mrad vertically with respect to the (HERMES) interaction point.

The principle of the spectrometer is sketched in Fig. 4.5. The front region before the spectrometer magnet consists of a silicon strip detector, drift chambers (DVC, FC1/2), and a trigger hodoscope (H0). The region behind the magnet includes drift chambers (BC1/2, BC3/4), a Ring-Imaging CHerenkov detector (RICH), a trigger hodoscope (H1), a Transition-Radiation Detector (TRD), a pre-shower detector (H2), a luminosity detector, and a lead-glass calorimeter. A set of MultiWire Proportional Chambers (MWPC) (MC1-3) is installed in the gap of the magnet. A number of muon hodoscopes is also installed between the field clamps and the body of the magnet, and directly behind hodoscope H1, as well as behind a one meter thick iron wall.

In the following sections we give a description of those components of the spectrometer which are important for the data analysis described in this thesis. The spectrometer magnet is described in section 4.3.1. The tracking detectors DVC, FCs, and BCs are described in section 4.3.2. In combination with the magnet, they can determine momenta of charged particles. For positrons with momenta between 3.5 and 27 GeV, the average angular resolution is 0.6-0.3 mrad and the average momentum resolution $\Delta P/P$

was 0.7-1.3%, which is mainly due to bremsstrahlung in the materials of the target cell and the vacuum exit window.

Particle IDentification (PID) is provided by the calorimeter, the pre-shower detector, the TRD, the RICH, and the H1 and H2 hodoscopes. The first three detectors are used to discriminate positrons from hadrons. The calorimeter plays a unique role in the DVCS study as it is the only detector that provides energy and position information for photons. Additional hadron PID is provided by the RICH [Asc00, Ako02] for pions, kaons, and protons in the momentum range from 2 to 15 GeV. The time-of-flight (TOF) technique using the H1 and H2 hodoscopes provides good PID for protons and pions in the momentum range up to 2.9 GeV and for kaons up to 1.5 GeV [Air05f]. In section 4.3.3, a description of the calorimeter, the pre-shower detector, and the TRD is presented.

The luminosity detector is described in section 4.3.4. In section 4.3.5 the HERMES trigger is described. The silicon strip detector, whose main purpose is to increase the acceptance for the decay products of Λ particles, the MCs, the RICH, the TOF technique, and the Muon hodoscopes, however, are not described in the following as they are not of relevance for the present study.

4.3.1 The Spectrometer Magnet

The HERMES spectrometer magnet is a H-frame type, dipole magnet. It occupies the 2.2 m-long space between the last FC and the first BC. The pole faces of the magnet are tilted in the vertical direction parallel to the limits of the angular acceptance ± 140 mrad. The gap between the pole faces in the horizontal direction is ± 170 mrad plus an additional 100 mrad starting from the halfway of the magnet ($z = 275$ cm) to allow for additional deflection in the magnet.

The magnet is operated with a field integral of $\int B \cdot dl = 1.3$ T·m. The deflecting power variates less than 10% in the acceptance. A septum iron plate, which limits the vertical angular acceptance to a minimum of ± 40 mrad, shields the positron and proton beams from the magnetic field. Since such passive shielding was insufficient, a correction coil with a deflecting power of 0.08 T·m is installed inside the septum plate in order to compensate the fringe field. The coil is also used to compensate the magnetic field of the target when operating with transverse polarization.

The field map of the magnet has been measured with a 3D-Hall probe. The results are reproducible to a level of 0.1% and agree with Monte Carlo calculations. The field map is integrated into the track reconstruction algorithm.

4.3.2 The Tracking Chambers

The DVC, FCs, and BCs consist of conventional drift chambers of horizontal-drift type. Every chamber module contains six layers of drift cells (U, U', X, X', V, V'), each of which consists of alternating anode-cathode wires between a pair of cathode foils. The cathode wires and foils are at negative high voltage with the anode sense wires at ground potential. The anode-cathode wires in the X and X' planes are oriented in the vertical direction, while the ones in the U and U' (V and V') planes are tilted by 30° to left (right). U', X', and V' planes are staggered by half the width of a drift cell with respect to the corresponding U, X, and V planes in order to solve left-right ambiguities. The gas mixture is the same for all the drift chambers: $Ar/CO_2/CF_4$ (90/5/5). The DC readout system consists of Amplifier/Shaper/Discriminator (ASD) cards mounted onboard the drift chambers, driving ECL signals to LeCroy 1877 FastBus time-to-digital converters (TDCs).

The DVC and FCs are used to determine the event vertex in the target cell, as well as to measure the scattering angles and the initial trajectories of charged particles before the magnet. The BCs are used to determine the trajectories of charged particles after the magnet, and to identify the hits in the PID detectors associated with each track.

Some parameters of the tracking chambers are given below. The coordinate system used at HERMES has the z-axis along the positron beam direction, the y-axis vertically upwards, and the x-axis horizontal, pointing towards the outside of the positron storage ring.

The Drift Vertex Chambers

The width of the drift cells of the Drift Vertex Chamber (DVC) is 6 mm. The distance between two neighboring anode and cathode planes is 3 mm. The DVC has an active area of 474×290 mm^2. It consists of two modules above and below the positron beam, and in total 1088 channels. The anode wires are made of gold-plated tungsten and have a diameter of 30 μm. The potential wires are made of gold-plated Be-Cu and have a diameter of 50 μm. The cathode planes are made of 34 μm thick, aluminized Mylar foils. A average spatial resolution of 220 μm per plane is reached by the DVC.

The Front Chambers

The design, construction and operation of the Front Chambers (FCs) and associated electronics are described in detail in Ref. [Bra01]. The width of the drift cells is 7 mm. The distance between two neighboring anode and cathode planes is 4 mm. The FCs have an active area of 660×180 mm^2. Each chamber consists of one module with 576 channels. The total number of channels is 2304. The anode wires are made of gold-plated tungsten and have a diameter of 20 μm. The potential wires are made of gold-plated Al and have a diameter of 76 μm. The cathode planes are made of 6.4 μm thick, double-sided aluminized Mylar foils. The single plane efficiency ranges from 97% near the anode wire to 99% at the center and edge of the cell. An average spatial resolution of 225 μm per plane is reached by the FCs.

The Back Chambers

The design, construction and operation of the Back Chambers (BCs) and associated electronics are described in detail in Ref. [Ber98]. The width of the drift cells is 15 mm. The distance between two neighboring anode and cathode planes is 8 mm. The BC1 and BC2 (BC3 and BC4) have an active area of 1880×520 (2890×710) mm^2 and 768 (1152) channels per module. The total number of channels is 7680. The anode wires are made of gold-plated tungsten and have a diameter of 25.4 μm. The potential wires are made of gold-plated Be-Cu and have a diameter of 127 μm. The cathode planes are made of 25 μm thick C coated Kapton. The average BC plane efficiency is well above 99% for electron and positron tracks, and drops to 97% when also hadronic tracks are considered. A average spatial resolution of 250 (275) μm per plane is reached by the BC1/2 (BC3/4).

4.3.3 Particle Identification Detectors

In certain kinematic regions of HERMES, the rate of positrons from DIS is lower by a factor of about 400 than that of hadrons (mostly pions) from photoproduction [Ack98]. A clear separation between leptons and hadrons together with efficient lepton selection is needed in order to keep data acquisition rates reasonable, and to keep the contamination of the lepton sample by hadrons sufficiently low. This is achieved by the HERMES PID system, which includes an electromagnetic calorimeter made of lead-glass, a pre-shower detector made of plastic scintillator preceded by two radiation lengths of lead, and a TRD consisting of 6 modules in each spectrometer half. A hadron rejection factor (HRF) of at least 10 is provided at the first level trigger stage by the pre-shower and the calorimeter, and of at least 10^4 in the offline analysis by the TRD in addition. The HRF is defined as the ratio of the total number of incident hadrons to the number of hadrons that are misidentified as positrons.

A description of the calorimeter, the pre-shower detector, and the TRD is given below.

The Calorimeter

The function of the HERMES calorimeter [Ava98] is 1) to provide a first level trigger for scattered positrons, 2) to separate positrons from pions with a rejection factor of more than 10 at the first level trigger stage and an additional factor of more than 100 in the offline analysis, 3) to measure the energy of DIS positrons and photons from radiative processes or from, e.g., π^0 decay, and 4) to give a coarse position measurement of scattered positrons and photons.

The calorimeter consists of 840 radiation-resistant F101 lead-glass blocks (see Fig. 4.6). Cherenkov light produced by electromagnetic showers is detected by Philips XP3451

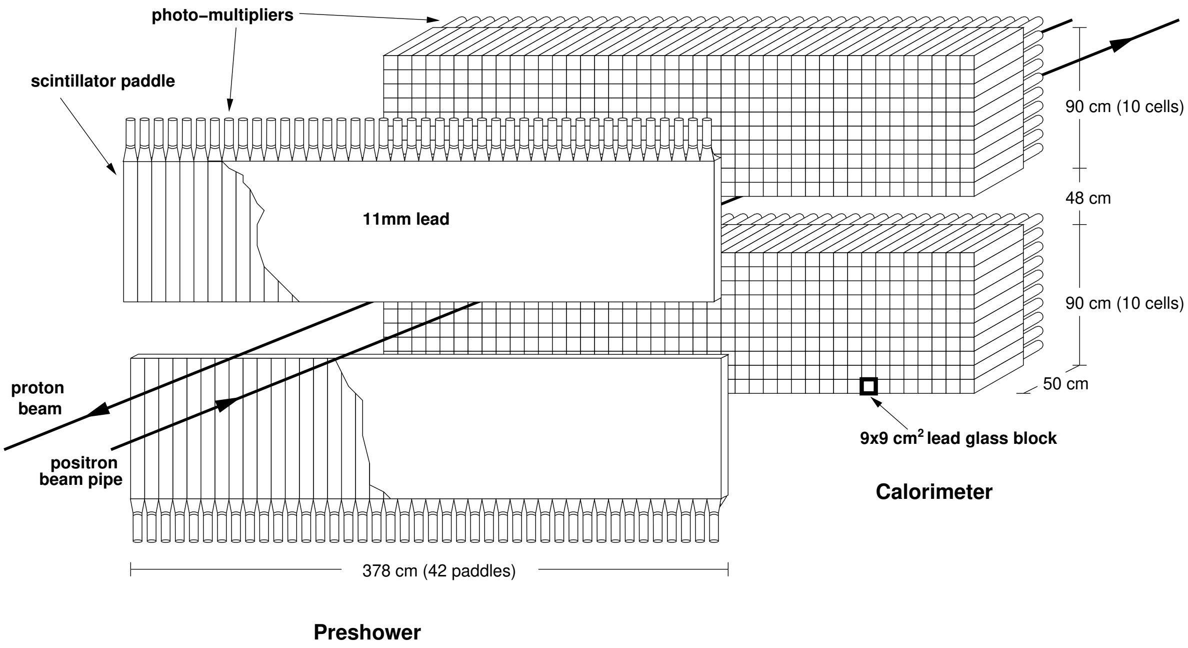

Figure 4.6: Schematic view of the calorimeter and the pre-shower detector.

photomultipliers (PMTs) of 7.5 cm diameter viewing from the rear side. The radiation length of F101 lead-glass is 2.78 cm, Moliere radius 3.28 cm, critical energy 17.97 MeV, refraction index 1.65, and density 3.86 g/cm^3. The area of the front face of the blocks is 9×9 cm^2, and the length 50 cm, which corresponds to $\sim$18 radiation lengths. The blocks are arranged into two 42×10 arrays, one above and the other below the positron beam. They were polished, wrapped with 50 μm thick aluminized mylar foils, and covered with a 125 μm thick tedlar foil to provide light isolation.

Each of the 840 lead-glass blocks has been calibrated to within 1% at DESY by a 3 GeV positron beam incident at the center of the block. The stability of the calorimeter response over the normal running periods has been evaluated and calibrated by looking at the ratio of the energy measured by the calorimeter to the momentum reconstructed by the tracking system of positrons, which are conservatively identified by the PID detectors. It has been found that the stability of the calorimeter response is within 1% per year [Ava98]. Such an observation is confirmed by a gain monitoring system (GMS) [Tan03] which monitors the possible gain variations of the PMTs during normal running.

The discrimination between positrons and hadrons of the calorimeter is based on the different topologies of electromagnetic and hadronic showers. Hadronic showers typically start much later and spread much wider than electromagnetic showers. With the chosen size of the lead-glass blocks, more than 99% electromagnetic shower energy is contained in a matrix of 3×3 blocks (defined as a cluster), while a large part of the hadronic shower energy leaks out of the calorimeter. A valid PID parameter is the ratio of the detected shower energy E_{cal} in the nine-block cluster to the momentum p of the incident particle measured by the tracking chambers. This ratio (E/p) is typically unity for positrons and photons and less than unity for hadrons.

The energy resolution of the calorimeter for scattered positrons can be described by the following parameterization [Ava98]:

$$\frac{\sigma(E)}{E}[\%] = \frac{5.1 \pm 1.1}{\sqrt{E(GeV)}} + (2.0 \pm 0.5) + \frac{10.0 \pm 2.0}{E(GeV)}. \tag{4.3}$$

Impact positions of positrons and photons in the calorimeter can be obtained from the energy distribution inside the nine-block cluster. It can be calculated by the following energy-weighted average position of the cluster:

$$x = \frac{\sum_i x_i \sqrt{E_i}}{\sum_i \sqrt{E_i}}, \tag{4.4}$$

$$y = \frac{\sum_i y_i \sqrt{E_i}}{\sum_i \sqrt{E_i}}, \tag{4.5}$$

where x_i and y_i are the central coordinates of the i-th block, and the square root of the corresponding energy, $\sqrt{E_i}$, is used as the weight. The position resolution can be evaluated by checking the difference between the positions of scattered positrons obtained in this way and the positions reconstructed from the tracking chambers [Ava98]. The above position reconstruction algorithm does not account for the exponential shape of the lateral shower profile and has been found to lead to a bias of several centimeters [Ely01]. An alternative algorithm, which uses a logarithmic weight, $w_i = max\,\{0, 4.8 + ln(E_i/E)\}$, improves significantly the resolution to approximately 0.5 cm [Ell04]. The latter algorithm is used in the study discussed in this thesis.

The Pre-shower Detector

The pre-shower detector [Ack98] provides important discrimination between positrons and hadrons. It consists of 84 vertical scintillator modules (42 each in the upper and lower halves), preceded by a passive radiator that initiates electromagnetic showers (see Fig. 4.6). Scintillation light is detected by Thorn EMI 9954 PMTs of 5.2 cm diameter viewing from the outside end (away from the beam). The scintillator modules are made of fast BC-412 scintillation material with large attenuation length (300-400 cm). They are 1 cm thick and 9.3×91 cm^2 in area. The passive radiator consists of 11 mm (two radiation lengths) of Pb, sandwiched between two 1.3 mm stainless steel sheets.

The discrimination between positrons and hadrons by the pre-shower detector is based on the fact that for positrons the radiator will initiate electromagnetic showers and hence produce much more scintillation light than for hadrons. A pion rejection factor (PRF) of $\sim$10 is provided by the pre-shower detector with 95% efficiency for positron detection.

The Transition-Radiation Detector

The TRD [Ack98] is used to provide a pion rejection factor of at least 100 with 90% positron efficiency and above. It consists of 12 modules above and below the beam. Each module includes a 6.35 cm thick radiator consisting of 267 dielectric layers of 17-20 μm diameter fibers, and a Xe/CH_4 (90:10) filled MWPC. The active area is 325×75 cm^2. The MWPC consists of 256 vertical anode wires of 75 μm gold coated Be-Cu separated by 1.27 cm, and cathode planes made of 50 μm thick, double-sided aluminized mylar foils.

Both positrons and hadrons deposit energy in the MWPC detectors. The positrons deposit, on average, approximately twice the energy as compared to hadrons due to transition radiation in the radiator and the larger dE/dx in the detector. Using a probability-based analysis to combine the responses of the six modules, a PRF of 1460$\pm$130 (489$\pm$25) is reached with 90(95)% positron efficiency. Using the truncated mean method, in which the largest signal from the six modules is disccarded and the average of the remaining five is used, the PRF is smaller, about 150 with 90% positron efficiency.

PID System Performance

The responses of the three PID detectors described above can be combined to provide good lepton/hadron identification. It is done based on a probability-based analysis [Kai97]. The responses of the calorimeter and the pre-shower detector are combined to produce the quantity PID2 defined as

$$PID2 = log_{10}\frac{P^e_{cal}P^e_{pre}}{P^h_{cal}P^h_{pre}}, \tag{4.6}$$

where P^i_j is the probability that a particle type i produced a given response in detector j. The P^i_j's are determined by comparing the detector responses for each track to typical response functions for each detector, called parent distributions. The latter are either derived from the data or modelled using Monte Carlo techniques. The use of momentum-dependent parent distributions is required to account for the varying responses of the detectors. PID5 is defined in a similar way to PID2 using only the TRD. For the DVCS analysis of the 2002-2004 data, the PID2+PID5 scheme was used which can provide an positron selection efficiency of 99% with hadron contamination of less than 1% in the offline analysis.

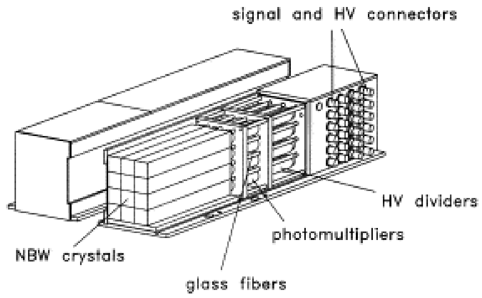

Figure 4.7: Schematic view of the luminosity detector.

4.3.4 The Luminosity Monitor

A precise knowledge of the relative luminosity is necessary for the measurement of cross section asymmetries between different beam/target polarization states. An absolute determination of the luminosity is required for the measurement of absolute cross sections and unpolarized structure functions. Luminosity is measured at HERMES by coincident detection of electron-positron and photon pairs, originating from the Bhabha scattering [Bha35] and the annihilation of the beam positrons with the target electrons. In the case of an electron beam, electron pairs are detected from the Möller scattering [Möl32] of the beam electrons with the target electrons.

The HERMES luminosity monitor [Ben01] consists of two calorimeters, each containing 12 Cherenkov crystals with a size of $22\times22\times200$ mm^3 arranged in 3×4 matrices (see Fig. 4.7). The radiation length of $NaBi(WO_4)_2$ is 1.03 cm, Moliere radius 2.38 cm, critical energy 9.75 MeV, refraction index 2.15, and density 7.57 g/cm^3. Cherenkov light is detected by Hamamatsu R4125Q PMTs of 19 mm diameter viewing from the rear side. The detector is located 7.2 m downstream the interaction point and has a horizontal angular acceptance of $\pm$(4.6-8.9) mrad, limited by the size of the beam pipe and the aperture inside the septum plate. Because of the high radiation background in the region close to the beam, $NaBi(WO_4)_2$ crystals are used with a very high radiation hardness of about 7×10^5 Gy.

The Bhabha scattering and annihilation (Möller scattering) events have a high energy deposition in both calorimeters, while most of the background events have a high energy deposition only in one calorimeter. A trigger signal is generated when there are coincident signals from both calorimeters exceeding a threshold of 4.5 GeV each. Event rates of this type are proportional to the absolute luminosity, which is given by

$$L = \frac{R}{\int_{\Delta\Omega} d\Omega \cdot \epsilon \cdot d\sigma/d\Omega}, \tag{4.7}$$

where ϵ is the detector efficiency, $d\sigma/d\Omega$ the cross section of the Möller (Bhabha and annihilation) process(es), and the integration is performed over the detector acceptance region $\Delta\Omega$. The systematic uncertainty for the absolute (relative) luminosity measurement is 6.3-6.4% (0.9-1.5%) in the years 1995-1999, and 3.0-3.2% (not estimated) in the years 2002-2004, which is relevant for cross section (asymmetry) measurements.

4.3.5 The Trigger System

The trigger signals are used to distinguish interesting events from background with high efficiency, and initiate digitization and readout of the detector signals [Ack98]. The main physics triggers at HERMES are originating from DIS and photoproduction processes. The DIS trigger (trigger 21) selects events with DIS positrons. The photoproduction trigger detects charged particles decaying from hadrons such as K, ρ, J/ψ, and Λ that are produced at low Q^2, where positrons have very small scattering angles and are usually not detected.

The DIS trigger is provided by requiring sufficient energy deposition in a localized spatial region in the calorimeter and hits in the three hodoscopes, H0, H1, and H2, in coincidence with HERA positron bunches. The H0 hodoscope upstream of the FCs is included to suppress triggers initiated from backward-going particles produced by the nearby-passing HERA proton beam. It consists of a single sheet of standard plastic scintillator, 3.2 mm thick (0.7% of a radiation length). Scintillation light is collected by Thorn EMI 9954SB PMTs of 5.08 cm diameter viewing from the edge, far from the beam axis. The suppression is based on the TOF information between the front H0 and the rear H1 and H2 scintillators. The requirement of hits in H0 and H1 for the DIS trigger suppresses neutral particle background from positron beam interactions in the upstream collimators, or photoproduction in the target. The charged particle background is reduced by setting the calorimeter threshold to 1.5 GeV for polarized target data taking in the years 2002-2004.

The photoproduction trigger is provided by requiring charged particle tracks in both the top and bottom halves of the spectrometer, as identified by the three hodoscopes and the drift chamber BC1, in coincidence with HERA positron bunches. The inclusion of BC1 eliminates those showers originating from the upstream collimators, which are confined near the beam pipe and hit the tips of the hodoscopes but not the wire chambers [Ack98].

4.4 Data Acquisition and Processing

The HERMES data acquisition (DAQ) system is based on Fastbus and VME protocols. It consists of a number of front-end crates, the event collector crate, and the event receiver crate connected to the online workstation cluster. CERN Host Interfaces (CHIs) act as Fastbus masters which in most places are equipped with Struck Fastbus Readout Engines (FRE), featuring one or two Motorola 96002 digital signal processors (DSPs).

One VME branch with 4 crates and three CAMAC branches with a total of 9 crates are connected to the event builder crate to handle special DAQ tasks, such as obtaining the positron bunch number, and slow control. The drift chamber signals are digitized using LeCroy 1877 Fastbus multi-hit multi-event 96 channel multiblock time-to-digital converters (TDCs). The resolution is 0.5 ns/channel and the full scale range is 16 bits. Charge from the various PMTs and the TRD is digitized by LeCroy 1881M Fastbus multi-event 64 channel multiblock analog-to-digital converters (ADCs). The resolution is 50 fc/channel and the full scale range is 13 bits above pedestal. The TOF signals are digitized by LeCroy 1875A Fastbus multi-event 64 channel TDCs. The resolution is 25 or 50 ps/channel depending on the detector with a full scale range of 12 bits. The deadtime during standard running is typically well below 10% and the contribution due to the DAQ system is estimated to be below 1% [Ack98].

Each event associated with a trigger condition goes to the DAQ data stream as a single event record. Scaler events are recorded approximately every 10 seconds in which all the scalers in the experiment are read out. Each period of time between scaler events defines a burst. A data file corresponding to a run is ended either automatically whenever 450 Mbytes of information have been collected, or manually by the shift crews. The output of the DAQ data stream is written in EPIO (experimental physics input output) format [Cer93a] to staging disks over the course of a fill of the storage rings and copied between fills to storage tape robots on the DESY main site. In parallel, they are stored on local DLT tape drives for redundancy.

The recorded data are processed through a production chain including the main production, the slow production and the micro data summary tape (μDST) production. The main production consists mainly of three programs:

- HERMES decoder (HDC), which decodes the online information and applies detector calibrations;

- HERMES reconstruction (HRC), which reconstructs all the tracking chamber hits into actual particle tracks, and associates information from the PID detectors with each track;

- ACE [Kol98], which computes the plane efficiencies of the tracking chambers.

The slow production is responsible for collecting and synchronizing data from the raw slow control files and external expert files containing offline calibrations. The μDST production uses the writeMCDST program to merge the information from the slow files and the HRC files, performs calculations that are not intrinsically related to the decoding and reconstruction tasks of HDC and HRC, and compresses the information from its input data streams into a relatively small format.

The produced μDST files are labelled by 4 characters consisting of the last two digits of the corresponding year, a letter indicating the production, and a cypher. Productions with a higher version (for a given year) are assumed to be of a higher quality. Detector calibrations from previous data taking period are used in the first production of μDST files (a-production). The a-production provides detector calibrations for a reproduction of μDST files (b-production). In the c-production, additional corrections with improved calibrations are taken into account. The cypher is increased for each slow production with improved slow control information. The data analysis presented in the next chapter is based on the data productions 02c0, 03c0 and 04b0.

Chapter 5

Data Analysis

In the years 2002-2004, HERMES took data with a transversely polarized hydrogen target while HERA was filled with positrons. This allowed, as described in section 3.3.1, access to GPDs via the Transverse Target-Spin Asymmetry (TTSA) associated with DVCS. In this chapter we present the data analysis performed to extract the two leading azimuthal amplitudes of the TTSA. The data quality criteria and event selection cuts for BH/DVCS processes are described in sections 5.1 and 5.2. Approximately 4,000 candidates for BH/DVCS events were selected from the HERMES 2002$-$2004 data. In section 5.3 Monte Carlo simulations are described and compared to the experimental data. Background contributions to the selected BH/DVCS event sample are estimated based on these MC simulations. In section 5.4, detector resolutions are studied in MC simulations. In section 5.5 we investigate the use of the method of least squares and the use of the method of maximum likelihood to extract the TTSA amplitudes. Monte Carlo tests reveal that the latter method is superior to the former. In section 5.6 and section 5.7 we describe corrections to the extracted TTSA amplitudes for detector responses and for background contributions.

5.1 Data Quality

The quality of the data is checked to ensure that the data were taken free of any problem in the beam, the target, or the detectors relevant for the present analysis. An event will be kept only if it belongs to a burst that satisfies the following requirements:

- The burst was not the first one in a run; the burst length was between 0 s and 11 s.
- The beam current was between 2 mA and 50 mA; the beam polarization was between -0.8 and 0.8; the beam polarization was measured within 5 minutes.
- The target was in a reasonable state.

- No trip or oscillation occurred in the tracking chambers; there was no problem in the calorimeter, the TRD, the pre-shower, or the luminosity monitor.
- The raw count rate of the luminosity monitor and its ratio to the beam current were reasonable; the fractional DAQ live time was between 0.8 and 1.0.

5.2 Event Selection

The final state particles of the BH/DVCS processes include a scattered positron, an emitted real photon, and a recoiling proton. The process is called elastic (associated) when the recoiling proton is in the ground (a resonance) state, i.e., $ep \to ep\gamma$ (e.g., $ep \to e\Delta^+\gamma$). In the present study we are mainly interested in the elastic processes. The latter are described by GPDs defined in section 2.1, while the associated DVCS process is described by transition GPDs discussed in section 2.6. Due to limited detector resolutions, the associated processes can not be distinguished from the elastic ones and act as a main background to the latter. Further discussions on how to treat the contribution from the associated processes will be given in section 5.7.

In comparison with the elastic BH process, the contribution of the associated BH process is smaller by an order of magnitude at HERMES kinematics. Since the cross sections of the elastic BH/DVCS processes decrease rapidly with the negative invariant momentum transfer to the target proton $-t$, most of the BH/DVCS events at HERMES have $-t < 1$ GeV^2. The recoiling protons in these events were of low momentum and hence not detectable by the forward spectrometer. With only the detection of the scattered positron and emitted real photon, the exclusivity of the measurement can still be maintained, although not unambiguously, through the missing mass squared M_X^2 of the reaction $ep \to eX\gamma$,

$$M_\mathrm{X}^2 \equiv (k + P - k' - q')^2, \tag{5.1}$$

where k (k'), P, and q' denote the four-momentum of the initial (final) positron, the target proton, and the real photon, respectively. In the laboratory frame M_X^2 is written as

$$M_\mathrm{X}^2 \overset{\text{lab.}}{=} m_P^2 + 2m_P(\nu - E_\gamma) - Q^2 - 2E_\gamma\left(\nu - \sqrt{\nu^2 + Q^2}\cos\theta_{\gamma^*\gamma}\right), \tag{5.2}$$

where m_P is the proton mass, and the other variables are as defined in section 3.1.

Ideally the reconstructed missing mass squared of a BH/DVCS event equals to the squared mass of the recoiling proton. However, due to limited detector resolutions, the reconstructed missing mass squared is different from the original value and sometimes can even be negative. Hence we define the missing mass M_X as,

$$M_\mathrm{X} = \begin{cases} \sqrt{M_\mathrm{X}^2}, & \text{for} \quad M_\mathrm{X}^2 \geq 0, \\ -\sqrt{-M_\mathrm{X}^2}, & \text{for} \quad M_\mathrm{X}^2 < 0. \end{cases} \tag{5.3}$$

Below we describe the event selection cuts related to the scattered positron and to the emitted real photon.

5.2.1 Cuts Related to the Scattered Positron

Candidates for BH/DVCS events are required to have the DIS trigger (trigger 21) fired, and to have exactly one track that satisfies the following requirements:

Geometrical Cuts

- The track was a “long” track, namely, it was detected by both the front (DVC/FCs) and the rear (BCs) tracking chambers.

- The primary interaction vertex, which was taken as the point on the track where it was the closest to the z axis, had its z position z_{vtx} between -18 and 18 cm. The target cell has an extension of ± 20 cm along the direction of the z axis. Given the resolution of the spectrometer for z_{vtx}, which is approximately 2 cm (see section 5.4), this cut assures that the particle had come from the target region. Indeed, as can be seen from Fig. 5.1, the z_{vtx} position distribution of the selected BH/DVCS sample follows the triangle profile of the target density shown in Fig. 4.4.

  On the other hand, there was no cut applied on the reconstructed transverse position of the primary interaction vertex, $r^T_{vtx} = \sqrt{x^2_{vtx} + y^2_{vtx}}$. Nevertheless, the reconstructed vertices were all contained inside the elliptical cross section (21×8.9 mm^2) of the target cell, as can be seen from the projections shown in Fig. 5.1.

- The absolute value of the impact x (y) position of the track was smaller than 175 cm (between 30 and 108 cm) at the center of its energy deposition in the calorimeter. The latter was taken at $z = 738$ cm accounting for shower development. The

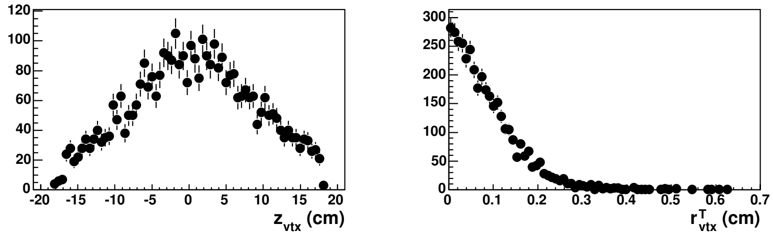

Figure 5.1: The distributions of the reconstructed z_{vtx} position and transverse position r^T_{vtx} of the BH/DVCS event sample selected from the 2002-2004 data. The z_{vtx} positions have been corrected for the influence of the transverse target magnet (section 5.6.1).

cut on the x position corresponds to the horizontal acceptance of ±170 mrad plus the additional 100 mrad starting from the middle of the spectrometer magnet. The cut on the y position corresponds to two-thirds of the outermost and the innermost rows of the calorimeter blocks.

- The absolute value of the x position of the track at the front (rear) field clamp was smaller than 31 (100) cm; the absolute value of the y position of the track at the septum plate (rear field clamp) was larger (less) than 7 (54) cm. These cuts were applied to eliminate secondary particles originating from scattering in these materials.

Kinematic Cuts

- The track was identified as a lepton by the cut PID2+PID5>2, which possesses the same charge as the beam particle.
- The correction for the influence of the transverse target magnet on track reconstruction (see section 5.6.1) was successful.
- The energy transfer ν from the incoming lepton to the virtual photon was less than 22 GeV. This cut discards the low lepton momentum region where the trigger efficiency of the calorimeter may not have reached a momentum plateau [Ell04].
- The invariant mass of the system of the virtual photon and target proton W^2 was larger than 9 GeV^2. This cut restricts the data to the regime where the fragmentation model of the Monte Carlo simulation is believed to work, e.g., it makes the estimation of background contributions more reliable.
- The negative squared four-momentum of the virtual photon Q^2 was larger than 1 GeV^2. Ideally one needs to satisfy the requirement $Q^2 \gg 1$ GeV^2 to assure the factorization of the DVCS process. However, such a cut would remove a dominant part of the data because of the fast decrease of the cross section with Q^2. As a compromise, we have chosen the cut at 1 GeV^2. Only moderate effects from power-suppressed corrections were found at HERMES kinematics [Bel00c].

5.2.2 Cuts Related to the Photon

Candidates for BH/DVCS events are required to contain exactly one trackless cluster in the calorimeter with energy above 5 GeV. With the 5 GeV cut, the cluster cannot be due to a charged particle that escaped detection of the tracking system. With the missing mass cut described below, neither can the cluster be due to a neutron. Hence the cluster must have come from a photon or photons. The latter can happen when two or more photons hit the same calorimeter block. As shown in Fig. 5.2, the 5 GeV cut

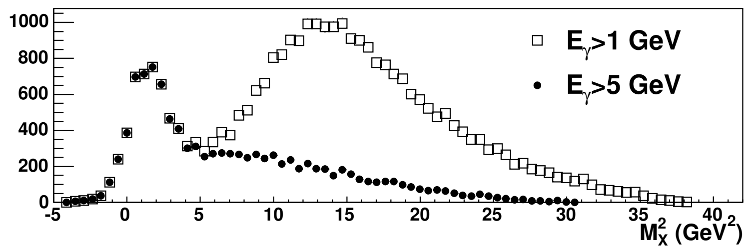

Figure 5.2: The distribution of the missing mass squared M_{X}^2 of the BH/DVCS event sample selected from the 2002-2004 data (solid circles). The same distribution but requiring $E_\gamma > 1$ GeV instead of $E_\gamma > 5$ GeV is also shown (open boxes).

has a negligible effect on the exclusive region ($M_{\mathrm{X}}^2 \sim m_p^2$), but has a significant effect on the non-exclusive region. This is due to the fact that the recoiling proton has a very low energy, thus energy conservation requires that the emitted real photon of a BH/DVCS event must carry most of the rest of the beam energy $E - E_e = \nu = \frac{W^2 - m_p^2}{2m_p(1-x_B)}$, which is larger than $\frac{9-m_p^2}{2m_p} = 4.3$ GeV due to the requirement $W^2 > 9$ GeV^2.

It is also required that a signal above 1 MeV correlated to the trackless cluster in the calorimeter was produced in the pre-shower detector. This requirement makes the reconstructed photon energy reliable. At HERMES, the calorimeter is calibrated based on the E/P ratio of a sample of positrons identified conservatively, whose energy deposition in the pre-shower detector was required to be more than that of minimum ionization particles. For photons which did not start showering in the pre-shower detector, the reconstructed photon energy can be wrong as much as 10% for photons of 15 GeV energy [Ely02]. Such a bias, which can lead to a poorer resolution in the missing mass and a less exclusive measurement, can be eliminated by the 1 MeV cut, although the cut will induce a 20% loss of statistics [Ely02]. Alternatively, one can introduce a calorimeter calibration depending on the pre-shower signal. Such an approach is at the moment being investigated and is not used in the present analysis.

For photons that start showering in the pre-shower detector the average z position of the energy deposition center in the calorimeter has been determined at $z = 732$ cm [Kra05]. This value is used in the analysis to calculate the photon-related kinematics. The other requirements on the trackless cluster are listed below:

Geometrical Cuts

- The absolute value of the x (y) position of the energy deposition center of the photon in the calorimeter was smaller than 125 cm (between 33 and 105 cm). The cut on the x position corresponds to the horizontal acceptance of $\pm$170 mrad. The cut on the y position corresponds to the outermost and innermost rows of the calorimeter blocks; it is used to ensure the whole cluster be contained inside the calorimeter and hence makes the reconstructed energy reliable.

Kinematic Cuts

- The angle between the real photon and the virtual photon, $\theta_{\gamma^*\gamma}$, was between 5 mrad and 45 mrad. As will be explained in section 5.7.1, the cut $\theta_{\gamma^*\gamma} < 45$ mrad is used to improve the signal-to-background ratio while, as will be shown in section 5.5.3, the cut $\theta_{\gamma^*\gamma} > 5$ mrad assures a more reliable extraction of the TTSA amplitudes.

- The missing mass squared M_X^2 was between -2.25 and 2.89 GeV^2. The invariant momentum transfer to the target proton t_c, calculated according to Eq. (3.11), was larger than -0.7 GeV^2. As can be seen in Fig. 5.2, the cut $M_X^2 > -2.25$ GeV^2 includes nearly all low missing mass events. The cut $M_X^2 < 2.89$ GeV^2 and the cut $t_c > -0.7$ GeV^2 are used to improve the signal-to-background ratio as will be explained in section 5.7.1.

- Two additional cuts, $0.03 < x_B < 0.35$ and $Q^2 < 10$ GeV^2, are applied to define a strict kinematic boundary for the analysis. Since for most of the events x_B and Q^2 satisfy these two cuts, their effect is negligible.

5.2.3 Beam Polarization Balancing

The beam has to be unpolarized to be free of the double-spin asymmetry (see section 3.3). This requirement is effectively satisfied by discarding data with beam polarization above 0.4. For the combined 2002-2004 data, the average beam polarization is 0.00 (0.03) after (before) applying this cut. The statistics is reduced by approximately 6%, as can be seen in Tab. 5.1.

	Year	2002	2003	2004	2002-2004
before balancing	$\langle P_B \rangle$	0.00	0.28	0.00	0.03
	$\mathbb{L}$ (pb^{-1})	12.7	5.8	50.7	69.2
	# of events	746	330	2954	4030
after balancing	$\langle P_B \rangle$	0.00	0.23	-0.02	0.00
	$\mathbb{L}$ (pb^{-1})	12.7	4.7	47.9	65.3
	# of events	746	268	2799	3813

Table 5.1: The average beam polarization weighted by luminosity $\langle P_B \rangle$, the integrated luminosities $\mathbb{L}$, and the number of candidates for BH/DVCS events before and after balancing the beam polarization.

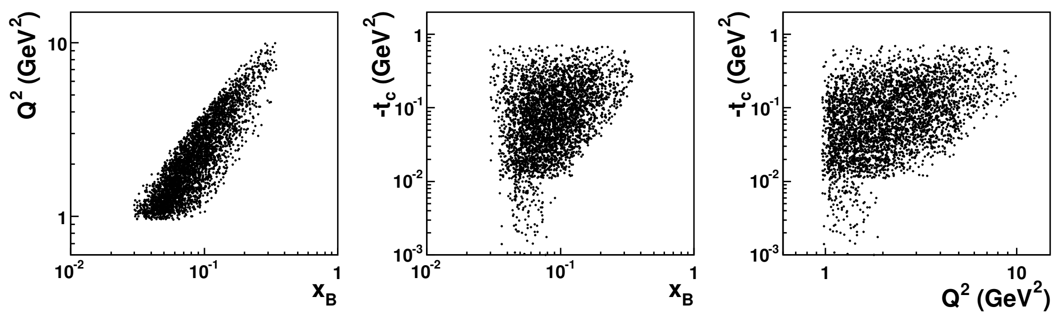

Figure 5.3: Kinematic $x_B - Q^2$, $x_B - t_c$, and $Q^2 - t_c$ planes covered by the selected BH/DVCS event sample from the 2002-2004 data.

In conclusion, a total number of 3813 candidates for BH/DVCS events has been selected out of the 2002-2004 data. The kinematic planes covered by these events are shown in Fig. 5.3.

5.3 Monte Carlo Simulation

Monte Carlo (MC) simulations are useful in many aspects for data analyses. In the present analysis, they are used to study detector resolutions (section 5.4), to test the methods to extract the TTSA amplitudes (section 5.5), to investigate the influence of the transverse target magnet on track reconstruction (section 5.6.1), and to check the misalignment effect (section 5.6.2) and the influence of a possible miscalibrated calorimeter (section 5.6.3) on the extracted TTSA amplitudes. MC simulations are also used to estimate the systematic uncertainties of the extracted TTSA amplitudes due to the smearing and acceptance effects (section 5.6.5), and to estimate and correct for background contributions (section 5.7.1).

In this section, we describe the MC simulations used in our analysis (section 5.3.1) and compare their outputs to the actual experimental data (section 5.3.2).

5.3.1 Generating MC Events

Due to the limited resolution of the HERMES spectrometer for M_{X}^2, events of the associated BH/DVCS processes are not distinguishable from events of the elastic BH/DVCS processes. In addition, semi-inclusive and exclusive productions of neutral mesons (mostly pions) decaying into photons also contribute to the selected BH/DVCS event sample. Three generators, gmc_dvcs, gmc_disNG, and gmc_exclpion, are used to simulate these processes.

The gmc_dvcs generator [Kra05] provides simulations of the elastic BH/DVCS processes. The unpolarized cross section for the elastic BH process is calculated using the Mo−Tsai formalism [Mo69]. Spin-dependent cross sections due to beam and target polarizations are modelled according to Ref. [Bel02]. The cross section for the elastic DVCS process is calculated according to Ref. [Bel02], based on the following GPD models [Kor02]:

1. GPDs are independent on ξ. Their x and t dependences factorize.
2. The dependence on x and ξ is modelled in the double-distribution representation [Rad99, Mus00]. The dependence on t factorizes. The parameter b, which controls the size of the ξ dependence, is set to one.
3. The same as the previous model but with $b = 3$.
4. In addition to the double-distribution contribution with $b = 1$, the D-term is added according to the predictions of the chiral quark-soliton model.
5. The same as the previous model but with $b = 3$.

The gmc_dvcs generator simulates also the associated BH process for resonance states of mass between 1.1 and 2 GeV. The total cross section is calculated using the Brasse parameterization [Bra76] for the inclusive cross section $\sigma_{tot}(\gamma^* p)$ in the resonance region measured at SLAC. The individual cross sections for single-meson decay channels (e.g., $\Delta^+ \to p\pi^0$) are modelled according to the MAID2000 model [Dre99]. The remaining contribution to the total cross section is assigned to multi-meson decay channels (e.g., $\Delta^+ \to p\pi^0\pi^0$) according to isospin relations. Due to lack of knowledge, the generator does not simulate the associated DVCS process.

The gmc_disNG generator simulates semi-inclusive DIS processes. The generator is an extension of the leptoproduction generator LEPTO [Ing97] which simulates polarized DIS processes. The fragmentation and decay of unstable particles are simulated with JETSET [Sjö94] based on the LUND string model [And83] and optimized for energies relevant to HERMES [Hil03]. Radiative processes are included with RADGEN [Aku99], which provides simulation of both the elastic and associated BH processes. However, in this code the simulation of the associated BH process is found to overestimate the cross section, especially below the Δ-resonance [Kra05]. Hence in our study, we will rely on gmc_dvcs for the simulation of BH/DVCS processes, and use gmc_disNG only to simulate semi-inclusive DIS processes with $W > 2$ GeV.

The gmc_exclpion generator simulates exclusive production of pions based on the model given in Ref. [Van99]. The generator can approximately reproduce the exclusive π^+ cross section measured at HERMES [Had04], as shown in Fig. 5.4. The model "VGG: LO+power corrections" that overestimates the measured cross section of exclusive production of π^+ is used to simulate exclusive production of π^0.

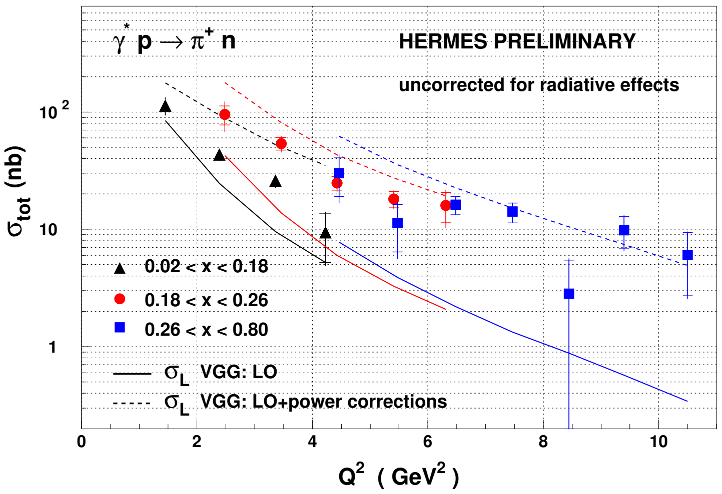

Figure 5.4: The total cross section σ_{tot} for exclusive production of π^+ as a function of x_B and Q^2. Two different model predictions are also shown.

The outputs of these three generators are combined according to their cross sections. The combined MC data are then processed by the HERMES Monte Carlo (HMC) program, which uses the GEANT3 [Cer93b] package to simulate the passage of particles through matter. The simulated responses of the detectors are converted into a digitized form to resemble the actual experimental data, based on resolutions and efficiency functions of the individual detectors obtained from measurements. In order to avoid wrong modelings of the calorimeter in HMC, the reconstructed photon energy in our study is not taken from the MC simulation, but numerically calculated according to the calorimeter resolution [Ava98]:

$$\frac{\sigma(E)}{E}[\%] = \frac{5.1 \pm 1.1}{\sqrt{E(GeV)}} + (2.0 \pm 0.5) + \frac{10.0 \pm 2.0}{E(GeV)}.$$

The output of HMC is processed by the HRC program to reconstruct tracks and clusters in the same way as for the experimental data. Finally the MC events are written into μDST files by the writeMCDST program.

5.3.2 Comparison between MC and Experimental Data

A comparison between the unpolarized yields from the MC simulations and from the experimental data is shown in Fig. 5.5. Both the MC and experimental yields are normalized by the respective integrated luminosity. As can be seen, the MC yield in the exclusive region $-2.25 < M_X^2 < 2.89$ GeV^2 changes by 10−20% with different GPD models, and the MC simulations overshoot the experimental data by approximately

15−30% in the exclusive region. The former spread is mainly due to the different predictions for the pure DVCS contribution as can be seen in Fig. 5.6. The latter problem can be understood by the fact that the experimental data are not corrected for detection inefficiencies and that the MC simulations do not include radiative corrections, which are known to play a substantial role in cross section measurements. For example, QED radiative corrections have been estimated at the kinematics of a lepton beam with energy 6 GeV, $x_B = 0.3$, and $Q^2 = 2$ GeV^2 and lead to a reduction of approximately 20% in the BH+DVCS cross section [Van00]. No estimates are available at higher beam energies.

Differences in the position of the exclusive peak between the MC simulations and the experimental data can also be seen in Fig. 5.5: the peaks of the MC simulations are located at lower values of M_X^2 than the experimental one. Such differences can be due to radiative corrections: events with additionally radiated photons which escaped detection were reconstructed at higher values of M_X^2. Therefore a simulation including radiative corrections should give a better MC-data agreement not only in the exclusive region, but also in the non-exclusive region. In addition, M_X^2 is very sensitive to the photon energy E_γ (see Eq. (5.2)). Given the average kinematics of the selected BH/DVCS event sample, $\langle\nu\rangle \sim 14$ GeV, $\langle E_\gamma\rangle \sim 14$ GeV, $Q^2 \sim 2.5$ GeV^2, $\langle\cos\theta_{\gamma^*\gamma}\rangle \sim 1$, 1% relative change in E_γ could result into 200 MeV^2 shift in M_X^2. Such an effect can be clearly seen by comparing Figs. 5.5 and 5.7, for the latter the reconstructed photon energies in the MC simulation are decreased by 1%. Neglecting the potential effect from radiative corrections, the better MC-data agreement in the exclusive peak position shown in Fig. 5.7 suggests that the calorimeter calibration might have been off by 1% in the experimental data. Further discussion on the calorimeter calibration wil be given in section 5.6.3.

One can reweight the BH/DVCS events with a global factor so that the total MC and experimental data yields in the exclusive region are the same. A rather good MC-data agreement in all kinematic distributions except in ϕ can be seen in Fig. 5.8, where the MC simulation does not include the DVCS interference. To see the possible influence of the contribution from the DVCS process and its interference to the BH process, the results from an MC simulation including the DVCS process based on one GPD model are shown in Fig. 5.9. As can be seen, the MC-data agreement in the ϕ distribution is improved, as expected.

As we do not attempt in the present analysis to measure an absolute cross section but a spin-dependent asymmetry, it is very helpful to know that radiative corrections to the spin-dependent asymmetries are small. For example, at the same kinematics mentioned above, QED radiative corrections lead to a relative change of approximately 5% in the beam-spin asymmetry [Van00]. The fact that radiative corrections are not included in the MC simulations should not affect the studies on detector resolutions, but it may have some influence on estimating background contributions. For the following studies, we will use the MC simulation without including the DVCS process as a default,

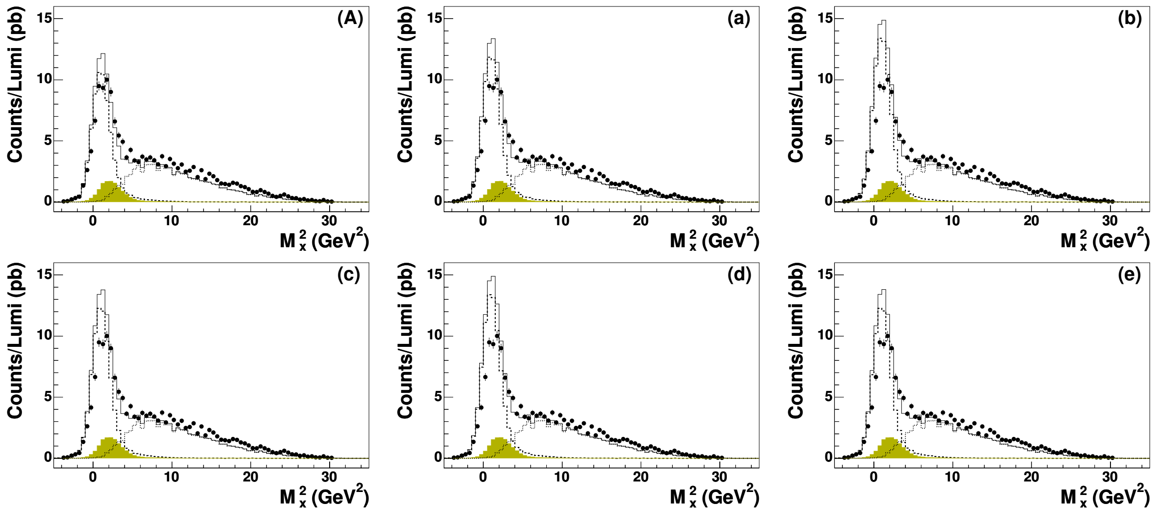

Figure 5.5: Comparison between the absolutely normalized M_X^2 distributions from the MC simulation (solid line) and from the experimental data (points). The BH/DVCS processes are either simulated for the BH process only (panel A), or for both the BH and DVCS processes (panels a−e) based on GPD models 1-5 in section 5.3.1. Also shown are individual contributions from elastic BH/DVCS processes (dashed line), associated BH processes (shaded area), and semi-inclusive processes (dotted line).

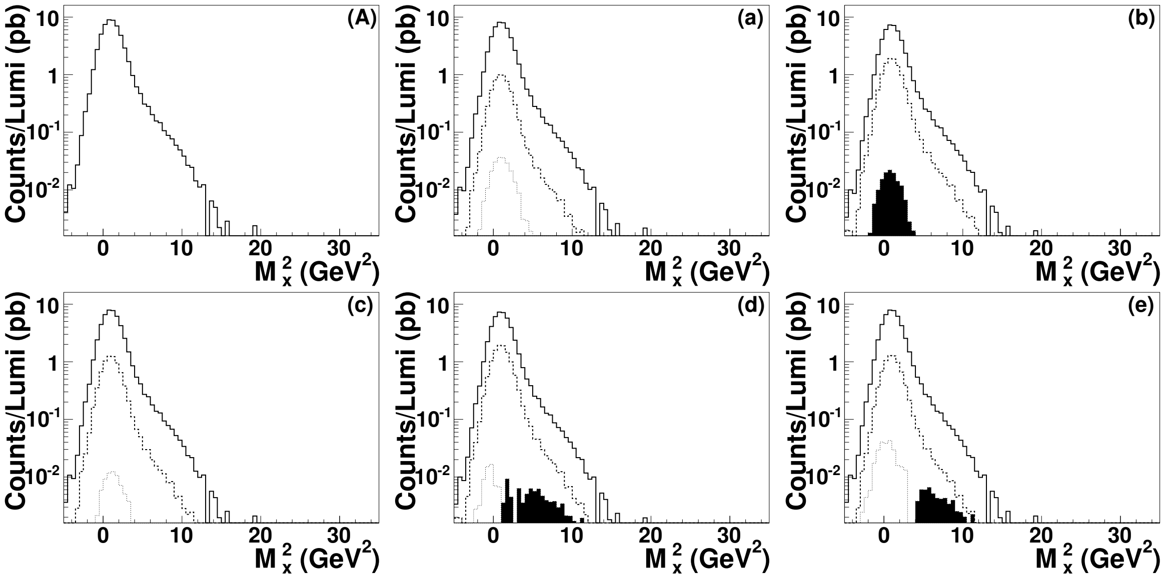

Figure 5.6: Contributions from the individual elastic BH/DVCS processes: solid line – pure BH, dashed line – pure DVCS, shaded area – BH-DVCS interference of positive values, dotted line – BH-DVCS interference of negative values. See Fig. 5.5 for more information.

and whenever it is necessary, e.g., in estimating background contributions, a systematic uncertainty will be assigned to account for the different results from the MC simulations including also the DVCS process.

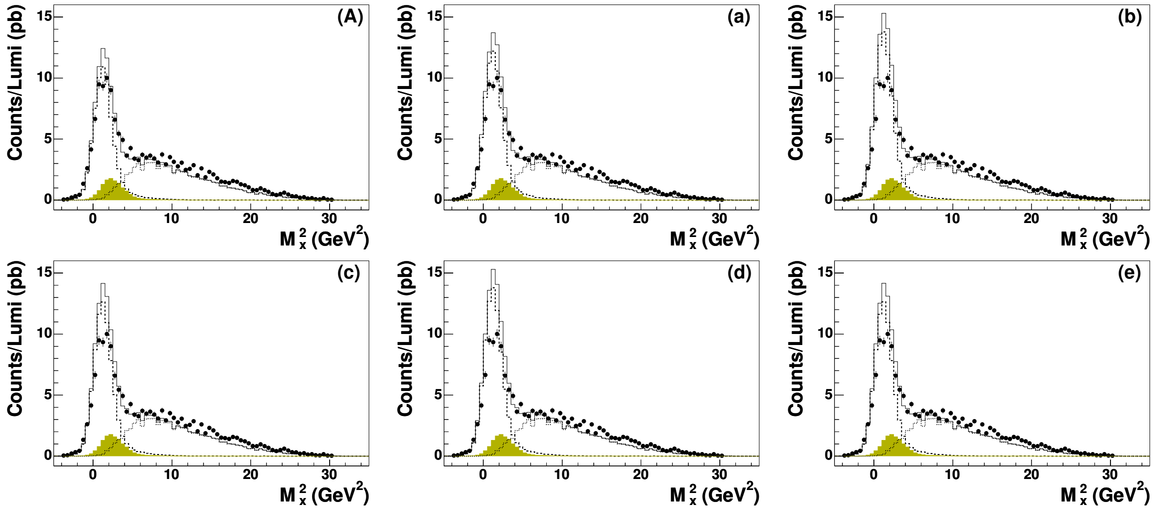

Figure 5.7: Same as Fig. 5.5 but the reconstructed photon energies in the MC simulation are decreased by 1%.

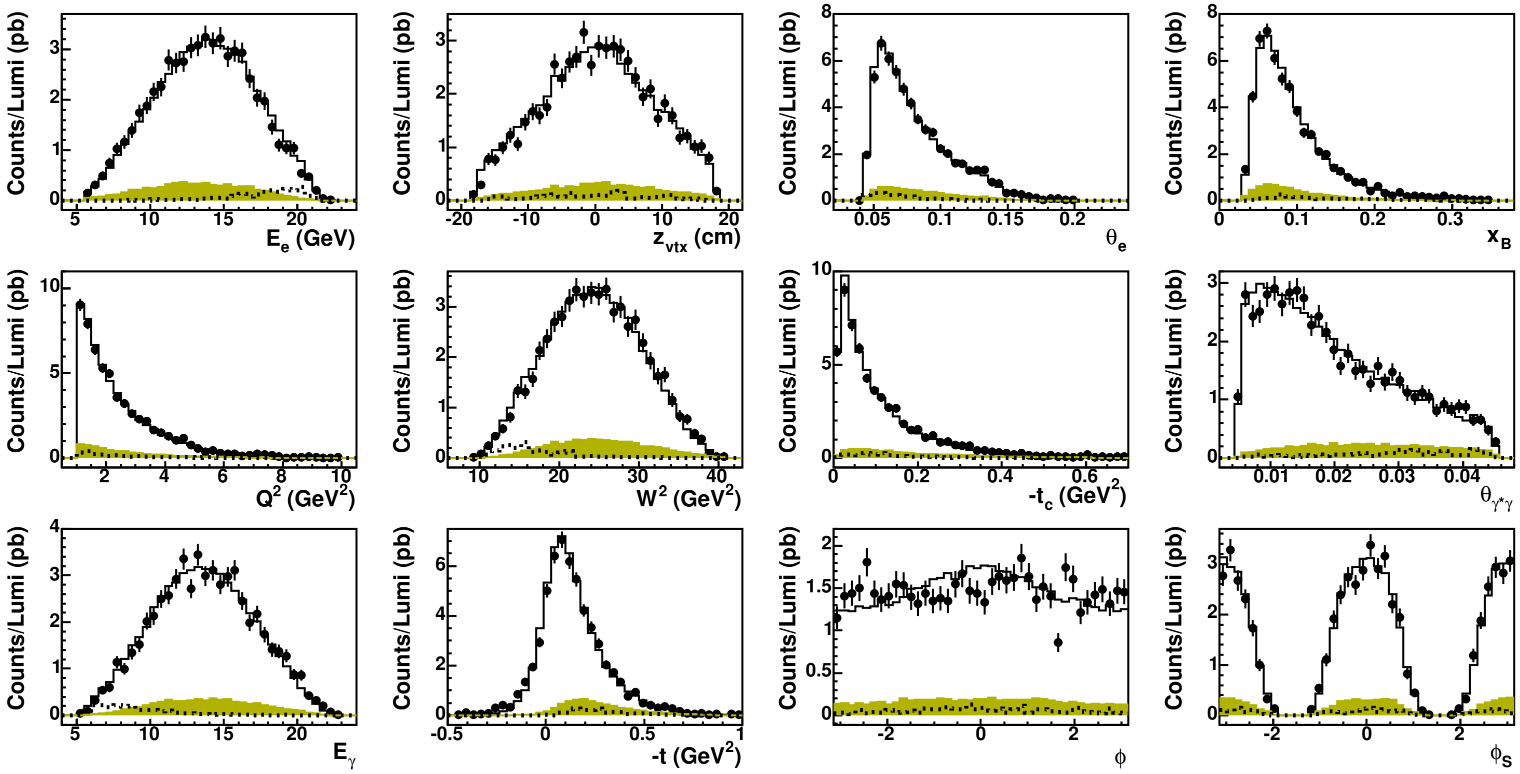

Figure 5.8: Comparison between the the MC simulation (solid lines) and the experimental data (points) in the exclusive region $-2.25 < M_X^2 < 2.89$ GeV^2. The MC simulation is performed without including the DVCS process, corresponding to panel (A) in Fig. 5.7. The BH events are reweighted so that the total exclusive yield of the MC simulation equals the experimental one. Also shown are individual contributions from associated BH processes (shaded area), and semi-inclusive processes (dotted line).

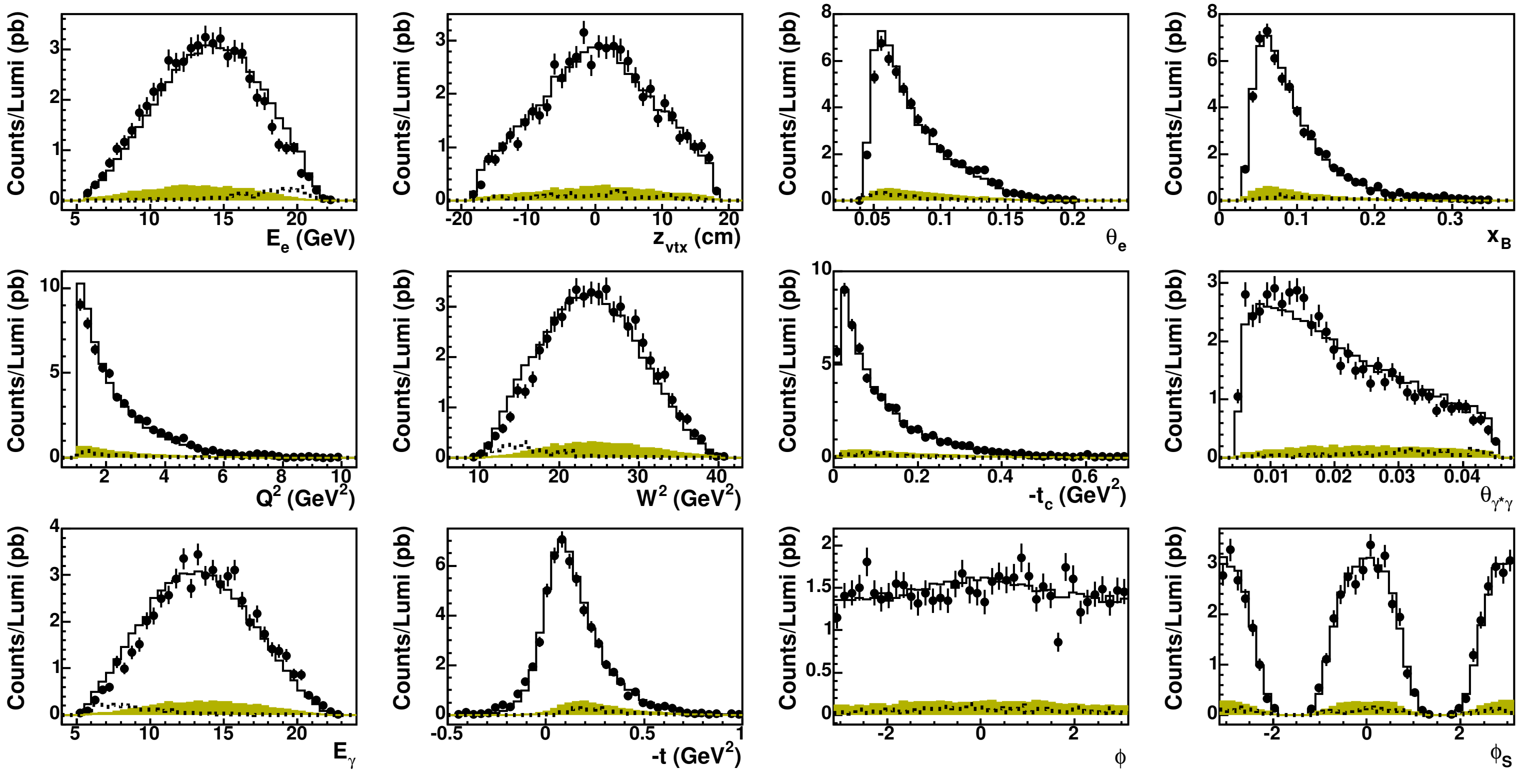

Figure 5.9: Same as Fig. 5.8 but the DVCS process is simulated using GPD model 2 in section 5.3.1, corresponding to panel (b) in Fig. 5.7.

5.4 Detector Resolutions

Detector resolutions can be studied in MC simulations. Correlations between the reconstructed and generated kinematic variables are shown in Fig. 5.10. Derived from the results shown in Fig. 5.10, the averages and standard deviations of the differences between the reconstructed and generated kinematic variables are shown (magnet off) in Figs. 5.11 and 5.12. Below we will mainly check the reconstruction of the kinematic variables x_B, Q^2, t, ϕ, and ϕ_S, on which the TTSA amplitudes depend.

As can be seen in Figs. 5.11 and 5.12, the generated invariant momentum transfer to the target proton t is much better measured by t_c given in Eq. (3.10) than by t given in Eq. (3.11). Such a difference is due to the fact that t_c is calculated using the charged track information from the tracking system and the position information of the trackless cluster in the calorimeter, while t in Eq. (3.11) is calculated using also information given by the calorimeter about the photon energy. At the average HERMES kinematics, $Q^2 \ll \nu^2$, $\cos\theta_{\gamma^*\gamma} \sim 1$, Eq. (3.10) can be approximated as

$$t \simeq -Q^2 \cdot \left[1 - \frac{E_\gamma}{\nu} + \frac{E_\gamma}{\nu} \cdot \frac{Q^2}{2\nu^2} + \frac{2E_\gamma}{x_B m_N} \sin^2 \frac{\theta_{\gamma^*\gamma}}{2}\right] + (\cdots), \tag{5.4}$$

where the ellipsis denotes terms of higher order in $\frac{Q^2}{\nu^2}$ and $\sin^2 \frac{\theta_{\gamma^*\gamma}}{2}$. Similarly we can

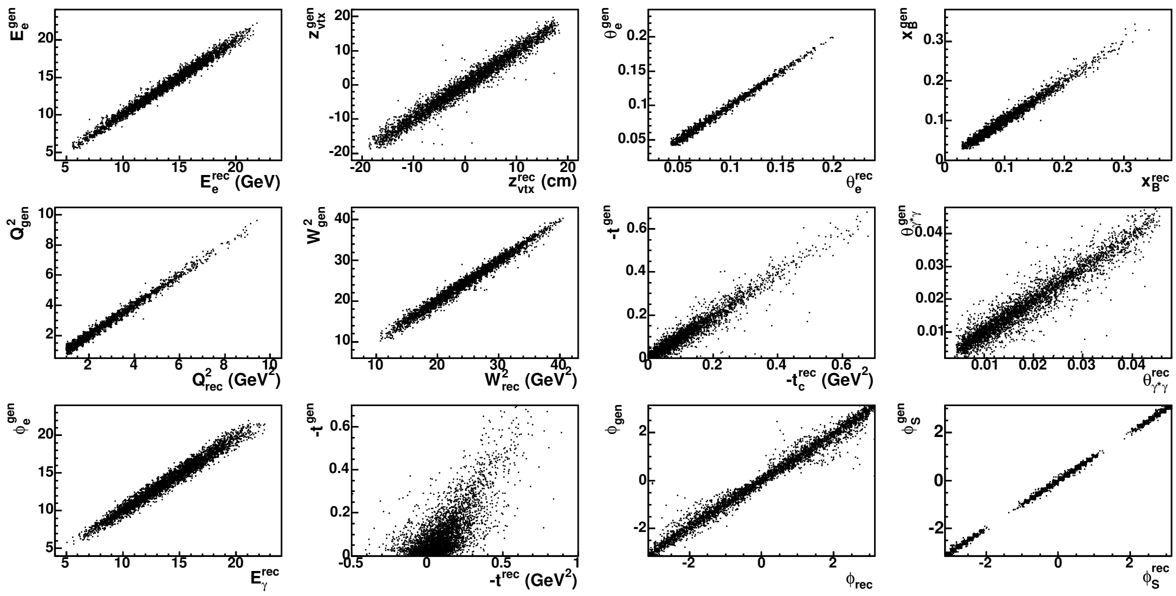

Figure 5.10: Correlations between the reconstructed (x axis) and generated (y axis) kinematic variables. The transverse target magnet was switched off in the simulation. The results are for the elastic BH events passing through all the cuts

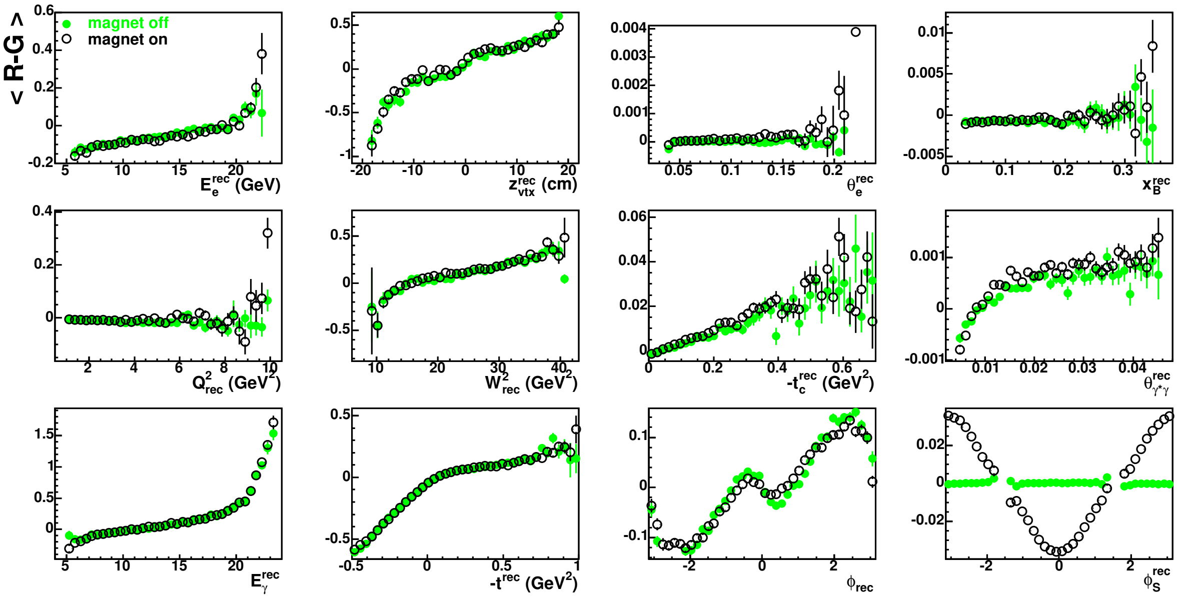

Figure 5.11: The average differences between the reconstructed and generated kinematic variables given as a function of the reconstructed kinematic variable. The transverse target magnet was either switched off (solid points) or switched on (open points) in the simulation. In the latter case, no correction was applied to track reconstruction. The error bars stand for statistical uncertainties.

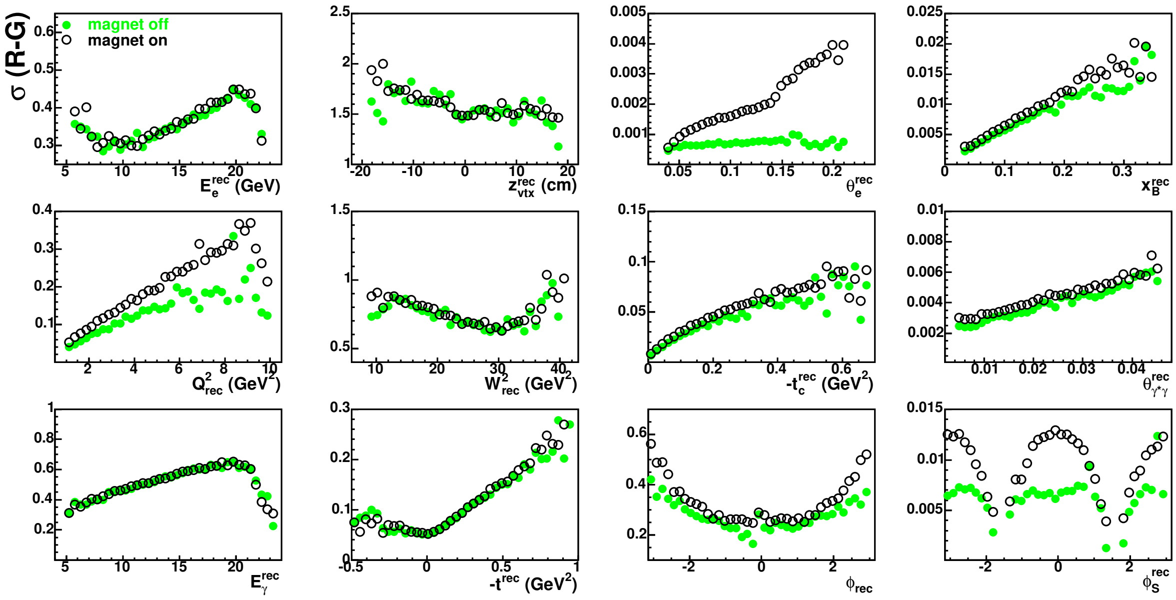

Figure 5.12: The standard deviations of the differences between the reconstructed and generated kinematic variables given as a function of the reconstructed kinematic variable. See Fig. 5.11 for more information.

write the approximation for Eq. (3.11)

$$t_c \simeq -Q^2 \cdot \left[\frac{Q^2}{2\nu^2} + \frac{2\nu}{x_B m_N} \sin^2 \frac{\theta_{\gamma^*\gamma}}{2} \right] + (\cdots). \tag{5.5}$$

After inserting Eqs. (3.5) and (3.6) into the two equations above, one finds that uncertainties in the measurement of ν contribute much more to t than to t_c, and uncertainties in the measurement of E_γ contribute only to t and not to t_c. Hence there is no surprise to see in Fig. 5.12 that t in Eq. (3.11) has a much worse resolution than t_c.

As can be seen from Fig. 5.11, ϕ tends to be reconstructed at larger absolute values than the true ones, while x_B, Q^2, t_c, and ϕ_S are reconstructed almost without bias. As can be seen in Fig. 5.12, the measurement resolutions for x_B, Q^2, and t_c have approximately linear dependences. Their relative resolutions are better than 5%, 3%, and 2%, respectively. The resolution for ϕ is approximately 0.25 rad at $\phi = 0$ and gets worse at larger absolute values of ϕ. The resolution for ϕ_S is approximately constant at 7 mrad and is much better than the resolution for ϕ.

5.5 Methods to Extract Azimuthal Asymmetries

Neglecting background contributions, the number of events of interest detected in a measurement depends on three things: the integrated luminosity of the measurement; the cross section of the physics process; and the detector responses, i.e., the detection efficiency as well as the smearing and acceptance effects of the detectors. This can be represented as:

$$N(\boldsymbol{x}') = \int d\tau\, L(\tau) \cdot \int d\boldsymbol{x}\, \frac{d\sigma(\boldsymbol{x})}{d\boldsymbol{x}} \cdot \epsilon(\boldsymbol{x}, \tau) \cdot S(\boldsymbol{x}'|\boldsymbol{x}). \tag{5.6}$$

Here N denotes the number of detected events, $\boldsymbol{x}$ ($\boldsymbol{x}'$) the true (measured) values of a set of kinematic variables which is (t, x_B, Q^2, ϕ, ϕ_S) in the present case, τ the time, L the luminosity, $d\sigma/d\boldsymbol{x}$ the differential cross section, ϵ the total detection efficiency (tracking and trigger) which describes the probability that an event leads to some measured value, and S describes the smearing and acceptance effects of the detectors: $S(\boldsymbol{x}'|\boldsymbol{x})$ gives the probability that an event of true kinematics at $\boldsymbol{x}$ be measured at $\boldsymbol{x}'$. The detection efficiency $\epsilon(\boldsymbol{x}, \tau)$ is written with explicit time dependence to account for possible changes of detector running conditions during the measurement. In order to disentangle $S(\boldsymbol{x}'|\boldsymbol{x})$ from $\epsilon(\boldsymbol{x}, \tau)$ for the following discussions, we require that by definition $0 < \epsilon(\boldsymbol{x}, \tau) < 1$, and $\int d\boldsymbol{x}'\, S(\boldsymbol{x}'|\boldsymbol{x}) = 1$ or 0, where 1 (0) means that the kinematic position is (is not) in the acceptance.

The HERMES transversely polarized target switched between positive and negative polarization states once per 90 s. It is reasonable to assume that the detection efficiency did not change during such a short period. One can also assume that, for events with the same positions of the particles crossing the detectors, the smearing and acceptance effects are the same. Note that the actual polarization vector $\vec{S}_\perp^{\pm} = \{0, \mp 1, 0\}$ is different for the positive and negative target polarization states at HERMES, where the superscript $\pm$ stands for the target polarization state. Hence for events with the same values of ϕ_S (neglecting the dependence on the other kinematic variables), the absolute positions of the particles crossing the detectors are different in different target polarization states; they are the same only when the values of ϕ_S in the two target polarization states differ by π. If one calculates ϕ_S according to Eq. (3.16) with a fixed target polarization vector $\vec{S}_\perp = \{0, -1, 0\}$ for the two target polarization states, the value denoted by ϕ_S^*, which is related to the actual value of ϕ_S by

$$\begin{aligned} &\phi_S^* = \phi_S, && \text{for the positive target polarization state;} \\ &\phi_S^* = \phi_S + \pi, && \text{for the negative target polarization state.} \end{aligned}$$

Hence we have

$$\begin{aligned} \epsilon^+(\boldsymbol{x}^*, \tau) = \epsilon^-(\boldsymbol{x}^*, \tau) \equiv \epsilon(\boldsymbol{x}^*, \tau), \\ S^+(\boldsymbol{x}^{*\prime}|\boldsymbol{x}^*) = S^-(\boldsymbol{x}^{*\prime}|\boldsymbol{x}^*) \equiv S(\boldsymbol{x}^{*\prime}|\boldsymbol{x}^*), \end{aligned} \tag{5.7}$$

and

$$A_{UT}(\phi, \phi_S) = A_{UT}(\phi, \phi_S^*) \equiv \frac{d\sigma^+(\phi, \phi_S^*) - d\sigma^-(\phi, \phi_S^*)}{d\sigma^+(\phi, \phi_S^*) + d\sigma^-(\phi, \phi_S^*)}, \tag{5.8}$$

where $A_{UT}(\phi, \phi_S)$ is the TTSA defined in Eq. (3.40).

As can be seen in Eq. (5.6), in order to extract the cross section from the number of detected events, one needs to correct for the detection efficiency as well as for the smearing and acceptance effects. While the detection efficiency may be extracted from the experimental data, the smearing and acceptance effects have to be studied either by means of external calibration experiments where the true value $\boldsymbol{x}$ is known a priori, or by using an MC simulation based on modeling the physical processes in the detectors. A complete correction for the smearing and acceptance effects can then be performed by applying the unfolding technique (see for example Ref. [Cow98]). It is known [Cow98], however, that unfolding may suffer from statistical instabilities even when dealing with one-dimensional problems. Since it is a multi-dimensional problem that is being considered here, statistical instabilities can be expected to be even larger and some complicated regularization method may have to be used. Hence in the present analysis, we do not perform an unfolding to extract the spin-dependent cross sections and consequently the TTSA in Eq. (3.40), but rather we will extract directly from the data the TTSA amplitudes given in Eqs. (3.41) and (3.42), utilizing the relations illustrated in Eq. (5.7).

In this section we will discuss two different approaches, namely, by using the method of least squares, or by using the method of maximum likelihood, to directly extract the TTSA amplitudes without extracting the cross sections. We will investigate in MC simulations the bias and efficiency properties of these two methods in our application. It will be shown below that the detection efficiency can be neglected in such approaches. For the smearing and acceptance effects, a simple but more direct correction will be applied to the extracted TTSA amplitudes, and a systematic uncertainty will be assigned to account for the remaining effects after the correction. For clarity of notation we will introduce a new variable $\beta^* \equiv \phi - \phi_S^*$ in the following.

5.5.1 The Method of Least Squares

The method of least squares (LS) [PDG04] relies on the fact that if $x_1, \cdots, x_n$ are n independent Gaussian random variables, the sum $\sum_i (x_i - \mu_i)^2/\sigma_i^2$ follows the χ^2 probability density function (p.d.f.) with n degrees of freedom. Consider a set of N independent measurements y_i, which are Gaussian distributed with mean $F(x;\boldsymbol{\theta})$ and known variance σ_i^2, at known points x_i. The estimator for the mean of the parameters $\boldsymbol{\theta}$ is given by the LS method as the point in the parameter space where

$$\chi^2 = \sum_i \frac{\left[y_i - F(x_i;\boldsymbol{\theta})\right]^2}{\sigma_i^2} \tag{5.9}$$

is at its minimum. The estimator for the variance of the parameters $\boldsymbol{\theta}$ is given by the tangent planes of the contour in the parameter space defined by

$$\chi^2(\boldsymbol{\theta}) = \chi^2_{\min} + 1. \tag{5.10}$$

The LS method has been used to extract the beam-spin asymmetry [Ely02, Air01], the beam-charge asymmetry [Ell04, Air06a], and the longitudinal target-spin asymmetry [Kop05] associated with DVCS. It has also been used in the early stage of this analysis to extract the TTSA associated with DVCS [Ye05]: the BH/DVCS event sample selected from the data is binned in two dimensions (ϕ, β^*), and the quantity

$$\mathbb{A}_{UT} = \frac{1}{\langle |P_T| \rangle} \frac{N_+ \cdot \mathbb{L}_- - N_- \cdot \mathbb{L}_+}{N_+ \cdot \mathbb{L}_- + N_- \cdot \mathbb{L}_+} \tag{5.11}$$

is calculated for each bin, where the subscript $\pm$ stands for the target polarization state, N denotes the number of detected events in the bin, $\mathbb{L}$ the integrated luminosity, and $\langle |P_T| \rangle$ the average of the absolute value of the target polarization. The quantity χ^2 to be minimized is given by

$$\chi^2 \equiv \sum_{i,j} \frac{\left[\mathbb{A}_{UT}^{i,j} - f(\phi_i, \beta_j^*;\boldsymbol{\theta})\right]^2}{\sigma^2\left(\mathbb{A}_{UT}^{i,j}\right)}, \tag{5.12}$$

where i (j) denotes the bin number in ϕ (β^*), f is a function containing the azimuthal dependence of the TTSA (see Eqs. (3.41) and (3.42)), e.g.,

$$f(\phi, \beta^*; \theta_1, \theta_2) = \theta_1 \cdot \sin\beta^* \cos\phi + \theta_2 \cdot \cos\beta^* \sin\phi, \tag{5.13}$$

and $\sigma^2(\mathbb{A}_{UT})$ denotes the variance of the quantity $\mathbb{A}_{UT}$.

For data samples with sufficiently large statistics, the bin widths in ϕ and in β^* can be chosen to be small. In such cases, the arguments ϕ_i and β_j^* entering into the fit function f in Eq. (5.12) can be taken either at the bin center or at the average of the events in each bin, and the variance $\sigma^2(\mathbb{A}_{UT})$ can be approximated by the first-order Taylor expansion around the estimate for the mean of $\langle|P_T|\rangle$, $\mathbb{L}_{\pm}$, and $N_{\pm}$,

$$\begin{aligned} \sigma^2(\mathbb{A}_{UT}) &\approx \left(\frac{\partial \mathbb{A}_{UT}}{\partial N_+}\right)^2 \cdot \sigma^2(N_+) + \left(\frac{\partial \mathbb{A}_{UT}}{\partial N_-}\right)^2 \cdot \sigma^2(N_-) \\ &= \frac{4}{(\langle|P_T|\rangle)^2} \cdot \frac{(n^+ + n^-)\, n^+ n^- \left(\mathbb{L}^- \mathbb{L}^+\right)^2}{\left(n^+ \mathbb{L}^- + n^- \mathbb{L}^+\right)^4}. \end{aligned} \tag{5.14}$$

On the right-hand side of the first line in the above equation, the contributions from the variances of $\langle|P_T|\rangle$ and $\mathbb{L}_{\pm}$ are neglected, and will be treated separately as systematic uncertainties in section 6.1.2. As the number of detected events in each bin follows the Poisson p.d.f., in the evolution of Eq. (5.14) from the first line to the second line, we have used the actual number of detected events $n_{\pm}$ to estimate the mean and the variance of the number of detected events $N_{\pm}$.

The above approach has several advantages: (a) if the measurement is fully differential in the kinematics, the detection efficiency is cancelled out by forming the ratio in Eq. (5.11) due to the relation illustrated in Eq. (5.7); (b) the fitted minimum value of χ^2 can be used as a goodness-of-fit statistic as it follows the χ^2 p.d.f.. On the other hand, such an approach has some obvious disadvantages: (a) information is lost by binning the data, e.g., larger bin width means worse resolution and thus larger smearing effects; (b) an additional systematic uncertainty is introduced from the arbitrary choice of the bin widths; (c) the variance $\sigma^2(N_{\pm})$ is underestimated when the actual number of detected events $n_{\pm}$ is small, say, less than five. In the latter case the fitted mean (variance) of the parameters $\boldsymbol{\theta}$ may be biased (underestimated).

5.5.2 The Method of Maximum Likelihood

For a set of independently measured quantities $\boldsymbol{x}$ following a p.d.f. $f(\boldsymbol{x}; \boldsymbol{\theta})$, where $\boldsymbol{\theta}$ is a set of parameters whose values are to be determined, the estimator for the mean of $\boldsymbol{\theta}$ is given by the method of maximum likelihood (ML) [PDG04] as the point in the parameter space where the likelihood function

$$L(\boldsymbol{\theta}) = \prod_i f(\boldsymbol{x}_i; \boldsymbol{\theta}) \tag{5.15}$$

is at its maximum, or equivalently, its negative logarithm

$$-\ln L(\boldsymbol{\theta}) = -\sum_i \ln f(\boldsymbol{x}_i;\boldsymbol{\theta}) \tag{5.16}$$

is at the minimum. The estimator for the inverse covariance matrix is given by

$$(\hat{V}^{-1})_{ij} = -\frac{\partial^2 \ln L}{\partial\theta_i \partial\theta_j}\big|_{\hat{\boldsymbol{\theta}}}. \tag{5.17}$$

The p.d.f. $f(\boldsymbol{x};\boldsymbol{\theta})$ is usually normalized to unit area, i.e., $\int d\boldsymbol{x}\ f(\boldsymbol{x};\boldsymbol{\theta}) = 1$. However, in applying the ML method, the normalization of the p.d.f. is not necessarily unity, but has to be fixed – independently of the fitted parameters. As one is only interested in the maximum of L and in ratios of L at different values of the parameters, any multiplicative factors in f that do not involve $\boldsymbol{\theta}$ may be dropped.

For DVCS data samples measured with an unpolarized beam on a transversely polarized target, the p.d.f. can be written as:

$$\begin{aligned} f_\pm(\phi,\phi_S^*;\boldsymbol{\theta}) &= \frac{1}{C_\pm(\boldsymbol{\theta})}\cdot\epsilon(\phi,\phi_S^*)\cdot\sigma_\pm(\phi,\phi_S^*;\boldsymbol{\theta}) \\ &= \frac{1}{C_\pm(\boldsymbol{\theta})}\cdot\epsilon(\phi,\phi_S^*)\cdot\sigma_U(\phi)\cdot\big[1\pm|P_T|\cdot A_{UT}(\phi,\phi_S^*;\boldsymbol{\theta})\big], \end{aligned} \tag{5.18}$$

where the dependence on t, x_B, and Q^2 has been omitted, the subscript $\pm$ stands for the target polarization state, $\boldsymbol{\theta}$ the parameters to be determined which enter the description of the azimuthal dependence of the TTSA $A_{UT}(\phi,\phi_S^*;\boldsymbol{\theta})$ (see, e.g., Eq. (5.13)), ϵ the detection efficiency, $\sigma_U = \frac{\sigma_+ + \sigma_-}{2}$ the polarization-averaged cross section, P_T the target polarization value, and $C_\pm$ the normalization integral that maintains fixed normalization for $f_\pm$:

$$\begin{aligned} C_\pm(\boldsymbol{\theta}) &= \int \epsilon(\phi,\phi_S^*)\cdot\sigma_U(\phi)\cdot\big[1\pm|P_T|\cdot A_{UT}(\phi,\phi_S^*;\boldsymbol{\theta})\big] \\ &= \int \epsilon(\phi,\phi_S^*)\cdot\frac{\sigma_+(\phi,\phi_S^*)+\sigma_-(\phi,\phi_S^*)}{2}\cdot\big[1\pm|P_T|\cdot A_{UT}(\phi,\phi_S^*;\boldsymbol{\theta})\big] \\ &= \int \frac{f_+(\phi,\phi_S^*;\boldsymbol{\theta})+f_-(\phi,\phi_S^*;\boldsymbol{\theta})}{2}\cdot\big[1\pm|P_T|\cdot A_{UT}(\phi,\phi_S^*;\boldsymbol{\theta})\big]. \end{aligned} \tag{5.19}$$

In fitting the parameters $\boldsymbol{\theta}$ by using the ML method, ϵ and σ_U can be omitted from the numerator on the right-hand side of Eq. (5.18) as these multiplicative factors do not depend on $\boldsymbol{\theta}$. However, they must be taken into account in evaluating the normalization integrals $C_\pm$ in Eq. (5.19) to maintain fixed normalization for $f_\pm$.

As the polarized data samples follow $f_{\pm}$, the $\boldsymbol{\theta}$-dependent part of the integrals in the last line of Eq. (5.19) can be numerically calculated by the sum over the polarization-averaged event set:

$$C'_{\pm}(\boldsymbol{\theta}) = \sum_{i=1}^{N_+} \frac{\left[1 \pm |P_T| \cdot A^i_{UT}(\phi, \phi^*_S; \boldsymbol{\theta})\right]}{\mathbb{L}^+} + \sum_{j=1}^{N_-} \frac{\left[1 \pm |P_T| \cdot A^j_{UT}(\phi, \phi^*_S; \boldsymbol{\theta})\right]}{\mathbb{L}^-}. \quad (5.20)$$

where $N_{\pm}$ denotes the number of detected BH/DVCS events. As ϵ and σ_U are independent on the fit parameters, they can be omitted from the numerator on the right-hand side of Eq. (5.18). Hence the reduced likelihood L' to be maximized is given by

$$L'(\boldsymbol{\theta}) = \prod_{i=1}^{N_+} \frac{\left[1 + |P_T| \cdot A^i_{UT}(\phi, \phi^*_S; \boldsymbol{\theta})\right]}{C'_+(\boldsymbol{\theta})} \cdot \prod_{j=1}^{N_-} \frac{\left[1 - |P_T| \cdot A^j_{UT}(\phi, \phi^*_S; \boldsymbol{\theta})\right]}{C'_-(\boldsymbol{\theta})}. \quad (5.21)$$

As binning is unnecessary in applying the ML method, it does not have the disadvantages listed above that the LS method has. Indeed, as will be shown in the following section, the bias and efficiency properties of the ML method are better than those of the LS method.

5.5.3 Performance of the Two Methods

The performance of the two methods described above in extracting the TTSA amplitudes can be examined in MC simulations. By randomly assigning the target polarization state to MC events according to the azimuthal dependence of the asymmetry, fake TTSAs can be generated in unpolarized MC data sets. Two fake TTSA amplitudes,

$$\begin{aligned} A_{UT}(\phi, \phi_S) &= -0.5 \cdot \sin(\phi - \phi_S) \cos\phi, \\ A_{UT}(\phi, \phi_S) &= -0.5 \cdot \cos(\phi - \phi_S) \sin\phi, \end{aligned}$$

constant over t, x, and Q^2, are generated separately in two gmc_dvcs MC data sets, each of which consists of approximately 90,000 unweighted, elastic BH events that pass through all the cuts. Shown in Fig. 5.13 are the TTSA amplitudes extracted from these two data sets by using the LS method with 8×8 bins in ϕ and $\phi - \phi_S$. The results are given as a function of $-t_c$, x_B, and Q^2 according to the binning used in the previous DVCS analyses [Ell04, Air06a]:

bin in $-t_c$	bin in x_B	bin in Q^2
0.00–0.06 GeV^2	0.03–0.07	1.0–1.5 GeV^2
0.06–0.14 GeV^2	0.07–0.10	1.5–2.3 GeV^2
0.14–0.30 GeV^2	0.10–0.15	2.3–3.5 GeV^2
0.30–0.70 GeV^2	0.15–0.35	3.5–10.0 GeV^2

Significant deficiencies in reconstructing the input TTSA amplitudes can be seen, especially in the first t_c and Q^2 bins. Shown in Fig. 5.14 are similar results obtained with 20×20 bins in ϕ and $\phi - \phi_S$. It can be seen that the situation gets improved by having more bins in ϕ and $\phi - \phi_S$. Such an observation confirms the previous suspicion that in using the LS method, larger bin widths in ϕ and $\phi - \phi_S$ lead to worse resolution and thus larger smearing effects.

Shown in Fig. 5.16 are results obtained by using the ML method. It can be seen that the ML method yields a satisfactory reproduction of the input TTSA amplitudes that is comparable to the results shown in Fig. 5.14. This observation is consistent with the fact that for 20×20 bins the bin widths in ϕ and in $\phi - \phi_S$ become compatible with the detector resolution, $\sigma_\phi \approx 0.2 - 0.4$ rad (see Fig. 5.27). Further increasing the number of bins above 20×20 in using the LS method, the intrinsic detector resolution would restrict any further improvement in the extraction of the input TTSA amplitudes. Altogether, the ML method and the LS method with 20×20 bins are comparable and both of them provide almost the best results.

As is described in section 5.2, the cut $\theta_{\gamma*\gamma} > 5$ mrad is used to assure a reliable extraction of the TTSA amplitudes. This can be seen in Fig. 5.15, where the TTSA amplitudes extracted from MC data with constant input TTSA amplitudes are given as a function of $\theta_{\gamma*\gamma}$. The extracted TTSA amplitudes differ from the input ones in the low $\theta_{\gamma*\gamma}$ region. This observation can be understood by the fact that the resolution of ϕ is worse at smaller $\theta_{\gamma*\gamma}$.

TTSA amplitudes reconstructed with the ML method using input TTSA amplitudes ranging from -0.5 to 0.5 are shown in Fig. 5.17. As can be seen, the reconstructed TTSA amplitudes depend linearly on the input ones, describable in a matrix form as

$$\begin{pmatrix} A_{UT,recon}^{\sin(\phi-\phi_S)\cos\phi} \\ A_{UT,recon}^{\cos(\phi-\phi_S)\sin\phi} \end{pmatrix} = \begin{pmatrix} S_{AA} & S_{AB} \\ S_{BA} & S_{BB} \end{pmatrix} \cdot \begin{pmatrix} A_{UT,gen}^{\sin(\phi-\phi_S)\cos\phi} \\ A_{UT,gen}^{\cos(\phi-\phi_S)\sin\phi} \end{pmatrix}, \tag{5.22}$$

where the matrix elements S_{ij} (which are referred to as smearing coefficients below) can be obtained from the slopes of linear fits of the reconstructed TTSA amplitudes with respect to the input ones. The diagonal elements S_{AA} and S_{BB} describe the dilution in the reconstructed TTSA amplitudes with respect to the generated ones, while the off-diagonal elements S_{AB} and S_{BA} describe the cross-talk between the two TTSA amplitudes in the extraction. The magnitudes of these coefficients reflect some but not all of the smearing and acceptance effects of the detectors in the reconstruction of the TTSA amplitudes, as the kinematic dependence is not simulated by the constant input TTSA amplitudes.

The smearing coefficients from the use of the LS method with 8×8 bins in ϕ and $\phi - \phi_S$, the LS method with 20×20 bins, and the ML method are shown in Figs. 5.18, 5.19, and 5.20, respectively. The results are consistent with the above conclusion that the ML method and the LS method with 20×20 bins in ϕ and $\phi - \phi_S$ reproduce better

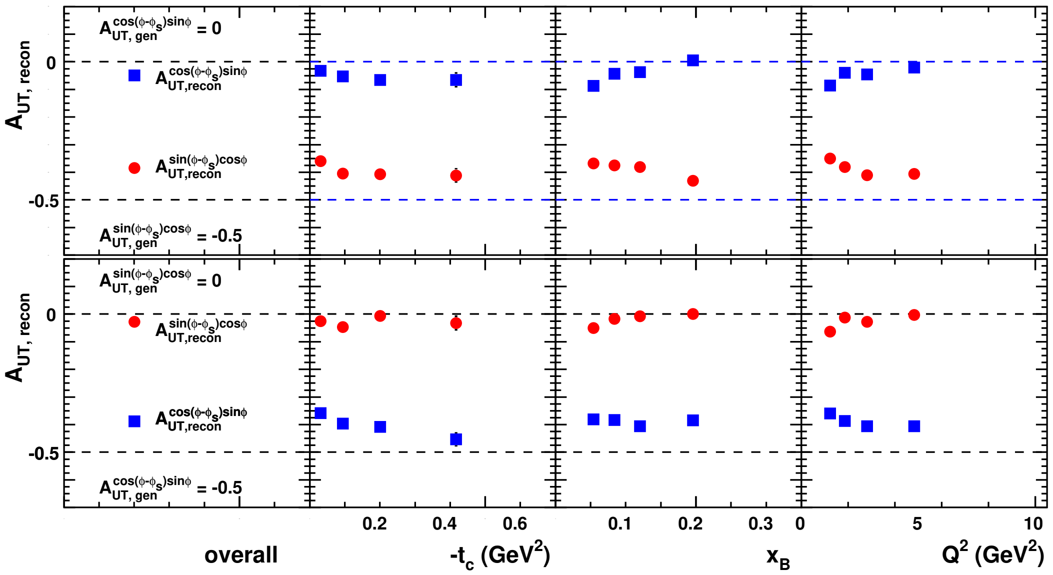

Figure 5.13: The TTSA amplitudes extracted from gmc_dvcs MC data sets by using the method of least squares with 8×8 bins in ϕ and $\phi - \phi_S$. The input TTSA amplitudes $A_{UT}^{\sin(\phi-\phi_S)\cos\phi}$ and $A_{UT}^{\cos(\phi-\phi_S)\sin\phi}$ equal to -0.5 and 0 (0 and -0.5), respectively, for the results shown in the top (bottom) panels.

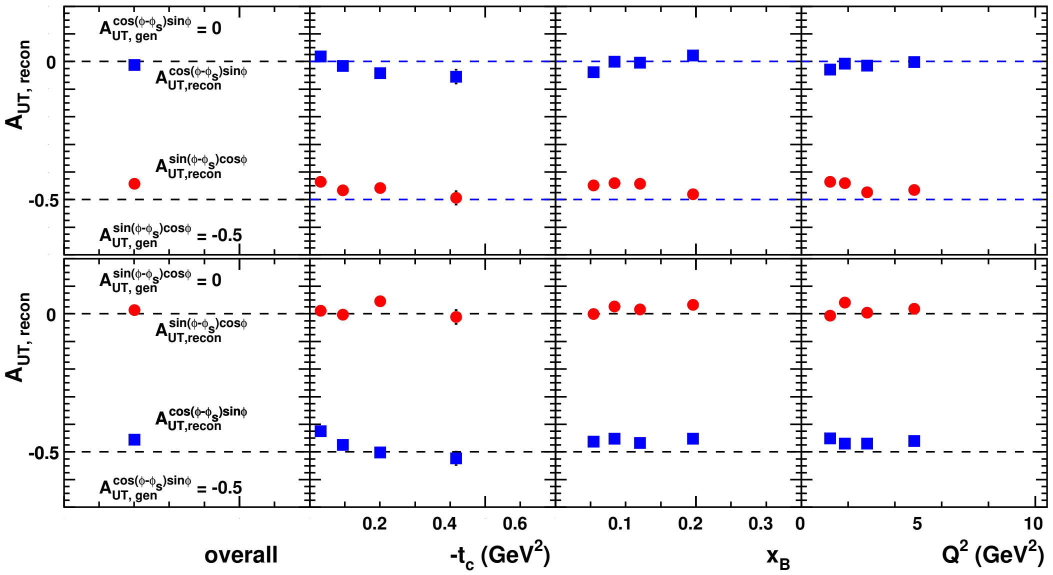

Figure 5.14: Same as Fig. 5.13 but obtained with 20×20 bins in ϕ and $\phi - \phi_S$.

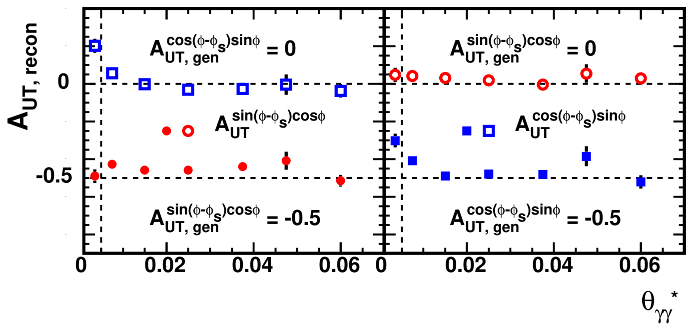

Figure 5.15: Extracted TTSA amplitudes given as a function of $\theta_{\gamma*\gamma}$. The input TTSA amplitudes $A_{UT}^{\sin(\phi-\phi_S)\cos\phi}$ and $A_{UT}^{\cos(\phi-\phi_S)\sin\phi}$ equal to -0.5 and 0 (0 and -0.5), respectively, for the results shown in the left (right) panel. The vertical dashed line indicates the position $\theta_{\gamma*\gamma} = 5$ mrad.

the input TTSA amplitudes than the LS method with 8×8 bins.

With the smearing coefficients known from MC simulations as described above, the generated values of the TTSA amplitudes can be obtained from the reconstructed ones by reversing Eq. (5.22),

$$\begin{pmatrix} A_{UT,gen}^{\sin(\phi-\phi_S)\cos\phi} \\ A_{UT,gen}^{\cos(\phi-\phi_S)\sin\phi} \end{pmatrix} = \begin{pmatrix} S_{AA} & S_{AB} \\ S_{BA} & S_{BB} \end{pmatrix}^{-1} \cdot \begin{pmatrix} A_{UT,recon}^{\sin(\phi-\phi_S)\cos\phi} \\ A_{UT,recon}^{\cos(\phi-\phi_S)\sin\phi} \end{pmatrix}. \tag{5.23}$$

In this way, the deficiencies to reconstruct the input TTSA amplitudes can be corrected. Such corrections certainly hold for both the LS method and the ML method, and the mean of the TTSA amplitudes is equally well estimated by these two methods after the correction. However, difference exists in the uncertainties of the corrected TTSA amplitudes. In performing the correction, the uncertainties of the reconstructed raw TTSA amplitudes need to be transfered into the uncertainties of the corrected results. Since the diagonal elements S_{AA} and S_{BB} are smaller than unity, the uncertainties in the corrected results are enlarged after the correction; the closer the diagonal elements are to unity, the smaller the uncertainties are in the corrected results. Hence the ML method and the LS method with 20×20 bins in ϕ and $\phi - \phi_S$ still give the best results in the sense that they provide the smallest uncertainties.

All the above studies are performed with sufficiently large statistics (∼90 k events) so that they are free of the problems described which arise with sparse data samples, namely, when the numbers of detected events in a certain number of bins are too small, the fitted mean (variance) of the parameters $\boldsymbol{\theta}$ may be biased (underestimated). In the following, we will examine the performance of the two methods on sparse MC data samples.

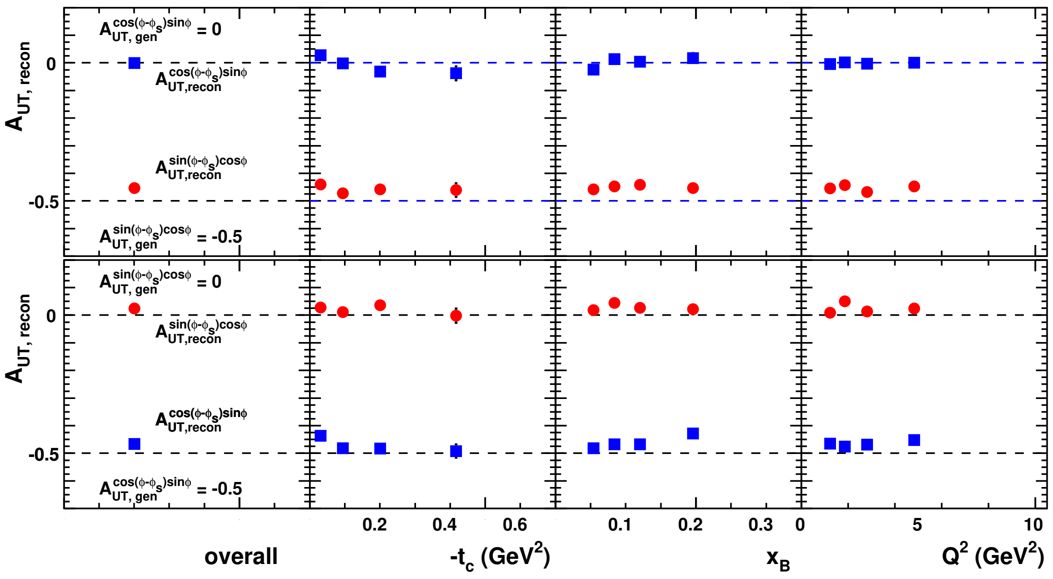

Figure 5.16: Same as Fig. 5.13 but obtained using the method of maximum likelihood.

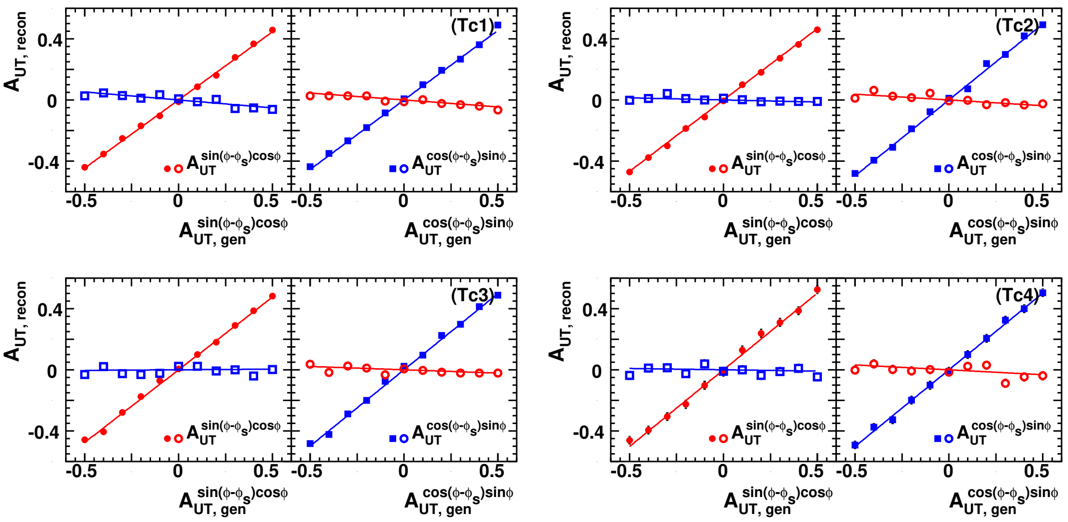

Figure 5.17: The extracted $A_{UT}^{\sin(\phi-\phi_S)\cos\phi}$ and $A_{UT}^{\cos(\phi-\phi_S)\sin\phi}$ amplitudes from gmc_dvcs MC data samples with different input TTSA amplitudes, obtained using the method of maximum likelihood (see Fig. 5.16). The solid lines correspond to a linear fit to the data points. Text at the upper right corner of a panel, e.g., Tc1, denotes for which kinematic bin the results are presented for.

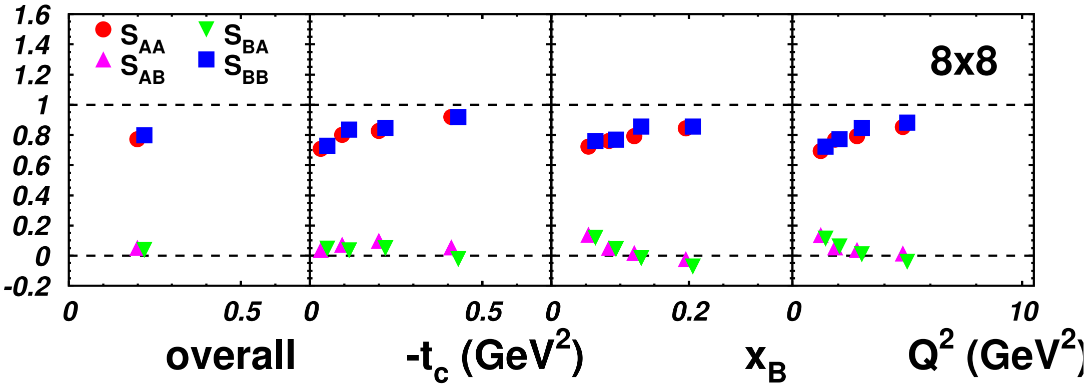

Figure 5.18: Smearing coefficients obtained using the method of least squares with 8×8 bins in ϕ and ϕ_S. See text for explanation.

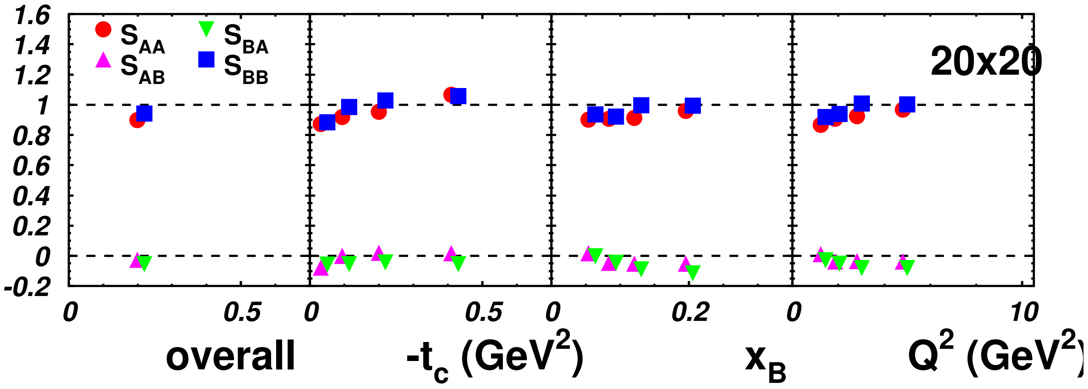

Figure 5.19: Smearing coefficients obtained using the method of least squares with 20×20 bins in ϕ and ϕ_S. See text for explanation.

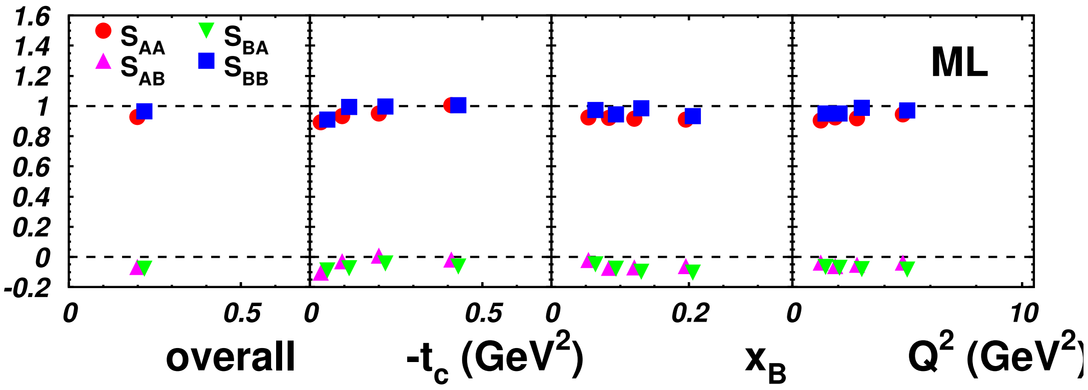

Figure 5.20: Smearing coefficients obtained using the method of maximum likelihood. See text for explanation.

Fake TTSAs are generated in 1000 unpolarized gmc_dvcs MC data sets, each of which contains approximately the same number ($\sim 4,000$) of unweighted, elastic BH events as the actual experimental data. In this case, we are not able to use the LS method with 20×20 bins as then most of the bins would be empty. Distributions of the extracted TTSA amplitudes and the estimated statistical uncertainties are shown in Fig. 5.21 for using the LS method with 8×8 bins in ϕ and ϕ_S. As can be seen, the LS method with 8×8 bins underestimates the actual statistical uncertainties: the spread (RMS) of the extracted TTSA amplitudes are larger than the average estimated statistical errors[1]. The underestimation can be expected to be even larger when using the LS method with 20×20 bins, as there the number of events in each bin will become smaller. Similar plots for using the ML method are shown in Fig. 5.22. It can be seen that the ML method does not underestimate the statistical uncertainties of the extracted TTSA amplitudes.

Profile plots for the distributions of the extracted TTSA amplitudes are shown in Fig. 5.23: the data positions correspond to the mean values of the 1000 sets of extracted TTSA amplitudes, while the error bars correspond to their RMS values. It can be clearly seen that the performance of the ML method on sparse data samples is also better than the one of the LS method with 8×8 bins in ϕ and $\phi - \phi_S$: the mean of the extracted TTSA amplitudes in using the ML method are closer to the input values, and the statistical uncertainties in using the ML method are smaller.

Summarizing all the above, the ML method is seen to be superior for the extraction of the TTSA amplitudes both from large and from sparse data samples. Hence it is used for the analysis of the experimental data in this thesis.

5.5.4 Sensitivity to the Fit Function and Cross Check

In order to check the dependence of the results on the form of the fitted function, the BH/DVCS event sample is fitted to three different functions:

$$\begin{aligned}
\text{2 parameters}: \quad & A_{UT}(\phi, \phi_S) = c_1 \cos\phi \cdot \sin(\phi - \phi_S) + s_1 \sin\phi \cdot \cos(\phi - \phi_S) \\
\text{3 parameters}: \quad & A_{UT}(\phi, \phi_S) = (c_0 + c_1 \cos\phi) \cdot \sin(\phi - \phi_S) + s_1 \sin\phi \cdot \cos(\phi - \phi_S) \\
\text{5 parameters}: \quad & A_{UT}(\phi, \phi_S) = (c_0 + c_1 \cos\phi + c_2 \cos 2\phi) \cdot \sin(\phi - \phi_S) \\
& \qquad\qquad\qquad + (s_1 \sin\phi + s_2 \sin 2\phi) \cdot \cos(\phi - \phi_S)
\end{aligned}$$

Only the leading TTSA amplitudes, $A_{UT}^{\sin(\phi-\phi_S)\cos\phi}$ and $A_{UT}^{\cos(\phi-\phi_S)\sin\phi}$, are included in the fit function with 2 parameters. The fit functions with 3 or 5 parameters also include other TTSA amplitudes which are expected to be kinematically suppressed. They are used to check if the extracted $A_{UT}^{\sin(\phi-\phi_S)\cos\phi}$ and $A_{UT}^{\cos(\phi-\phi_S)\sin\phi}$ amplitudes would be changed by including these additional terms. The extracted $A_{UT}^{\sin(\phi-\phi_S)\cos\phi}$ ($A_{UT}^{\cos(\phi-\phi_S)\sin\phi}$) amplitude, abbreviated in these fit functions by c_1 (s_1), is shown in Fig. 5.24. It can be

[1]See, e.g., Fig. 5.21: the RMS values of the extracted TTSA amplitude distribution is 0.1511, while the mean value of the estimated statistical error distributions is 0.1392.

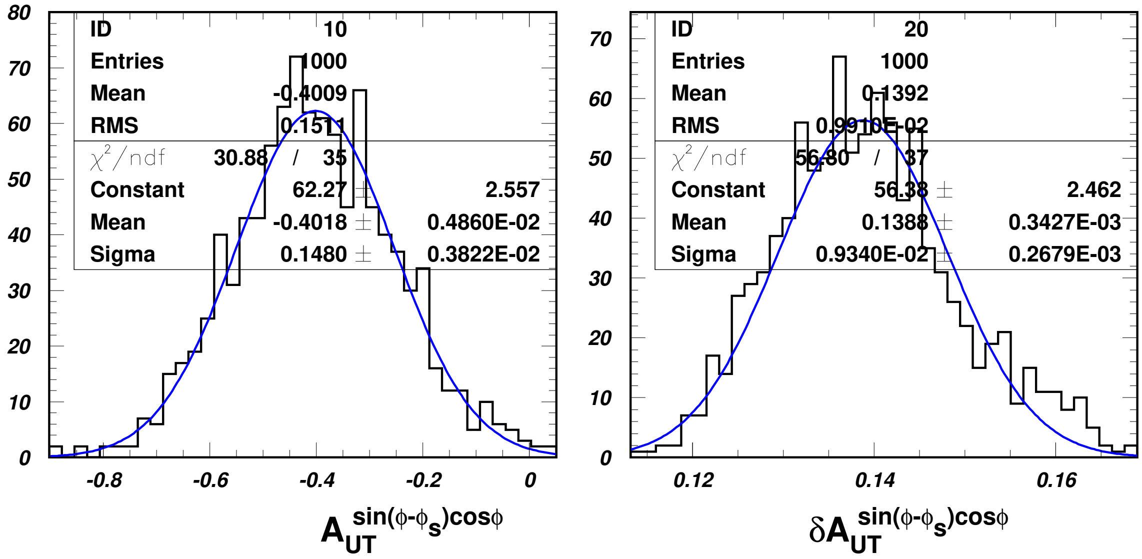

Figure 5.21: Distributions of the extracted TTSA amplitudes (A) and the estimated statistical errors (δA) from 1000 MC data sets with $A_{UT,gen}^{\sin(\phi-\phi_S)\cos\phi} = -0.5$ and $A_{UT,gen}^{\cos(\phi-\phi_S)\sin\phi} = 0$, obtained using the method of least squares with 8×8 bins in ϕ and ϕ_S. The results are shown for the 4th t-bin.

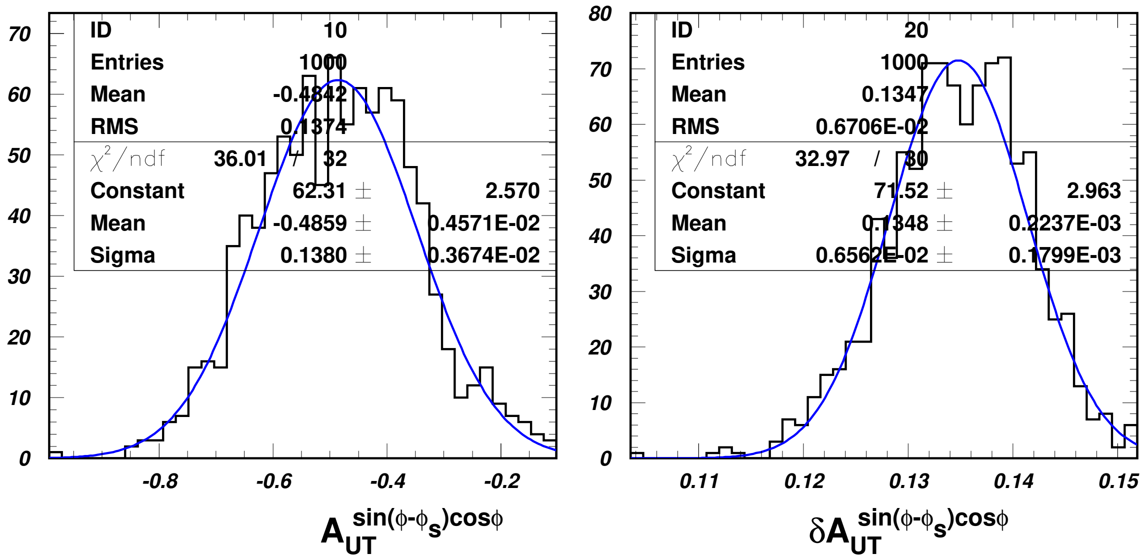

Figure 5.22: Same as Fig. 5.21 but obtained using the method of maximum likelihood.

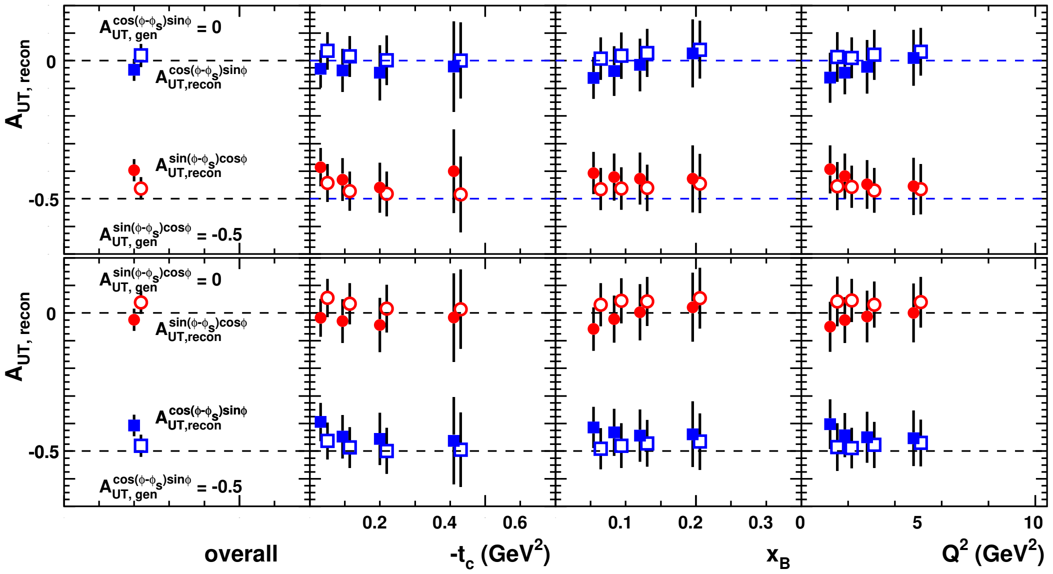

Figure 5.23: Profile plots for the mean and the RMS values of the extracted TTSA amplitudes from 1000 MC data sets (see Fig. 5.21 and Fig. 5.22). Solid points are for the method of least squares with 8×8 bins in ϕ and ϕ_S, and open points are for the method of maximum likelihood. The input TTSA amplitudes $A_{UT}^{\sin(\phi-\phi_S)\cos\phi}$ and $A_{UT}^{\cos(\phi-\phi_S)\sin\phi}$ equal to -0.5 and 0 (0 and -0.5), respectively, for the results shown in the top (bottom) panels.

seen that the fit result is not changed by another choice of the fit function. For the final results the 2-parameter fit function is chosen, while the maximum difference between these and those from the other two fit functions is attributed as a systematic uncertainty.

The TTSA amplitudes extracted from the 2002-2004 data are shown in Fig. 5.25. Additionally, results obtained by an independent second analysis code ("Andy") [Mil06] are shown. An excellent agreement between the two sets of results can be seen. The results ("Zhenyu") shown in Fig. 5.25 will be used in the following studies.

5.6 Corrections for Detector Responses

5.6.1 Influence of the Transverse Target Magnet

A magnetic field perpendicular to the beam direction was used to establish the transverse target polarization (section 4.2). The transverse target magnet has a non-negligible influence on the track reconstruction as it deflects the charged particles. This influence is investigated in MC studies by including a measured field map of the magnet in the simulation of HMC. With the transverse target magnet switched on ("magnet on"), the averages and standard deviations of the differences between the reconstructed and generated kinematic variables are determined and shown in Fig. 5.11 and 5.12. It can be seen that the measured azimuthal angle ϕ_S^{meas} is statistically biased; the bias follows a cosine function with an amplitude of 0.04 rad. The resolutions for θ_e, Q^2, ϕ, and ϕ_S degrade. Such degradations in the measurement may lead to additional systematic uncertainties in the extracted TTSA amplitudes. Hence the TMC program [Aug04] was designed to correct for the influence of the transverse target magnet.

Two algorithms are implemented in TMC: one based on transfer matrices (TMC1) and the other based on reference tracks (TMC2). The first one uses MIT-RAYTRACE [Kow86] to track in MC simulations particles through the measured field map of the transverse target magnet. A set of Taylor series expansion coefficients, which describe the transfer of particles from the initial to the final coordinates, is calculated. For the actual experimental data, the intercept positions in the DVC and FCs are known. By reversing the dependence of these positions on the initial particle coordinates, the vertices and scattering angles of the particles before the transverse target magnet can be obtained. The second method implemented in TMC uses the zgoubi program [Méo05] to track particles through the measured field map of the transverse target magnet. A set of relations between the initial and final particle coordinates is recorded. The vertices and scattering angles of the particles before the transverse target magnet are obtained by searching in the recorded information for the trajectory that gives the minimum distance to the measured intercept positions in the DVCS and FCs.

The performance of the two correction methods implemented in TMC is checked in an MC simulation. The TMC program is used in the same way as for the experimental

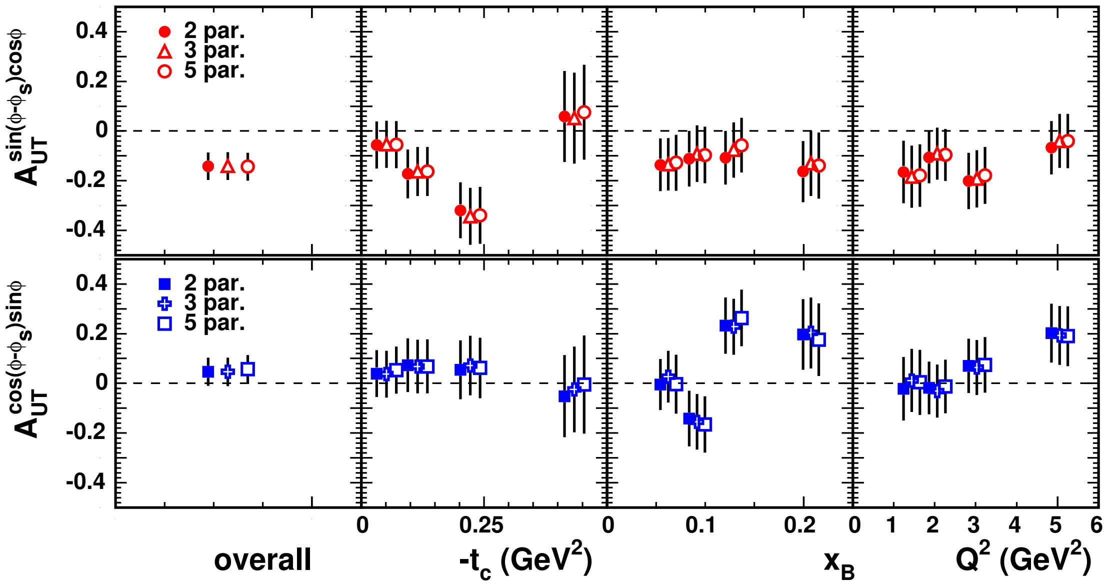

Figure 5.24: TTSA amplitudes extracted using different fit functions.

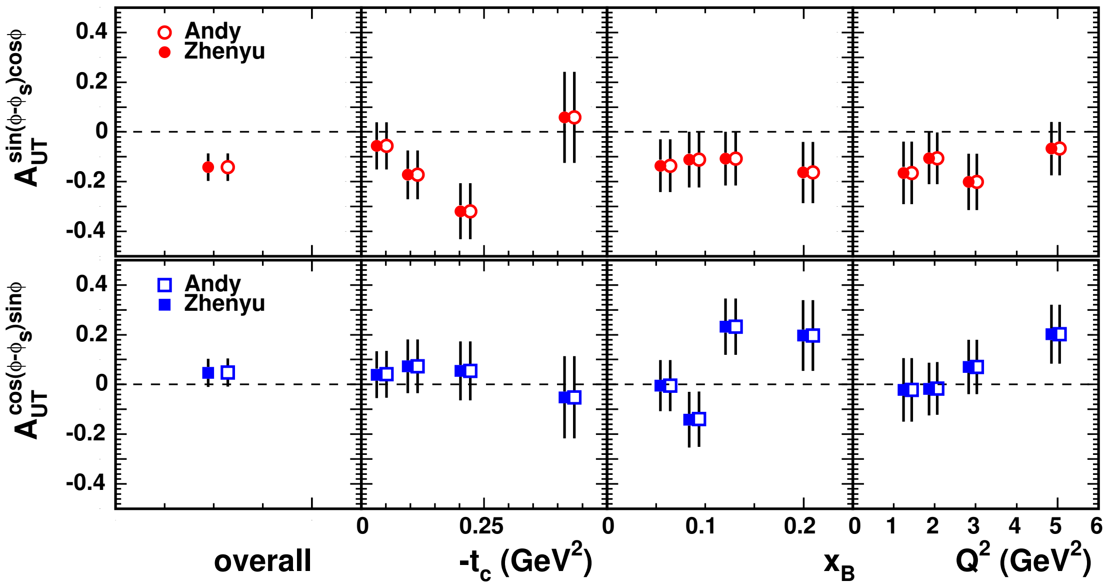

Figure 5.25: TTSA amplitudes extracted from the HERMES 2002-2004 data using the ML method. The results obtained by two independent analysis codes are shown.

data. The averages and standard deviations of the differences between the reconstructed kinematic variables after correction and the generated ones are shown in Figs. 5.26 and 5.27. As can be seen, the bias in the reconstructed ϕ_S values has been greatly reduced by both correction methods. The resolutions for θ_e, Q^2, ϕ, and ϕ_S are also improved after the correction. Although some biases are introduced into z_{vtx} and θ_e by one or the other method, the biases are so small that they do not affect the measurement of x_B, Q^2, or t_c. It can also be seen that the resolution for z_{vtx} is worse by using the TMC2 method. However, due to the small contribution outside of and close to the ± 18 cm edges, such a degradation in the resolution for z_{vtx} should have very small, if any, effect on the event selection. Also observed between the TMC1 and TMC2 methods are differences in bias and resolution for ϕ_S. However, as the measurement performance for ϕ dominates over the one for ϕ_S, such a difference will not play any role in extracting the TTSA amplitudes $A_{UT}^{\sin(\phi-\phi_S)\cos\phi}$ and $A_{UT}^{\cos(\phi-\phi_S)\sin\phi}$, in which both ϕ and ϕ_S enter.

In conclusion, by applying either of the two correction methods implemented in TMC, there should be no more influence of the transverse target magnet on the present analysis. Hence no systematic uncertainty will be assigned for it.

5.6.2 Misalignment of the Spectrometer and Beam

In reality, detector positions differ from their designed places (Fig. 5.28.b). These differences have to be taken into account in reconstruction. However, due to difficulties in the determination of the actual detector positions, the information used sometimes deviates from the truth. Such a deviation can affect the reconstructed kinematic quantities and lower the reconstruction efficiency. At HERMES there exists also an effect introduced by the beam when it shifts or is tilted away from the z-axis (Fig. 5.28.c). Due to the fact that the beam is assumed to coincide with the z-axis in the vertex reconstruction, reconstructed positions of the primary interaction vertices can be incorrect. Moreover, when the beam has an angle with respect to the z-axis, kinematic quantities calculated with the beam direction assumed to be parallel to the z-axis will deviate from the truth. The effects described above are known as “misalignment effects”. In this section we present a study of the misalignment effects of the spectrometer and the beam on the extracted TTSA amplitudes.

There are two kinds of detector misalignments: internal misalignment and external one. Internal means relative shifts and rotations of detectors with respect to each other; external means that the detectors are shifted and rotated as a whole with respect to a reference coordinate system. The internal misalignment of the HERMES spectrometer is determined in special “alignment” runs, which are taken several times per year with the spectrometer magnet switched off. In these runs, particle trajectories are straight and thus provide necessary information to determine the relative positions of the detectors with respect to each other. With enough statistics, the precision in doing this can, in principle, reach a level better than the intrinsic resolution of the individual detectors.

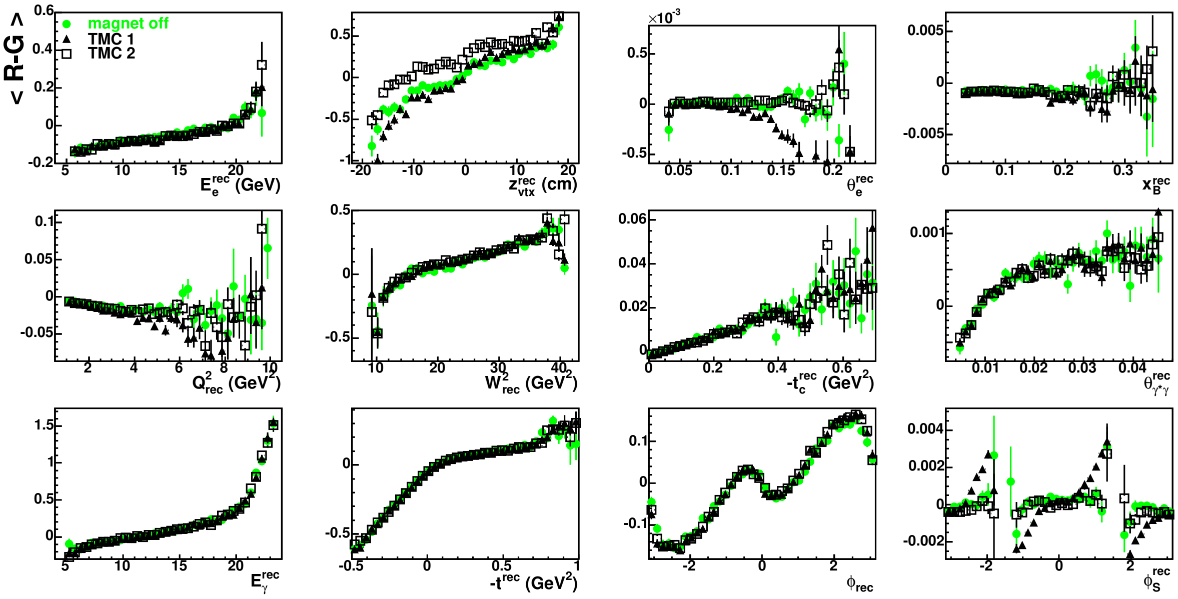

Figure 5.26: Same as Fig. 5.11 but either the TMC1 or the TMC2 correction method was used when the transverse target magnet was switched on.

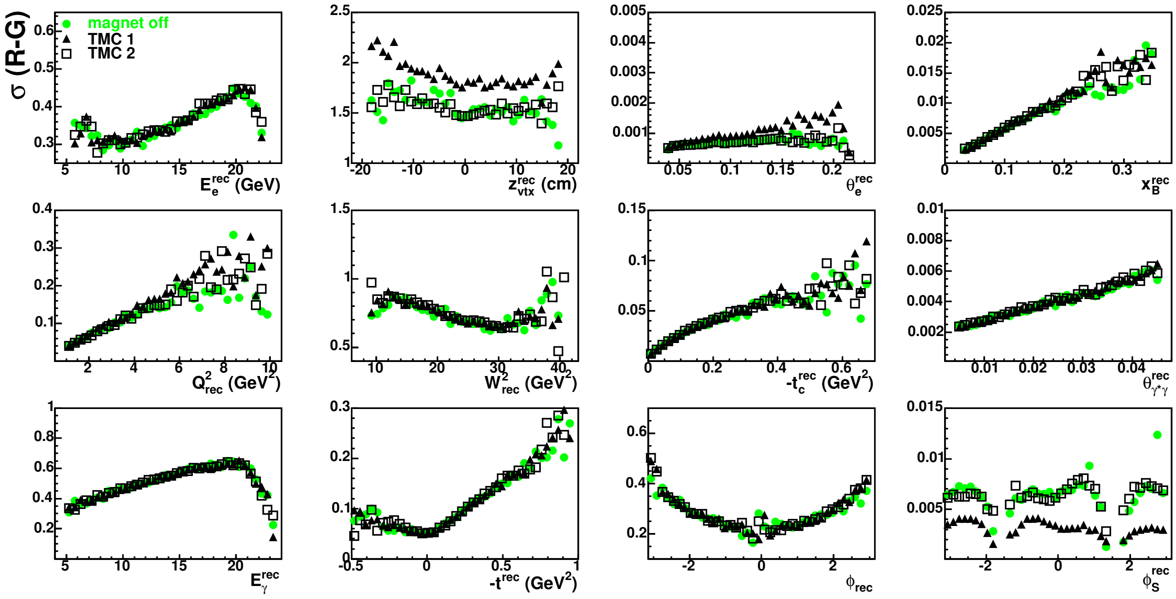

Figure 5.27: Same as Fig. 5.12 but either the TMC1 or the TMC2 correction method was used when the transverse target magnet was switched on.

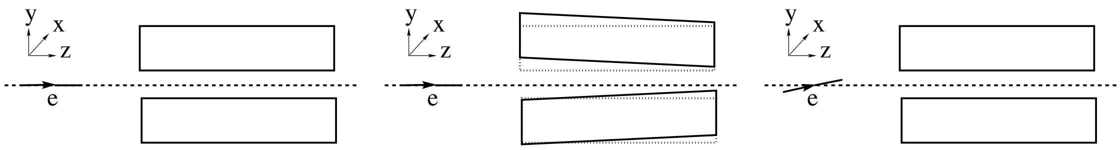

Figure 5.28: Sketch of misalignment of the spectrometer and the beam: (a) the spectrometer and the beam in their ideal places; (b) misalignment of the spectrometer; (c) misalignment of the beam.

2002-2004	x-slope (mrad)	y-slope (mrad)	x-offset (cm)	y-offset (cm)
Top	-0.18	-0.62	0.30	-0.08
Bottom	-0.42	0.49	0.29	0.11

Table 5.2: Misalignment of the spectrometer in the years 2002-2004 [Brü03].

2002-2004	x-slope (mrad)	y-slope (mrad)	x-offset (cm)	y-offset (cm)
Mean	-0.041	-0.13	0.005	0.046
RMS	0.095	0.059	0.016	0.045

Table 5.3: Beam slopes and offsets in the years 2002-2004.

Hence it is reasonable to assume that the internal misalignment does not have any influence on the present analysis.

The external misalignment of the spectrometer has been determined in Ref. [Brü03]. The results are listed in Tab. 5.2. Comparing the spectrometer offsets to the minimum distance of the impact position of the photon to the beam axis, which is 33 cm in the calorimeter, it is obvious that the influence of the spectrometer offsets may be discarded.

The beam slopes and offsets in the years 2002-2004 have been measured by several sets of beam position monitors located closely before and after the HERMES spectrometer. The results are listed in Tab. 5.3 and shown in Fig. 5.29. Following the same argument as above, the influence of the beam offsets may be discarded. Comparing the beam slopes to the resolution for the lepton scattering angle θ_e, which is approximately 0.5 mrad (see Fig. 5.27, the 3rd panel from the left in the first row), it can be seen that only the mean value of the y-slope is non-negligible.

The misalignment effect on the extracted TTSA amplitudes has been studied in MC simulations. The values for spectrometer misalignment and beam misalignment given in Tabs. 5.2 and 5.3 are input to MC simulations. The two leading TTSA amplitudes are then extracted from the "misaligned" MC simulations. The results are shown in Fig. 5.30. As can be seen, the misalignment effect on the extracted TTSA amplitudes

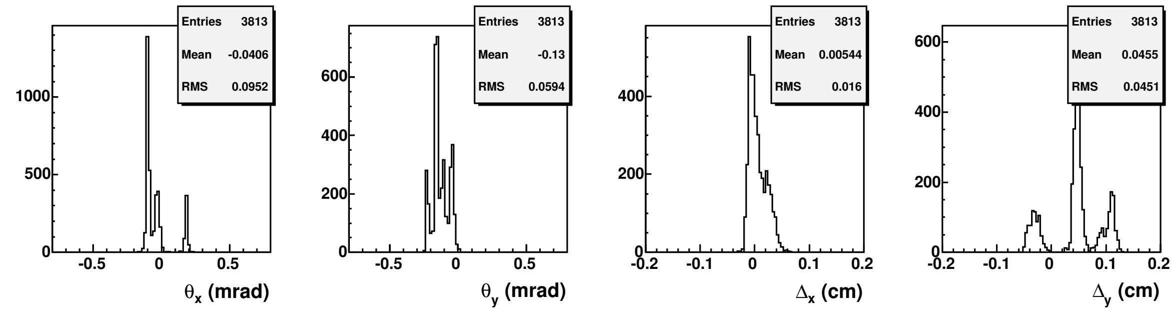

Figure 5.29: Beam slopes and offsets in the years 2002-2004.

is rather small.

Given the known rotations of the spectrometer and beam, it is possible to correct for them in the present analysis. It is done by subtracting the rotation angles of the spectrometer from the reconstructed lepton scattering angle, and by taking the actual beam direction when calculating the kinematics. The results after correction are shown in Fig. 5.31. As can be seen, the misalignment effect on the extracted TTSA amplitudes is rather small. As will be explained in section 6.1.2, the extracted TTSA amplitudes are not corrected for the misalignment of spectrometer and beam but rather a systematic uncertainty is assigned.

5.6.3 Miscalibration of the Calorimeter

As shown in section 5.3.2, the missing mass squared M_{X}^2 is very sensitive to the photon energy and thus to the calorimeter calibration. The influence of a possible miscalibrated calorimeter on the present analysis is restricted because, other than M_{X}^2, the kinematic variables do not depend on the photon energy[2]. Hence, a miscalibrated calorimeter can only affect the present analysis in the event selection due to, e.g., the cut on M_{X}^2. Consequently, its systematic influence on the extracted TTSA amplitudes can only be a change in the background contributions, although because of limited statistics, the extracted TTSA amplitudes can also be changed because of some events may become lost or selected in addition. In this section, we present a study on the influence of a possible miscalibrated calorimeter on the extracted TTSA amplitudes.

The calorimeter is calibrated at HERMES by looking at the ratio of the energy E measured by the calorimeter to the reconstructed momentum P of a sample of DIS leptons. It has been done once for every individual period in which the running condition of the calorimeter was stable. The E/P ratios are extracted independently in this

[2]Note that we use t_c defined in Eq. (3.11) instead of t in Eq. (3.10) to calculate the invariant momentum transfer t to the target proton.

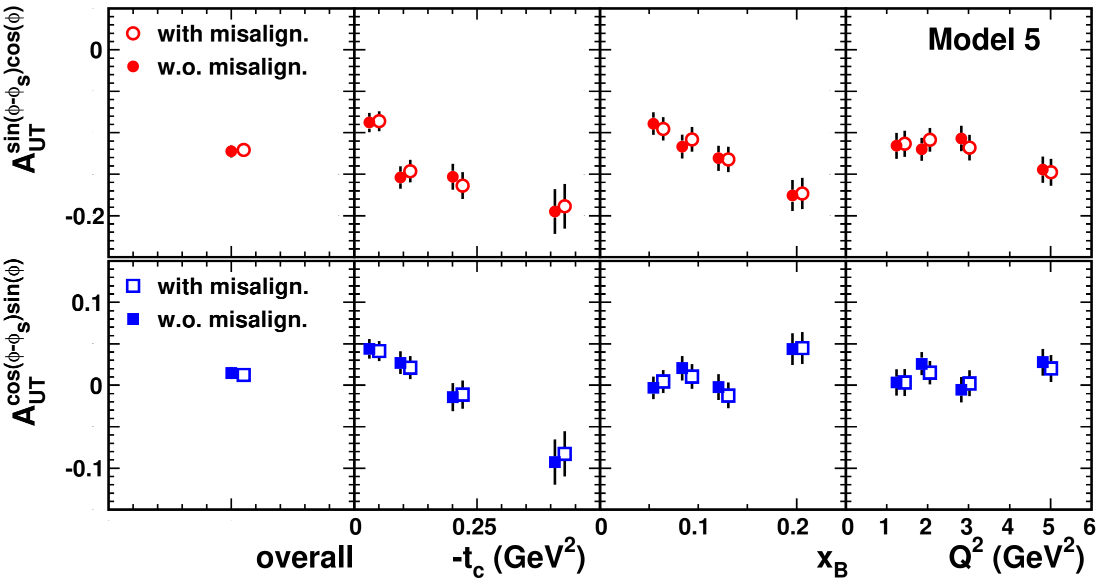

Figure 5.30: The TTSA amplitudes extracted from polarized gmc_dvcs MC data samples, based on GPD model 5 in section 5.3.1. Solid points: the spectrometer and beam are not misaligned; open points: the spectrometer and beam are misaligned.

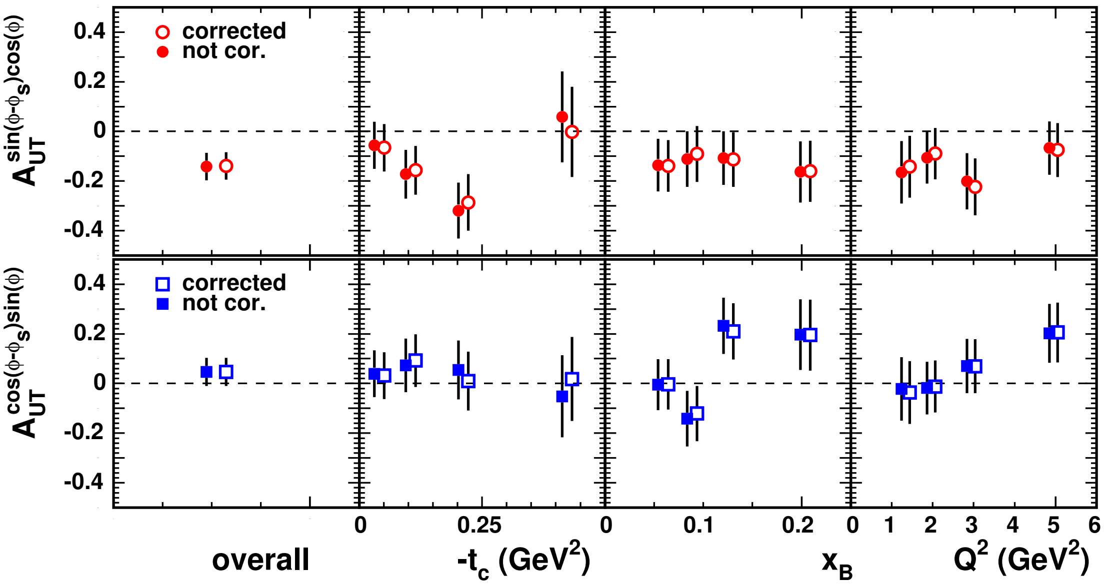

Figure 5.31: The TTSA amplitudes extracted from the 2002-2004 data. Solid points: misalignment of spectrometer and beam is not corrected for; open points: misalignment of the spectrometer and beam is corrected for.

analysis, based on the events satisfying the cuts in section 5.2.1. The mean value of the E/P ratio is found to be the same in the years 2002-2004, as can be seen in Fig. 5.32. The E/P distributions are then fitted to a function of the form

$$f(x) = A \cdot \left\{ P_0 + P_1 \cdot x + \exp\left[-\frac{(x-M)^2}{2S^2} \right] \right\}. \tag{5.24}$$

From Fig. 5.32, the fit results for the parameters describing the shape of the E/P distribution are compatible among the years within statistical uncertainties. Hence we conclude that there is no relative miscalibration of the calorimeter in the data.

Measurements from the calorimeter of the deposited energy of leptons depend upon the energy (momentum) of the particle, and upon the pre-shower signal. The reconstructed momentum of leptons can be off by 4% in the lower and higher momentum regions[3]. Hence by using the E/P ratios of DIS leptons, it will be rather difficult to make an absolute calibration for the calorimeter with a precision better than 1%. There exists, however, an indication of a possible 1% miscalibration of the calorimeter in the real data, as dicussed in section 5.3.2. There it has been observed that the exclusive peak in the missing-mass spectrum of the data agrees well with the MC simulation with the photon energy reduced by 1%. In order to study the influence of the calorimeter miscalibration of such a size on the extracted TTSA amplitudes, an MC study has been performed. TTSA amplitudes are extracted from an MC simulation in which the photon energy is reduced by 1%. The results and the ones without such an artificial miscalibration are shown in Fig. 5.33. As can be seen, the extracted TTSA amplitudes are hardly affected by the calorimeter calibration. Such an observation is consistent with the expectation described in the beginning of this section.

Assuming the calorimeter calibration is 1% too low in the 2002-2004 data, it is possible to correct for it. This is done by increasing the photon energy measured by the calorimeter by 1%. The TTSA amplitudes are then extracted from the corrected data and shown in Fig. 5.34. As can be seen, the calorimeter miscalibration has a very small influence on the extracted TTSA amplitudes. As will be explained in section 6.1.2, such an influence is treated as a systematic uncertainty.

5.6.4 Detection Efficiency

A non-uniform detection efficiency over the acceptance will change the kinematic distribution of the detected events. At HERMES, this can introduce a problem into the extraction of a beam-spin (beam-charge) asymmetry when the detection efficiency is different for different beam polarization (charge) states; false asymmetries may be obtained without accounting for such differences. On the other hand, measurements of target-spin asymmetries are much less sensitive to the problem described above. During

[3]See the top-left panel in Fig. 5.26, where E_e denotes the reconstructed lepton momentum.

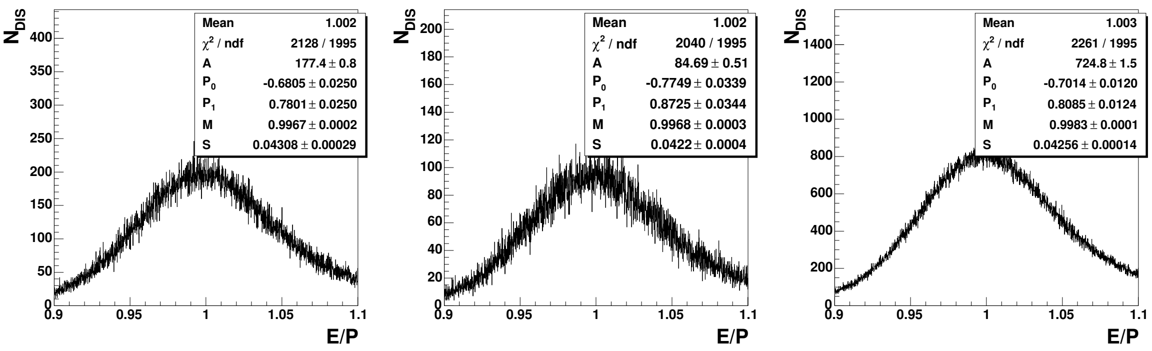

Figure 5.32: Ratio of the energy E measured by the calorimeter to the reconstructed momentum P of DIS leptons in 2002 (left), 2003 (center), and 2004 (right). Also shown are the fitted results (solid line) using the function (5.24).

the data taking, the target polarization direction flipped once per every 90 s (see section 4.2). In such a short period, the detection efficiency can be expected to have been stable and thus be cancelled out in measurements of asymmetries being fully differential in kinematics. Nevertheless, a non-uniform detection efficiency can play a role in measurements which integrate over certain phase spaces, whereas the measured asymmetry is an average over the integrated phase space and is weighted by the kinematic distribution of the detected events.

In this section we investigate the possible influence of the detection efficiency on the present analysis.

The detection efficiencies involved in the present analysis include the efficiency of the trigger system, the efficiency of the tracking system in reconstructing the scattered positron, and the efficiency of the calorimeter to detect the emitted real photon. The tracking efficiencies of the individual tracking chambers and the global tracking efficiencies of the front and back partial tracking subsystems, separately for the top half and the bottom half of the spectrometer, have been estimated by the ACE program [Kol98]. In the years 2002-2004, the average global tracking efficiencies are found to be very close to unity, $\epsilon > 99.8\%$. Hence the tracking efficiency should not influence the present analysis. Without other sources of information being available, the efficiency of the calorimeter in detecting photons, which start showering in the pre-shower detector, may be expected to be similar to the trigger efficiency of the calorimeter. Therefore in the following we determine the possible influence of the non-uniform detection efficiency on the extracted TTSA amplitudes by studying the influence of the trigger efficiency.

The trigger used in the present analysis is trigger 21 (see section 4.3.5), which requires signals coincident in time with HERA positron bunches from the H0, H1, H2 hodoscopes, and the calorimeter. The trigger efficiencies of the individual detectors can be estimated

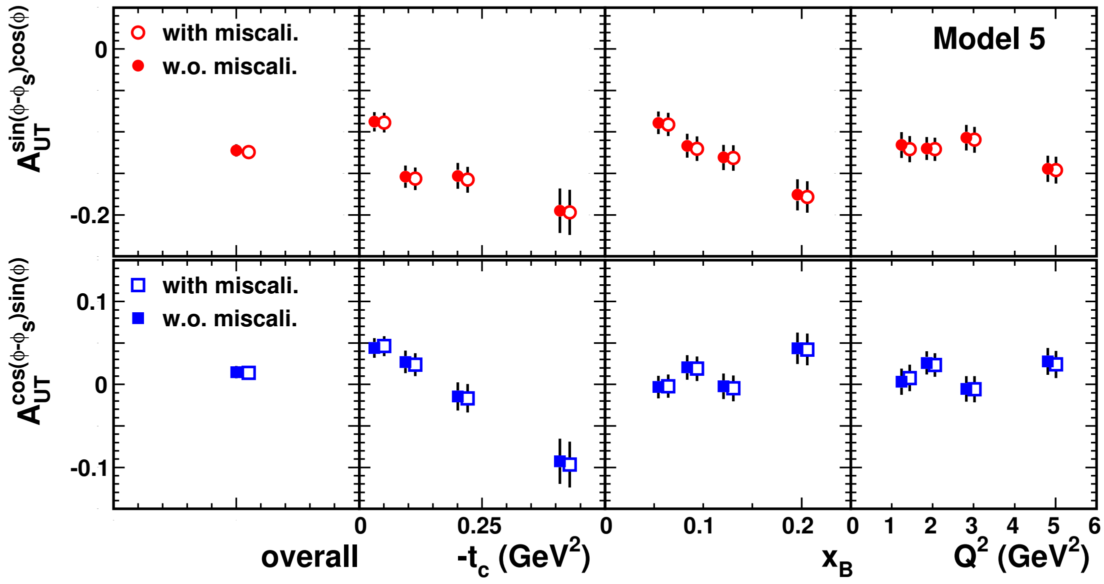

Figure 5.33: The TTSA amplitudes extracted from polarized gmc_dvcs MC data samples, based on GPD model 5 in section 5.3.1. Solid points: photon energy not scaled; open points: photon energy scaled by 0.99.

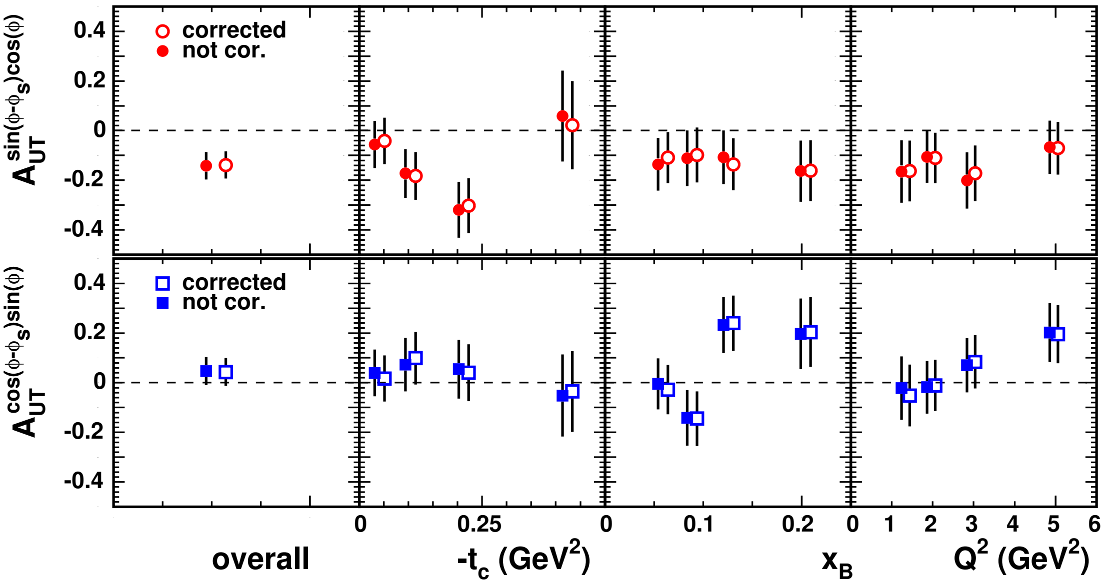

Figure 5.34: The TTSA amplitudes extracted from the 2002-2004 data. Solid points: photon energy not scaled; open points: photon energy scaled by 0.99.

by counting the number of events wherein trigger 21 was fired, N_{tr21}, and the number of events wherein all the other detectors but not the detector under consideration were fired. For example, the trigger efficiency of the H0 hodoscope $\epsilon_{\rm H0}$ can be estimated as,

$$\epsilon_{\rm H0} = \frac{N_{tr21}}{N_{H1*H2*calo}}, \tag{5.25}$$

where $N_{H1*H2*calo}$ denotes the number of events in which the H1, H2 hodoscopes, and the calorimeter but not the H0 hodoscope gave a signal above the trigger threshold. The total efficiency of trigger 21 $\epsilon_{\rm tr21}$ is given by the product,

$$\epsilon_{\rm tr21} = \epsilon_{\rm H0} \cdot \epsilon_{\rm H1} \cdot \epsilon_{\rm H2} \cdot \epsilon_{\rm calo}. \tag{5.26}$$

The trigger efficiencies in the years 2002-2004 have been estimated by the HERMES trigger group [Gap06]. They are estimated as a function of the momentum of the scattered lepton p_e, and of the scattering angles $\theta_x = \theta \cos\phi$ and $\theta_y = \theta \sin\phi$. The trigger efficiencies are found to be very close to unity. The variation of the trigger efficiencies with p_e is found to be below 0.1% in the kinematic region of the present analysis. On the other hand, the dependence of the trigger efficiency of the H0 hodoscope on θ_x and on θ_y is stronger by more than a factor of 2 than the ones of the H1, H2 hodoscopes, and the calorimeter, which have a variation wtih θ_x and θ_y below 0.3%. Therefore we only consider the angular dependence of the trigger efficiency of the H0 hodoscope in the following study.

The trigger efficiency of the H0 hodoscope $\epsilon_{\rm h0}$ has been calculated in a grid of 2 cm by 2 cm cells over the H0 surface. The results are shown in Fig. 5.35. It can be seen that in the years 2002 and 2004 the H0 efficiency was close to unity in most of the area, but it went down to 0.9 in some areas in the year 2003. The extracted TTSA amplitudes have been corrected for the H0 efficiency shown in Fig. 5.35 by assigning each event a weight of $\epsilon_{\rm h0}^{-1}$. The influence of the H0 efficiency on the extracted TTSA amplitudes is found to be very small compared to the statistical uncertainties of the extracted TTSA amplitudes, as can be seen in Fig. 5.36.

Based on the above observation, we conclude that the influence of the non-uniform trigger efficiency on the extracted TTSA amplitudes is negligible. Therefore the detection efficiency is not corrected for the extracted TTSA amplitudes, and no systematic uncertainties are assigned in the present analysis.

5.6.5 Smearing and Acceptance Effects

Due to the limited resolution of a detector, the measured value of an obeservable is usually different from the truth. Such an effect in the present study on the extracted TTSA amplitudes, called smearing effect, may be described by Eq. (5.22) and can in principle be corrected by inverting this equation. However, due to the limitation in statistics, we are unable to make a measurement that is fully differential in kinematics and have hence to integrate over a certain phase space region. The smearing effect depends not only on the kinematic dependence of the unpolarized cross section but also on the one of the TTSA amplitudes because of the integration. Thus it may not be fully reflected by the smearing coefficients shown in Fig. 5.20, which are obtained with constant input TTSA amplitudes. On the other hand, the acceptance of the HERMES spectrometer plays a role in our measurement as well. This is due to the fact that the extracted TTSA amplitudes are obtained from a certain phase space region defined by the acceptance and the cuts applied in the analysis. It is essential to know the difference between the TTSA amplitudes measured at HERMES and the ones that would be measured in another experiment with different acceptance, or with 4π solid angle acceptance in the best case.

In this section, we will study the above mentioned effects, the smearing and acceptance effects, on the extracted TTSA amplitudes.

We first look at the acceptance effect. Shown in Fig. 5.37 are the yields in 4π acceptance and in the HERMES acceptance, of elastic BH+DVCS events from an unpolarized gmc_dvcs MC data sample. Only the gmc_dvcs generator is used in the simulation, the HMC and HRC programs are not used. As can be seen, the photon energy E_γ distribution of the yield in 4π acceptance is significantly different from the one in the HERMES acceptance. The former is non-vanishing at a lower photon energy region than the latter, and increases continuously with the photon energy while the latter peaks at around 12 GeV; in other words, the events with very low or very high photon energy don't fall into the HERMES acceptance. The fact that the events with very low photon energy are not in the HERMES acceptance is mainly due to the cut $\theta_{\gamma^*\gamma} < 45$ mrad, while the fact that the events of very high photon energy are not in the HERMES acceptance is mainly due to the geometrical acceptance of the calorimeter, which vanishes in the region close to the beam direction where the events of high photon energy concentrate.

After integration over the other kinematic variables the BH and DVCS amplitudes depend differently on the photon energy E_γ. Such a difference can be seen in Fig. 5.38,

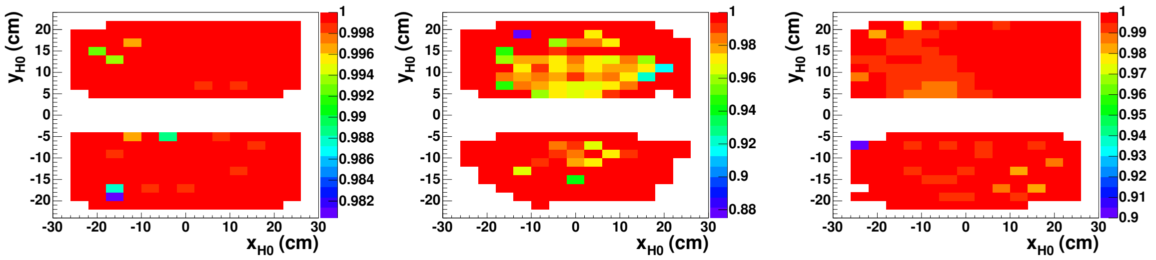

Figure 5.35: H0 efficiency (in color) in 2002 (left), 2003 (center) and 2004 (right).

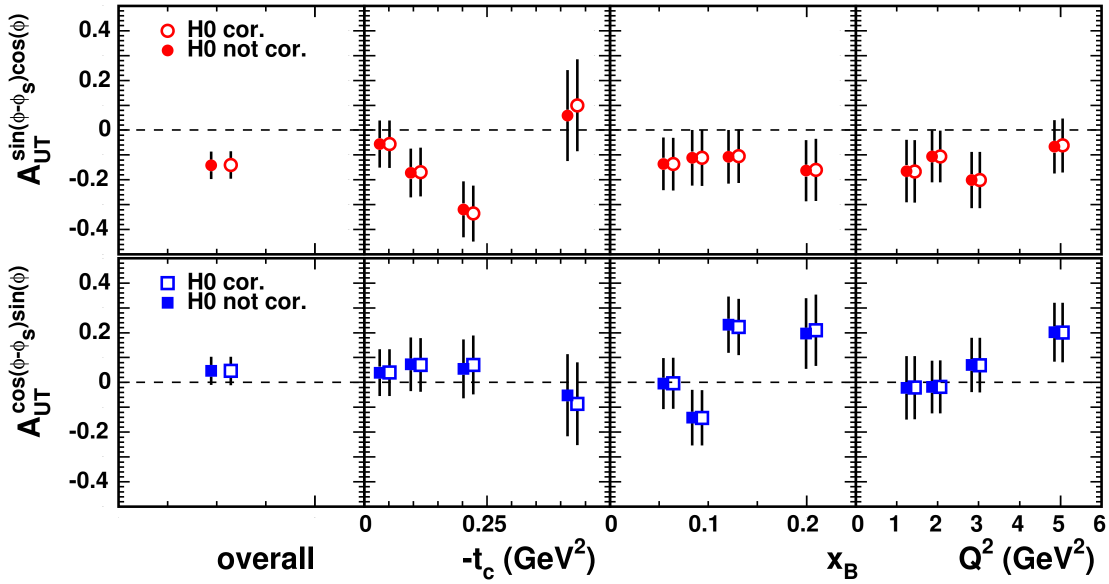

Figure 5.36: Extracted TTSA amplitudes with/without correction for H0 inefficiency.

which shows that the pure BH cross section increases with the photon energy, the pure DVCS cross section decreases with the photon energy, and that the BH-DVCS interference contribution remains approximately flat. Hence, compared to the case in 4π acceptance, the contribution in the HERMES acceptance from the pure DVCS cross section and the BH-DVCS interference is enhanced, while the contribution from the pure BH cross section is reduced (see Fig. 5.39). Moreover, the averages of kinematic variables in the HERMES acceptance[4] are different to the ones in 4π acceptance. Therefore it can be expected that the TTSA amplitudes shown in Fig. 5.25, which are given as a function of one kinematic variable (t, x_B, or Q^2) while integrating over the other two, will be significantly different compared to the ones from a measurement in 4π acceptance, e.g.,

$$\langle A_{UT}(t)\rangle_{HERMES} \neq \langle A_{UT}(t)\rangle_{4\pi}. \tag{5.27}$$

Here

$$\langle A_{UT}(t)\rangle \equiv \frac{\int_{t_{min}}^{t_{max}} dt \int_{0.03}^{0.35} dx_B \int_1^{10} dQ^2 \sigma_U(t, x_B, Q^2) \cdot A_{UT}(t, x_B, Q^2)}{\int_{t_{min}}^{t_{max}} dt \int_{0.03}^{0.35} dx_B \int_1^{10} \sigma_U(t, x_B, Q^2)} \tag{5.28}$$

is one of the TTSA amplitudes given as a function of t while integrating over x_B and Q^2 in the HERMES acceptance or in 4π acceptance. Based on the above arguments, we

[4]The overall average HERMES kinematics are the ones integrated over the full HERMES acceptance. The average HERMES kinematics in a given t, x_B, or Q^2 bin are the ones integrated over the kinematic limits of the bin within the HERMES acceptance.

conclude that the HERMES acceptance must be taken into account when comparing the TTSA amplitudes measured at HERMES with theoretical predictions which integrate over kinematic regions or the TTSA amplitudes measured at other experiments.

The smearing effect is investigated in an MC simulation, in which the gmc_dvcs generator, the HMC and HRC programs are used. The TTSA amplitudes extracted from the reconstructed kinematics are compared to the ones extracted using the generated kinematics. Hence in the former case, both the smearing effect and the acceptance effect are simulated, while in the latter case only the acceptance effect is simulated. Results for only one GPD model are shown in Fig. 5.40 but the conclusion is the same for the other GPD models. As can be seen, the smearing effect makes the size of the amplitude $A_{UT}^{\sin(\phi-\phi_S)\cos\phi}$ smaller, and has a small influence on the amplitude $A_{UT}^{\cos(\phi-\phi_S)\sin\phi}$. Such an observation is consistent with the expectation which one may make, taking into account the actual values of the TTSA amplitudes shown in Fig. 5.40 and the smearing coefficients shown in Fig. 5.20.

By solving Eq. (5.22) with the smearing coefficients shown in Fig. 5.20, it has been tried to correct the results shown in Fig. 5.40 for the smearing effect. The results after correction are compared with the ones free of the smearing effect in Fig. 5.41. As can be seen, the difference between the two sets of results are smaller but remain. Due to the limited statistics and the small size of the smearing effect, it is difficult to make a solid conclusion here if the smearing effect is completely corrected or not. For the final results, no correction for the smearing effect is performed. The differences between the two sets of results shown in Fig. 5.40 will be used as an estimation of the systematic uncertainty of the extracted TTSA amplitudes due to the smearing effect.

Shown in Fig. 5.41 are also theoretical predictions on the TTSA amplitudes at the average HERMES kinematics for each bin[5]. As can be seen, the TTSA amplitudes measured by the HERMES spectrometer are close to these theoretical predictions. In order to make it less difficult to compare the HERMES results to theoretical predictions or results from other experiments, one may interpret the HERMES results as the ones measured at the average HERMES kinematics. Such an interpretation is used in setting a constraint on the total angular momentum of quarks in the nucleon (section 6.2).

5.7 Correction for Background Contributions

The extracted TTSA amplitudes shown in Fig. 5.25 receive contributions not only from the asymmetry of the elastic BH/DVCS processes, but also from the ones of background processes, namely, the associated BH/DVCS processes, semi-inclusive DIS processes, and exclusive π^0 production. In principle, if all background contributions and asymmetries

[5]The averages of the kinematics measured experimentally are used in theoretical calculations.

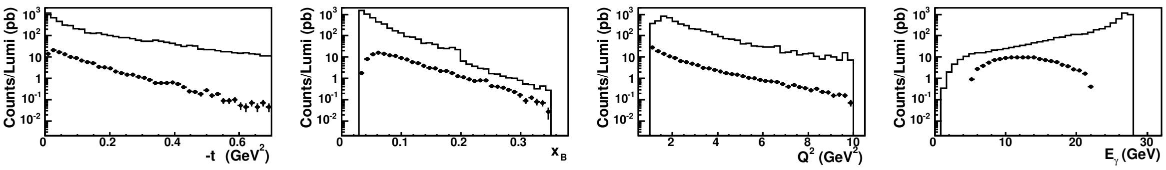

Figure 5.37: The yield of elastic BH+DVCS events in the range of $-t > 0.7$ GeV^2, $0.03 < x_B < 0.35$, $1 < Q^2 < 10$ GeV^2 from an unpolarized gmc_dvcs MC data sample, based on GPD model 5 in section 5.3.1. Solid curve: yield in 4π, points: yield in the HERMES acceptance.

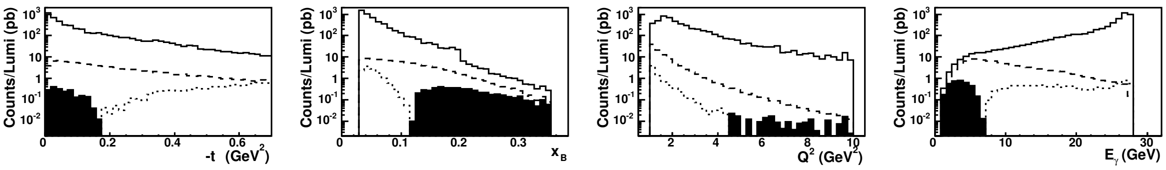

Figure 5.38: The yield in 4π of elastic BH+DVCS events in the range of $-t > 0.7$ GeV^2, $0.03 < x_B < 0.35$, $1 < Q^2 < 10$ GeV^2 from an unpolarized gmc_dvcs MC data sample, based on GPD model 5 in section 5.3.1. Solid curve: the total BH+DVCS contribution, dashed curve: pure DVCS contribution, shaded area (dotted curve): positive (negative) contribution from the BH-DVCS interference.

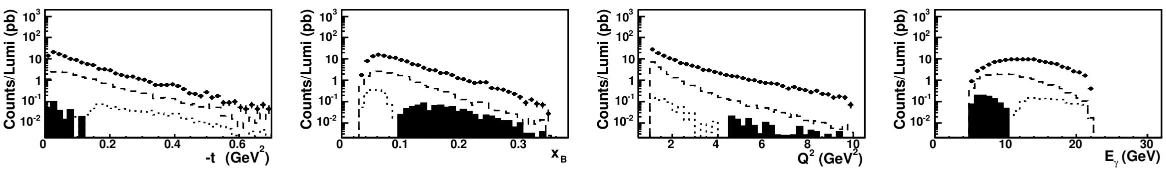

Figure 5.39: Same as Fig. 5.38 but in the HERMES acceptance.

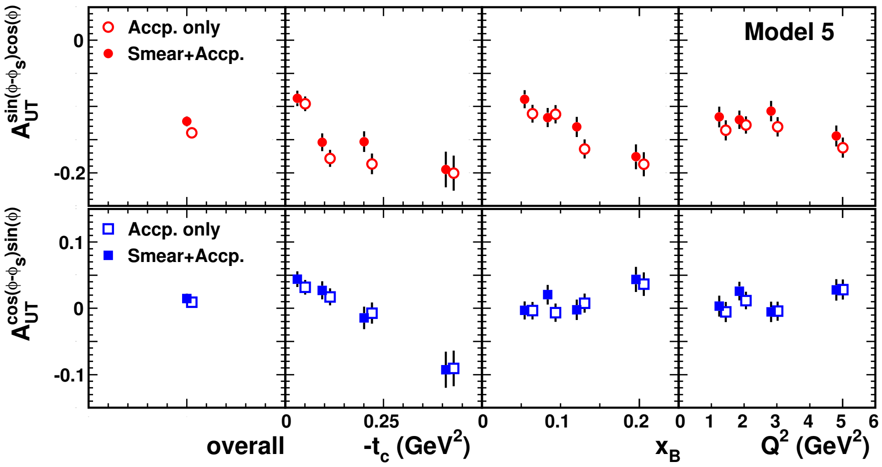

Figure 5.40: The $A_{UT}^{\sin(\phi-\phi_S)\cos\phi}$ and $A_{UT}^{\cos(\phi-\phi_S)\sin\phi}$ amplitudes extracted from a polarized gmc_dvcs MC data sample, based on GPD model 5 in section 5.3.1. Solid points: both the smearing effect and the acceptance effect are included in the simulation; open points: only the acceptance effect is simulated.

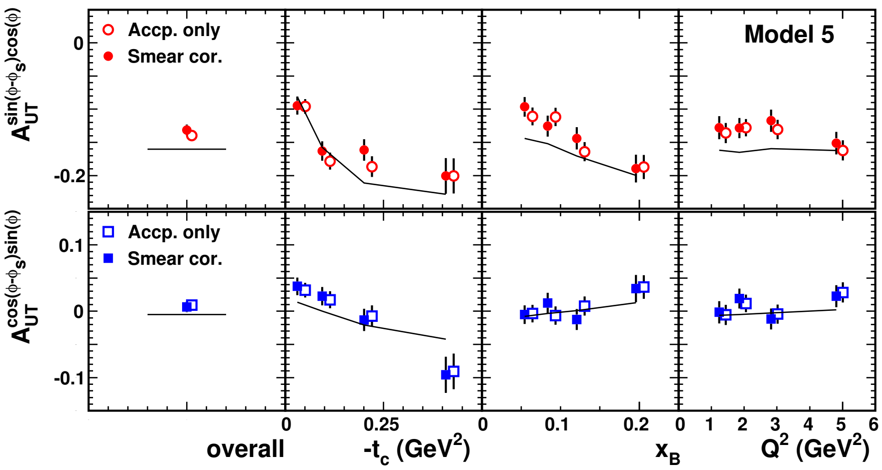

Figure 5.41: The $A_{UT}^{\sin(\phi-\phi_S)\cos\phi}$ and $A_{UT}^{\cos(\phi-\phi_S)\sin\phi}$ amplitudes extracted from a polarized gmc_dvcs MC data sample, based on GPD model 5 in section 5.3.1. Solid points: both the smearing effect and the acceptance effect are included in the simulation, but the smearing effect is corrected using smearing coefficients shown in Fig. 5.16; open points: only the acceptance effect is simulated. The solid curves represent the theoretical predictions at the average HERMES kinematics of the solid points, connected in between simply with straight lines.

are known, they can be used to correct the measured asymmetry $A_{meas.}$ as,

$$A_{ela.} = \frac{1}{f_{ela.}} \cdot \left(A_{meas.} - f_{ass.} A_{ass.} - f_{SIDIS} A_{SIDIS} - f^{\pi^0}_{excl.} A^{\pi^0}_{excl.} \right) , \tag{5.29}$$

where f (A) denotes the relative contribution (asymmetry) of the individual processes. Background contributions can be estimated in MC simulations. The results based on the MC simulations described in section 5.3 are presented in section 5.7.1. As shown in section 5.7.1, semi-inclusive processes with π^0 produced dominate the semi-inclusive DIS background contribution. The asymmetry of the semi-inclusive π^0 background $A^{\pi^0}_{SIDIS}$ can be extracted from the experimental data, as described in section 5.7.2. Nevertheless, due to the limited statistics, the asymmetry of exclusive π^0 production $A^{\pi^0}_{excl.}$ is not extracted. Due to the limited M^2_{X} resolution, neither can the asymmetry of the associated BH/DVCS processes $A_{ass.}$ be extracted from the experimental data. As the contribution of exclusive π^0 production is found to be small in section 5.7.1, its influence to the extracted TTSA amplitudes is well under control. On the other hand, the contribution of the associated BH/DVCS processes is non-negligible and has to be taken into account. The final results on the TTSA amplitudes are not corrected for the associated BH/DVCS processes, i.e., they have to be interpreted as the ones describing both elastic and associated production simultaneously, namely

$$A_{excl.} = \frac{f_{ela.} A_{ela.} + f_{ass.} A_{ass.}}{f_{ela.} + f_{ass.}} = \frac{1}{1 - f_{SIDIS} - f^{\pi^0}_{excl.}} \cdot \left(A_{meas.} - f_{SIDIS} A_{SIDIS} - f^{\pi^0}_{excl.} A^{\pi^0}_{excl.} \right) . \tag{5.30}$$

5.7.1 Background Contributions

As described in section 5.2, the upper cut on the missing mass squared $M^2_{\mathrm{X}} < 2.89$ GeV^2 has been optimized to improve the signal-to-background ratio. This can be seen in Fig. 5.42, which shows the relative contribution of the elastic BH/DVCS processes and the contributions of background processes, given as a function of M^2_{X}. As can be seen, $M^2_{\mathrm{X}} = 2.89$ GeV^2 is approximately the position where the elastic BH/DVCS processes and background processes contribute equally. Similar studies which are not shown here have been performed for the dependence of the contributions on $\theta_{\gamma^*\gamma}$ and $-t_c$. The cuts $\theta_{\gamma\gamma^*} < 45$ mrad and $t_c > -0.7$ GeV^2 have been chosen to improve the signal-to-background ratio [Ell04].

The relative contributions of different processes in the exclusive region $-2.25 < M^2_{\mathrm{X}} < 2.89$ GeV^2 are shown in Fig. 5.43 and listed in Tab. 5.4, given as a function of t_c, x_B, and Q^2. The mean of the contributions is estimated from the MC simulation which does not include the DVCS process, while the maximum difference among the results of the simulations with and without the DVCS process is assigned as a systematic uncertainty. As can be seen, the associated BH/DVCS processes are the dominant background contribution, amounting to approximately 12% on average. The contribution from exclusive π^0 production is found to be very small ($\leq 0.6\%$), while the contribution from the semi-inclusive background is approximately 4% on average. It is also found (not shown here) that approximately 80% of the semi-inclusive background is due to events where the trackless cluster in the calorimeter is produced by decay photon(s) of neutral pions, while the rest is mostly due to photons decaying from the η ($\sim$15%). For the semi-inclusive background due to neutral pions, the energy transfer from the beam to the pion, $z \equiv E_{\pi^0}/\nu$, is found to be large ($\sim$0.9) and independent on the kinematic bins, as can be seen in Fig. 5.44.

As the event selection is affected by the calorimeter calibration, which is mainly due to the cut on the missing mass squared M_X^2, background contributions might be different with a miscalibrated calorimeter. Background contributions are estimated in MC simulations with photon energies scaled by 0.99 and are compared in Fig. 5.43 to the ones without scaling. As can be seen, the changes in the background contributions are small compared to the uncertainties already assigned. Therefore the changes in background contributions due to calorimeter calibration are not considered further in the following.

kinematic bin		elastic BH/DVCS	associated BH	semi-incl. DIS	exclusive π^0
overall		$83.9 \pm 2.2\%$	$11.6 \pm 2.1\%$	$4.1 \pm 0.3\%$	$0.4 \pm 0.0\%$
$-t_c$ (GeV^2)	0.00–0.06	$92.3 \pm 0.9\%$	$5.1 \pm 0.7\%$	$2.4 \pm 0.4\%$	$0.3 \pm 0.0\%$
	0.06–0.14	$82.4 \pm 2.7\%$	$11.6 \pm 2.4\%$	$5.5 \pm 0.7\%$	$0.5 \pm 0.0\%$
	0.14–0.30	$74.8 \pm 5.1\%$	$19.1 \pm 4.6\%$	$5.7 \pm 0.7\%$	$0.4 \pm 0.0\%$
	0.30–0.70	$64.6 \pm 8.4\%$	$30.7 \pm 7.9\%$	$4.4 \pm 0.7\%$	$0.3 \pm 0.0\%$
x_B	0.03–0.07	$87.8 \pm 2.4\%$	$10.6 \pm 2.3\%$	$1.3 \pm 0.3\%$	$0.3 \pm 0.0\%$
	0.07–0.10	$84.4 \pm 2.2\%$	$11.2 \pm 2.0\%$	$4.0 \pm 0.6\%$	$0.4 \pm 0.0\%$
	0.10–0.15	$82.6 \pm 2.3\%$	$12.4 \pm 2.2\%$	$4.5 \pm 0.6\%$	$0.4 \pm 0.0\%$
	0.15–0.35	$73.7 \pm 2.5\%$	$14.2 \pm 2.5\%$	$11.7 \pm 1.1\%$	$0.4 \pm 0.0\%$
Q^2 (GeV^2)	1.0–1.5	$85.7 \pm 3.1\%$	$9.2 \pm 2.4\%$	$4.5 \pm 0.8\%$	$0.6 \pm 0.0\%$
	1.5–2.3	$85.1 \pm 2.2\%$	$11.0 \pm 2.1\%$	$3.4 \pm 0.4\%$	$0.4 \pm 0.0\%$
	2.3–3.5	$82.8 \pm 1.7\%$	$12.7 \pm 1.7\%$	$4.4 \pm 0.5\%$	$0.4 \pm 0.0\%$
	3.5–10.0	$80.4 \pm 1.5\%$	$15.1 \pm 1.6\%$	$4.3 \pm 0.6\%$	$0.3 \pm 0.0\%$

Table 5.4: Relative contributions of different processes to the exclusive region $-2.25 < M_X^2 < 2.89$ GeV^2. The errors represent the quadratic sum of the statistical and systematic uncertainties.

5.7.2 Asymmetry of the Semi-inclusive Background

As described in the previous section, the semi-inclusive background is dominated by events in which the trackless cluster in the calorimeter is produced by decay photon(s)

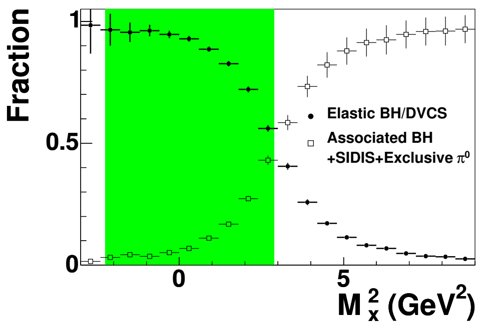

Figure 5.42: Relative contributions from the elastic BH/DVCS processes (solid circles) and from background processes (open boxes) – associated BH+semi-inclusive DIS+exclusive π^0 production – given as a function of M_X^2. The shaded area defines the exclusive region $-2.25 < M_X^2 < 2.89$ GeV^2. The MC simulation does not include the DVCS process. The vertical error bars represent statistical uncertainties only.

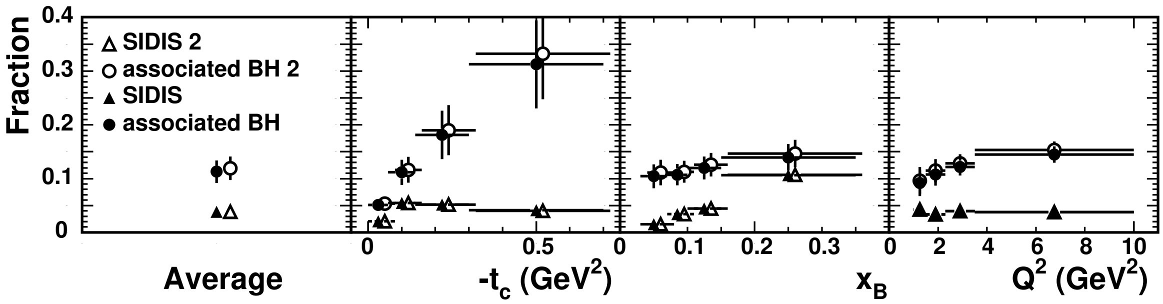

Figure 5.43: Background contributions to the exclusive region $-2.25 < M_X^2 < 2.89$ GeV^2 from associated BH processes (solid circles), and semi-inclusive DIS processes (solid triangles). The vertical error bars represent the quadratic sum of statistical and systematic uncertainties. Background contributions estimated with the photon energy scaled by 0.99 are also shown as open points.

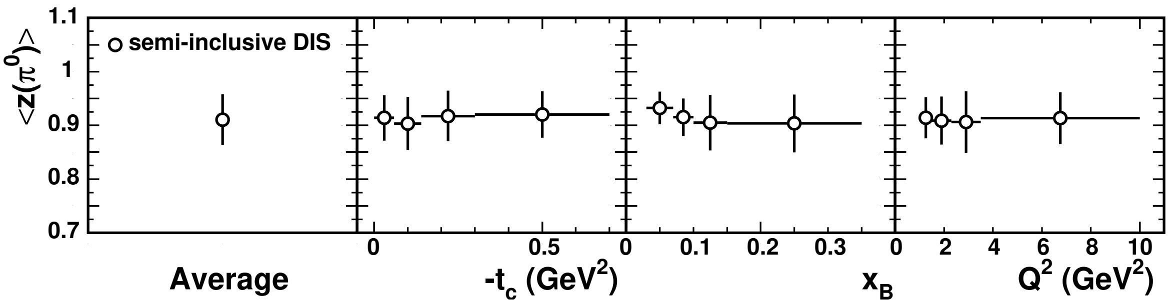

Figure 5.44: The average value of z for the semi-inclusive π^0 background in the exclusive region $-2.25 < M_X^2 < 2.89$ GeV^2. The vertical error bars represent the standard deviations of the z^{π^0} distributions.

of a neutral pion. The cluster can be due to two decay photons. When two photons are too close to each other, the calorimeter attributes them into one cluster. The cluster can also be due to one single decay photon when the other photon escaped detection. In the former case that the cluster is produced by two photons, the cluster actually gives a measure of the neutral pion, and thus the background asymmetry $A^{(2\gamma)}_{SIDIS}$ which enters in Eq. (5.29) equals to A_{π^0}, the asymmetry of the neutral pion itself. In the latter case that the cluster is produced by only one of the decay photons, the background asymmetry $A^{(\gamma)}_{SIDIS}$ is not necessarily equal to the asymmetry of the neutral pion itself. The relationship between $A^{(\gamma)}_{SIDIS}$ and A_{π^0} can be investigated by MC simulations. A sample of semi-inclusive MC events with π^0 production is generated by the gmc_disNG generator and is processed through the whole HERMES MC chain (see section 5.3). A constant fake TTSA amplitude of the π^0 is generated in the sample (see section 5.5.3). The new sample containing the generated π^0 asymmetry is analyzed in the same way as the experimental data for BH/DVCS events. The extracted asymmetry $A^{\gamma+2\gamma}_{SIDIS}$ is shown in Fig. 5.45, given as a function of the generated π^0 asymmetry. As can be seen, the asymmetry transfer from the neutral pion to the decay photon(s),

$$f_{\gamma/\pi^0} \equiv A^{\gamma+2\gamma}_{SIDIS}/A_{\pi^0}, \tag{5.31}$$

is always close to unity for the whole M_{X} region, and in the exclusive region $-2.25 < M^2_{\mathrm{X}} < 2.89$ GeV^2 it is 1.01±0.15. For the following study we will take $f^{\gamma/\pi^0}_{SIDIS} = 1.0 \pm 0.2$ and use $f_{\gamma/\pi^0} \cdot A_{\pi^0}$ to estimate the semi-inclusive background asymmetry $A^{\gamma+2\gamma}_{SIDIS}$.

In order to extract the asymmetry A_{π^0} from the data, a two-photon analysis is performed. Instead of requiring one trackless cluster in the calorimeter (see section 5.2), two trackless clusters are required with energy deposition in the pre-shower detector being larger than 1 MeV. The energy deposition of the 'leading' cluster in the calorimeter is required to be larger than 5 GeV, while the other cluster has to have an energy more than 1 GeV. Assuming that both of the clusters were photons and originated from the primary interaction vertex, the invariant mass of these two photons $m_{\gamma\gamma}$ is calculated. The resulting invariant mass spectrum is shown in Fig. 5.46 (panel (a)), where a clear peak near the π^0 mass can be seen. A fairly good description of the spectrum is provided by a 'Gaussian+Constant' fit with the fitted mean of the Gaussian being close to the PDG value of the π^0 mass.

The cuts used to select the candidates for BH/DVCS events (see section 5.2) are applied on the two-photon events, with the kinematics calculated either with respect to the 'leading' photon or with respect to the reconstructed neutral pion. A problem arises when applying the cut on the missing mass squared $-2.25 < M^2_{\mathrm{X}} < 2.89$ GeV^2: the statistics is so low, as shown in Fig. 5.46 (panel (b)), that no asymmetry can be extracted. In order to increase the statistics, instead of the cut on M^2_{X} the cut $z_{\pi^0} > 0.8$ is applied, based on the observation shown in Fig. 5.44. The resulting invariant mass spectrum is shown in Fig. 5.46 (panel (c)). Out of those events which also satisfy

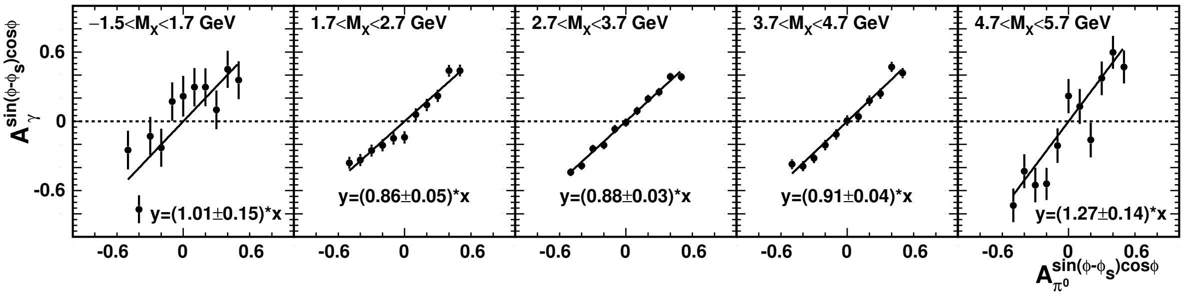

Figure 5.45: Reconstructed asymmetry of decay photon(s) given as a function of the generated π^0 asymmetry. Also shown are the results of a linear fit to the data points.

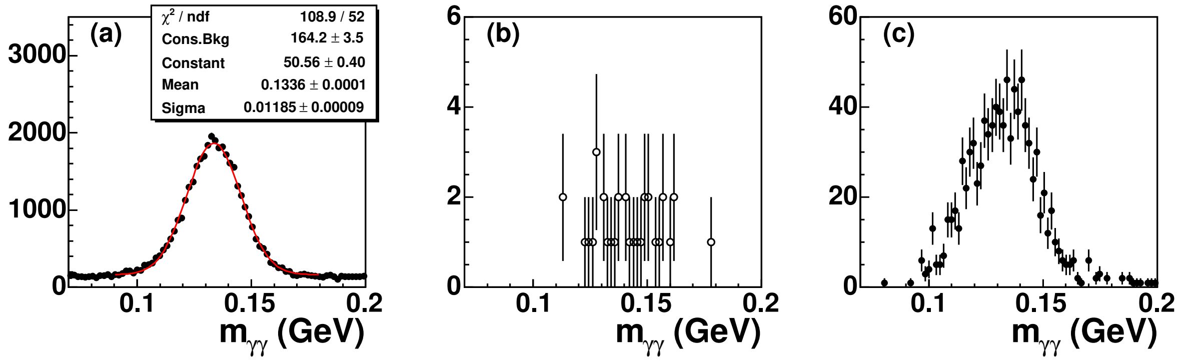

Figure 5.46: The invariant mass distributions from the two-photon analysis (see text): (a) all the events; (b) events satisfying all the selection cuts described in section 5.2; (c) events satisfying the cut z_{π^0} >0.8 and all the other cuts described in section 5.2 except the cut $-2.25 < M_X^2 < 2.89$ GeV^2. Also shown in panel (a) is the result of a 'Gaussian+Constant' fit.

$0.1 < m_{\gamma\gamma} < 0.17$ GeV, the TTSA amplitudes are extracted, as shown in Fig. 5.47. As can be seen, the TTSA amplitudes of the 'leading' photon are compatible to the ones of the neutral pion, and no kinematic dependence of the two TTSA amplitudes can be seen within the given statistical uncertainties. Therefore the average (overall) TTSA amplitudes of the neutral pion are used to correct for the semi-inclusive π^0 background. The TTSA amplitudes corrected for this background are shown in Fig. 5.48. A discussion on the systematic uncertainty due to this correction for the semi-inclusive π^0 background and due to other uncorrected background contributions will be given in section 6.1.2.

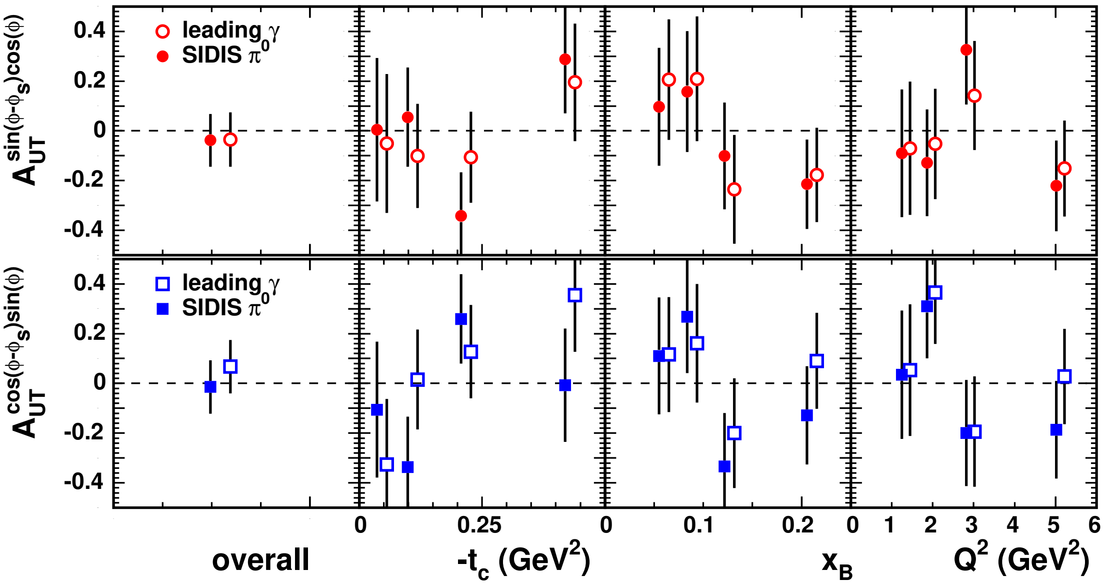

Figure 5.47: Extracted TTSA amplitudes of the semi-inclusive π^0 background from the HERMES 2002-2004 data. The error bars represent statistical uncertainties only.

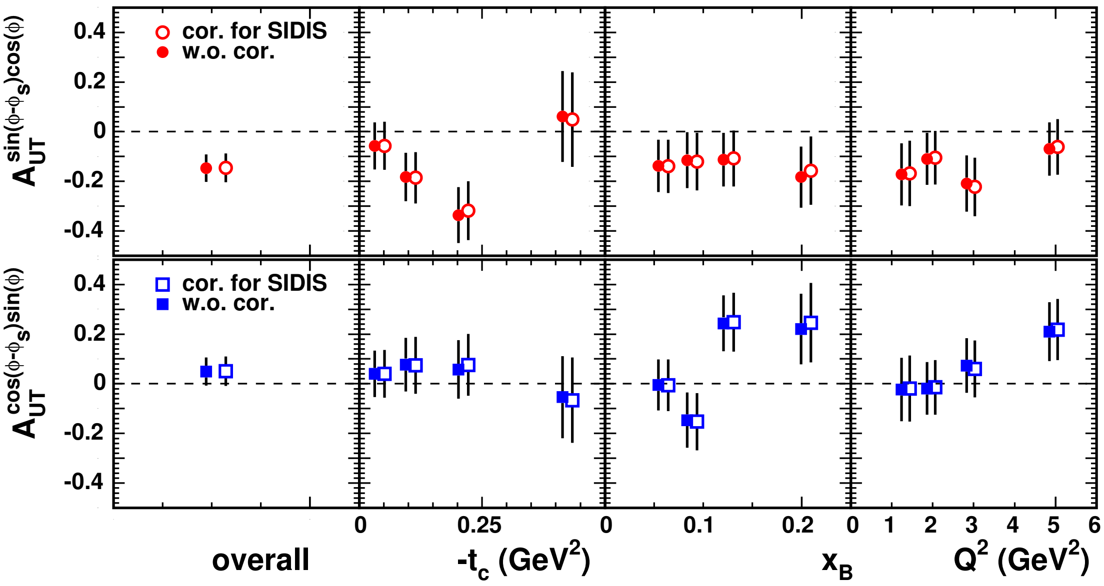

Figure 5.48: TTSA amplitudes from the HERMES 2002-2004 data corrected for the semi-inclusive π^0 background. The error bars represent statistical uncertainties only.

Chapter 6

Results and Discussion

The data analysis to extract from the HERMES 2002-2004 data the two Transverse Target-Spin Asymmetry (TTSA) amplitudes, $A_{UT}^{\sin(\phi-\phi_S)\cos\phi}$ and $A_{UT}^{\cos(\phi-\phi_S)\sin\phi}$, has been described in the previous chapter. In section 6.1, we summarize the conclusions of the studies performed, and present the final results on the extracted TTSA amplitudes, including the estimated statistical and systematic uncertainties. In section 6.2 a model-dependent constraint on J_u and J_d is obtained by comparing the HERMES results on $A_{UT}^{\sin(\phi-\phi_S)\cos\phi}$ with theoretical predictions based on a Generalized Parton Distribution (GPD) model.

6.1 Transverse Target-Spin Asymmetry Amplitudes

6.1.1 Statistical Uncertainties

In the Monte Carlo (MC) test described in section 5.5.3, it has been shown that by using the method of maximum likelihood, the two leading TTSA amplitudes can be extracted reliably, and the statistical uncertainties are calculated correctly. Hence no further treatment is performed for the statistical uncertainties.

6.1.2 Systematic Uncertainties

Target Polarization

The average value of the target polarization in the years 2002-2004 is estimated to be [Els05]: $\langle P_T \rangle = \pm 0.754 \pm 0.050$. A relative systematic uncertainty of $0.050/0.754 \simeq 6.6\%$ is assigned to the extracted TTSA amplitudes due to this uncertainty in determining the target polarization value.

Luminosity

The extraction of the TTSA amplitudes uses the information of the integrated luminosity provided by the luminosity monitor. An alternative approach is to use the number of DIS events, which should be proportional to the actual integrated luminosity. It is found that the changes in the extracted TTSA amplitudes are less than 0.0001. Therefore no systematic uncertainty is assigned to the extracted TTSA amplitudes for the uncertainty in determining the integrated luminosities.

Fit Function

It has been shown in section 5.5.4 that the TTSA amplitudes obtained using the method of maximum likelihood are insensitive to the form of the fit function (Fig. 5.24). The final results on the TTSA amplitudes are based on the fit function with two parameters, while the maximum absolute difference among the results obtained with different fit functions is assigned as a systematic uncertainty.

Transverse Target Magnet

The transverse target magnet has a non-negligible influence on charged particles. As is described in section 5.6.1, two different algorithms have been implemented to correct for such an influence in track reconstruction. The final results on the TTSA amplitudes are based on the data after the correction. As MC simulations have shown that the influence of the transverse target magnet can be removed almost completely by applying either of the two algorithms, no systematic uncertainty is assigned to the extracted TTSA amplitudes.

Misalignment of the Spectrometer and Beam

Misalignment effects have been investigated in section 5.6.2. The influence of a possible spectrometer or beam misalignment on the extracted TTSA amplitudes is studied in MC simulations and is found to be small. Based on the best knowledge on the spectrometer misalignment and the measured beam slopes and offsets, the spectrometer and beam misalignment is corrected in the experimental data and only small changes in the extracted TTSA amplitudes are found (Fig. 5.31). With these changes assigned as a systematic uncertainty, the TTSA amplitudes extracted without correction for spectrometer or beam misalignment are given as the final results.

Miscalibration of the Calorimeter

In section 5.6.3, the influence of a miscalibrated calorimeter on the extracted TTSA amplitudes has been studied. The calorimeter calibration in the years 2002-2004 is checked by looking at the ratio of the energy measured by the calorimeter over the momentum reconstructed by the tracking system of a sample of DIS leptons. No evidence for a relative calorimeter miscalibration in this data set has been found. There exists, however, an indication that the absolute calorimeter calibration in the years 2002-2004 might be too low by 1%. It is argued that a miscalibrated calorimeter can only affect the present analysis in the event selection and does not affect the kinematics relevant for extracting TTSA amplitudes. This argument is supported by the finding in MC simulations that the extracted TTSA amplitudes do not change after decreasing the reconstructed photon energies by 1%. Consistently, the TTSA amplitudes extracted from the experimental data do not change significantly after the photon energies are increased by 1% (Fig. 5.34). With these changes assigned as a systematic uncertainty, the TTSA amplitudes without correction for photon energies are given as the final results.

Detection Efficiency

In section 5.6.4, the influence of the detection efficiency on the extracted TTSA amplitudes has been investigated. With the advantage of continuous fast flipping of the target polarization state, measurements of target-spin asymmetries at HERMES are insensitive to time-dependent changes in the detection efficiency. The possible influence of a non-uniformity of the detection efficiency on the extracted TTSA amplitudes was studied in the experimental data. It has been found that among all the detection efficiencies relevant to the present analysis, the trigger efficiency of the H0 hodoscope has the most significant non-uniformity, which is its angular dependence. The changes in the extracted TTSA amplitudes are very small after correcting for the angular-dependence of the H0 efficiency (Fig. 5.36). It is concluded that the extracted TTSA amplitudes are not affected by the detection efficiency. For the final results, no correction is performed and no systematic uncertainty is assigned for the detection efficiency.

Smearing and Acceptance Effects

In section 5.6.5, the smearing and acceptance effects on the extracted TTSA amplitudes have been studied in MC simulations. It was shown that by using the smearing coefficients extracted in section 5.5.3, a part of the smearing effect can be corrected. For the final results, no correction is performed. The differences between the two sets of results shown in Fig. 5.40 are used to estimate the systematic uncertainty of the extracted TTSA amplitudes due to the smearing effect.

The acceptance effect is found to be very important when interpreting the TTSA amplitudes measured at HERMES. When comparing the HERMES results with theoretical predictions, which integrate over kinematic regions, the HERMES acceptance has to be taken into account. However, one may interpret the HERMES results being for the average HERMES kinematics. In doing so, such differences as shown in Fig. 5.41 between the results in which only the acceptance effect in simulated, and the theoretical predictions at the average kinematics may be used to estimate the systematic uncertainty due to the acceptance effect. For this purpose, the largest value among the differences as shown in Fig. 5.41 of the five GPD models in gmc_dvcs is used. This uncertainty will be taken into account in constraining the total angular momentum of quarks in the nucleon in section 6.2.

Background Contributions

In section 5.7, background contributions have been estimated in MC simulations, and the asymmetry of semi-inclusive π^0 background has been extracted from the experimental data. Due to limited statistics, no information can be obtained on the background asymmetry of the other semi-inclusive processes, which on average contributes to the selected BH+DVCS event sample with 0.8%, and the background asymmetry in exclusive π^0 production, which on average contributes with approximately 0.4%. As these background contributions are so small, their asymmetry amplitudes are taken between +1 and -1 and are then transfered into a systematic uncertainty for the extracted TTSA amplitudes. The final results for the TTSA amplitudes are the ones without correcting for background contributions, with a corresponding systematic uncertainty being assigned to be the absolute difference between the TTSA amplitudes with and without corrections for semi-inclusive background and exclusive π^0 background.

6.1.3 Summary

The individual contributions to the systematic uncertainties of the extracted TTSA amplitudes are given in Tabs. 6.1 and 6.2. (Here and below the invariant momentum transfer t is measured by the value of t_c in Eq. (3.10).) The final results on the TTSA amplitudes are listed in Tab. 6.3 and are shown in Fig. 6.1. Not including the systematic uncertainty due to the acceptance effect, the systematic uncertainties listed in Tabs. 6.1 and 6.2 are added quadratically. A comparison between the HERMES results and theoretical predictions (see App. B for details) at the average HERMES kinematics based on a phenomenological model of GPDs [Goe01] are shown in Fig. 6.1. The curves represent the TTSA amplitudes evaluated with different u-quark total angular momentum J_u as a model parameter, while fixing the d-quark total angular momentum $J_d = 0$. As can be seen, the experimental results are in agreement with theoretical predictions.

$A_{UT}^{\sin(\phi-\phi_S)\cos\phi}$		δ_{tpl}	δ_{fit}	$\delta_{misalign.}$	$\delta_{cali.}$	$\delta_{smear.}$	$\delta_{bkd.}$	$\delta_{acc.}$
overall		0.009	0.015	0.003	0.003	0.017	0.021	0.026
$-t$ (GeV^2)	0.00–0.06	0.004	0.003	0.010	0.014	0.008	0.018	0.017
	0.06–0.14	0.011	0.010	0.016	0.010	0.024	0.030	0.028
	0.14–0.30	0.021	0.024	0.033	0.017	0.034	0.039	0.029
	0.30–0.70	0.004	0.018	0.060	0.037	0.006	0.017	0.028
x_B	0.03–0.07	0.009	0.008	0.004	0.027	0.022	0.008	0.046
	0.07–0.10	0.007	0.020	0.020	0.013	0.005	0.019	0.044
	0.10–0.15	0.007	0.051	0.006	0.028	0.033	0.021	0.010
	0.15–0.35	0.011	0.033	0.003	0.002	0.011	0.058	0.014
Q^2 (GeV^2)	1.0–1.5	0.011	0.019	0.023	0.002	0.020	0.026	0.029
	1.5–2.3	0.007	0.015	0.016	0.004	0.008	0.017	0.041
	2.3–3.5	0.013	0.022	0.022	0.029	0.024	0.024	0.029
	3.5–10.0	0.004	0.028	0.008	0.004	0.018	0.017	0.010

Table 6.1: Systematic uncertainties of the extracted TTSA amplitude $A_{UT}^{\sin(\phi-\phi_S)\cos\phi}$ due to the uncertainty in determining the target polarization (δ_{tpl}), due to the fit function (δ_{fit}), due to the misalignment effect ($\delta_{misalign.}$), due to the calorimeter miscalibration ($\delta_{cali.}$), due to the smearing effect ($\delta_{smear.}$), due to background contributions ($\delta_{bkd.}$), and due to the acceptance effect when interpreting the results as the ones at the average HERMES kinematics ($\delta_{acc.}$).

$A_{UT}^{\cos(\phi-\phi_S)\sin\phi}$		δ_{tpl}	δ_{fit}	$\delta_{misalign.}$	$\delta_{cali.}$	$\delta_{smear.}$	$\delta_{bkd.}$	$\delta_{acc.}$
overall		0.003	0.010	0.000	0.004	0.006	0.016	0.018
$-t$ (GeV^2)	0.00–0.06	0.003	0.014	0.008	0.023	0.012	0.009	0.021
	0.06–0.14	0.005	0.006	0.019	0.026	0.010	0.022	0.022
	0.14–0.30	0.004	0.017	0.045	0.014	0.007	0.021	0.016
	0.30–0.70	0.003	0.047	0.034	0.017	0.002	0.016	0.057
x_B	0.03–0.07	0.000	0.032	0.002	0.023	0.000	0.006	0.005
	0.07–0.10	0.009	0.024	0.021	0.003	0.027	0.020	0.005
	0.10–0.15	0.016	0.030	0.023	0.007	0.010	0.027	0.009
	0.15–0.35	0.013	0.021	0.002	0.007	0.007	0.060	0.028
Q^2 (GeV^2)	1.0–1.5	0.002	0.034	0.014	0.030	0.009	0.015	0.001
	1.5–2.3	0.001	0.012	0.006	0.008	0.014	0.012	0.017
	2.3–3.5	0.005	0.006	0.001	0.014	0.001	0.017	0.005
	3.5–10.0	0.013	0.012	0.003	0.007	0.001	0.022	0.030

Table 6.2: Same as Tab. 6.1 but for the TTSA amplitude $A_{UT}^{\cos(\phi-\phi_S)\sin\phi}$.

kinematic bin		$\langle -t \rangle$ (GeV^2)	$\langle x_B \rangle$	$\langle Q^2 \rangle$ (GeV^2)	$A_{UT}^{\sin(\phi-\phi_S)\cos\phi}$ $\pm\delta_{stat} \pm \delta_{syst}$	$A_{UT}^{\cos(\phi-\phi_S)\sin\phi}$ $\pm\delta_{stat} \pm \delta_{syst}$
overall		0.116	0.0953	2.46	-0.146 ± 0.055 ± 0.032	0.047 ± 0.057 ± 0.020
$-t$ (GeV^2)	0.00–0.06	0.0312	0.0769	1.93	-0.056 ± 0.095 ± 0.028	0.039 ± 0.094 ± 0.032
	0.06–0.14	0.0945	0.0990	2.51	-0.172 ± 0.098 ± 0.045	0.073 ± 0.108 ± 0.041
	0.14–0.30	0.202	0.116	2.97	-0.319 ± 0.112 ± 0.071	0.054 ± 0.118 ± 0.055
	0.30–0.70	0.414	0.125	3.70	0.058 ± 0.183 ± 0.075	-0.052 ± 0.165 ± 0.041
x_B	0.03–0.07	0.0914	0.0542	1.45	-0.136 ± 0.105 ± 0.038	-0.005 ± 0.102 ± 0.040
	0.07–0.10	0.0992	0.0835	2.14	-0.111 ± 0.112 ± 0.037	-0.142 ± 0.111 ± 0.047
	0.10–0.15	0.131	0.121	3.13	-0.108 ± 0.108 ± 0.071	0.233 ± 0.113 ± 0.050
	0.15–0.35	0.197	0.199	4.98	-0.163 ± 0.123 ± 0.068	0.197 ± 0.143 ± 0.066
Q^2 (GeV^2)	1.0–1.5	0.0768	0.0563	1.24	-0.165 ± 0.126 ± 0.046	-0.022 ± 0.127 ± 0.050
	1.5–2.3	0.0969	0.0777	1.87	-0.106 ± 0.104 ± 0.030	-0.018 ± 0.106 ± 0.025
	2.3–3.5	0.133	0.108	2.83	-0.201 ± 0.113 ± 0.056	0.071 ± 0.110 ± 0.023
	3.5–10.0	0.185	0.170	4.85	-0.067 ± 0.107 ± 0.038	0.202 ± 0.119 ± 0.030

Table 6.3: The final results on the TTSA amplitudes, obtained from the HERMES 2002-04 data. Acceptance effects are not included in the systematic uncertainties.

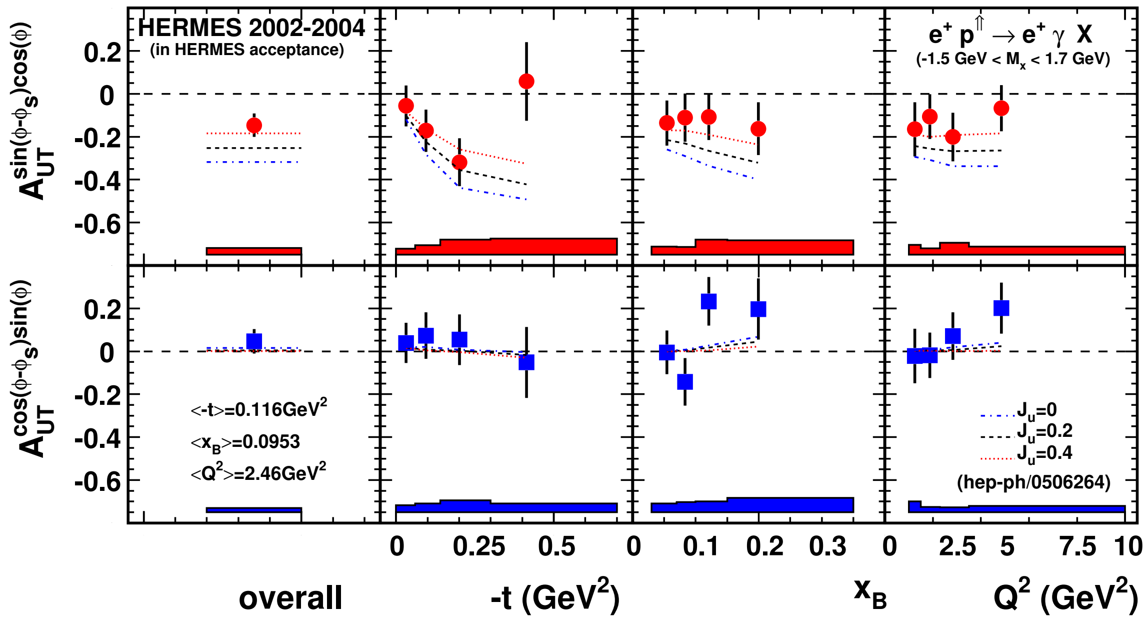

Figure 6.1: HERMES results on the TTSA amplitudes in Tab. 6.3 compared with theoretical predictions based on the GPD model proposed in Ref. [Goe01]. The D-term is modeled according to the chiral quark-soliton model result [Goe01]. See text for further details.

6.2 Constraint on the Total Angular Momentum of Quarks in the Nucleon

At present the only known strategy to "extract" GPDs from experimental measurements is to assume a functional form of GPDs with a number of adjustable parameters, and to fit these parameters by comparing the resulting observables with experimental data [Die03]. A general parameterization for GPDs has been given by Goeke, Polyakov and Vanderhaeghen [Goe01]. For this GPD model it has been shown in section 3.3.1 that $A_{UT}^{\sin(\phi-\phi_S)\cos\phi}$ is sensitive to the quark total angular momentum in the nucleon, J_q ($q = u$, d), and is less sensitive to the other parameters. Therefore, reasonable constraints on J_u and J_d within such a GPD model may be expected from measurements on the TTSA associated with DVCS.

In this section, we describe a model-dependent constraint on J_u and J_d obtained by comparing the HERMES results on the TTSA amplitude $A_{UT}^{\sin(\phi-\phi_S)\cos\phi}$ with theoretical predictions based on the GPD model in Ref. [Goe01]. A brief description of the above parameterization of GPDs is given in section 6.2.1. In section 6.2.2, it is described how the constraint on J_u and J_d can be obtained.

6.2.1 A Parameterization of GPDs

Assuming a factorized t-dependence, the quark GPD H^q is given by [Goe01]

$$H^q(x, \xi, t) = H^q(x, \xi) \cdot F_1^q(t), \tag{6.1}$$

according to the relations to the form factors (FFs) described in section 2.3.3. At small values of $-t$, the proton and neutron Dirac FFs, F_1^p and F_1^n, can be described by the dipole form,

$$\begin{aligned} F_1^p(t) &= \frac{1 - (1+\kappa_p) \cdot t/4m_p^2}{(1 - t/4m_p^2) \cdot (1 - t/m_D^2)^2}, \\ F_1^n(t) &= 0, \end{aligned} \tag{6.2}$$

$$\tag{6.3}$$

where κ_p is the proton anomalous magnetic moment, m_p the proton mass, and $m_D^2 = 0.71$ GeV^2. Assuming isospin symmetry and that the strange quark contribution to the nucleon form factor vanishes, the Dirac FFs of u-quarks and d-quarks, F_1^u and F_1^d, are given by:

$$\begin{aligned} F_1^u &= 2F_1^p + F_1^n, \\ F_1^d &= 2F_1^n + F_1^p. \end{aligned} \tag{6.4}$$

The t-independent part of the quark GPD, $H^q(x,\xi)$, is most commonly parameterized in terms of double distributions [Rad99, Mus00] complemented with the D-term [Pol99]. It is written as

$$H^q(x,\xi) = H^q_{DD}(x,\xi) + \theta\left(\xi - |x|\right) D^q\left(x/\xi\right), \tag{6.5}$$

where H^q_{DD} is the part that can be obtained from the double distribution F^q,

$$H^q_{DD}(x,\xi) = \int_{-1}^{1} d\beta \int_{-1+|\beta|}^{1-|\beta|} d\alpha\, \delta(x-\beta-\alpha\xi) F_q(\beta,\alpha), \tag{6.6}$$

and $D^q(x/\xi)$ is the D-term. For the double distributions F_q the suggestion of Ref. [Rad99] is used,

$$F_q(\beta,\alpha) = h(\beta,\alpha)q(\beta), \tag{6.7}$$

where the profile function is given by [Mus00]:

$$h(\beta,\alpha) = \frac{\Gamma(2b+2)}{2^{2b+1}\Gamma^2(b+1)} \frac{\left[(1-|\beta|)^2-\alpha^2\right]^b}{(1-|\beta|)^{2b+1}}. \tag{6.8}$$

For $\beta > 0$, $q(\beta) = q_{val}(\beta) + \bar{q}(\beta)$ is the ordinary PDF for the quark flavor q. The negative β range corresponds to the antiquark PDF: $q(-\beta) = -\bar{q}(\beta)$. The parameter b characterizes to what extent the GPD depends on the skewness ξ. In the limit $b \to \infty$ the GPD is independent on ξ, *i.e.*, $H(x,\xi) = q(x)$. Note that b is a free parameter for valence quarks (b_{val}) or sea quarks (b_{sea}) and thus can be used as a fit parameter in the extraction of GPDs from hard electroproduction data.

The spin-flip quark GPDs E_q in the factorized ansatz are given by [Goe01]:

$$E_q(x,\xi,t) = E_q(x,\xi) \cdot F_2^q(t)/\kappa^q. \tag{6.9}$$

Here $F_2^q(t)$ denotes the Pauli FF for quark flavor q, and is parameterized by

$$F_2^q = \frac{\kappa^q}{(1-t/4m_p^2)\cdot(1-t/m_D^2)^2}, \tag{6.10}$$

where κ_q is the anomalous magnetic moment of quarks of flavor q. The t-independent part of the quark GPDs, $E_q(x,\xi)$, is parameterized analogously to Eq. 6.5,

$$E_q(x,\xi) = E_q^{DD}(x,\xi) - \theta(\xi-|x|)D_q\left(\frac{x}{\xi}\right). \tag{6.11}$$

The part of the GPD E that can be obtained from the double distribution has a form analogous to the spin-nonflip case:

$$E_q^{DD}(x,\xi) = \int_{-1}^{1} d\beta \int_{-1+|\beta|}^{1-|\beta|} d\alpha\, \delta(x-\beta-\alpha\xi)\; K_q(\beta,\alpha) \tag{6.12}$$

with:

$$K_q(\beta, \alpha) = h(\beta, \alpha) e_q(\beta). \tag{6.13}$$

Here $e_q(\beta)$ denotes the spin-flip PDF which can not be extracted from inclusive deep-inelastic scattering data, and which is unknown. It can be represented by a sum of valence and sea quarks contributions. In the chiral quark-soliton model (see section 2.5.3) the sea part was found to be very narrowly peaked around $x = 0$, and the shape of the valence quark part was similar to that of the spin non-flip PDF. The whole distribution is thus written as [Goe01]:

$$e_q(x) = A_q \cdot q_{val}(x) + B_q \cdot \delta(x). \tag{6.14}$$

The coefficients A_q and B_q are constrained by the total angular momentum sum rule (2.27) and the normalization condition

$$\int_{-1}^{+1} dx\, e_q(x) = \kappa_q, \tag{6.15}$$

where κ_q is the anomalous magnetic moment of quarks of flavor q,

$$\begin{aligned} \kappa_u &= 2\kappa_p + \kappa_n = 1.67, \\ \kappa_d &= \kappa_p + 2\kappa_n = -2.03. \end{aligned} \tag{6.16}$$

The constraints yield:

$$A_q = \frac{2J_q - M_q^{(2)}}{M_{q_{val}}^{(2)}}, \tag{6.17}$$

$$B_u = 2\left[\frac{1}{2}\kappa_u - \frac{2J_u - M_u^{(2)}}{M_{u_{val}}^{(2)}}\right], \tag{6.18}$$

$$B_d = \kappa_d - \frac{2J_d - M_d^{(2)}}{M_{d_{val}}^{(2)}}. \tag{6.19}$$

In Eqs. (6.17-6.19) $M_q^{(2)}$ and $M_{q_{val}}^{(2)}$ are the parton momentum contributions to the proton momentum:

$$\begin{aligned} M_{q_{val}}^{(2)} &= \int_0^1 x q_{val}(x) dx, \\ M_q^{(2)} &= \int_0^1 x \left[q_{val}(x) + 2\bar{q}(x)\right] dx. \end{aligned} \tag{6.20}$$

In the given scenario the total angular momenta carried by u-quarks and d-quarks, J_u and J_d, enter directly as free parameters in the parameterization of the spin-flip GPD $E_q(x,\xi,t)$. Hence the parameterization (6.14) can be used to investigate the sensitivity of hard electroproduction observables to variations in J_u and J_d.

The factorized ansatz is the simplest way of modeling GPDs. However, experimental studies of elastic diffractive processes indicate that the t-dependence of the cross section is entangled with its dependence on the photon-nucleon invariant mass [Col77]. Recent evidence comes from lattice QCD calculations [Neg04, Goc05a] and phenomenological considerations [Die05a, Gui05]. A non-factorized ansatz can be based on soft Regge-type parameterizations. In this case, the t-dependence is not factorized out and not controlled by a FF as in Eqs. (6.1) and (6.9). Instead, it is kept in Eqs. (6.5, 6.6) and (6.11, 6.12). The t-dependence of double distributions is then modeled as [Goe01]:

$$F_q(\beta,\alpha,t) = F_q(\beta,\alpha)\frac{1}{|\beta|^{\alpha' t}}, \tag{6.21}$$

which is referred to as Regge ansatz in the following. Here α' is the slope of the Regge trajectory, $\alpha'_q = 0.8$ GeV^{-2} for quarks.

As an example, Fig. 6.2 shows the t-independent part of various GPDs at $\xi = 0.1$, based on the MRST98 [Mar98] parameterization of PDFs at Q^2=4 GeV^2. Using instead CTEQ6L PDFs [Pum02] as input, the results for $u(d)$ quark GPDs are changed by less than 3%(10%); the GPD H_g is up to 40% larger at $x = 0$. Because of u-quark dominance in electroproduction, uncertainties originating from d-quark PDFs can be safely neglected. Since gluons are absent in leading-order DVCS, uncertainties resulting from gluon PDFs are of little influence for DVCS asymmetries. For the following calculations the MRST98 PDF set is taken.

6.2.2 Constraining J_u vs J_d

At present, there exists a code (VGG) [Van03] (see App. B) designed to calculate observables in the exclusive reaction $ep \to ep\gamma$ to LO precision in perturbative theory. It is based on the GPD model proposed in [Goe01]. In the code, one can choose between the Regge ansatz and the factorized ansatz to parameterize the t-dependence of the GPDs. The difference between the calculated TTSA amplitudes using these two ansätze has been found to be very small, as shown in section 3.3.1. As the factorized ansatz is now considered to be oversimplified and also disfavored by lattice QCD calculations and phenomenological considerations, the Regge ansatz is used in the following studies.

One can also choose between having the D-term contribution to the GPDs H and E equal to zero and modeling it according to the chiral quark-soliton model (CQSM) result [Goe01]. As the D-term only contributes to the real part of the Compton form factors $\mathcal{H}$ and $\mathcal{E}$, it will only contribute to the denominator of the right-hand-side of Eq. (3.41) through the unpolarized DVCS cross section and the unpolarized BH-DVCS

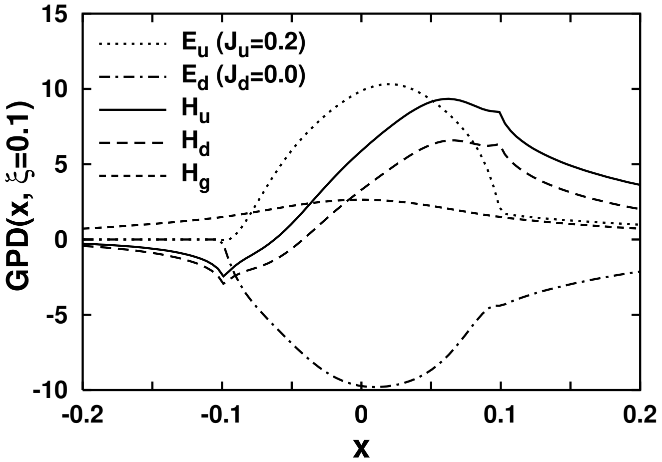

Figure 6.2: t-independent part of quark and gluon GPDs at Q^2=4 GeV^2, ξ=0.1 (MRST98 PDFs are used).

interference term, and to the numerator through the polarized DVCS cross section. Since at HERMES kinematics the denominator (numerator) of the right-hand side of Eq. (3.41) is dominated by the unpolarized BH cross section (polarized BH-DVCS interference), the impact on the predicted values of the TTSA amplitudes of having D-term=0 or D-term=CQSM is expected to be small. Such an expectation is confirmed by explicit calculations that will be presented later. In the following studies, we will perform our calculations both for D-term=0 and D-term=CQSM.

In order to compare the results from theoretical calculations with the TTSA amplitudes extracted from the HERMES 2002-04 data, χ^2_{exp} is calculated as:

$$\chi^2_{exp}(J_u, J_d) = \sum_{i=1}^{n} \frac{\left[A_{UT,i}^{\sin(\phi-\phi_S)\cos\phi}|_{exp} - A_{UT,i}^{\sin(\phi-\phi_S)\cos\phi}|_{VGG}(J_u, J_d)\right]^2}{\delta A^2_{stat,i} + \delta A^2_{syst,i} + \delta A^2_{acc,i}}. \tag{6.22}$$

Here n denotes the number of the kinematic bins: for the overall data set, $n = 1$, for the data binned in one of the kinematic variables t, x_B and Q^2, $n = 4$. $A_{UT,i}^{\sin(\phi-\phi_S)\cos\phi}|_{VGG}$ denotes the results from theoretical calculations performed at the mean kinematics listed in Tab. 6.3. δA_{stat}, δA_{syst} and δA_{acc} are the statistical uncertainties, the systematic uncertainties excluding the acceptance effects, and the ones due to the acceptance effects, respectively. In Eq. (6.22), the contribution from $A_{UT}^{\cos(\phi-\phi_S)\sin\phi}$ is neglected following the observation that variations in J_u and J_d show only minor changes in $A_{UT}^{\cos(\phi-\phi_S)\sin\phi}$, as is expected from Eq. (3.41) and can be seen in Fig. 6.1. Since the calculations done by the VGG code are time-consuming, TTSA amplitudes are calculated in steps of 0.2 in the (J_u, J_d) plane, for J_u and J_d ranging from 0 to 1. The values $\chi^2_{exp}(J_u, J_d)$ are interpolated in between by fitting a 5th order polynomial function[1]. The area in which the value of the fitted polynomial is not larger by one unit than the minimum corresponds to the one standard deviation constraint on J_u and J_d, obtained by the experimental uncertainty in determining the TTSA amplitudes from the HERMES 2002-04 data.

The constraints on J_u and J_d obtained for the extracted TTSA amplitudes from the overall data set and the ones from data binned in one kinematic variable are shown in Fig. 6.3. As J_q is subject to Q^2 evolution, it is desirable to vary J_u and J_d for different kinematic bins in performing the theoretical calculations. However, it could not be done in this way as no tool is available at present to perform the Q^2 evolution for J_q, so that the small differences between the results observed in Fig. 6.3 may be due to having not performed the evolution of J_q. Such differences can also be due to statistical fluctuations in the extracted TTSA amplitudes, or due to a lack of fine tuning of the other model parameters, which is however beyond the scope of the TTSA analysis in this thesis. As the Q^2-evolution of J_q is not performed, we will use the extracted $A_{UT}^{\sin(\phi-\phi_S)\cos\phi}$ obtained from the overall data set in the following studies.

Setting the profile parameters b_{val} and b_{sea} to either one or infinity, TTSA amplitudes are calculated at the mean kinematics of the overall HERMES 2002-04 data for J_u (J_d) ranging from 0 to 1 (-1 to 1) in steps of 0.2. The corresponding one standard deviation ($1\sigma_{exp}$) contours in the J_u and J_d plane are shown in Figs. 6.4 and 6.5, obtained with D-term=0 and D-term=CQSM, respectively. It can be seen that the uncertainty in constraining J_u and J_d due to the undetermined profile parameters b_{val} and b_{sea} is dominated by the experimental uncertainty in measuring $A_{UT,i}^{\sin(\phi-\phi_S)\cos\phi}$. Such an observation is consistent with the study performed for the beam-spin and beam-charge asymmetries [Ell04]. It can also be seen in these figures that the $1\sigma_{exp}$ contours can be described by simple parameterizations, shown as the dashed lines in the plots. The slope of the parallel dashed lines, i.e., $-1/2.9$, is determined by minimizing the distance between them while they still enclose the $1\sigma_{exp}$ contour. This number describes the ratio of the sensitivities of the TTSA amplitude $A_{UT}^{\sin(\phi-\phi_S)\cos\phi}$ to the model parameters J_u^{VGG} and J_d^{VGG}. Its value is determined by the GPD model used, the theory for DVCS, and the HERMES kinematics. Taking the approximation in Eq. (3.41), and the parameterizations of the GPDs, one has

$$\frac{\partial A_{UT,i}^{\sin(\phi-\phi_S)\cos\phi}}{\partial J_u^{VGG}} : \frac{\partial A_{UT,i}^{\sin(\phi-\phi_S)\cos\phi}}{\partial J_d^{VGG}} \simeq \frac{e_u^2}{e_d^2} \cdot \frac{M_{d_{val}}^{(2)}}{M_{u_{val}}^{(2)}} \cdot \frac{u_{val}(\xi = x_B/(2-x_B))}{d_{val}(\xi = x_B/(2-x_B))} = 4 \cdot \frac{0.14}{0.34} \cdot 1.67 \approx 2.8, \tag{6.23}$$

which is consistent with the value given above.

Taking the mean value of the four sets of constraints shown in Fig. 6.4 or 6.5 as the final result, and assigning the maximum difference between the four sets of constraints

[1] A proof for the validity to use a 5th order polynomial function to describe the estimated $\chi^2_{exp}(J_u, J_d)$ values can be seen in Fig. 6.6.

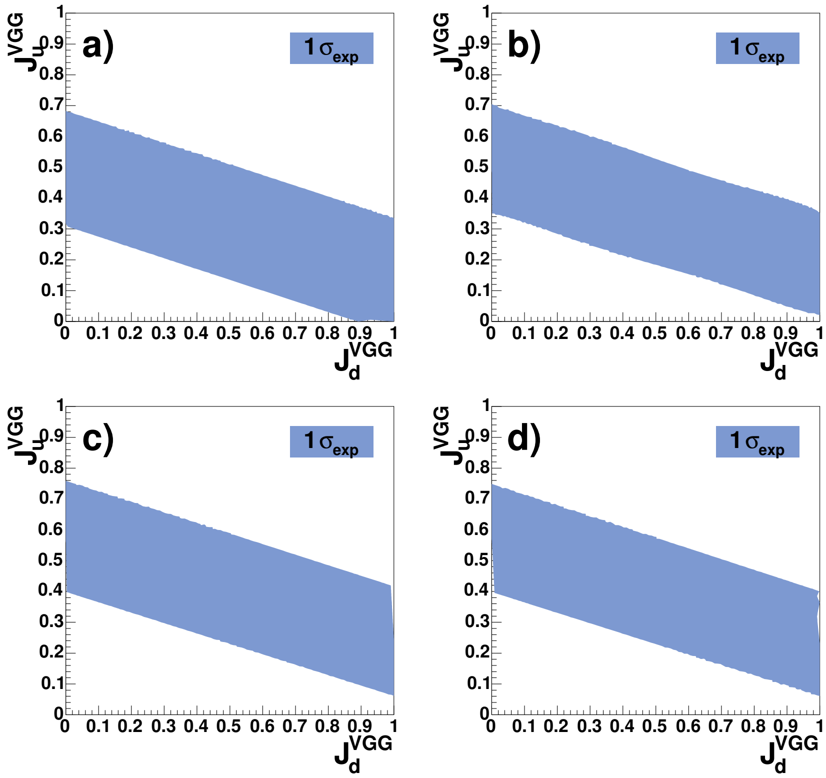

Figure 6.3: Constraints on J_u and J_d from $A_{UT}^{\sin(\phi-\phi_S)\cos\phi}$ extracted from the HERMES 2002-04 data using the ML method for (a) the overall data set, or data binned in one of the kinematic variables (b) t, (c) x_B or (d) Q^2 at a time, while integrating over the other two. The shaded areas correspond to one standard deviation of the total experimental uncertainty in determining $A_{UT}^{\sin(\phi-\phi_S)\cos\phi}$. Theoretical calculations are performed with $b_{val} = 1$, $b_{sea} = \infty$, and D-term$\neq$0.

and their mean value as the uncertainty due to the undetermined profile parameters, the model-dependent constraint on J_u and J_d is obtained as

$$J_u + J_d/2.9 = 0.42 \pm 0.21(exp) \pm 0.06(b_{v,s} \in [1, \infty]) \tag{6.24}$$

when the D-term is set to zero, or

$$J_u + J_d/2.9 = 0.53 \pm 0.21(exp) \pm 0.06(b_{v,s} \in [1, \infty]) \tag{6.25}$$

when the D-term is modeled according to the CQSM result.

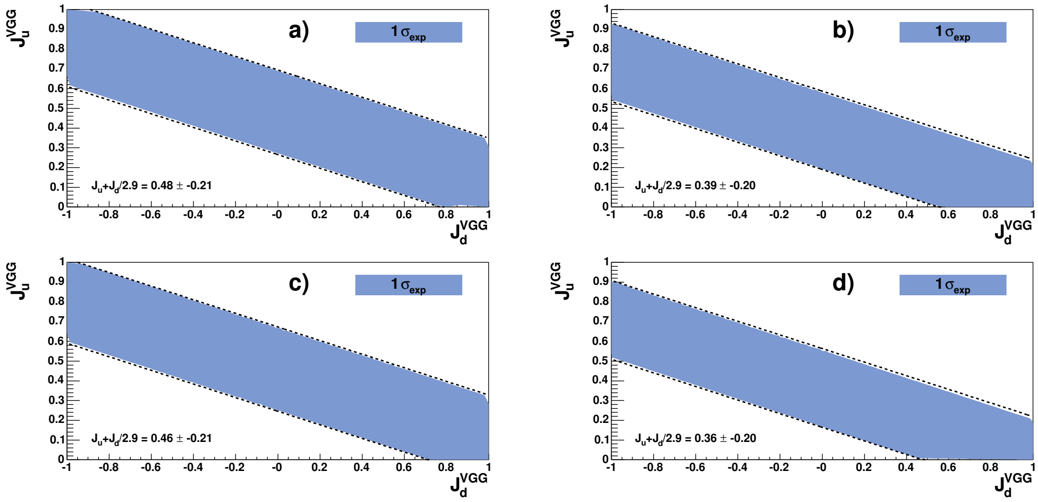

Figure 6.4: Constraints on J_u and J_d from $A_{UT}^{\sin(\phi-\phi_S)\cos\phi}$ extracted from the HERMES 2002-04 data using the ML method for the overall data set. Theoretical calculations are performed with D-term=0: (a) $b_{val} = 1$ and $b_{sea} = 1$; (b) $b_{val} = 1$ and $b_{sea} = \infty$; (c) $b_{val} = \infty$ and $b_{sea} = 1$; (d) $b_{val} = \infty$ and $b_{sea} = \infty$. The shaded areas correspond to one standard deviation of the total experimental uncertainty in determining $A_{UT}^{\sin(\phi-\phi_S)\cos\phi}$. The dashed lines are described by (a) $J_u + J_d/2.9 = 0.48 \pm 0.21$, (b) $J_u + J_d/2.9 = 0.39 \pm 0.20$, (c) $J_u + J_d/2.9 = 0.46 \pm 0.21$ and (d) $J_u + J_d/2.9 = 0.36 \pm 0.20$, respectively.

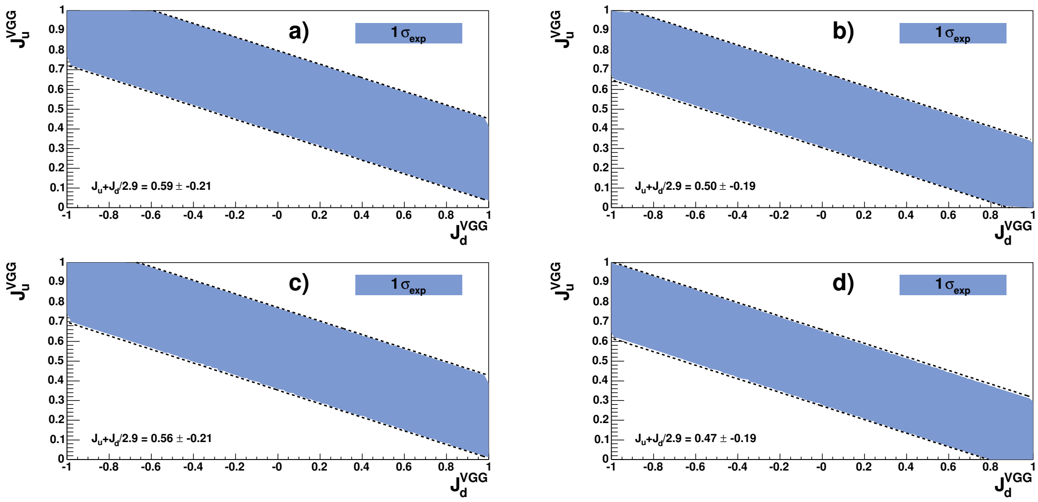

Figure 6.5: Same as Fig. 6.4 but calculated with the D-term modeled according to the chiral quark-soliton model result [Goe01]. The dashed lines are described by (a) $J_u + J_d/2.9 = 0.59 \pm 0.21$, (b) $J_u + J_d/2.9 = 0.50 \pm 0.19$, (c) $J_u + J_d/2.9 = 0.56 \pm 0.21$ and (d) $J_u + J_d/2.9 = 0.47 \pm 0.19$, respectively.

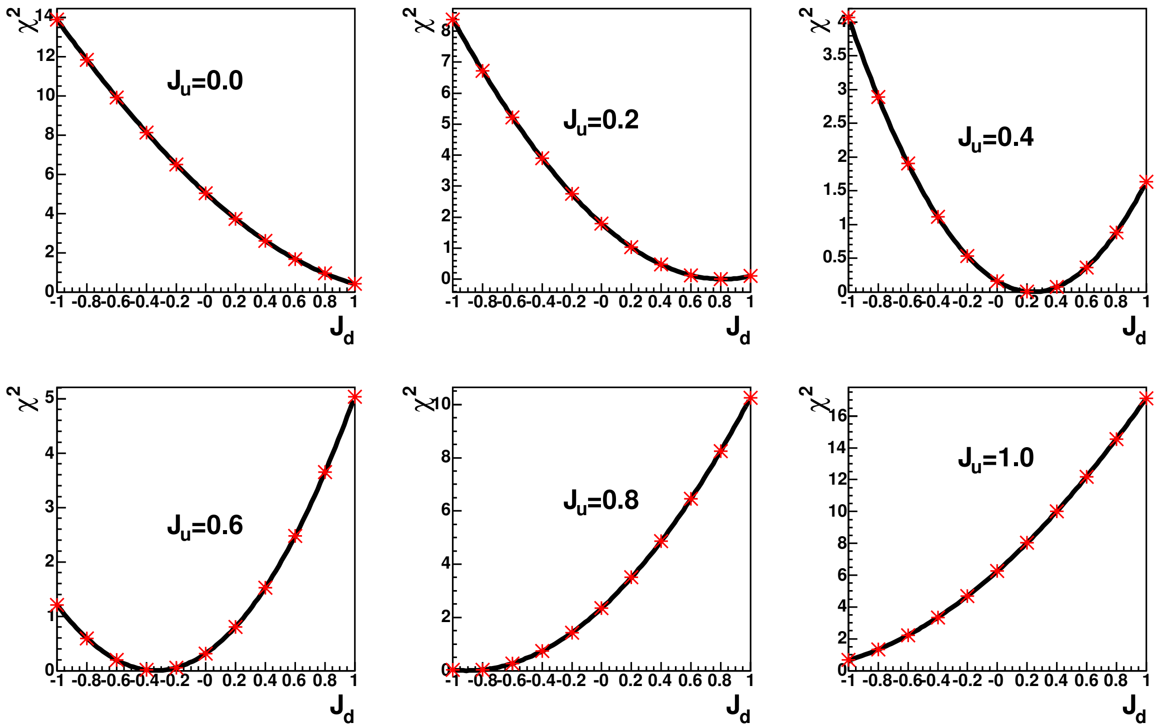

Figure 6.6: χ^2 slices in J_u for Fig. 6.4 panel a). The points are the $\chi^2_{exp}(J_u, J_d)$ values estimated by Eq. (6.22), while the lines are the fitted 5th order polynomial function evaluated at different J_u and J_d values. The difference between the points and the polynomial function is found to be less than 0.006.

6.2.3 Summary and Discussion

The area in the (J_u, J_d)-plane, in which the reduced χ^2 value is not larger than one, is defined as the one standard deviation constraint on J_u vs J_d. It is obtained to be $J_u + J_d/2.9 = 0.42 \pm 0.21 \pm 0.06$ (see Fig. 6.7). The first uncertainty is due to the experimental uncertainty in the measured TTSA amplitude. The second one is a model uncertainty, obtained by varying from one to infinity the unknown profile parameter b which controls the skewness dependence of GPDs [Goe01] (see Fig. 6.8). The t-dependence of GPDs is modelled using the Regge ansatz [Goe01]. The impact of using it or its alternative – the factorized ansatz – on the theoretical predictions on the TTSA amplitudes has been found to be negligible. The D-term contribution to the GPDs H and E is set to zero, as suggested by the HERMES results on the beam-charge asymmetry [Air06a]. If the D-term were modelled according to the chiral quark-soliton model [Goe01], the resulting constraint is shifted to $J_u + J_d/2.9 = 0.53 \pm 0.21 \pm 0.06$.

As the HERMES results on the TTSA amplitudes are not corrected for the associated BH/DVCS processes, they have to be interpreted as the ones describing both elastic and associated production simultaneously. On the other hand, theoretical predications from the VGG code [Van03] are only concerned about elastic production. This will introduce an uncertainty into the obtained constraints as described above. Attempts were made in Ref. [Gui03] to obtain a quantitative description of the associated production in measurements of beam-spin asymmetry. A modification factor $R_{BSA}(W_{max})$ is introduced [Gui03] which relates the observed asymmetry A_{LU}^{exp} up to the final state mass W_{max} to the asymmetry of the elastic production A_{LU} by $A_{LU} = R_{BSA} \cdot A_{LU}^{exp}$. For typical HERMES kinematics and a proton target the expected correction is in the order of 10% with the associated production as a small dilution. As such a study has not been performed for TTSA measurements, some knowledge is missing before a systematic uncertainty can be assigned to the present analysis.

Further theoretical uncertainties in the obtained model-dependent constraint on J_u and J_d include the intrinsic model dependence, the QED and QCD radiative corrections, and the power-suppressed corrections, i.e., target mass corrections and twist-4 contributions. While the one from the model dependence is difficult to estimate and little is known about the power-suppressed corrections, there are indications that the QED radiative corrections are very small [Afa06, Van00], and the QCD radiative corrections are moderate[2] [Bel00b].

[2] For example, calculations for the beam-spin asymmetry based on a different GPD model, performed for the HERMES kinematics, give the LO result to be -0.28, and the NLO one -0.23 [Fre03].

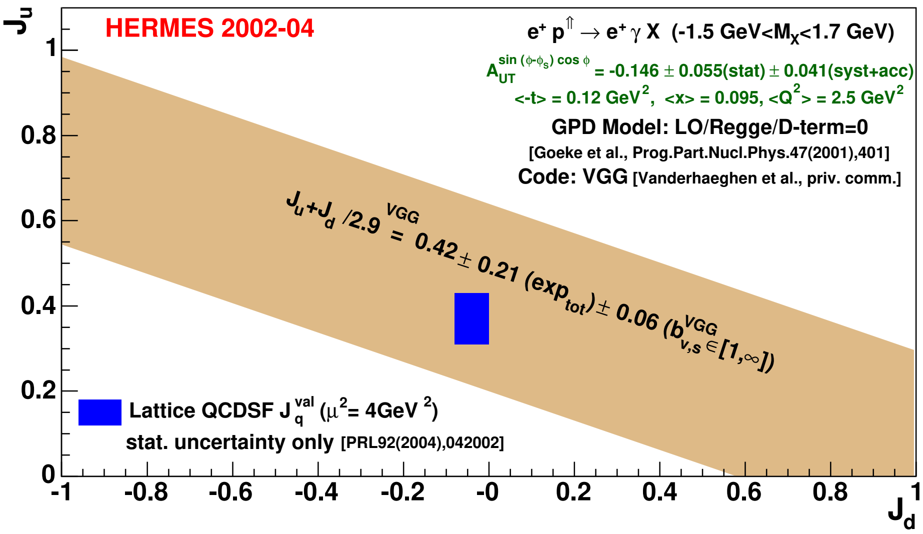

Figure 6.7: Model-dependent constraint on u-quark total angular momentum J_u vs d-quark total angular momentum J_d, obtained by comparing the experimental result and theoretical predictions on the TTSA amplitude $A_{UT}^{\sin(\phi-\phi_S)\cos\phi}$. Also shown is a Lattice result from the QCDSF collaboration, obtained at the scale $\mu^2 = 4$ GeV^2 for valence quark contributions only.

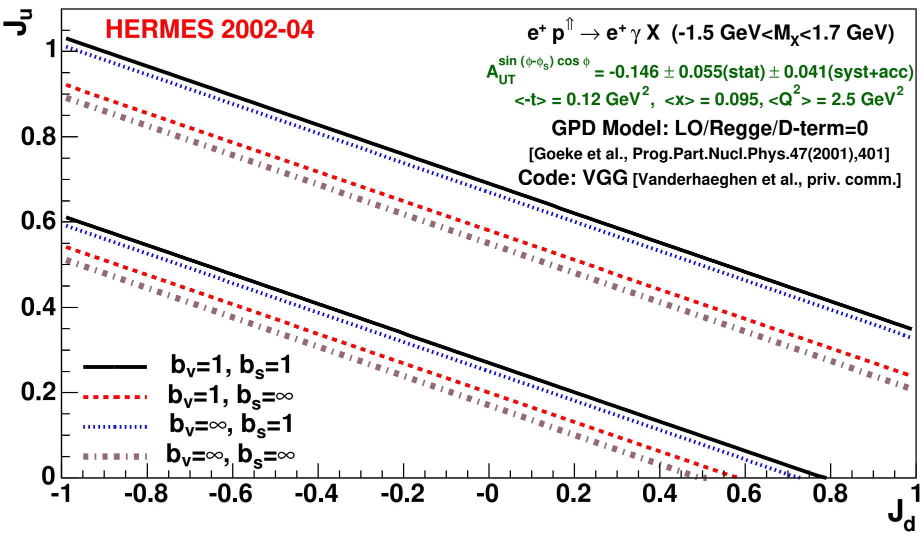

Figure 6.8: Model-dependent constraints on u-quark total angular momentum J_u vs d-quark total angular momentum J_d for different values of the profile parameter b.

Chapter 7

Summary and Outlook

The structure of the nucleon was first studied in elastic electron scattering experiments about half a century ago. These experiments showed persuasively that the proton was not point-like, but of finite spatial extension. In these and following studies, nucleon Form Factors (FFs) have been measured which contain information about the distributions of charge and magnetic moment in the nucleon. With increasing beam energies becoming available, the nucleon structure continues to be studied by exploring Deep-Inelastic Scattering (DIS) in fixed-target experiments and in *ep* collider experiments. Parton Distribution Functions (PDFs), which characterize the longitudinal momentum distributions of partons in the nucleon, have been measured to a great precision in these experiments. DIS experiments have played an essential role to identify the point-like constituents in the nucleon to be the spin-1/2 quarks, and to help understanding the physics of the strong interaction.

While measurements on nucleon FFs and PDFs are still going on, a new domain to study the nucleon structure has been opened recently. Generalized Parton Distributions (GPDs) are universal, non-perturbative quantities entering hard exclusive processes. They contain a wealth of information about the quark and gluon structure of the nucleon, generalizing from nucleon FFs and PDFs. The total angular momentum carried by quarks and gluons, and three-dimensional distributions of partons in the nucleon may be accessed through GPDs.

Non-perturbative model calculations and Lattice QCD can help in improving the knowledge about GPDs. On the other hand, GPDs can be studied experimentally in hard exclusive processes, among which Deeply Virtual Compton Scattering (DVCS) is the theoretically cleanest. It has been proved that, at large Q^2 and fixed x_B and $-t$, the leading twist amplitude of DVCS can be factorized into a partonic scattering amplitude calculable perturbatively, and a non-perturbative part parameterized in terms of GPDs. Higher-order corrections and higher-twist contributions in DVCS have been studied to a precision comparable to the one in DIS. Hard scattering amplitudes of the partonic subprocesses have been fully calculated to next-to-leading order (NLO) in α_S, and partial results at next-to-next-to-leading order (NNLO) also exist. Higher twist contributions have been calculated to LO and NLO.

Compared to the considerable progress on the theoretical side in studying GPDs, the progress on the experimental side is determined by the highly demanding requirements on luminosity and on the detector capabilities to measure exclusive processes. The HERMES experiment at the HERA storage ring at DESY studies the spin structure of the nucleon by scattering longitudinally polarized 27.6 GeV electrons/positrons on internal polarized gaseous hydrogen, deuterium, and helium-3 targets. DVCS studies have been carried out at HERMES by measuring the azimuthal asymmetries induced mainly from the interference of the DVCS and Bethe-Heitler (BH) processes. HERMES has provided one of the first two measurements on the Beam-Spin Asymmetry (BSA), and the first measurement on the Beam-Charge Asymmetry (BCA) associated with DVCS. The azimuthal asymmetries with respect to the longitudinal spin of the proton and deuteron have also been measured.

Based on the data taken in the years 2002-2005 with a transversely polarized hydrogen target, HERMES has been able to perform the first measurement on the transverse target-spin asymmetry (TTSA) associated with DVCS on the proton. It has been shown in this thesis that measurements of the TTSA provide the rare possibility to access the nucleon helicity-flip GPD E, and thus to the total angular momentum of quarks in the nucleon, J_q ($q = u, d, \ldots$), within certain GPD models. The data analysis to extract the two leading azimuthal TTSA amplitudes is described, which were based on the HERMES 2002-2004 data using positron beams. Results are presented and compared to theoretical predictions based on a phenomenological model of GPDs. A model-dependent constraint on the total angular momenta of u-quarks and d-quarks, J_u and J_d, is obtained which provides the first constraint on the total angular momentum of quarks in the nucleon.

The sensitivities of the TTSAs to GPDs and hence to J_u and J_d are different for different beam charges since there are both charge-dependent and charge-independent contributions to the TTSA: the former arises from the interference between the BH and DVCS processes and the latter from the DVCS process alone. The study at HERMES on the TTSA will be continued through the analysis of the 2005 data taken with an electron beam. It will be of interest to see if the new results will agree with the theoretical predictions, which are expected to be of similar size but of different sign compared to the ones presented here. Finally, it will be a non-trivial task to combine the two sets of results into one, then more precise constraint on J_u and J_d.

HERMES has dedicated its last data taking period, until middle of 2007, to the study of exclusive processes, in particular the DVCS process. A recoil detector, consisting of a silicon strip detector, a scintillating fibre detector, and a tungsten-scintillator detector, has been built and installed to detect the recoiling protons produced in exclusive processes. With the help of the recoil detector, it is expected that the semi-inclusive background will be largely suppressed, and so also the associated BH+DVCS processes in which the recoiling protons were excited to a resonance state. For the data taking period with the recoil detector, it has been decided to use unpolarized targets instead of polarized ones in order to increase the luminosity, and also by technical reasons. Here new results on BSAs and BCAs with improved statistics and fewer background contributions can be expected.

Measurements of DVCS were performed recently at Jefferson National Laboratory (JLab) using the 6 GeV longitudinally polarized electron beam with hydrogen and deuterium targets. It has been shown [Ava06] that the high luminosity of the experiments will allow a multi-dimensional "mapping" of the kinematic dependence of the beam-spin asymmetry and cross section differences. This eventually will facilitate a discrimination between certain (parameter sets of) GPD models.

Future studies on GPDs via DVCS are planned at several facilities. The collider experiments H1 and ZEUS at HERA have measured the DVCS cross sections at very small values of x_B. The newly installed spin rotators make the polarized beam also available to them. Together with several detector upgrades, the two experiments will be able to measure the azimuthal dependence of beam-spin and beam-charge asymmetries. The experiments at JLab and the COMPASS experiment at CERN have devoted a considerable part of their future physics programme to studies of GPDs. The 12 GeV upgrade of the Continuous Electron Beam Accelerator at JLab aims at accurate measurements of cross sections and single-spin asymmetries with respect to beam helicity and target spin [Car01]. The COMPASS experiment at the SPS muon beam is able to measure the DVCS cross sections at moderate values of x_B. The anticipated accuracy of a DVCS cross section measurement at $E_\mu = 190$ GeV amounts to a few percents [Bur03b]. As the SPS muon beam can be operated with both beam charges, the beam-charge asymmetry will also be measurable at COMPASS [Hos02].

Appendix A

Conventions

The metric tensor $g_{\mu\nu}$ is given as

$$g_{\mu\nu} = \begin{pmatrix} 1 & 0 & 0 & 0 \\ 0 & -1 & 0 & 0 \\ 0 & 0 & -1 & 0 \\ 0 & 0 & 0 & -1 \end{pmatrix}, \tag{A.1}$$

where μ and ν run over 0, 1, 2, 3. The scalar product of two four-vectors $x = (x^0, x^1, x^2, x^3)$ and $y = (y^0, y^1, y^2, y^3)$ reads

$$x \cdot y = g_{\mu\nu} x^\mu y^\nu, \tag{A.2}$$

where the Einstein summation convention is applied.

A.1 Light-Cone Coordinates

The definitions of GPDs in chapter 2 are given in light-cone coordinates

$$x^\pm = \frac{1}{\sqrt{2}} \left(x^0 \pm x^3 \right), \tag{A.3}$$

$$\vec{x}_T = \left(x^1, x^2 \right) \tag{A.4}$$

for any four-vector $x = (x^0, x^1, x^2, x^3)$, whose $\pm$ components are along the light-cone. The scalar product of two four-vectors x and y reads

$$x \cdot y = x^+ y^- + x^- y^+ - \vec{x}_T \cdot \vec{y}_T. \tag{A.5}$$

A.2 Dirac Matrices

The Dirac matrices γ^μ (μ =0, 1, 2, 3) are defined by means of the Pauli matrices σ^i (i=1, 2, 3):

$$\gamma^0 = \begin{pmatrix} 0 & I \\ I & 0 \end{pmatrix}, \qquad \gamma^i = \begin{pmatrix} 0 & \sigma^i \\ \sigma^i & 0 \end{pmatrix}, \tag{A.6}$$

where I is the 2×2 unit matrix. The Dirac matrix γ^5 is defined as

$$\gamma^5 = i\gamma^0\gamma^1\gamma^2\gamma^3. \tag{A.7}$$

The Dirac matrices γ^μ can be expressed in the light-cone coordinates with

$$\gamma^\pm = \left(\gamma^0 \pm \gamma^3\right)/\sqrt{2}. \tag{A.8}$$

The antisymmetric matrix $\sigma^{\mu\nu} = \frac{i}{2}\left[\gamma^\mu, \gamma^\nu\right]$ has the property

$$\gamma^5\sigma^{\mu\nu} = \frac{i}{2}\epsilon^{\mu\nu\rho\sigma}\sigma_{\rho\sigma}, \tag{A.9}$$

where $\epsilon^{\mu\nu\rho\sigma}$ is the totally antisymmetric tensor with $\epsilon_{0123} = 1$.

Appendix B

VGG Code

B.1 Description of the Code

A code [Van03] was designed to calculate observables in the exclusive reaction $ep \to ep\gamma$ to LO precision in perturbative theory. It is based on the GPD model proposed in [Goe01]. The coordinate system and angles defined in the code are the same as depicted in Fig. 3.2. The polarization of the target in the code is defined according to the virtual photon direction. The code can be used to calculate one of the following items:

- 5-fold DIFFERENTIAL CROSS SECTION for $ep \to ep\gamma$ as function of t;
- e^+e^- asymmetry for DVCS;
- electron single spin asymmetry (SSA);
- doubly polarized cross sections for DVCS – polarized electron and target;
- differential cross section for DVCS as function of Q^2;
- differential cross section for DVCS as function of t;
- parton distributions;
- GPDs;
- sum rules;
- form factors from GPDs and WACS;
- accuracy test of integrals for twist-2 amplitude;
- accuracy test of integrals for twist-3 amplitude.

The double polarization cross cross sections are selected to calculate the Transverse Target-Spin Asymmetry (TTSA) in this study. In the following, the technical details of the inputs and outputs of the code used in the present study are described.

B.1.1 Inputs

- MECHANISM: DVCS+BH;
- TARGET: Proton;
- GPD MODEL: ξ dependent parametrization with MRST98 distribution;
- PARTON DISTRIBUTION EVOLUTION: Evolution with Q^2;
- PROFILE FUNCTION OF VALENCE and SEA QUARKs: b_{val}, b_{sea};
- GPD H MODEL: Factorized/Regge ansatz;
- D-TERM in H: Yes/No;
- GPD E MODEL: Double Distribution+D-term;
- DOUBLE DISTRIBUTION of GPD E: Valence quark + Vector meson contributions;
- J_u: between -1 and 1;
- J_d: between 0 and 1;
- if π POLE for GPD $\widetilde{\mathrm{E}}$: Yes;
- TWIST-3 CORRECTION: Yes for Longitudinal photon in WW approximation;
- PROTON POLARIZATION: x/y;
- LEPTON: e^+;
- BEAM ENERGY: 27.57 GeV;
- FIXED OUT-OF-PLANE ANGLE or ϕ-SCAN: Scan in ϕ at fixed t;
- Q^2, x_B, $-t$: as listed in Tab. B.1 or in Tab. 6.3;
- ϕ: 0°, 10°, . . . , 180°.

Q^2 bin (GeV^2)	1.00-1.50	1.50-2.30	2.30-3.50	3.50-6.00	6.00-10.0
$\langle Q^2 \rangle$ (GeV^2)	1.2	1.8	2.8	4.4	7.1
$\langle x_B \rangle$	0.06	0.08	0.10	0.15	0.24
$\langle -t \rangle$ (GeV^2)	0.07	0.09	0.12	0.17	0.24
$stat.\ \delta A_{LU}^{\sin\phi}$	0.053	0.050	0.061	0.070	0.163
x_B bin	0.03-0.07	0.07-0.10	0.10-0.15	0.15-0.20	0.20-0.35
$\langle Q^2 \rangle$ (GeV^2)	1.4	2.2	3.1	4.5	6.1
$\langle x_B \rangle$	0.05	0.08	0.12	0.17	0.24
$\langle -t \rangle$ (GeV^2)	0.08	0.10	0.12	0.17	0.22
$stat.\ \delta A_{LU}^{\sin\phi}$	0.048	0.053	0.060	0.099	0.145
$-t$ bin (GeV^2)	0.00-0.06	0.06-0.14	0.14-0.30	0.30-0.50	0.50-0.70
$\langle Q^2 \rangle$ (GeV^2)	2.0	2.5	3.0	3.6	3.9
$\langle x_B \rangle$	0.08	0.10	0.11	0.12	0.12
$\langle -t \rangle$ (GeV^2)	0.03	0.09	0.20	0.37	0.57
$stat.\ \delta A_{LU}^{\sin\phi}$	0.041	0.052	0.066	0.126	0.263

Table B.1: Average kinematic values for Q^2, x_B, $-t$ bins and statistical errors, taken from a measurement of the beam-spin asymmetry at HERMES [Ell04].

B.1.2 Outputs

The output of the code is a table of differential cross-sections scanning over ϕ as in the Tab. B.2. We know that $\frac{1}{2}(\sigma_{e\uparrow p\uparrow} + d\sigma_{e\downarrow p\uparrow})$ gives the differential cross-section of unpolarized beam on a target polarized parallel to the selected direction, while $\frac{1}{2}(\sigma_{e\uparrow p\downarrow} + d\sigma_{e\downarrow p\downarrow})$ gives the differential cross-section of unpolarized beam on a target polarized anti-parallel to the selected direction. So the calculation done with target polarized in x direction gives the cross-section at $\phi_S = 0$ or π. The calculation done with target polarized in y direction gives the cross-section at $\phi_S = \pi/2$ or $3\pi/2$.

ϕ	$d\sigma_{e\uparrow p\uparrow}$	$d\sigma_{e\uparrow p\downarrow}$	$d\sigma_{e\downarrow p\uparrow}$	$d\sigma_{e\downarrow p\downarrow}$	$\bar{d\sigma}$
0°	...	...	...	...	...
10°	...	...	...	...	...
...	...	...	...	...	...
180°	...	...	...	...	...

Table B.2: Output of the VGG.

B.2 TTSA Calculation

For a transversely polarized target, the target polarization direction can be chosen either in the lepton plane (x direction) or perpendicular to it (y direction). The former corresponds to $\phi_S = 0$ or π, the latter to $\phi_S = \pi/2$ or $3\pi/2$. Therefore the following intermediate asymmetries can be calculated:

$$\begin{aligned} A_x(\phi) &= \frac{d\sigma_{\phi_S=0}(\phi) - d\sigma_{\phi_S=\pi}(\phi)}{d\sigma_{\phi_S=0}(\phi) + d\sigma_{\phi_S=\pi}(\phi)}, \\ A_y(\phi) &= \frac{d\sigma_{\phi_S=\frac{\pi}{2}}(\phi) - d\sigma_{\phi_S=\frac{3\pi}{2}}(\phi)}{d\sigma_{\phi_S=\frac{\pi}{2}}(\phi) + d\sigma_{\phi_S=\frac{3\pi}{2}}(\phi)}. \end{aligned} \tag{B.1}$$

Defining the following functions

$$\begin{aligned} A_1(\phi) &= A_x \cdot \sin\phi - A_y \cdot \cos\phi, \qquad \text{(B.2)} \\ A_2(\phi) &= A_x \cdot \cos\phi + A_y \cdot \sin\phi, \end{aligned}$$

the contribution of the transverse target polarization component of the interference term $\mathcal{I}_{TP}$ to the total cross section in Eq. (3.38) can be expressed as:

$$d\sigma_{TP} = d\sigma_{unp}\Big[A_1(\phi) \cdot \sin(\phi - \phi_S) + A_2(\phi) \cdot \cos(\phi - \phi_S)\Big]. \tag{B.3}$$

Therefore the asymmetry amplitudes defined in Eqs. (3.41) and (3.42) can be computed as:

$$\begin{aligned} A_{UT}^{\sin(\phi-\phi_S)\cos\phi} &= A_1^{\cos\phi}, \\ A_{UT}^{\cos(\phi-\phi_S)\sin\phi} &= A_2^{\sin\phi}. \end{aligned} \tag{B.4}$$

List of Tables

2.1 Normalization of nucleon form factors, with κ being the anomalous magnetic moment of the nucleon, g_A the nucleon axial charge, and $m_{p,n}$ (m_π) the nucleon (pion) mass. 10

5.1 The average beam polarization weighted by luminosity $\langle P_B \rangle$, the integrated luminosities $\mathbb{L}$, and the number of candidates for BH/DVCS events before and after balancing the beam polarization. 53
5.2 Misalignment of the spectrometer in the years 2002-2004 [Brü03]. 82
5.3 Beam slopes and offsets in the years 2002-2004. 82
5.4 Relative contributions of different processes to the exclusive region $-2.25 < M_{\mathrm{X}}^2 < 2.89$ GeV^2. The errors represent the quadratic sum of the statistical and systematic uncertainties. 95

6.1 Systematic uncertainties of the extracted TTSA amplitude $\mathrm{A}_{\mathrm{UT}}^{\sin(\phi-\phi_{\mathrm{S}})\cos\phi}$ due to the uncertainty in determining the target polarization (δ_{tpl}), due to the fit function (δ_{fit}), due to the misalignment effect ($\delta_{misalign.}$), due to the calorimeter miscalibration ($\delta_{cali.}$), due to the smearing effect ($\delta_{smear.}$), due to background contributions ($\delta_{bkd.}$), and due to the acceptance effect when interpreting the results as the ones at the average HERMES kinematics ($\delta_{acc.}$). 105
6.2 Same as Tab. 6.1 but for the TTSA amplitude $\mathrm{A}_{\mathrm{UT}}^{\cos(\phi-\phi_{\mathrm{S}})\sin\phi}$. 105
6.3 The final results on the TTSA amplitudes, obtained from the HERMES 2002-04 data. Acceptance effects are not included in the systematic uncertainties. 106

B.1 Average kinematic values for Q^2, x_B, $-t$ bins and statistical errors, taken from a measurement of the beam-spin asymmetry at HERMES [Ell04]. . 125
B.2 Output of the VGG. 125

List of Figures

2.1 Diagram illustrating the definition of the generalized parton distributions. 6

2.2 Figure taken from Ref. [Pet98]: the flavor-singlet GPD $H^{u+d}(x, \xi, \Delta_T^2)$ for $\Delta_T^2 = 0$ ($\Delta_T^2 \equiv -\Delta^2 - \xi^2 m_N^2$) and $\xi = 0.15$ (the ξ in the figure as defined in Ref. [Pet98] is two times of the ξ used here). *Dashed line*: contribution from the discrete level. *Dashed-dotted line*: contribution from the Dirac continuum. *Solid line*: the total distribution (sum of the dashed and dashed-dotted curves). The vertical lines mark the crossover points $x = \pm\xi$. 13

2.3 Figure taken from Ref. [Goe01]: The GPD $E^{u-d}(x, \xi = 0, t = 0) = e^u(x) - e^d(x)$ as a function of x. Dashed curve: contribution from valence level. Solid curve: contribution of the Dirac continuum. 15

3.1 (a) Diagram for deeply virtual Compton scattering, the blob connecting the incoming and outgoing nucleons as described by GPDs; (b) diagram for the Bethe-Heithler process, the blob connecting the incoming and outgoing nucleons as described by nucleon FFs. 18

3.2 Kinematics of real photon production in the target rest frame. The z-direction is chosen along the three-momentum of the virtual photon. . . . 20

3.3 Beam-charge asymmetry A_C on the proton measured at HERMES [Air06a]. The $A_C^{\cos\phi}$ amplitude as a function of $-t$, after background correction. The error bars (band) represent(s) the statistical (systematic) uncertainties. The calculations based on GPD models [Van99, Goe01] use either a factorized t-dependence with (dashed-dotted) or without (dotted) the D-term contribution, or a Regge inspired t-dependence with (dashed) or without (solid) the D-term contribution. 23

3.4 Beam-spin asymmetry A_{LU} on the proton measured at HERMES (left panel) [Air01] and CLAS (right panel) [Ste01]. Left: the dashed curve represents a $\sin\phi$ dependence with an amplitude of 0.23, while the solid curve represents the result of a model calculation at twist-three level from Ref. [Kiv01]. The error band below shows the systematic uncertainty. Right: the shaded regions represent the experimental results, while the curves represent model calculations from Refs. [Van99, Goe01]. The dashed (dotted) curve is a calculation with ξ-independent (ξ-dependent) GPDs at leading-twist. The solid curve includes twist-three effects. . . . 25

3.5 Longitudinal target-spin asymmetry A_{UL} on the proton and deuteron measured at HERMES [Kop05]. The $A_{UL}^{\sin\phi}$ amplitude is shown as a function of $-t$, after background correction. Error bars and bands represent the statistical and systematic uncertainties, respectively. The curves shown are calculations based on GPD models [Goe01] for the proton, using either a factorized or a Regge inspired t-dependence with or without twist-three effects in the Wandzura-Wilczek (WW) approximation [Goe01]. 25

3.6 DVCS cross section measured at H1 and ZEUS [Akt05, Che03]. Also shown are NLO QCD calculations (bands) using a parameterization of the GPDs proposed in Ref. [Fre03]. 28

3.7 Theoretical predictions on the TTSA amplitudes $A_{UT}^{\sin(\phi-\phi_S)\cos\phi}$ and $A_{UT}^{\cos(\phi-\phi_S)\sin\phi}$ in the Regge ansatz for $b_{val} = 1$, $b_{sea} = \infty$, $J_u^{VGG} = 0.4\,(0.2, 0)$, $J_d^{VGG} = 0$. $E = 0$ denotes zero effective contribution from the quark GPDs E_q. The D-term is modeled according to the chiral quark-soliton model result [Goe01]. The predictions are made at the values of the kinematic variables given in Tab. B.1. See App. B for further details. 29

3.8 Same as Fig. 3.7 but for $b_{val} = 1$, $b_{sea} = 1$. 30

4.1 Schematic diagram of the HERA storage ring layout as of the year 2000, with the location of the four experiments. Also shown are the locations of the spin rotators and the two polarimeters. 32

4.2 Beam polarization values measured by the transverse and longitudinal polarimeters. It is difficult to distinguish between the results of the two polarimeters as they overlap on each other. Such a fact proves the good performance of the polarization measurements. 34

4.3 Schematic view of the HERMES longitudinally polarized target. From left to right: Atomic Beam Source (ABS), target chamber with cell and magnet, and diagnostic system composed by Target Gas Analyzer (TGA) and Breit-Rabi Polarimeter (BRP). 35

4.4 The profile of the target density from Monte Carlo. 36

4.5 Side view of HERMES spectrometer configuration in the years 2001-2005. 37

4.6 Schematic view of the calorimeter and the pre-shower detector. 41

4.7 Schematic view of the luminosity detector. 44

5.1 The distributions of the reconstructed z_{vtx} position and transverse position r^T_{vtx} of the BH/DVCS event sample selected from the 2002-2004 data. The z_{vtx} positions have been corrected for the influence of the transverse target magnet (section 5.6.1). 50

5.2 The distribution of the missing mass squared M^2_{X} of the BH/DVCS event sample selected from the 2002-2004 data (solid circles). The same distribution but requiring $E_\gamma > 1$ GeV instead of $E_\gamma > 5$ GeV is also shown (open boxes). 52

5.3 Kinematic $x_B - Q^2$, $x_B - t_c$, and $Q^2 - t_c$ planes covered by the selected BH/DVCS event sample from the 2002-2004 data. 54

5.4 The total cross section σ_{tot} for exclusive production of π^+ as a function of x_B and Q^2. Two different model predictions are also shown. 56

5.5 Comparison between the absolutely normalized M^2_{X} distributions from the MC simulation (solid line) and from the experimental data (points). The BH/DVCS processes are either simulated for the BH process only (panel A), or for both the BH and DVCS processes (panels a−e) based on GPD models 1-5 in section 5.3.1. Also shown are individual contributions from elastic BH/DVCS processes (dashed line), associated BH processes (shaded area), and semi-inclusive processes (dotted line). 58

5.6 Contributions from the individual elastic BH/DVCS processes: solid line – pure BH, dashed line – pure DVCS, shaded area – BH-DVCS interference of positive values, dotted line – BH-DVCS interference of negative values. See Fig. 5.5 for more information. 58

5.7 Same as Fig. 5.5 but the reconstructed photon energies in the MC simulation are decreased by 1%. 59

5.8 Comparison between the the MC simulation (solid lines) and the experimental data (points) in the exclusive region $-2.25 < M^2_{\mathrm{X}} < 2.89$ GeV^2. The MC simulation is performed without including the DVCS process, corresponding to panel (A) in Fig. 5.7. The BH events are reweighted so that the total exclusive yield of the MC simulation equals the experimental one. Also shown are individual contributions from associated BH processes (shaded area), and semi-inclusive processes (dotted line). 60

5.9 Same as Fig. 5.8 but the DVCS process is simulated using GPD model 2 in section 5.3.1, corresponding to panel (b) in Fig. 5.7. 61

5.10 Correlations between the reconstructed (x axis) and generated (y axis) kinematic variables. The transverse target magnet was switched off in the simulation. The results are for the elastic BH events passing through all the cuts 62

5.11 The average differences between the reconstructed and generated kinematic variables given as a function of the reconstructed kinematic variable. The transverse target magnet was either switched off (solid points) or switched on (open points) in the simulation. In the latter case, no correction was applied to track reconstruction. The error bars stand for statistical uncertainties. 63

5.12 The standard deviations of the differences between the reconstructed and generated kinematic variables given as a function of the reconstructed kinematic variable. See Fig. 5.11 for more information. 63

5.13 The TTSA amplitudes extracted from gmc_dvcs MC data sets by using the method of least squares with 8×8 bins in ϕ and $\phi - \phi_S$. The input TTSA amplitudes $A_{UT}^{\sin(\phi-\phi_S)\cos\phi}$ and $A_{UT}^{\cos(\phi-\phi_S)\sin\phi}$ equal to -0.5 and 0 (0 and -0.5), respectively, for the results shown in the top (bottom) panels. 71

5.14 Same as Fig. 5.13 but obtained with 20×20 bins in ϕ and $\phi - \phi_S$. 71

5.15 Extracted TTSA amplitudes given as a function of $\theta_{\gamma*\gamma}$. The input TTSA amplitudes $A_{UT}^{\sin(\phi-\phi_S)\cos\phi}$ and $A_{UT}^{\cos(\phi-\phi_S)\sin\phi}$ equal to -0.5 and 0 (0 and -0.5), respectively, for the results shown in the left (right) panel. The vertical dashed line indicates the position $\theta_{\gamma*\gamma} = 5$ mrad. 72

5.16 Same as Fig. 5.13 but obtained using the method of maximum likelihood. 73

5.17 The extracted $A_{UT}^{\sin(\phi-\phi_S)\cos\phi}$ and $A_{UT}^{\cos(\phi-\phi_S)\sin\phi}$ amplitudes from gmc_dvcs MC data samples with different input TTSA amplitudes, obtained using the method of maximum likelihood (see Fig. 5.16). The solid lines correspond to a linear fit to the data points. Text at the upper right corner of a panel, e.g., Tc1, denotes for which kinematic bin the results are presented for. 73

5.18 Smearing coefficients obtained using the method of least squares with 8×8 bins in ϕ and ϕ_S. See text for explanation. 74

5.19 Smearing coefficients obtained using the method of least squares with 20×20 bins in ϕ and ϕ_S. See text for explanation. 74

5.20 Smearing coefficients obtained using the method of maximum likelihood. See text for explanation. 74

5.21 Distributions of the extracted TTSA amplitudes (A) and the estimated statistical errors (δA) from 1000 MC data sets with $A_{UT,gen}^{\sin(\phi-\phi_S)\cos\phi} = -0.5$ and $A_{UT,gen}^{\cos(\phi-\phi_S)\sin\phi} = 0$, obtained using the method of least squares with 8×8 bins in ϕ and ϕ_S. The results are shown for the 4th t-bin. 76

5.22 Same as Fig. 5.21 but obtained using the method of maximum likelihood. 76

5.23 Profile plots for the mean and the RMS values of the extracted TTSA amplitudes from 1000 MC data sets (see Fig. 5.21 and Fig. 5.22). Solid points are for the method of least squares with 8×8 bins in ϕ and ϕ_S, and open points are for the method of maximum likelihood. The input TTSA amplitudes $A_{UT}^{\sin(\phi-\phi_S)\cos\phi}$ and $A_{UT}^{\cos(\phi-\phi_S)\sin\phi}$ equal to -0.5 and 0 (0 and -0.5), respectively, for the results shown in the top (bottom) panels. . 77
5.24 TTSA amplitudes extracted using different fit functions. 79
5.25 TTSA amplitudes extracted from the HERMES 2002-2004 data using the ML method. The results obtained by two independent analysis codes are shown. 79
5.26 Same as Fig. 5.11 but either the TMC1 or the TMC2 correction method was used when the transverse target magnet was switched on. 81
5.27 Same as Fig. 5.12 but either the TMC1 or the TMC2 correction method was used when the transverse target magnet was switched on. 81
5.28 Sketch of misalignment of the spectrometer and the beam: (a) the spectrometer and the beam in their ideal places; (b) misalignment of the spectrometer; (c) misalignment of the beam. 82
5.29 Beam slopes and offsets in the years 2002-2004. 83
5.30 The TTSA amplitudes extracted from polarized gmc_dvcs MC data samples, based on GPD model 5 in section 5.3.1. Solid points: the spectrometer and beam are not misaligned; open points: the spectrometer and beam are misaligned. 84
5.31 The TTSA amplitudes extracted from the 2002-2004 data. Solid points: misalignment of spectrometer and beam is not corrected for; open points: misalignment of the spectrometer and beam is corrected for. 84
5.32 Ratio of the energy E measured by the calorimeter to the reconstructed momentum P of DIS leptons in 2002 (left), 2003 (center), and 2004 (right). Also shown are the fitted results (solid line) using the function (5.24). 86
5.33 The TTSA amplitudes extracted from polarized gmc_dvcs MC data samples, based on GPD model 5 in section 5.3.1. Solid points: photon energy not scaled; open points: photon energy scaled by 0.99. 87
5.34 The TTSA amplitudes extracted from the 2002-2004 data. Solid points: photon energy not scaled; open points: photon energy scaled by 0.99. . . 87
5.35 H0 efficiency (in color) in 2002 (left), 2003 (center) and 2004 (right). . . . 89
5.36 Extracted TTSA amplitudes with/without correction for H0 inefficiency. 90
5.37 The yield of elastic BH+DVCS events in the range of $-t > 0.7$ GeV^2, $0.03 < x_B < 0.35$, $1 < Q^2 < 10$ GeV^2 from an unpolarized gmc_dvcs MC data sample, based on GPD model 5 in section 5.3.1. Solid curve: yield in 4π, points: yield in the HERMES acceptance. 92

5.38 The yield in 4π of elastic BH+DVCS events in the range of $-t > 0.7$ GeV^2, $0.03 < x_B < 0.35$, $1 < Q^2 < 10$ GeV^2 from an unpolarized gmc_dvcs MC data sample, based on GPD model 5 in section 5.3.1. Solid curve: the total BH+DVCS contribution, dashed curve: pure DVCS contribution, shaded area (dotted curve): positive (negative) contribution from the BH-DVCS interference. 92

5.39 Same as Fig. 5.38 but in the HERMES acceptance. 92

5.40 The $A_{UT}^{\sin(\phi-\phi_S)\cos\phi}$ and $A_{UT}^{\cos(\phi-\phi_S)\sin\phi}$ amplitudes extracted from a polarized gmc_dvcs MC data sample, based on GPD model 5 in section 5.3.1. Solid points: both the smearing effect and the acceptance effect are included in the simulation; open points: only the acceptance effect is simulated. 93

5.41 The $A_{UT}^{\sin(\phi-\phi_S)\cos\phi}$ and $A_{UT}^{\cos(\phi-\phi_S)\sin\phi}$ amplitudes extracted from a polarized gmc_dvcs MC data sample, based on GPD model 5 in section 5.3.1. Solid points: both the smearing effect and the acceptance effect are included in the simulation, but the smearing effect is corrected using smearing coefficients shown in Fig. 5.16; open points: only the acceptance effect is simulated. The solid curves represent the theoretical predictions at the average HERMES kinematics of the solid points, connected in between simply with straight lines. 93

5.42 Relative contributions from the elastic BH/DVCS processes (solid circles) and from background processes (open boxes) – associated BH+semi-inclusive DIS+exclusive π^0 production – given as a function of M_X^2. The shaded area defines the exclusive region $-2.25 < M_X^2 < 2.89$ GeV^2. The MC simulation does not include the DVCS process. The vertical error bars represent statistical uncertainties only. 96

5.43 Background contributions to the exclusive region $-2.25 < M_X^2 < 2.89$ GeV^2 from associated BH processes (solid circles), and semi-inclusive DIS processes (solid triangles). The vertical error bars represent the quadratic sum of statistical and systematic uncertainties. Background contributions estimated with the photon energy scaled by 0.99 are also shown as open points. 96

5.44 The average value of z for the semi-inclusive π^0 background in the exclusive region $-2.25 < M_X^2 < 2.89$ GeV^2. The vertical error bars represent the standard deviations of the z^{π^0} distributions. 96

5.45 Reconstructed asymmetry of decay photon(s) given as a function of the generated π^0 asymmetry. Also shown are the results of a linear fit to the data points. 98

5.46 The invariant mass distributions from the two-photon analysis (see text): (a) all the events; (b) events satisfying all the selection cuts described in section 5.2; (c) events satisfying the cut z_{π^0} >0.8 and all the other cuts described in section 5.2 except the cut $-2.25 < M_X^2 < 2.89$ GeV^2. Also shown in panel (a) is the result of a 'Gaussian+Constant' fit. 98

5.47 Extracted TTSA amplitudes of the semi-inclusive π^0 background from the HERMES 2002-2004 data. The error bars represent statistical uncertainties only. 100

5.48 TTSA amplitudes from the HERMES 2002-2004 data corrected for the semi-inclusive π^0 background. The error bars represent statistical uncertainties only. 100

6.1 HERMES results on the TTSA amplitudes in Tab. 6.3 compared with theoretical predictions based on the GPD model proposed in Ref. [Goe01]. The D-term is modeled according to the chiral quark-soliton model result [Goe01]. See text for further details. 106

6.2 t-independent part of quark and gluon GPDs at Q^2=4 GeV^2, ξ=0.1 (MRST98 PDFs are used). 111

6.3 Constraints on J_u and J_d from $A_{UT}^{\sin(\phi-\phi_S)\cos\phi}$ extracted from the HERMES 2002-04 data using the ML method for (a) the overall data set, or data binned in one of the kinematic variables (b) t, (c) x_B or (d) Q^2 at a time, while integrating over the other two. The shaded areas correspond to one standard deviation of the total experimental uncertainty in determining $A_{UT}^{\sin(\phi-\phi_S)\cos\phi}$. Theoretical calculations are performed with $b_{val} = 1$, $b_{sea} = \infty$, and D-term$\neq$0. 113

6.4 Constraints on J_u and J_d from $A_{UT}^{\sin(\phi-\phi_S)\cos\phi}$ extracted from the HERMES 2002-04 data using the ML method for the overall data set. Theoretical calculations are performed with D-term=0: (a) $b_{val} = 1$ and $b_{sea} = 1$; (b) $b_{val} = 1$ and $b_{sea} = \infty$; (c) $b_{val} = \infty$ and $b_{sea} = 1$; (d) $b_{val} = \infty$ and $b_{sea} = \infty$. The shaded areas correspond to one standard deviation of the total experimental uncertainty in determining $A_{UT}^{\sin(\phi-\phi_S)\cos\phi}$. The dashed lines are described by (a) $J_u + J_d/2.9 = 0.48 \pm 0.21$, (b) $J_u + J_d/2.9 = 0.39 \pm 0.20$, (c) $J_u + J_d/2.9 = 0.46 \pm 0.21$ and (d) $J_u + J_d/2.9 = 0.36 \pm 0.20$, respectively. 114

6.5 Same as Fig. 6.4 but calculated with the D-term modeled according to the chiral quark-soliton model result [Goe01]. The dashed lines are described by (a) $J_u + J_d/2.9 = 0.59 \pm 0.21$, (b) $J_u + J_d/2.9 = 0.50 \pm 0.19$, (c) $J_u + J_d/2.9 = 0.56 \pm 0.21$ and (d) $J_u + J_d/2.9 = 0.47 \pm 0.19$, respectively. 114

6.6 χ^2 slices in J_u for Fig. 6.4 panel a). The points are the $\chi^2_{exp}(J_u, J_d)$ values estimated by Eq. (6.22), while the lines are the fitted 5th order polynomial function evaluated at different J_u and J_d values. The difference between the points and the polynomial function is found to be less than 0.006. . . 115
6.7 Model-dependent constraint on u-quark total angular momentum J_u vs d-quark total angular momentum J_d, obtained by comparing the experimental result and theoretical predictions on the TTSA amplitude $A_{UT}^{\sin(\phi-\phi_S)\cos\phi}$. Also shown is a Lattice result from the QCDSF collaboration, obtained at the scale $\mu^2 = 4$ GeV^2 for valence quark contributions only. 117
6.8 Model-dependent constraints on u-quark total angular momentum J_u vs d-quark total angular momentum J_d for different values of the profile parameter b. 117

Bibliography

[Ack98] K. Ackerstaff *et al.* (the HERMES collaboration), *Nucl. Instr. and Meth. A* **417** (1998) 230, hep-ex/9806008.

[Ack98a] K. Ackerstaff *et al.* (the HERMES collaboration), *Phys. Rev. Lett.* **81** (1998) 5519, hep-ex/9807013.

[Adl01] C. Adloff *et al.* (the H1 collaboration), *Phys. Lett. B* **517** (2001) 47, hep-ex/0107005.

[Afa06] A.V. Afanasev, M. I. Konchatnij, N. P. Merenkov, *J. Exp. Theor. Phys.* **102** (2006) 220, hep-ph/0507059.

[Air01] A. Airapetian *et al.* (the HERMES collaboration), *Phys. Rev. Lett.* **87** (2001) 182001, hep-ex/0106068.

[Air03] A. Airapetian *et al.* (the HERMES collaboration), *Phys. Lett. B* **567** (2003) 339, hep-ex/0210067.

[Air04] A. Airapetian *et al.* (the HERMES collaboration), *Phys. Lett. B* **585** (2004) 213, hep-ex/0312044.

[Air05a] A. Airapetian *et al.* (the HERMES collaboration), *Phys. Rev. D* **71** (2005) 012003, hep-ex/0407032.

[Air05b] A. Airapetian *et al.* (the HERMES collaboration), *Phys. Rev. Lett.* **95** (2005) 242001, hep-ex/0506018.

[Air05c] A. Airapetian *et al.* (the HERMES collaboration), *Phys. Rev. D* **71** (2005) 032004, hep-ex/0412027.

[Air05d] A. Airapetian *et al.* (the HERMES collaboration), *Phys. Rev. Lett.* **94** (2005) 012002, hep-ex/0408013.

[Air05e] A. Airapetian *et al.* (the HERMES collaboration), *Nucl. Instr. and Meth. A* **540** (2005) 68.

[Air05f] A. Airapetian *et al.*, *Nucl. Instr. and Meth. A* **540** (2005) 305.

[Air06a] A. Airapetian *et al.* (the HERMES collaboration), The beam-charge azimuthal asymmetry and deeply virtual Compton scattering, submitted to *Phys. Rev. Lett.*, hep-ex/0605108.

[Air06b] A. Airapetian *et al.* (the HERMES collaboration), Precision determination of the spin-dependent structure function g_1 of proton, deuteron and neutron, submitted to *Phys. Rev. D* (2006), hep-ex/0609039.

[Air06c] A. Airapetian *et al.* (the HERMES collaboration), *Phys. Rev. Lett.* **96** (2006) 162301, hep-ex/0510030.

[Ako02] N. Akopov *et al.*, *Nucl. Instr. and Meth. A* **479** (2002) 511.

[Akt05] A. Aktas *et al.* (the H1 collaboration), *Eur. Phys. J. C* **44** (2005) 1, hep-ex/0505061.

[Aku99] I.Akushevich, H.Böttcher, and D.Ryckbosch, RADGEN 1.0: Monte Carlo generator for radiative events in DIS on polarized and unpolarized targets, talk presented at the workshop "Monte Carlo generators for HERA physics", Hamburg, 1999, hep-ph/9906408.

[Alg76] M. J. Alguard *et al.*, *Phys. Rev. Lett* **37** (1976) 1261.

[Alg78] M. J. Alguard *et al.*, *Phys. Rev. Lett* **41** (1978) 70.

[Alt77] G. Altarelli and G. Parisi, *Nucl. Phys.B* **126** (1977) 298.

[And83] B.Andersson, *et al. Phys. Rept.* **97** (198 3) 31.

[And01] A. Andreev *et al.*, *Nucl. Instr. and Meth. A* **465** (2001) 482.

[Asc00] E. Aschenauer *et al.*, *Nucl. Instr. and Meth. A* **440** (2000) 338.

[Asc05] E.C. Aschenauer, private communication.

[Ash88] J. Ashman *et al.* (the EMC collaboration), *Phys. Lett. B* **206** (1988) 364.

[Ash89] J. Ashman *et al.* (the EMC collaboration), *Nucl. Phys. B* **328** (1989) 1.

[Aug04] W. Augustyniak *et al.*, TMC – vertex reconstruction in the presence of the HERMES transverse target magnet, version 1.0, unpublished (2004).

[Ava96] H. Avakian *et al.*, *Nucl. Instr. and Meth. A* **378** (1996) 155.

[Ava98] H. Avakian *et al.*, *Nucl. Instr. and Meth. A* **417** (1998) 69.

[Ava06] H. Avakian, Hard exclusive processes at JLab, contribution to the 2nd Workshop on the QCD Structure of the Nucleon (QCD-N^{06}), Monte Porzio Catone, Rome, Italy, June 12-16, 2006.

[Bha35] H. J. Bhabha, *Proc. Roy. Soc. (London) A* **154** (1935) 195.

[Bar93] D. P. Barber *et al.*, *Nucl. Instr. and Meth. A* **329** (1993) 79.

[Bar95] D. P. Barber *et al.*, *Phys. Lett. B* **343** (1995) 436.

[Bau80] G. Baum *et al.*, *Phys. Rev. Lett* **45** (1980) 2000.

[Bau83] G. Baum *et al.*, *Phys. Rev. Lett* **51** (1983) 1135.

[Bau02] C. Baumgarten *et al.*, *Nucl. Instr. and Meth. A* **82** (2002) 606.

[Bau03a] C. Baumgarten *et al.*, *Nucl. Instr. and Meth. A* **496** (2003) 277.

[Bau03b] C. Baumgarten *et al.*, *Nucl. Instr. and Meth. A* **508** (2003) 268.

[Bec02] M. Beckmann *et al.*, *Nucl. Instr. and Meth. A* **479** (2002) 334.

[Bel00a] A. V. Belitsky, A. Freund, and D. Müller, *Nucl. Phys. B* **574** (2000) 347, hep-ph/9912379.

[Bel00b] A. V. Belitsky *et al.*, *Phys. Lett. B* **474** (2000) 163, hep-ph/908337.

[Bel00c] A. V. Belitsky and D. Müller, *Nucl. Phys. B* **589** (2000) 611, hep-ph/0007031.

[Bel02] A. V. Belitsky, D. Müller, and A. Kirchner, *Nucl. Phys. B* **629** (2002) 323, hep-ph/0112108.

[Bel05] A. V. Belitsky and A. V. Radyushkin, *Phys. Rept.* **418** (2005) 1, hep-ph/0504030.

[Ben01] T. Benisch, *et al.*, *Nucl. Instr. and Meth. A* **471** (2001) 314.

[Ber98] S. Bernreuther *et al.*, *Nucl. Instr. and Meth. A* **416** (1998) 45.

[Bjo69] J. D. Bjorken, *Phys. Rev.* **179** (1969) 1547.

[Blo69] E. Bloom *et al.*, *Phys. Rev. Lett.* **23** (1969) 930.

[Bof03] S. Boffi, B. Pasquini, and M. Traini, *Nucl. Phys. B* **649** (2003) 243, hep-ph/0207340.

[Bof04] S. Boffi, B. Pasquini, and M. Traini, *Nucl. Phys. B* **680** (2004) 147, hep-ph/0311016.

[Bra76] F. W. Brasse *et al.*, *Nucl. Phys. B* **110** (1976) 413.

[Bra01] J. T. Brack *et al.*, *Nucl. Instr. and Meth. A* **469** (2001) 47.

[Bre69] M. Breidenbach *et al.*, *Phys. Rev. Lett.* **23** (1969) 935.

[Brü03] A. Brüll and A. Kisselev, Top/bottom misalignment for 1996-2003 data, Mailing list: offline-list@hermes.le.desy.de, June 9, 2003.

[Buc06] W. Buchmüller and C. Lüdeling, Field theory and Standard Model, lectures given at the European School of High-Energy Physics, August 2005, Kitzbühel, Austria, hep-ph/0609174.

[Buo86] J. Buon and K. Steffen, *Nucl. Instr. and Meth. A* **245** (1986) 248.

[Bur00] M. Burkardt, *Phys. Rev. D* **62** (2000) 071503, *Erratum-ibid. D* **66** (2002) 119903, hep-ph/0005108.

[Bur03a] M. Burkardt, *Int. J. Mod. Phys. A* **18** (2003) 173, hep-ph/0207047.

[Bur03b] E. Burtin *et al.*, *Nucl. Phys. A* **721** (2003) 368c.

[Cal69] C. G. Callan and D. J. Gross, *Phys. Rev. Lett.* **22** (1969) 156.

[Cam06] C. Muñoz Camacho *et al.* (the Jefferson Lab Hall A Coolaboration), Scaling tests of the cross-section for deeply virtual compton scattering (2006), nucl-ex/0607029

[Car01] L. S. Cardman *et al.*, White Paper: The Science driving the 12 GeV Upgrade of CEBAF, http://www.jlab.org/12GeV/collaboration.html (2001).

[Cer93a] CERN-Computing and network division, EPIO-experimental physics input output package, CERN program library long writeup I101 (1993).

[Cer93b] CERN-Computing and network division, GEANT: Detector description and simulation tool, CERN program library long writeup W5013 (1993).

[Che03] S. Chekanov *et al.* (the ZEUS collaboration), *Phys. Lett. B* **573** (2003) 46, hep-ex/0305028.

[Che06] S. Chen *et al.* (the CLAS Collaboration), *Phys. Rev. Lett.* **97** (2006) 072002, hep-ex/0605012.

[Cho74] A. Chodos, *et al.*, *Phys. Rev. D* **9** (1974) 3471.

[Cho01] See for example, H.-M. Choi, C.-R. Ji, and L. S. Kisslinger, *Phys. Rev. D* **64** (2001) 093006, hep-ph/0104117.

[Col77] P. D. B. Collins, An introduction to Regge theory and high-energy physics, (Cambridge, 1977).

[Col97] J. C. Collins, L. L.Frankfurt, and M. Strikman, *Phys. Rev. D* **56** (1997) 2982, hep-ph/9611433.

[Col99] J. C. Collins and A. Freund, *Phys. Rev. D* **59** (1999) 074009, hep-ph/9801262.

[Cow98] G. Cowan, Statistical data analysis (Oxford University Press, Oxford, 1998).

[Dia88] D. I. Diakonov, V. Yu. Petrov, and P. V. Pobylitsa, *Nucl. Phys. B* **306** (1988) 809.

[Die01] M. Diehl, *Eur. Phys. J. C* **19** (2001) 485, hep-ph/0101335.

[Die03] M. Diehl, *Phys. Rept.* **388** (2003) 41, hep-ph/0307382.

[Die05a] M. Diehl *et al.*, *Eur. Phys. J. C* **39** (2005) 1, hep-ph/0408173.

[Die05b] M. Diehl and S. Sapeta, *Eur. Phys. J. C* **41** (2005) 515, hep-ph/0503023.

[Dok77] Y. L. Dokshitzer, *Sov. Phys.JETP* **46** (1977) 641.

[Dre99] D.Drechsel *et al.*, *Nucl. Phys. A* **645** (1999) 145, nucl-th/9807001.

[Efr80] A. V. Efremov and A. V. Radyushkin, *Phys. Lett. B* **94** (1980) 245.

[Ell04] F. Ellinghaus, Beam-charge and beam-spin azimuthal asymmetries in deeply-virtual Compton scattering, Ph.D thesis, Berlin Humboldt-Universität, 2004.

[Ell05] F. Ellinghaus, W.-D. Nowak, A.V. Vinnikov and Z. Ye, *Eur. Phys. J. C* **46** (2006) 729, hep-ph/0506264.

[Els03] U. Elschenbroich, G. Schnell, R. Seidl, Single Spin Azimuthal Asymmetries in SIDIS off a Transversely Polarized Proton Target - MC Studies, HERMES internal report 03-007 (2003).

[Els05] U. Elschenbroich, M. Diefenthaler, Single-spin azimuthal asymmetries in semi-inclusive deep-inelastic scattering on a transversely polarirised hydrogen target, HERMES Release Report, (2005).

[Ely01] J. Ely, HERMES calorimeter position reconstruction study, HERMES internal report 01-056 (2001).

[Ely02] J. Ely, Measurement of the single spin azimuthal asymmetry in the predominantly exclusive electroproduction of photons from the proton, Ph.D thesis, University of Colorado, 2002.

[Erb68] R. Erbe *et al.* (the ABBHHM collaboration), *Phys. Rev.* **175** (1968) 1669.

[Est37] I. Estermann, O. C. Simpson, and O. Stern, *Phys. Rev.* **52** (1937) 535.

[Fey72] R. P. Feynman, Photon hadron interactions, Benjamin, (New Yorck, 1972).

[Fre03] A. Freund, M. McDermott, and M. Strikman, *Phys. Rev. D* **67** (2003) 036001, hep-ph/0208160.

[Gap06] Galina Gapienko, private communication (2006).

[Gel64] M. Gell-Mann, *Phys. Lett.* **8** (1964) 214.

[Goe01] K. Goeke, M. V. Polyakov, and M. Vanderhaeghen, *Prog. Part. Nucl. Phys.* **47** (2001) 401, hep-ph/0106012.

[Goc04] M. Gockeler *et al.* (the QCDSF collaboration), *Phys. Rev. Lett.* **92** (2004) 042002, hep-ph/0304249.

[Goc05a] M. Gockeler *et al.* (the QCDSF collaboration), *Nucl. Phys. A* **755** (2005) 537, hep-lat/0501029.

[Goc05b] M. Gockeler *et al.* (the QCDSF collaboration), *Phys. Lett. B* **627** (2005) 113, hep-lat/0507001.

[Gri72] V. N. Garibo and L. N. Lipatov, *Sov. J. Nucl. Phys.* **15** (1972) 438.

[Gro73] D. J. Gross and F. Wilczek, *Phys. Rev. Lett.* **30** (1973) 1343.

[Gui03] P. A. M. Guichon, L. Mosse, and M. Vanderhaeghen, *Phys. Rev. D* **68** (2003) 034018, hep-ph/0305231.

[Gui05] M. Guidal *et al.*, *Phys. Rev. D* **72** (2005) 054013, hep-ph/0410251.

[Had04] C. Hadjidakis, proceedings for 12th International Workshop on Deep Inelastic Scattering and QCD (DIS2004), Strbske Pleso, High Tatras, Slovakia, April 14-18, 2004, hep-ex/0405078.

[Hag03] P. Hagler *et al.* (the LHPC collaboration), *Phys. Rev. D* **68** (2003) 034505, hep-lat/0304018.

[Hil03] A.Hillenbrand (for the HERMES collaboration), Proceedings of the 11th international workshop on deep-inelastic scattering, St.Petersburg, Russia, April 2003.

[Hof61] R. Hofstadter, The electron-scattering method and its aplication to the structure of nuclei and nucleons, **Nobel Lecture**, December 11, 1961.

[Hof00] G. Hoffstaetter, proceedings for 7th European Particle Accelerator Conference (EPAC 2000), Vienna, Austria, June 26-30, 2000.

[Hos02] N. d'Hose *et al*, *Nucl. Phys. A* **711** (2002) 160c.

[Ing97] G. Ingelman, A. Edin, and J. Rathsman, *Comput. Phys. Commun.* **101** (1997) 108.

[Jaf90] R. L. Jaffe and A. Manohar, *Nucl. Phys. B* **337** (1990) 509.

[Jam80] F. James, *Nucl. Phys. B* **172** (1980) 475.

[Ji97a] X. Ji, *Phys. Rev. Lett.* **78** (1997) 610, hep-ph/9603249.

[Ji97b] X. Ji, *Phys. Rev. D* **55** (1997) 7114, hep-ph/9609381.

[Ji97c] X. Ji, W. Melnitchouk, and X. Song, *Phys. Rev. D* **56** (1997) 5511, hep-ph/9702379.

[Ji98a] X. Ji, *J. Phys. G* **24** (1998) 1181, hep-ph/9807358.

[Ji98b] X. Ji and J.Osborne, *Phys. Rev. D* **57** (1998) 1337, hep-ph/707254.

[Ji98c] X. Ji and J.Osborne, *Phys. Rev. D* **58** (1998) 094018, hep-ph/9801260.

[Kai97] R. Kaiser (for the HERMES PID group), Particle identification at HERMES, HERMES internal report 97-025 (1997).

[Kis06] A. Kisselev, private communication, 2006.

[Kiv01] N. Kivel, M. V. Polyakov, and M. Vanderhaeghen, *Phys. Rev. D* **63** (2001) 114014, hep-ph/0012136.

[Kiv03] N. Kivel and L. Mankiewicz, *Nucl. Phys. B* **672** (2003) 357, hep-ph/0305207.

[Kol98] M. Kolstein, Exclusive ρ^0–meson electroproduction at HERMES, Ph.D thesis, Vrije Universiteit Amsterdam, 1998.

[Kop05] M. Kopytin (for the HERMES collaboration), *AIP Conf. Proc.* **792** (2005) 424.

[Kor02] V. A. Korotkov and W.-D. Nowak, *Eur. Phys. J. C* **23** (2002) 455, hep-ph/0108077.

[Kow86] S. Kowalski and H. A. Enge, computer code RAYTRACE, unpublished (1986).

[Kra05] B. Krauss, Deeply virtual Compton scattering and the HERMES recoil detector, Ph.D thesis, Erlangen-Nürnberg Universität, 2005.

[Kro95] P. Kroll, M. Schurmann, and P. A. M. Guichon, *Nucl. Phys. A* **598** (1996) 435, hep-ph/9507298.

[Lea88] E. Leader and M. Anselmino, *Z. Phys. C* **41** (1988) 239.

[Lea01] E. Leader, *Spin in Particle Physics* (Cambridge Monographs in Particle Physics, Nuclear Physics and Cosmology (No. 15), 2001).

[Lep79] G. P. Lepage and S. J. Brodsky, *Phys. Lett. B* **87** (1979) 359.

[Lip75] L. N. Lipatov, *Sov. J. Nucl. Phys.* **20** (1975) 94.

[Lyk06] J. D. Lykken, *the standard model: Alchemy and Astrology*, presented at the conference "Physics at LHC", 3-8 July 2006, hep-ph/0609274.

[Man98] L. Mankiewicz *et al.*, *Phys. Lett. B* **425** (1998) 186, hep-ph/9712251.

[Man99] L. Mankiewicz *et al.*, *Phys. Rev. D* **59** (1999) 017501, hep-ph/9712508.

[Mar98] A. D. Martin *et al.*, *Eur. Phys. J. C* **4** (1998) 463, hep-ph/9803445.

[Méo05] F. Méot and S. Valero, zgoubi users' guide, DAPNIA-02-395 (2002).

[Mil06] A. Miller, private communication (2006).

[Mo69] L. W. Mo and Y. S. Tsai, *Rev. Mod. Phys.* **41** (1969) 205.

[Möl32] C. Möller, *Ann. Phys.* **14** (1932) 531.

[Mul94] D. Müller *et al.*, *Fortschr. Phys.* **42** (1994) 101, hep-ph/9812448.

[Mul06] D. Müller, *Phys. Lett. B* **634** (2006) 227, hep-ph/0510109.

[Mus00] I. V. Musatov and A. V. Radyushkin, *Phys. Rev. D* **61** (2000) 074027, hep-ph/9905376.

[Nas03] A. Nass *et al.*, *Nucl. Instr. and Meth. A* **505** (2003) 633.

[Neg04] J. W. Negele *et al.* (the LHPC collaboration), *Nucl. Phys. B (Proc. Suppl.)* **128** (2004) 170, hep-lat/0404005.

[Nez05] P. D. Nezza, private communication (2005).

[Nog04] S. Noguera, L. Theussl, and V.. Vento, *Eur. Phys. J. A* **20** (2004) 483, hep-ph/0409059.

[Oss05] J. Ossmann *et al.*, *Phys. Rev. D* **71** (2005) 034011, hep-ph/0411172.

[Par76] G. Parisi and R. Petronzio, *Phys. Lett. B* **62** (1976) 331.

[Pas05] B. Pasquini, M. Pincetti, and S. Boffi, *Phys. Rev. D* **72** (2005) 094029, hep-ph/0510376.

[PDG04] S. Eidelman et al., Review of particle physics, *Phys. Lett. B* **592** (2004) 1.

[Pen00] M. Pettinen, M. V. Polyakov, and K. Goeke, *et al.*, *Phys. Rev. D* **62** (2000) 014024, hep-ph/9909489.

[Pet98] V. Y. Petrov *et al.*, *Phys. Rev. D* **57** (1998) 4325, hep-ph/9710270.

[Pol73] H. D. Politzer, *Phys. Rev. Lett.* **30** (1973) 1346.

[Pol99] M. V. Polyakov and C. Weiss, *Phys. Rev. D* **60** (1999) 114017, hep-ph/9902451.

[Pum02] J. Pumplin *et al.*, JHEP **0207** (2002) 012, hep-ph/0201195.

[Rad97] A. V. Radyushkin, *Phys. Rev. D* **56** (1997) 5524, hep-ph/9704207.

[Rad98] A. V. Radyushkin, *Phys. Rev. D* **58** (1998) 114008, hep-ph/9803316.

[Rad99] A. V. Radyushkin, *Phys. Rev. D* **59** (1999) 014030, hep-ph/9805342.

[Rad01] A. V. Radyushkin, At the Frontier of Particle Physics / Handbook of QCD, edited by M. Shifman (World Scientific, Singapore, 2001), hep-ph/0101225.

[Sch02] P. Schweitzer, S. Boffi, and M. Radici, *Phys. Rev. D* **66** (2002) 114004, hep-ph/0207230.

[Sch03] P. Schweitzer, M. Colli, and S. Boffi, *Phys. Rev. D* **67** (2003) 114022, hep-ph/0303166.

[Sco03] S. Scopetta and V. Vento, *Eur. Phys. J. A* **16** (2003) 527, hep-ph/0201265.

[Sco04] S. Scopetta and V. Vento, *Phys. Rev. D* **69** (2004) 094004, hep-ph/0307150.

[Sco05a] S. Scopetta and V. Vento, *Phys. Rev. D* **71** (2005) 014014, hep-ph/0410191.

[Sco05b] S. Scopetta, *Phys. Rev. D* **72** (2005) 117502, hep-ph/0509287.

[Sjö94] T. Sjöstrand, *Comput. Phys. Commun* **82** (1994) 74.

[Sok64] A. A. Sokolov and I. M. Ternov, *Sov. Phys. Doklady* **8** (1964) 1203.

[Ste01] S. Stepanyan *et al.* (the CLAS collaboration), *Phys. Rev. Lett.* **87** (2001) 182002, hep-ex/0107043.

[Suz98] K. Suzuki and W. Weise, *Nucl. Phys. A* **634** (1998) 141.

[Tan03] H. Tanaka *et al.*, *Nucl. Instr. and Meth. A* **515** (2003) 725.

[Tib03] B. C. Tiburzi and G. A. Miller, *Phys. Rev. D* **67** (2003) 113004, hep-ph/0212238.

[Van99] M. Vanderhaeghen, P. A. M. Guichon, M. Guidal, *Phys. Rev. D* **60** (1999) 094017, hep-ph/9905372.

[Van00] M. Vanderhaeghen, *et al.*, *Phys. Rev. C* **62** (2000) 025501, hep-ph/0001100.

[Van03] M. Vanderhaeghen, P. A. M. Guichon, M. Guidal, private communication, 2003.

[Ye05] Z. Ye (for the HERMES collaboration), proceedings of International Europhysics Conference on High Energy Physics, Lisboa, Portugal, July 21-27, 2005 (HEP2005), *PoS(HEP2005)120*, hep-ex/0512010.

[Zwe64] G. Zweig, *CERN preprint* 8419/TH-412 (1964).

Acknowledgements

I would like to thank my advisor Wolf-Dieter Nowak for his kind support and guidance in general and in particular on the data analysis. He gave me the opportunity to work on the HERMES experiment with very interesting topics. I would like to thank my advisor James Stewart for his kind support and guidance during my detector studies, from which I have gained valuable knowledge. My advisors were always there for my questions and discussions.

I would like to thank Prof. Rolf-Dieter Heuer for taking over the role as my official advisor at Universität Hamburg. I would like to thank Yorck Holler for providing me a Ph. D student position at DESY and for all the supports throughout this period. I would like to thank Elke Aschenauer who suggested and helped me to become a Ph. D stuent at HERMES, and provided continuous advices on my studies.

Concerning my data analysis on DVCS, I would like to thank Hayg Guler, Mikhail Kopytin, Andy Miller, Morgan Murray, and all the other HERMES DVCS group members, for a great collaboration. Special thanks to Frank Ellinghaus for helping me to start the analysis, and for all the answers to my numerous questions and discussions. I would like to thank Jochen Volmer for explaining me how to run the VGG code, and Bernhard Krauss for his help on Monte Carlo simulations. Thanks to Markus Diehl and Andrey Vinnikov for answers to my questions on theory and discussions.

Concerning my detector studies, I would like to thank Martin Dohlus, Andre Gade, Ingrid Gregor, Ivana Hristova, Jörg Ludwig, Scott Lumsden, Jorgen Lund-Nielsen, Matthias Reinecke, Phil Tait, Arne Vandenbroucke, Christian Vogel, and Susan Wipf. Special thanks to Volker Prahl and Manfred Wendt. Without them, I would not have been able to make the RF test for the silicon recoil detector.

I would like to thank Paolo Lenisa, who supported me for studying the intra-beam scattering effect in Atomic Beam Souces. Thanks to Alexander Nass, Davide Reggiani, Michelle Stancari, Phil Tait, and Marco Capiluppi, for valuable help and discussions.

Thanks to Morgan Murray for a careful reading of the thesis, and to Andrey Vinnihov for proofreading chapters 2 and 3.

I have enjoyed the great atmosphere inside the HERMES collaboration. Special thanks to Ulrike Elschenbroich, Larry Felawka, Dominik Daniel Gabbert, Galina Gapienko, Sebastian Haan, Cythia Hadjidakis, Delia Hasch, Alexander Kisselev, Sabine Krohn, Prof. Yajun Mao, Pasquale Di Nezza, Evelyn Olabisi, and Caroline Riedl.

Finally, I would like to thank my wife, Wenjuan, for all the understandings and supports throughout these years.